

PULSAR POLARISATION AS A DIAGNOSTIC TOOL

A THESIS SUBMITTED TO THE UNIVERSITY OF MANCHESTER
FOR THE DEGREE OF DOCTOR OF PHILOSOPHY
IN THE FACULTY OF ENGINEERING AND PHYSICAL SCIENCES

2013

By

Phrudth Jaroenjittichai

School of Physics and Astronomy
Jodrell Bank Centre for Astrophysics

Contents

Declaration	10
Copyright Statement	11
Publications	12
Acknowledgements	13
1 Introduction	19
1.1 Pulsar Toy Model	27
1.2 Known Methods	33
2 Obtaining the Geometry	39
2.1 Polarisation Data	39
2.2 Combined- χ^2 Method	43
2.3 Fitting Routine	47
2.4 Results	49
2.4.1 Interesting Cases	49
2.5 Discussions	56
2.5.1 On the RVM $_{\rho-W}$ Method	56
2.5.2 Beam Alignment	57
2.5.3 Averaged Beam Map	60
3 Modes of Wave Propagation	66
3.1 Theoretical Background	67
3.2 Observational Consequences	74
3.3 Prediction versus Observations	79
3.4 Conclusions	83

4	Polarisation Calibration	85
4.1	Mathematical Basis	86
4.2	Pre-calibration	89
4.3	Measurement Equation Modelling	97
4.4	Matrix Template Matching	111
4.5	Polarisation Calibration of PSR B1822–09	121
4.6	Summary	127
5	A Study of PSR B1822–09	129
5.1	Known Characteristics	129
5.1.1	Petrova’s Model	132
5.2	Observations	134
5.3	Results	137
5.3.1	Mode-separated Pulse Profiles	137
5.3.2	Single-pulse Analysis	152
5.3.3	Modal Statistics	169
5.4	Discussions	180
5.4.1	Pulse Profiles	180
5.4.2	Petrova’s Model: the PC-IP dilemma	186
6	From Pulse Radiation to Pulsar Kinetics	190
6.1	B1931+24: The One Where It All Began	190
6.2	A Magnetospheric Model	193
6.3	From Intermittency to Profile-switching	198
6.3.1	Charged Current and Flux Density	198
6.3.2	Impact On Polarisation Properties	201
6.4	Conclusions	205
7	Summary	206
A	Plots of $\text{RVM}_{\rho-W}$ Fits	211
B	Simulations of the Propagation Model	238

total word count: 49500

List of Tables

2.1	Solutions from the RVM and RVM $_{\rho-W}$ methods.	50
3.1	Combinations of plasma parameters.	74
3.2	Summary of distortions from plasma parameters.	74
3.3	Statistics of the mode classification.	80
4.1	Details of the twelve observations of PSR B1822–09.	127
5.1	Relative amplitudes of the PC and IP.	148
5.2	Relative amplitudes of the LD, MD and TR.	149
5.3	Relative amplitudes and S of the LD, MD and TR.	162
5.4	Mode-switching statistics of twelve 40-min observations.	170
5.5	Modal properties of PSRs B1822–09 and B0943+10.	181
5.6	Profile reversal of PSRs B1822–09 and B0826–34.	181
6.1	Properties of intermittent pulsars and PSR B1822–09.	193
6.2	The $\dot{\nu}$ ratio and relationship between S and $\bar{\rho}$	201
B.1	$r_{em} = 100$ km, $\lambda = 100$	239
B.2	$r_{em} = 100$ km, $\lambda = 1000$	240
B.3	$r_{em} = 100$ km, $\lambda = 10000$	241
B.4	$r_{em} = 300$ km, $\lambda = 100$	242
B.5	$r_{em} = 300$ km, $\lambda = 1000$	243
B.6	$r_{em} = 300$ km, $\lambda = 10000$	244
B.7	$r_{em} = 500$ km, $\lambda = 100$	245
B.8	$r_{em} = 500$ km, $\lambda = 1000$	246
B.9	$r_{em} = 500$ km, $\lambda = 10000$	247

List of Figures

1.1	$P - \dot{P}$ diagram.	22
1.2	Configuration of the pulsar magnetosphere.	23
1.3	Pulse profile of PSR J0742-2822 (3 GHz).	25
1.4	Diagram of the hollow cone beam.	25
1.5	Configuration of the pulsar beam.	29
1.6	The RVM diagram, and inner and outer LOS definitions	30
1.7	The beam width and dipole geometry	31
1.8	Simulated ρ_{90} as a function of P	35
1.9	Simulation to determine the accuracy of $\frac{W_{core}}{2} \approx \frac{\rho_{core}}{\sin \alpha}$	37
2.1	Example of the diverging problem (PSR J0304+1932).	41
2.2	Simulated PPA swings of α from 0° to 180°	42
2.3	Fitting improvements with the RVM $_{\rho-W}$ (PSR B0738-4042).	48
2.4	Orthogonal-rotator solutions of PSR J1057-5226.	52
2.5	Aligned-rotator solutions of PSR J1057-5226.	54
2.6	Comparison of α and α_{halfk}	57
2.7	Resulting PDFs for the beam alignment analysis.	61
2.8	Statistics of the PDFs for the beam alignment analysis.	62
2.9	The averaged beam maps.	63
3.1	Refractive indices and the angle between \mathbf{k} and \mathbf{B}	67
3.2	Beskin & Philippov (2012) diagram of the hollow-core-cone model.	70
3.3	The initial plasma distribution.	72
3.4	Examples of the simulated plasma perturbation.	77
3.5	Plasma simulations with different values of α	78
3.6	Contradictory case of PSR J1146-6030.	82
4.1	CAL file and the <i>pac</i> solutions.	90
4.2	<i>pac</i> -calibrated profile of PSR B0740-28.	91

4.3	<i>EPN</i> profiles of PSRs B0740–28 and B0950+08.	92
4.4	Example of PSR B0950+08 and CAL files (<i>pac</i>).	93
4.5	<i>pac</i> solutions derived from the two CAL file in Fig. 4.4	94
4.6	Example of the <i>MEM</i> method by van Straten (2004).	99
4.7	<i>pac</i> -calibrated profiles and template of PSR B0355+54 (<i>MEM</i>).	101
4.8	<i>pac</i> solutions of the four CAL files in the previous plot.	102
4.9	Unsuccessful calibration by the <i>MEM</i> method.	103
4.10	Recovered profiles from the <i>MEM</i> method.	104
4.11	Fitting χ^2 and G by the <i>MEM</i> method.	105
4.12	Resulting γ and ϕ from the <i>MEM</i> method.	106
4.13	Resulting ϵ from the <i>MEM</i> method.	107
4.14	Resulting θ from the <i>MEM</i> method.	108
4.15	Calibrated PPA as a function of frequency.	109
4.16	Calibrated PPA as a function of frequency (<i>continued</i>).	110
4.17	Template of PSR B0950+08 for <i>MTM</i> method.	114
4.18	Calibrated results from self-test of <i>MTM</i> method.	115
4.19	Best-fit solutions of self-test of <i>MTM</i> method.	116
4.20	Best-fit χ^2 and leakage of self-test of <i>MTM</i> method.	117
4.21	Resulting profiles of July observation by <i>MTM</i> method.	118
4.22	Frequency-dependence check of the results in the previous figure.	119
4.23	Best-fit solutions of July observation by <i>MTM</i> method.	120
4.24	Best-fit χ^2 of July observation by <i>MTM</i> method.	121
4.25	<i>pac</i> -calibrated observations of PSR B1822–09.	122
4.26	<i>pac</i> -calibrated observations of PSR B1822–09 (<i>continued</i>).	123
4.27	Frequency dependency check of PSR B1822–09.	124
4.28	Frequency dependency check of PSR B1822–09 (<i>continued</i>).	125
4.29	Frequency dependency check of PSR B1822–09 (<i>continued</i>).	126
5.1	Mode-separated profiles of PSR B1822–09.	131
5.2	The PPAs after profile alignment.	134
5.3	Mode-separated profiles of individual observation.	138
5.4	Mode-separated profiles of individual observation (<i>continued</i>).	139
5.5	Mode-separated profiles of individual observation (<i>continued</i>).	140
5.6	Mode-separated profiles of individual observation (<i>continued</i>).	141
5.7	Overlays plots of PPAs and MPs of the B and Q modes.	142
5.8	Overlays plots of IPs of the B and Q modes.	143

5.9	Comparisons of the B- and Q-mode PPAs.	143
5.10	Overlay plots at 325 MHz (BMR10).	145
5.11	Average profiles by the GMRT and Parkes telescopes.	146
5.12	The PPAs at 325, 600 and 1532 MHz.	151
5.13	Example of mode-switching in 40 minutes.	153
5.14	Sequence of single pulses in the B mode.	155
5.15	Sequence of single pulses in the Q mode.	156
5.16	Phase-resolved fluctuation spectrum of the Q-mode MP.	157
5.17	Phase-resolved fluctuation spectrum of the B-mode MP.	158
5.18	Pulse's peak locations as a function of pulse number.	160
5.19	Average profiles of the LD, MD and TR.	161
5.20	Flux density distribution of the MD, LD and TR.	164
5.21	Peak fluxes of the MP and IP with pulse number.	165
5.22	Peak fluxes of the PC and IP with pulse number.	166
5.23	PPA histograms of the B- and Q-mode MPs.	168
5.24	PPA histogram of the PC.	169
5.25	Lyne et al. (2010) plot of A_{PC} vs. MJD.	170
5.26	Relative amplitudes of the PC and IP of twelve observations.	172
5.27	A_{PC-B} and S_B/S_Q of twelve observations.	173
5.28	Relative amplitudes of DFB observations since November 2008.	174
5.29	Histograms of A_{PC} of DFB observations since November 2008.	175
5.30	Histograms of simulated A_{PC} to reproduce the observation.	176
5.31	Simulated A_{PC} as a function of B-mode time.	177
5.32	Overlay plots of B1822-09 at 325 Mhz (LMR12).	182
5.33	Overlay plots of the profiles of PSR B0943+10.	183
5.34	Overlay plots of the B-mode profiles observed at different epoch.	183
5.35	Plot comparing the shifted PPAs and the observed PPAs.	186
5.36	Best-fit of the RVM to the PPAs in shifted PPAs.	188
6.1	Li et al. (2012b) plot of $\dot{\nu}_{ON}/\dot{\nu}_{OFF}$ vs. α	194
6.2	Pulse profile of PSR B1931+24 by Arecibo Telescope.	196
6.3	Pulse profile of PSR J1832+0029 by the Lovell Telescope.	197
6.4	The beam map diagram for S vs. $\bar{\rho}$ relation.	202
A.1	PSR J0631+1036.	212
A.2	PSR J0738-4042.	213

A.3	PSR J0742-2822.	214
A.4	PSR J0835-4510.	215
A.5	PSR J0907-5157.	216
A.6	PSR J0922+0638.	217
A.7	PSR J1048-5832.	218
A.8	PSR J1057-5226.	219
A.9	PSR J1110-5637.	220
A.10	PSR J1253-5820.	221
A.11	PSR J1352-6803.	222
A.12	PSR J1535-4114.	223
A.13	PSR J1536-3602.	224
A.14	PSR J1539-5626.	225
A.15	PSR J1641-2347.	226
A.16	PSR J1645-0317.	227
A.17	PSR J1700-3312.	228
A.18	PSR J1705-1906.	229
A.19	PSR J1733-3716.	230
A.20	PSR J1807-0847.	231
A.21	PSR J1835-1106.	232
A.22	PSR J1901-0906.	233
A.23	PSR J1904+0004.	234
A.24	PSR J1917+1353.	235
A.25	PSR J1932+1059.	236
A.26	PSR J2048-1616.	237

The University of Manchester

ABSTRACT OF THESIS submitted by Phrudth Jaroenjittichai
for the Degree of Doctor of Philosophy and entitled
“Pulsar Polarisation As A Diagnostic Tool”,
March 2013

The geometry of pulsar beams is one of the intrinsic properties of neutron stars, governing the pulse-profile phenomenon and other aspects of pulsar astronomy. With a number of pulsars in our dataset, their beam geometry is derived from the polarisation position angle (PPA) using the simple polar cap emission and dipole field model. This includes the rotating vector model (RVM), for which the solutions can hardly be constrained or fail to be consistent because of the limitations of the model itself. The inconsistencies in the results suggest that the initial PPAs can be strongly perturbed by additional parameters above the emission altitude, such as the plasma medium or rotational aberration effects, after which their characteristic shape is no longer related to the geometry via the RVM. We investigate further into the effects of wave propagation in the pulsar magnetosphere, and find an indication that, in most cases, the RVM-calculated PPAs are likely to be altered by plasma effects.

In recent years, there have been an increasing number of intermittent and mode-switching pulsars observed to have their radio pulse profiles correlated with the change in pulsar spin frequency ($\dot{\nu}$) (e.g. Lorimer et al. 2012, Lyne et al. 2010). These two phenomena are understood to be related via the states of plasma in the magnetosphere. As one such pulsar, and also one with known geometry and other astonishing behaviour, PSR B1822–09 is studied in terms of the mode-switching properties, the hollow-cone model and the wave propagation in the magnetosphere. We also study the model for explaining the intermittent pulsars PSRs B1931+24, J1841+0500 and J1832+0029, and find it can be consistently applied for PSRs B1822–09 and B0943+10, and other profile-switching pulsars. However, aspects of the conclusions are limited because of the lack of understanding of the connection between the radio flux and the states of plasma. We are also able to use the difference in the PPAs between two states of PSR B0943+10 to predict the change in plasma states and $\dot{\nu}$, which cannot be measured directly from timing analysis as its switching timescale is too short.

Declaration

No portion of the work referred to in this thesis has been submitted in support of an application for another degree or qualification of this or any other university or other institution of learning.

Copyright Statement

- i. The author of this thesis (including any appendices and/or schedules to this thesis) owns certain copyright or related rights in it (the Copyright) and he has given The University of Manchester certain rights to use such Copyright, including for administrative purposes.
- ii. Copies of this thesis, either in full or in extracts and whether in hard or electronic copy, may be made only in accordance with the Copyright, Designs and Patents Act 1988 (as amended) and regulations issued under it or, where appropriate, in accordance with licensing agreements which the University has from time to time. This page must form part of any such copies made.
- iii. The ownership of certain Copyright, patents, designs, trade marks and other intellectual property (the Intellectual Property) and any reproductions of copyright works in the thesis, for example graphs and tables (Reproductions), which may be described in this thesis, may not be owned by the author and may be owned by third parties. Such Intellectual Property and Reproductions cannot and must not be made available for use without the prior written permission of the owner(s) of the relevant Intellectual Property and/or Reproductions.
- iv. Further information on the conditions under which disclosure, publication and commercialisation of this thesis, the Copyright and any Intellectual Property and/or Reproductions described in it may take place is available in the University IP Policy¹, in any relevant Thesis restriction declarations deposited in the University Library, The University Librarys regulations² and in The Universitys policy on presentation of Theses

¹<http://www.campus.manchester.ac.uk/medialibrary/policies/intellectualproperty.pdf>

²<http://www.manchester.ac.uk/library/aboutus/regulations>

Publications

Refereed Publications and Conference Contributions

- Guillemot, L., Johnson, T. J., Venter, C., Kerr, M., Pancrazi, B., Livingstone, M., Janssen, G. H., **Jaroenjittichai, P.**, Kramer, M., Cognard, I., Stappers, B. W., Harding, A. K., Camilo, F., Espinoza, C. M., Freire, P. C. C., Gargano, F., Grove, J. E., Johnston, S., Michelson, P. F., Noutsos, A., Parent, D., Ransom, S. M., Ray, P. S., Shannon, R., Smith, D. A., Theureau, G., Thorsett, S. E. and Webb, N, “Pulsed Gamma Rays from the Original Millisecond and Black Widow Pulsars: A Case for Caustic Radio Emission?”, *ApJ*, 744, 33.

In preparation

- Beskin, V. S., **Jaroenjittichai, P.**, Kramer, M., Philippov A. A., “On the Mean Profiles of Radio Pulsars II: Identifying the mode”.
- **Jaroenjittichai, P.**, Kramer, M., et al., “From Intermittency to Mode-switching Phenomena of Radio Pulsars: A case study of PSR B1822–09”.

Acknowledgements

This thesis would have been impossible without the guidance, help and a truck load of patience from everyone, one way or another.

First and foremost, my gratitude to Prof. Michael Kramer who, apart from all the supervision and encouragement, has taught me that doing research is not always about getting ground-breaking discoveries, but rather the joy along the way.

I would also like to thank:

Patrick Weltevrede for countless discussions and technical help, especially that he used up his pen in correcting my thesis!, and also thank to Ben Stappers—whom I didn't have much time to write a proper acknowledgement for helping me with my MSc thesis—for always having time for any pulsar- or non-pulsar-related queries and certainly a smooth ride to Jodrell on (almost) every Tuesday.

Prof. Andrew Lyne, Christ Jordan, Cristobal, Gemma and Cees, and past and present staffs and students in the JBCA-Bonn Pulsar family. I specially thank to Mark Purver (yes, it is the same Mark who read my MSc thesis) for help proof-reading this thesis as well, and also for being our generous landlord.

Our collaborators Simon Johnston for the polarisation data from the Parkes telescope, Vasily Beskin and Alexander Sasha Philippov for our work on the propagation model.

Ajarn Busaba Kramer for all the supports and introducing me to the pulsar group, and also for lending me the rice cooker every time I was in Bonn.

Venerable Khammai Dhammasami, my friends Doi and Top, and also the sat-down comedian, His Emptiness Ajarn Brahm, for truly showing, if not a stairway

to heaven, the door to heart of Buddhism.

For all the friendships, P' Tor, P' Nawin, P' Yai, P' Kai, P' Yim, P' Pak, P' Su, Adyda, P' Jonathan, Kao Issariya, Ying Tamu, Surasak (Ken), members of the TSM, and our kind landlady and staffs at the Crazy Wendy's.

Being an introvert as one can be, I would also like to thank to those almost-special friends, living afar in the future (GMT+7), at the present (GMT) and in the past (GMT-4). They have been giving me comfort, sometimes unknowingly.

Lastly, I would like to thank my parents, who raised me well to be a rebellious curiosity-led character, and also many thanks to my little sister, who, apart taking out the thrash, cooked me slowly-prepared-but-delicious meals for over two years, while she was in the UK.

It feels really unnatural for me to reserve these thankfulness to those who actually involved in this thesis (that I am aware of). A more convenient way is for me to therefore thank to all the things and beings in the past, those at the present moment—as I'm currently typing and deleting back and forth, while constantly looking at the clock—and in the future to those who is reading this very line—at least to remind my future self that we actually did accomplish something :-)

This PhD-studentship is gratefully supported by the Thai Ministry of Science and Technology, i.e. of all the taxes from *almost* all the Thai people.

Phrudth Jaroenjittichai
Manchester, March 2013

Dedicated to suchness

...

So, so you think you can tell
Heaven from Hell,
Blue skies from pain.
Can you tell a green field from a cold steel rail?
A smile from a veil?
Do you think you can tell?
And did they get you to trade your heroes for ghosts?
Hot ashes for trees?
Hot air for a cool breeze?
Cold comfort for change?
And did you exchange a walk on part in the war
For a lead role in a cage?
How I wish, how I wish you were here.
We're **all** just lost souls swimming in a fish bowl, year after year,
Running over the same old ground.
What have you found?
The same old fears.
Wish you were here.

...

–Wish You Were Here, PF–

Chapter 1

Introduction

Pulsars are believed to be rapidly rotating, strongly magnetised neutron stars, which are remnants of massive stars. Due to their strong co-rotating magnetic fields ($\sim 10^{8-14}$ G), they produce radio photons, originating from accelerated charged particles, which form into conic emission beams from both of the magnetic poles. And as the stars rotate, the radio beams sweep past the Earth through the vast space of the galaxy (known as ‘the lighthouse effect’). Series of radio pulses with periods equal to the stars’ rotational periods can be observed if one or both beams sweep past the Earth.

Neutron stars are born from supernova explosions, the catastrophic gravitational collapse of exhausted massive stars ($\sim 6 - 15$ solar masses) (Lyne & Smith 2004). The collapse of a star conserves the angular momentum and the magnetic flux of the progenitor star, which results in a rapid rotating object with a strong magnetic field. Theoretical models predicts neutron star masses ranging from $0.5 - 2$ solar masses and radii of $10 - 12$ km, depending on assumptions about their composition (Lattimer & Prakash 2001). The only possible mass measurements have been made through timing binary systems. Pulsar timing is the process where a ‘timing model’, which contains rotational information (and orbital information for binary systems) about the star, is created or improved using the measured ‘times of arrival’ (TOAs) of pulses. From 24 binary systems, the measured masses range from 0.7 to 2.7 solar masses (Stairs 2004; Freire et al. 2008). Astronomers often use canonical values of 1.4 solar masses and 10 km for the star’s mass and radius for the purposes of calculations.

Because pulsars lose their rotational energy mostly via the magnetic dipole radiation of an oblique rotator (Jackson 1962) and a braking-torque mechanism

due to the electric current caused by the escaping charged particles (pulsar winds) (e.g. Harding et al. 1999), their pulse periods (P) slightly increase over time which can be measured as the rate of the change in P (\dot{P}). P and \dot{P} serve astronomers as two ‘direct’ observables, which are used further to calculate other properties, e.g. the characteristic magnetic field strength (B), the characteristic age (τ) and the loss rate of rotational energy (\dot{E}). The P - \dot{P} diagram in Fig. 1.1 shows a distribution of P and \dot{P} of known pulsars and the contours of B , τ and \dot{E} .

Pulsars can be categorised into two main types, normal pulsars (main group in the middle) and millisecond pulsars (bottom left corner). Having shorter periods and weaker magnetic fields, millisecond pulsars (MSPs) were born as normal pulsars but have been ‘spun up’ during the mass transfer phase when their companion stars were in a red giant phase (e.g. Lyne & Smith 2004). They are sometimes called ‘recycled pulsars’.

Assuming that pulsars lose all of their rotational energy through magnetic dipole radiation¹, one can relate the surface magnetic field B_s with P and \dot{P} as

$$B_s = \sqrt{\frac{3c^2}{8\pi^2} \frac{I P \dot{P}}{r^6 \sin^2 \alpha}}, \quad (1.1)$$

where c is the speed of light in a vacuum, and I and r are the moment of inertia and the radius of neutron star. α is the inclination angle, measured from the rotation to the magnetic axes. The characteristic age of a pulsar (τ) is derived as

$$\tau = \frac{P}{2\dot{P}}. \quad (1.2)$$

Using canonical values for $I = 10^{38}$ kg m² and $r = 10$ km and assuming $\alpha = 90^\circ$, the above two characteristic properties can be calculated as

$$\begin{aligned} B_s &= 3.2 \times 10^{19} \times \sqrt{P \dot{P}} \text{ Gauss}, \\ \tau &= 15.8 \times 10^{-15} \times \frac{P}{\dot{P}} \text{ Myr}, \end{aligned} \quad (1.3)$$

which are plotted in Fig. 1.1. See Lorimer & Kramer (2005) for more details.

Because of the extremely strong induced electric field, caused by the rotating

¹This is not strictly true as it has been shown that the energy loss due to pulsar winds is also significant (Kramer et al. 2006).

magnetic dipole, streams of charged particles are extracted from the neutron star surface and accelerated upwards. Goldreich & Julian (1969) show that the induced electric fields, for an aligned rotator case, will extract plasma from the star until the electric field due to the charges balances the induced fields. The required charge density is known as the ‘Goldreich-Julian density’,

$$\rho_{GJ} = \frac{B_s}{cP}. \quad (1.4)$$

Fig. 1.2 shows a configuration of the magnetic field structure which depends on the inclination angle (α) and on the size of the light cylinder, an abstract cylinder in which the tangential velocity of the co-rotating field lines reaches the speed of light ($R_{LC} = cP/2\pi$). The pulsar’s magnetised plasma-filled atmosphere (or ‘magnetosphere’), which is strongly governed by the field’s structure, is divided into the open- and closed-field-line regions.

In the open-field-line zone above the magnetic poles, or the ‘polar cap’, streams of charged particles are accelerated upwards along the magnetic field lines, from which radio photons are generated and form two emission beams centred on the magnetic axis at opposite sides of the neutron star. The fact that pulsars have high brightness temperatures (10^{35} K) indicates that the radio emission mechanism must be coherent. However, it has been suggested that the Goldreich-Julian density is not enough to produce sufficient luminosity and a plasma multiplication process is required. Such a process is predicted to take place in a charge depletion region or plasma gap in the polar cap (Sturrock 1971; Ruderman & Sutherland 1975). In this gap, the charged particles are accelerated along the field lines, approaching relativistic energies (the Lorentz factor $\gamma 10^{6-7}$), because pulsars keep losing the charged particles in the open-field-line zone and never reach a saturated state. Via curvature radiation, these accelerating charged particles emit γ -ray photons which split into electron-positron pairs in the presence of strong magnetic fields (pair-production) (e.g. Arons 1983). As a result, the particles’ energy distribution is reduced, while the particle number density is increased by a factor of 10 to 10^4 (e.g. Hibschan & Arons 2001). The second and later generations of charged particles travel further along the field lines, which can then produce radio photons.

In contrast to the open-field-line zone, the closed-field-line region is filled with plasma which is tightly confined within the magnetic field and is co-rotating with the neutron star.

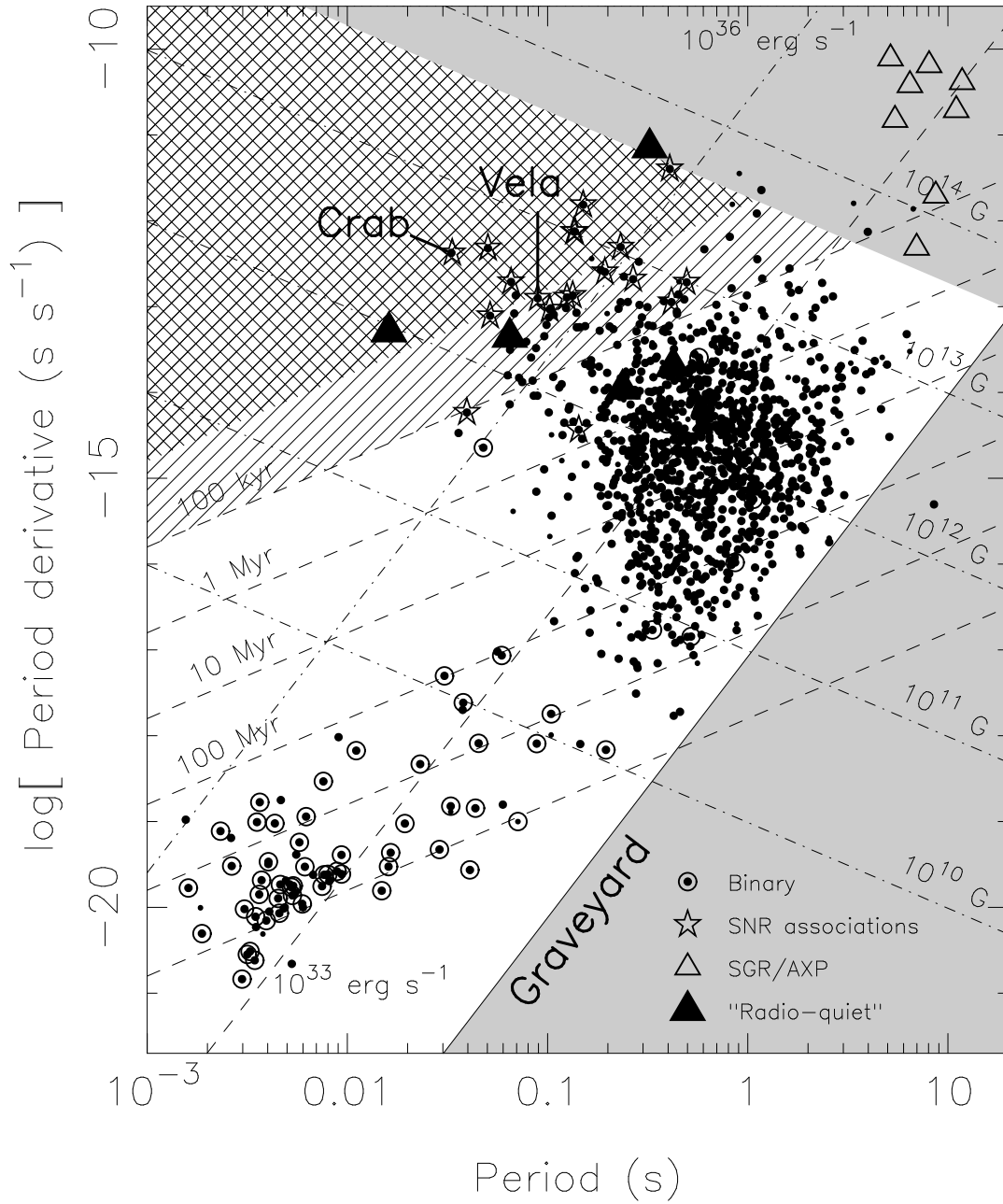


Figure 1.1: Analogous to the Hertzsprung-Russell diagram, which astronomers use to study stars based on their spectra and brightnesses, pulsars can be classified from the timing observables (P and \dot{P}). The diagram shows various types of pulsar (labelled), where in this thesis we only focus on normal solitary radio pulsars (*filled circles*). The *double* and *single* hashed regions indicate the very young or ‘Crab-like’ type ($\tau \leq 10$ kyr) and the relatively young or ‘Vela-like’ type ($10 \text{ kyr} \leq \tau \leq 100 \text{ kyr}$). The *grey* regions indicate the parameter space where radio emission is not allowed according to theoretical models (Lorimer & Kramer 2005).

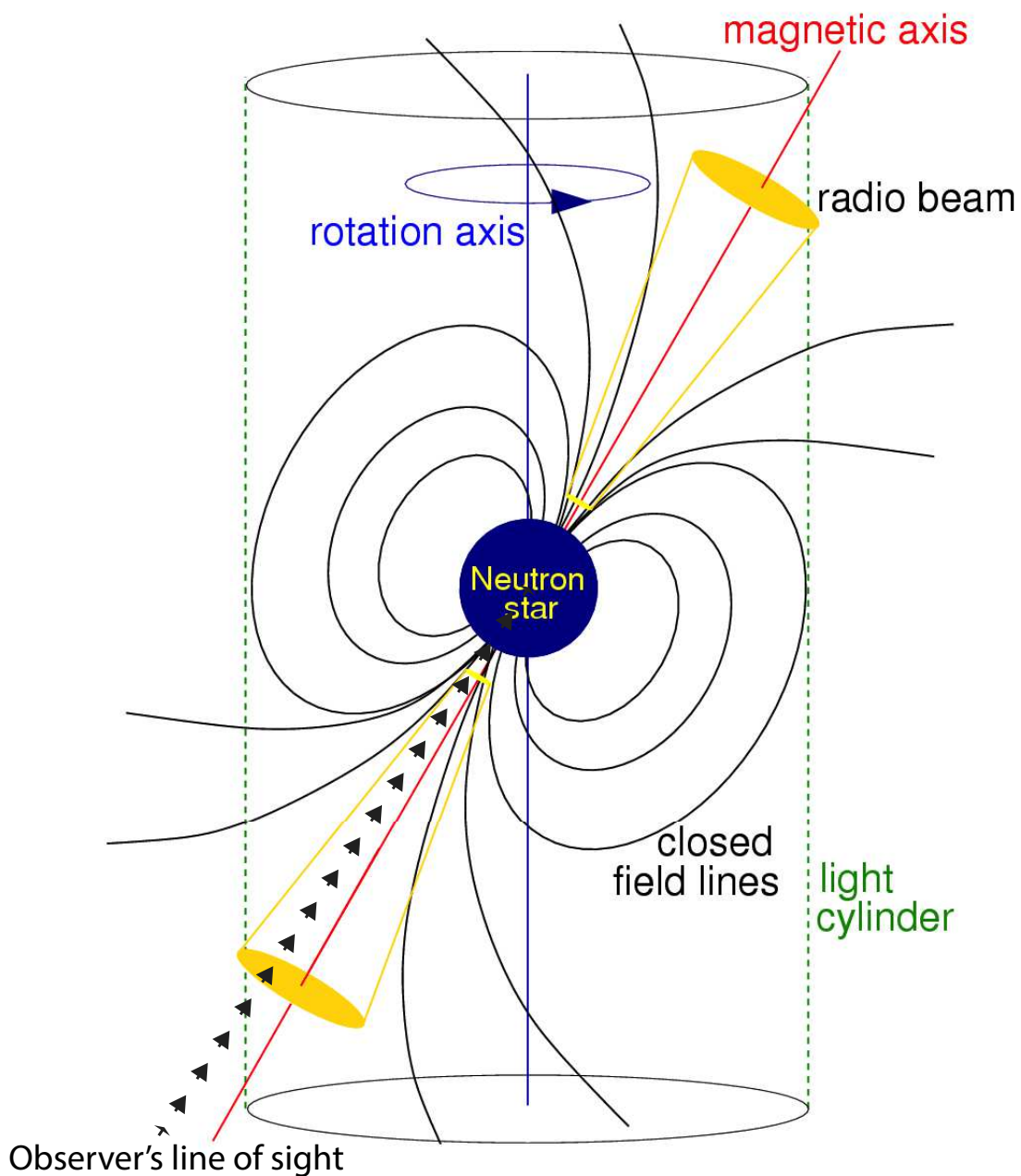


Figure 1.2: The configuration of the pulsar magnetosphere. The light cylinder, an imaginary cylinder at which the co-rotational tangential velocity reaches the speed of light, divides the magnetic field lines into the open and closed regions. See text for more detail (Lorimer & Kramer 2005).

Because pulsars are weak radio sources, astronomers normally add a large number of pulses ($\gtrsim 1000$) together, according to their periods, and subtract the baseline to make a high-signal-to-noise (S/N) pulse profile. Fig. 1.3 shows an average pulse profile of PSR J0742-2822 from over 5000 pulses. In general, pulse profiles of pulsars are 10 to 20 degrees wide, depending on the geometry of the beam. They often have very high degrees of linear polarisation (L) (*red*), which can be different for each component. The circular polarisation (V) (*blue*) is typically 10% – 15% of total intensity (I). The *top* panel shows the polarisation position angle (PPA) which seems to be systematically changing with pulse phase. This is related to the geometry of the magnetic field lines that the observer’s line of sight (LOS) observes, which provides a method to measure the geometry of the pulsar beams (more detail in the next section). An average pulse profile represents a long-time exposure of the pulsar emission, which is unique for an individual pulsar and, supposedly, is stable over time. However, a number of pulsars appear to ‘switch’ between two stable profiles, one of which is PSR B1822–09, which will be studied in Chapter 5.

In a simple model, radio beams of pulsars are known to be comprised of two types of components: a core centred on the magnetic axis and one (or two) concentric cone(s) (Komesaroff et al. 1970; Rankin 1990; Rankin 1993). This so-called hollow cone model is illustrated in Fig. 1.4. For symmetric profiles, the number and types of the components depend on the LOS. However, because not all pulse profiles are symmetric as sketched in Fig. 1.4, Lyne & Manchester (1988) suggest an alternative model in which the beam is instead filled with random patches of active field lines. In Chapter 2 the measured geometry of individual pulsars are combined to make an average beam map for making comparisons to the model.

The interstellar medium also plays an important role in studying radio pulsars. Free electrons along the observer’s LOS affect the radio waves via two main mechanisms. Firstly, propagating in a dispersive medium, the group velocity depends on the wave’s frequency, so that radio pulses at lower observing frequency arrive later than those at higher frequency. The delay between two frequencies, f_1 and f_2 , can be derived as

$$\Delta t = \frac{e^2}{2\pi m_e c} \times (f_1^{-2} - f_2^{-2}) \times DM \text{ s}, \quad (1.5)$$

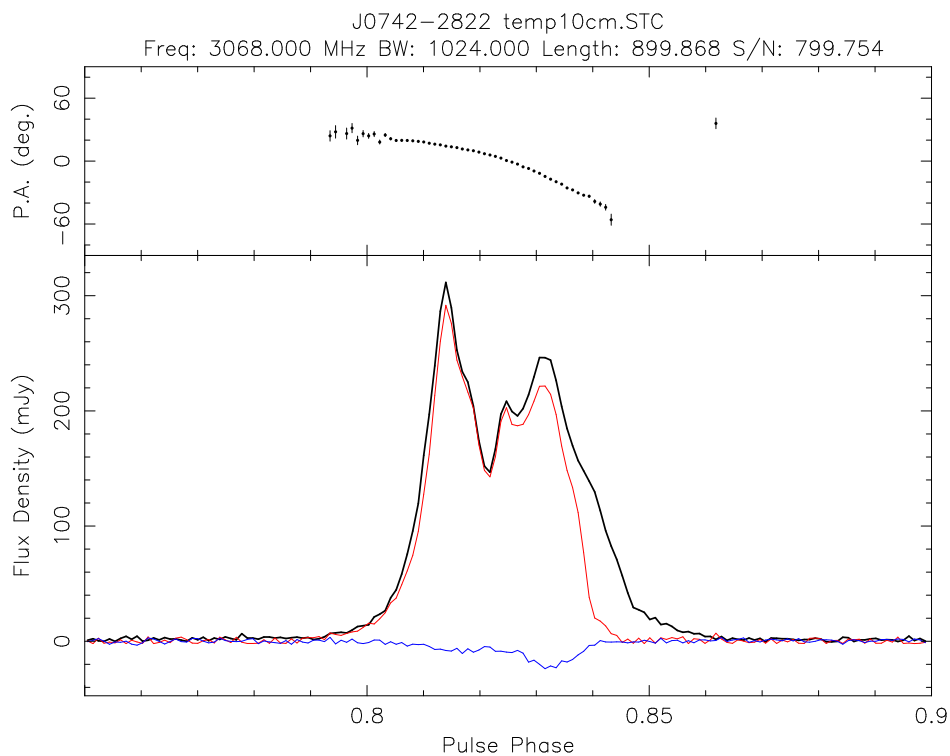


Figure 1.3: The pulse profile of PSR J0742-2822 at 3 GHz (from the Lovell Telescope). The *top* panel shows the polarisation position angle (or ‘PPA’) swing over pulse phase. (*Bottom* panel) The *black*, *red* and *blue* lines are the pulse intensity, and degrees of linear and circular polarisation, respectively. Pulse profiles represent a long-time exposure of pulsars, which typically are stable after averaging several hundreds or thousands of individual pulses.

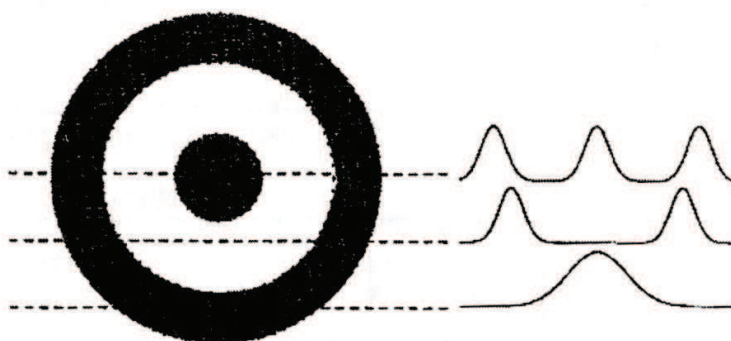


Figure 1.4: The hollow cone model is able to explain pulse morphology for symmetric profiles by proposing that single, double and triple types are produced by different LOS cuts through the beam (Lyne & Smith 2004).

where m_e is the electron mass and the units of f_1 and f_2 are MHz. Dispersion measure (DM) is the total number of the electrons per unit area along the LOS,

$$DM = \int_0^d n_e dl, \quad (1.6)$$

where d is the distance from Earth to the pulsar. Taking the presence of the Galactic magnetic field along the LOS (B_{\parallel}) into account, the interstellar medium is now considered as a cold magnetised plasma, which also changes the phase velocity of the left- and right-hand circularly polarised waves. This effect, which is known as Faraday rotation, is crucially important in polarisation studies as it will rotate the $U - Q$ plane, i.e. change the polarisation position angle (PPA) value, with observing frequency as

$$\Delta\Psi = \left(\frac{c}{f}\right)^2 \cdot RM, \quad (1.7)$$

where rotation measure (RM) is

$$RM = \frac{e^3}{2\pi m_e^2 c^4} \int_0^d n_e B_{\parallel} dl. \quad (1.8)$$

In practice, for the process of DM correction the frequency band is divided into a number of sub-bands, and the time delay (Eq. 1.5) is corrected for individual sub-bands according to their frequencies and the pulsar's known DM value. In the work of surveying for new pulsars, where the DM value serves as one of the unknown parameters, one has to scan through the DM space for the best value, which maximises the signal-to-noise of the average pulse profile. This process is one of the most computationally intensive tasks in pulsar searching algorithms. Similarly, the RM correction (Eq. 1.7) is done to individual sub-bands to maximise the degree of linear polarisation of the profile.

1.1 Pulsar Toy Model

In this thesis, the word ‘geometry’ is used to describe the pulsar beam in the context of, for example, the beam’s opening angle, the inclination angle, the structure of the emission in the beam, and the observer’s line-of-sight (LOS) angle.

Knowing the geometry is extremely vital for astronomers to have a constraint on locations of the emission regions. In addition, the geometry is also related to other studies, such as pulsar population (e.g. Tauris & Manchester 1998) and the proper motion (e.g. Johnston et al. 2005). In later sections, we provide a brief review of the pulsar beam model based on a dipole field, as well as previously known methods of determining the geometry.

The angles of interest are defined as in Fig. 1.5. The emission cone of angular radius (ρ) is concentric with the magnetic axis. The inclination angle (α) is measured from the rotational axis to the magnetic axis. As the beam sweeps past the Earth, the observer’s LOS cuts the beam resulting as a pulsation of width W . The impact angle (β) measures the minimum distance between the LOS and the magnetic axis. Using knowledge of spherical geometry, one can obtain the following equation which describes (ρ) as a function of W , α and β ,

$$\cos \rho = \cos \alpha \cos(\alpha + \beta) + \sin \alpha \sin(\alpha + \beta) \cos \left(\frac{W}{2} \right) \quad (1.9)$$

(Gil et al. 1984). This relation simply relates the beam size (ρ) to the observable pulse width (W), which depends upon α and β . In practice, W is assumed to be measured from edge to edge of the beam, which can be ambiguous. One has to consider both the pulse shape, i.e. symmetry, and characteristics of polarisation position angle to determine whether the measured W represents the full beam.

With a vague understanding of pulsars at the time, Radhakrishnan & Cooke (1969) proposed a mechanism to explain a peculiar, yet systematic, changing or ‘rotating’ of the polarisation position angle (PPA) of PSR B0833–45. The rotation of the PPA is due to the change in the orientation of the magnetic field lines across which the LOS passes, and the model is therefore known as ‘the rotating vector model’ (RVM) (see Fig 1.6, *left*). In a modern context, the RVM is based on three assumptions: 1) the magnetic field structure is a perfect dipole; 2) the PPA can be either parallel, orthogonal, or at constant offset to the field lines; 3) this

offset angle in 2) does not vary during the pulse, which implies a fixed emission altitude (r_{em}). Once propagating upwards, the photons can still be affected by the magnetised plasma medium, causing the PPAs to be distorted. The altitude at which the PPAs become fixed, due to a transition from plasma-rich to vacuum regime, is known as the ‘polarisation-limiting radius’ (r_{PLR}) (Barnard & Arons 1986). The propagation effects will be considered in Chapter 3, and for the ‘classic’ RVM it is assumed that the emission radius (r_{PLR}) is equal to r_{em} .

As the LOS passes the beam, it cuts through different magnetic field lines, inhabiting different angles respective to the fiducial plane (defined in Fig. 1.5). As a result, the observed PPA (Ψ) is then gradually changing across the pulse phase, where its characteristic S-shape depends on the geometry; α and β . Employing spherical geometry and Eq. 1.9, the RVM function predicts a PPA swing as

$$\tan(\Psi - \Psi_0) = \frac{\sin \alpha \sin(\phi - \phi_0)}{\sin(\alpha + \beta) \cos \alpha - \cos(\alpha + \beta) \sin \alpha \cos(\phi - \phi_0)}, \quad (1.10)$$

where ϕ is the pulse phase in degrees, ϕ_0 represents the location of the fiducial plane, and Ψ_0 is the PPA value at ϕ_0 , which is essentially related to the plane of the pulsar’s rotating axis. Note that, while Eq. 1.10 is free from any assumptions about the beam, i.e. shapes or symmetries, Eq. 1.9 assumes axis-symmetry of the beam, i.e. the leading and trailing edges of the beam must be symmetrical around the magnetic axis.

Examples of RVM swings are shown in Fig. 1.6 (*right*), with different combinations of α and β . The two middle vertical lines denote the usual range of a pulse window where emission is observed, which is merely 5% of the total pulse phase, which is indeed one of the difficulties to effectively use this model. Another useful convention which will be discussed later on is the concept of ‘inner’ and ‘outer’ LOS solutions. The geometry which is considered to be ‘inner’ LOS is when the LOS’s path is between the rotational axis and the magnetic axis, i.e. if $\beta < 0^\circ$, $\alpha < 90^\circ$ or if $\beta > 0^\circ$, $\alpha > 90^\circ$. And the ‘outer’ LOS is when the magnetic axis is between the rotational axis and the LOS’s path, i.e. if $\beta < 0^\circ$, $\alpha > 90^\circ$ and if $\beta > 0^\circ$, $\alpha < 90^\circ$ (for example, see Fig. 1.6, *right*).

The beam size (ρ) can be determined from the size of the first closed-field-lines² region (Fig. 1.7). Assuming an aligned dipole configuration ($\alpha = 0^\circ$), one can use the supposedly known dipole structure of the magnetic field ($\sin^2 \theta/r$

²Which is indeed equivalent to the last open-field line.

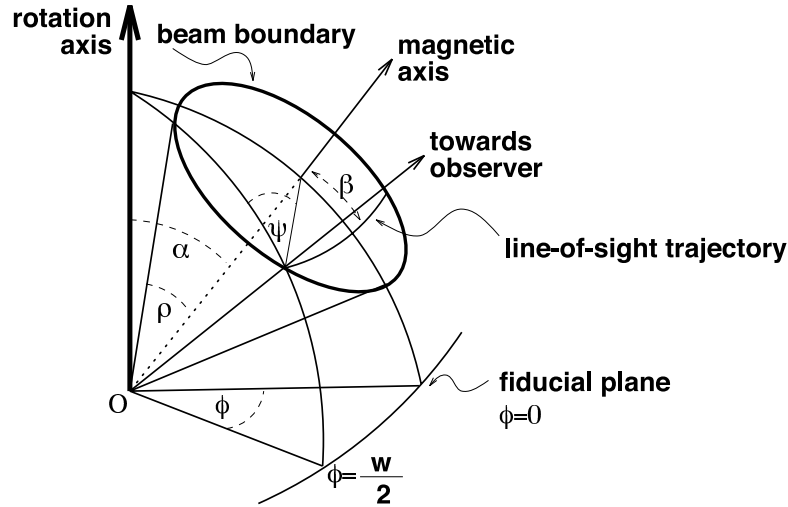


Figure 1.5: A diagram showing the pulsar's beam configuration. The rotational axis makes an angle (α) with the magnetic axis. A profile of a pulse width $W = 2\phi$ is produced as the observer's LOS cuts the emission cone, of an opening angle ρ , at the impact angle β , measured from the magnetic axis in the fiducial plane $\phi = 0$. For each pulse phase ϕ , the polarisation position angle (PPA) (ψ) can be determined (See next figure) (Lorimer & Kramer 2005).

is constant, in polar coordinates) to measure ρ as a function of P . By knowing that the point where the first closed-field line touches the light cylinder is $(r, \theta) = (R_{LC}, 90^\circ)$, the coordinates of the edge of the beam at the emission point (r_{em}, θ_{em}) are related to the dipole structure as

$$\frac{\sin^2 \theta}{r} = \frac{\sin(90^\circ)}{R_{LC}} = \frac{1}{cP/2\pi} = \frac{\sin^2 \theta_{em}}{r_{em}}, \quad (1.11)$$

where the radius of the light cylinder (R_{LC}) is a imaginative radius at which the tangential velocity reaches the speed of light. The polar angle of the edge of the beam θ_{em} can then be calculated as

$$\theta_{em} = \sin^{-1} \sqrt{\frac{2\pi r_{em}}{cP}}. \quad (1.12)$$

For non-alignment case ($\alpha \neq 0^\circ$), the above calculation still holds but the circular-shape beam will be compressed in N-S direction by at most $\sim 60\%$ when $\alpha = 90^\circ$ (McKinnon 1993; Kapoor & Shukre 1998; Weltevrede & Johnston 2008a). This is certainly a vital point for considering as a selection effect for population studies.

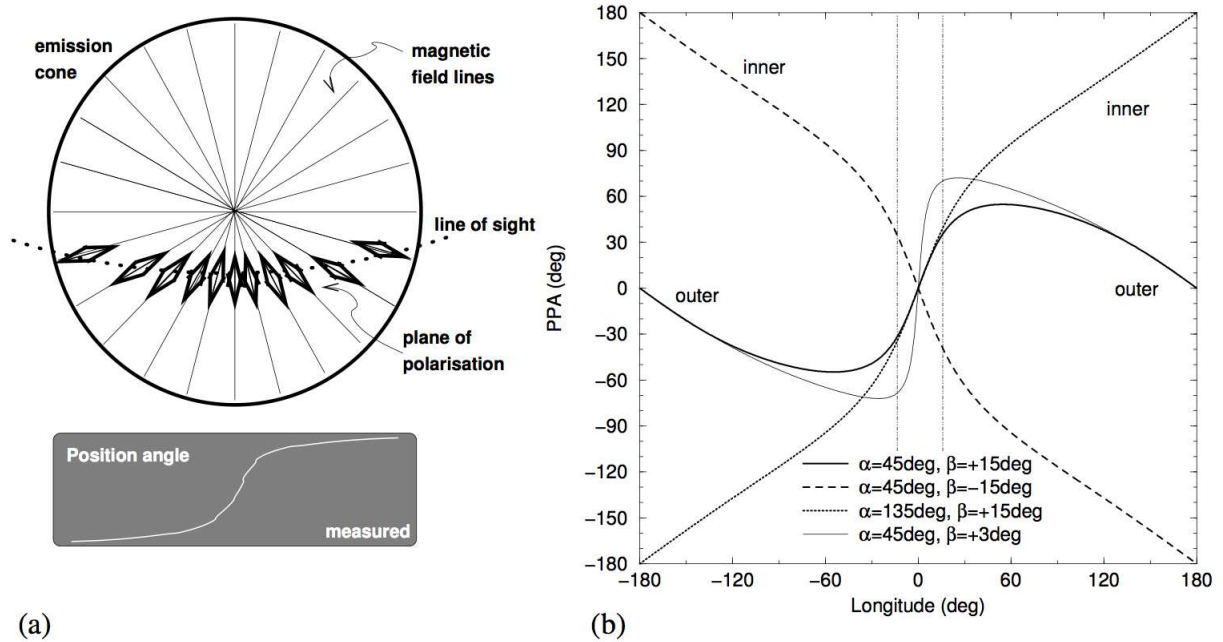


Figure 1.6: (*left*) A diagram demonstrating how the observer's LOS passes the beam at different angle with the magnetic field lines, which results in a characteristic PPA curve of the RVM. (*right*) The RVM swing is parameterised by α and β , in which their combinations are defined into two kinds of curves; the inner and the outer LOS. See text for more details. (Lorimer & Kramer 2005)

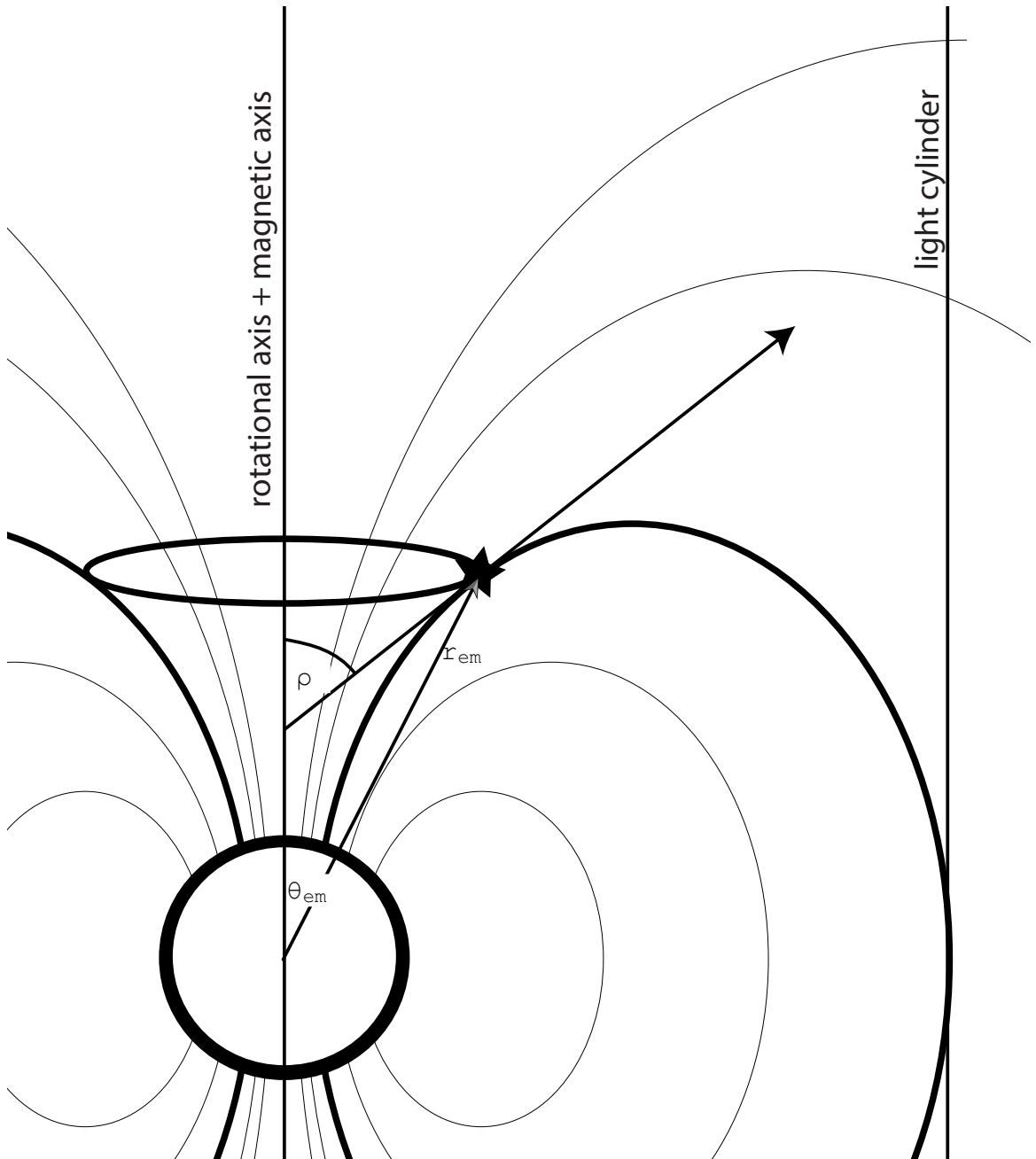


Figure 1.7: The beam opening angle (ρ) is determined, by the last open-field line (*thick*), whose size is governed by pulsar's rotational period, i.e. the light cylinder radius ($R_{LC} = 2\pi/cP$). The *arrow* vector indicates the direction of the wave which is tangent to the field line at the emission point (\star). The diagram is not to scale!

Nevertheless, we note that this beam compression will not be considered in this work. As the beam is compressed in N-S direction, it has the least effect on the LOS trace, and hence W and ρ , which is more about the E-W plane.

Eq. 1.12 is not yet an accurate representation of the opening angle of the emission beam, as demonstrated in Fig. 1.7 that ρ is not actually equivalent to θ_{em} . The relationship between ρ and θ_{em} is given as

$$\tan \theta_{em} = -\frac{3}{2 \tan \rho} \pm \sqrt{2 + \left(\frac{3}{2 \tan \rho}\right)^2} \quad (1.13)$$

(Gangadhara & Gupta 2001). For the emission region relatively close to the surface $\theta \ll 1$ and Eq. 1.13 is reduced to $\theta_{em} \simeq 2\rho/3$, and now we obtain ρ from Eq. 1.12 as

$$\rho \simeq \frac{3}{2}\theta_{em} = \sqrt{\frac{9\pi r_{em}}{2cP}} = 3.92^\circ (r_{em} \cdot P)^{-1/2}, \quad (1.14)$$

where r_{em} is in kilometres, and P is in seconds. In practice, this relation is often taken as

$$\rho = k \cdot P^{-1/2}, \quad (1.15)$$

where k is measured from observational data, by either ρ , W or r_{em} measurements of a sample of pulsars (e.g. Rankin 1993; Lyne & Manchester 1988; Gould 1994; Kramer et al. 1994; Weltevrede et al. 2010). This equation will be incorporated with Eq. 1.9 and 1.10, to obtain a better constrained geometry in Chapter 2.

Another geometrical concept which has not been considered is the aberration effect, which is caused by the fact that trajectories of the charged particles in the open-field-line region ‘appear’ to be bent forward (to the rotation direction) with respect to the observer’s frame of reference (Blaskiewicz et al. 1991; Hibschan & Arons 2001; Dyks 2008³). The difference in the trajectories between the particle’s frame and observer’s frame has two consequences: 1) the emission beam appears to be earlier in pulse phase with respect to that in the particle’s frame; 2) the fiducial plane (the trajectory which the particles appear to move in a straight line) is delayed to later pulse phase, as opposed to being at the centre of the beam in the particle’s frame. On the condition that every part of the pulse profile is generated at the same altitude at a given observing frequency, the pulse-phase separation between the centre of the intensity profile

³In this paper, they somewhat, while the resulting formula is identical, clarify the interpretation of the effects.

and ϕ_0 as observed in the the PPA swing (Eq. 1.10) is

$$\phi_0 - \phi_{intensity} = 4 \frac{r_{em}}{R_{LC}} \text{ rad}, \quad (1.16)$$

where ϕ_0 and $\phi_{intensity}$ are the phase location of the centre of the PPA swing (i.e. the steepest gradient point) and the centre of the pulse profile. The magnitude of the aberration shift depends on the emission altitude, i.e. higher altitude = larger shift. Consequently, if the fixed altitude condition does not hold, one would expect a distortion on the RVM swing because different parts of the profile, which originate from different altitude, have different amount of the aberration shift.

1.2 Known Methods

Methods for obtaining important parameters describing the geometry, i.e. α and β , and ρ , can be summarised into those using only Eq. 1.10 and those with Eq. 1.9 and Eq. 1.15.

For the first group (e.g. Narayan & Vivekanand 1982; Blaskiewicz et al. 1991; von Hoensbroech & Xilouris 1997a,b; Everett & Weisberg 2001), it is very straightforward to simply employ the least χ^2 fitting technique to obtain the best-fit solutions. Two cautious notes by Everett & Weisberg (2001), who faced difficulty in comparing results from different conventions: 1) the direction (clockwise or counter-clockwise) of which the PPA increases on the sky has to be the same as which Eq. 1.10 is derived, which is that the PPA increases clockwise on the sky. This if set incorrectly will flip the characteristic S swing upside down, and consequently reverse the sign of β , and 2) convention of how α is defined, i.e. measured from the nearest north-south pole, having a range between 0° to 90° , or measured from the rotation vector, having a range between 0° to 180° . In this chapter we take the convention of having α measured from the rotation vector, and the PPA increases *clockwise* on the sky.

When the RVM model is fitted to the PPA swing, a χ^2 distribution is obtained as a function of α and β . One common known difficulty is where the resulting χ^2 map, in α vs. β space, has the shape of a ‘banana’ (for an example, see Fig. 2.3 *top*), indicating a poorly constrained outcome and a co-dependent relation between α and β . The reason is that the RVM equation (Eq. 1.10) is a function of the pulse phase ϕ and the position angle Ψ whose shape is parameterised by

α and β , and ϕ_0 and Ψ_0 which are the offsets of the curve. And, unfortunately, typically only 5% of full 360° rotation is observed centred around ϕ_0 , and the lack of information from the ‘wings’ of the profiles cause the entanglement between α and β . Nevertheless, the steepest gradient of the PPA swing can be precisely determined for most cases, as

$$c = \sin \alpha / \sin \beta. \quad (1.17)$$

Another more subtle issue is when the fitting solutions converge to the origin ($\alpha \rightarrow 0^\circ$ or 180° , $\beta \rightarrow 0^\circ$) as first addressed by Everett & Weisberg (2001). While ϕ_0 , Ψ_0 , c and χ_{min}^2 remain consistent, we found that this problem is neither caused by the quality nor the width of the profiles, but rather an issue with the RVM itself. This so called ‘diverging’ issue will be discussed in Chapter 2.

For the second group, the geometry is measured by indirect/empirical methods by Lyne & Manchester (1988), Rankin (1990) and Gould (1994) (hereafter LM88, RAN90 and GOU94, respectively). Additional constraints are required and for instance, LM88 make another assumption that the beam is axis-symmetric and active from edge to edge, allowing the use of W in Eq. 1.9. They categorised their multi-frequency dataset of over 200 pulsars according to the mean morphology defined by Huguenin et al. (1971) and measured 10%-maximum-intensity width on 400 MHz data. The essence of LM88’s method is that, depending on the measured W , the expected ρ is at its minimum when α is 90° , e.g. when $\alpha \neq 90^\circ$, ρ will consequently be smaller than ρ_{90} . And with a number of measurements from different pulsars the lower limit of the plot between ρ_{90} and P will then represent the true $\rho - P$ relation of Eq. 1.15. To derive ρ_{90} from the assumption of $\alpha = 90^\circ$, Eq. 1.9 requires the measured $W_{10\%}$ and β_{90} . β_{90} follows from Eq. 1.17 by setting $\alpha = 90^\circ$. As shown in Fig. 1.8, we carried out a simulation to demonstrate how ρ_{90} , determined from a set of solutions of W , P , α and β , is overestimated from the true ρ . The fit of the lower-bound of the results will be used as observational measurement of Eq. 1.15, where LM88 found that

$$\rho = 6.5^\circ \cdot P^{-1/3}. \quad (1.18)$$

The fact that the power index of P is flatter, i.e. $-1/3$ instead of $-1/2$, could be understood as an indication that there is some P -dependency in r_{em} from Eq. 1.14 (as will be quantified in Eq. 1.24 below).

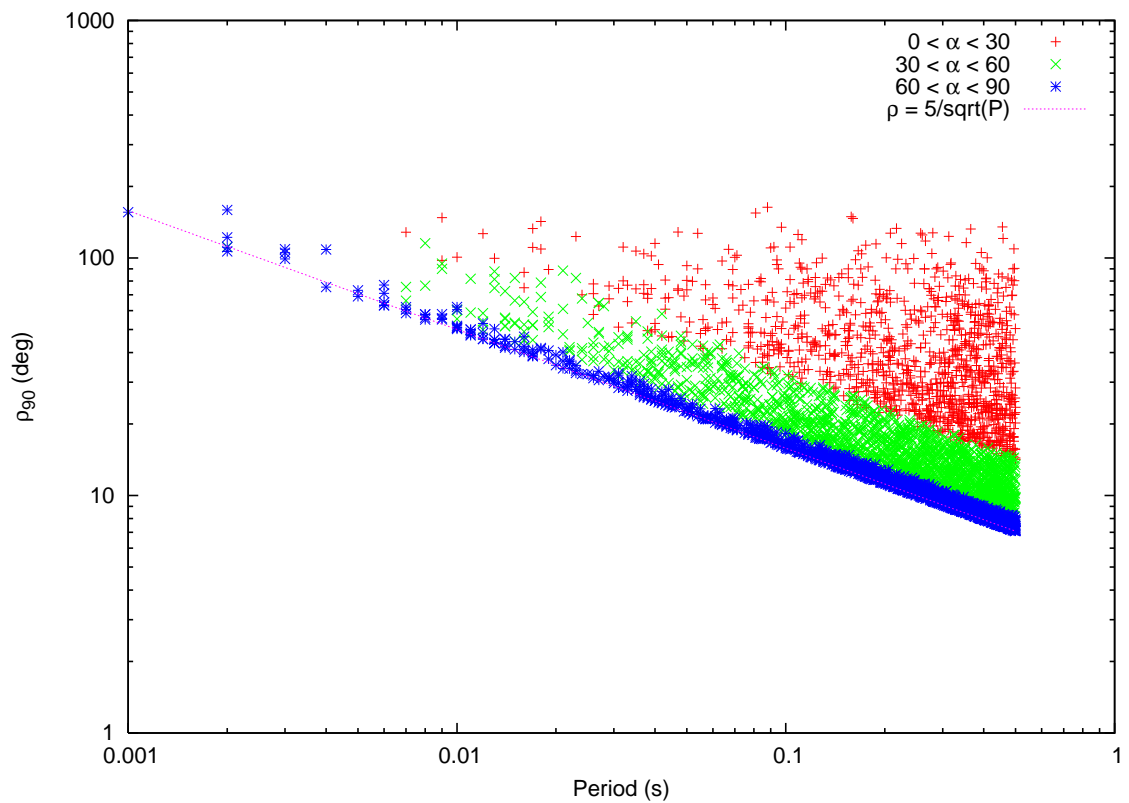


Figure 1.8: A distribution of ρ_{90} which is calculated from random values of P , α and β , using Eq. 1.15 with $k = 5^\circ$ and Eq. 1.9 with a fixed W . Different layers of the solutions, depending on α , demonstrate how ρ_{90} will be overestimated from the ‘true’ ρ , which ideally will all lie on the lower-bound of the distribution (*dotted* line).

Based on a similar approach, GOU94 worked on a larger sample of around 300 pulsars and found a similar relation

$$\rho = \begin{cases} 5.4^\circ \cdot P^{-1/2} & \text{for 2-3 component pulsars,} \\ 7.7^\circ \cdot P^{-1/2} & \text{for 4-5 component pulsars.} \end{cases} \quad (1.19)$$

RAN90 determined her measurements of Eq. 1.15, using the FWHM, i.e. $W_{50\%}$, of 50 core-dominated pulsars at 1 GHz, in which she found the lower-bound of the plot of W_{core} and P to be $W_{core}^{lower-bound} = 2^\circ.45 \cdot P^{-1/2}$. Her method is similar as in the ρ_{90} technique, but this case is of W , rather than ρ_{90} .

Because observing the core-component suggests that $\beta \sim 0^\circ$, RAN90 reduced Eq. 1.9 to

$$\frac{W_{core}}{2} \approx \frac{\rho_{core}}{\sin \alpha}. \quad (1.20)$$

Consistent with her $W - P$ measurements, the relation is then generalised to be $W_{core} \approx 2^\circ.45 \cdot P^{-1/2} / \sin \alpha$ as W is expected to increase for a decreasing α . Consequently, this implies

$$\rho_{core} = 1.23^\circ \cdot P^{-1/2}. \quad (1.21)$$

For conal pulsars, Rankin (1993) (hereafter RAN93) applied Eq. 1.21 to those which contain both the core and conal components. The derived ρ_{core} in Eq. 1.21 gives an estimation of α which is then used in Eq. 1.20. Therefore, ρ of the pulsars could be determined. The following results were found:

$$\rho = \begin{cases} 4.33^\circ \cdot P^{-0.5} & \text{inner cone,} \\ 5.75^\circ \cdot P^{-0.5} & \text{outer cone.} \end{cases} \quad (1.22)$$

It is understood that the disagreement in k in Eq. 1.19 and Eq. 1.22 is mostly due to the fact that W was measured at different intensity levels and at different observing frequencies.

Independently, it has been found that the measured $\rho - P$ relations organise themselves into two values of k , without having to categorise the profiles first as in GOU94 (e.g. RAN93, Kramer et al. 1994 and Mitra & Rankin 2011). This leads to a conclusion that the conal component can be organised into the inner and outer conal structure.

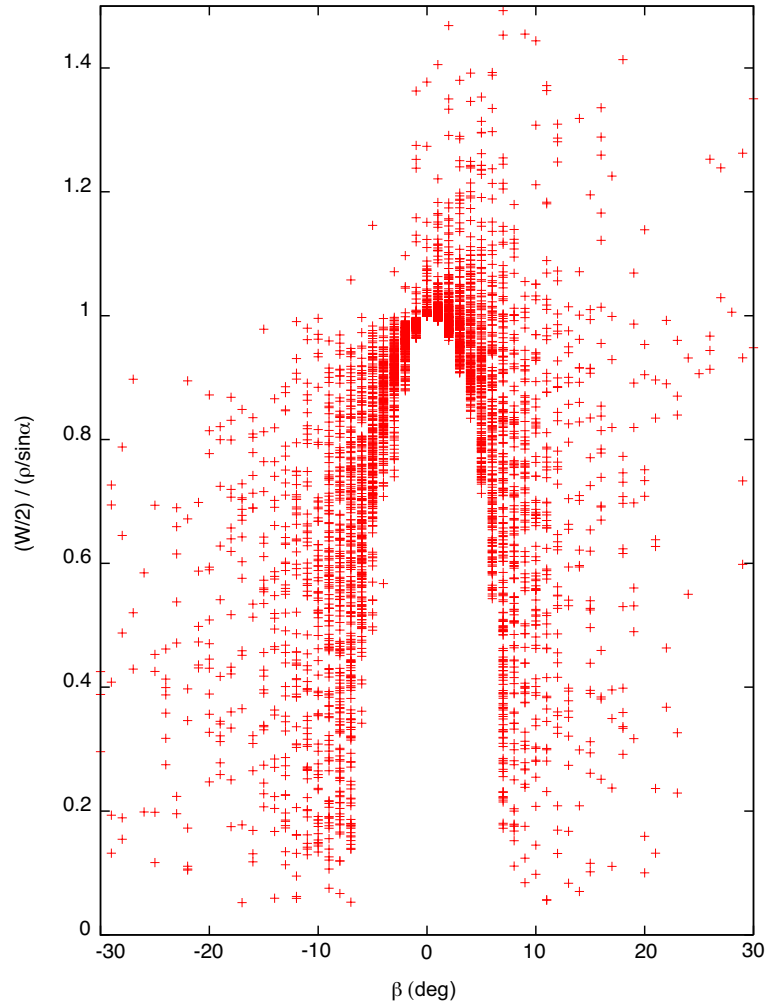


Figure 1.9: The accuracy of Eq. 1.20, i.e. $(W/2)/(\rho/\sin \alpha)$ as a function of β , which is $\sim 80\%$ at $|\beta| \sim 5^\circ$, before quickly reduces and becomes unreliable for $|\beta| > 5^\circ$.

Because Eq. 1.20 is derived on the condition that $\beta \sim 0^\circ$, we evaluate its accuracy for non-zero β as in Chapter 6 it will be used to determine α for pulsars. Combinations of α , β and ρ are substituted in Eq. 1.9 to calculate the corresponding values of W , which are used to calculate $\frac{W/2}{\rho \sin \alpha}$, plotted as a function of β in Fig. 1.9. The results indicate that the approximation can be used for $|\beta| \leq 5^\circ$ at an uncertainty level of $\sim 20\%$.

The constant k is also related to r_{em} . Gil & Kijak (1993) rewrite Eq. 1.15 as

$$\rho = 0.39 \cdot s \cdot r_{em}^{1/2} \cdot P^{-1/2}, \quad (1.23)$$

where the s parameter, $0 < s \leq 1$, describes a portion of the open field lines which

is ‘active’ ($s = 1$ means the full beam is active). They derived ρ , using Eq. 1.9 with α and β from Blaskiewicz et al. (1991) and Wu et al. (1993), in which they found that $r_{em} \propto P^{1/2}$. This is in contrast to the work by LM88, GOU94 and RAN94 where the emission height, hence k , is assumed to have no dependency on P . In a more recent work, Kijak & Gil (2003) generalise the resulting r_{em} by Kijak & Gil (1997,1998) to include the observing frequency (f) and the pulsar’s period (P) and period derivative (\dot{P}), and derive the follow relation,

$$r_{em} = (400 \pm 80) \cdot f_{GHz}^{-0.26 \pm 0.09} \cdot \dot{P}_{-15}^{0.07 \pm 0.03} \cdot P^{0.30 \pm 0.05} \text{ km.} \quad (1.24)$$

The P -dependency in r_{em} indicates that the power law index of P in Eq. 1.15 is not -0.5 but -0.35 which is rather close to LM88’s results. Weltevrede & Johnston (2008b) also found a similar value of $-1/3$ but of a fit of the distribution between W and P , rather than a lower-bound fit as used by LM88 and RAN90. Therefore this is still an open question. Note also that a possibility is that the s parameter may have some dependency on period as well, further complicating this type of analysis.

As has been shown in this Section, the measured values of k and the power index of P , from different techniques, appear to be fairly consistent with each other; however there is a considerably large variation in the measurements which is understood to be due to the fact that W , which is frequency-dependent, was measured at different intensity level. The change from a proportionality with $P^{-0.35}$ to $P^{-0.5}$ will affect ρ by up to 5° for typical pulsars with $P \sim 0.1 - 1$ s, which is considerably smaller than the uncertainty level from the geometry measured by the RVM. Because the pulsars in our sample have their periods within that range, for our work in the next chapter, we therefore remain with the power index of $-1/2$.

Chapter 2

Obtaining the Geometry

We present a new technique (Section 2.2) to improve the constraints obtained from the RVM, using the basic equations of the Toy Model presented in Chapter 1. The technique is applied to a polarisation dataset from the Parkes telescope (Section 2.1). The derived geometry (Section 2.4) is then used to study a possible progressive-alignment of the inclination angle (α) with the pulsar characteristic age (τ), and to create an averaged pulsar beam map (Section 2.5).

2.1 Polarisation Data

The polarisation data were obtained with the Parkes 64-metre radio telescope in Australia. The observations were carried out from 2004 to 2006 using the H-OH receiver observing at 1.4 GHz and the 10/50 cm receiver observing at 3.1 and 0.67 GHz. Both receivers use orthogonal linear feed systems attached to a pulsed calibration signal emitter at a position angle of 45° . Our dataset has been published by Karastergiou & Johnston (2006) and Johnston et al. (2008) for various studies. The signal processing process is similar to what was done by Noutsos et al. (2008), who use polarisation properties to study the interstellar medium.

The data quality of the polarisation position angle (Ψ) can be measured from the ‘signal-to-noise’-ratio (S/N) of the degree of the linear polarisation L to the average noise level in the off-pulse region. The degree of linear polarisation L and the polarisation position angle Ψ can be calculated from the Stokes parameters

U and Q ,

$$\begin{aligned} L &= \sqrt{Q^2 + U^2} \\ \Psi &= \frac{1}{2} \text{atan} \frac{U}{Q}. \end{aligned} \quad (2.1)$$

As the ‘noise’ in the data is often assumed to be random and normally distributed (Rice 1995), the Stokes parameters obey Gaussian statistics with standard deviations $\sigma_I, \sigma_Q, \sigma_U$ and σ_V .

For the linear polarised intensity, however, its noise statistics (σ_L) at low signal strength can no longer be considered Gaussian due to the quadrature summation of σ_Q and σ_U , as discussed in Wardle & Kronberg (1974), where they proposed the best estimate of L to be calculated from (L_{true}),

$$L_{true} = \begin{cases} L\sqrt{1 - (\frac{\sigma_I}{L})^2} & \text{if } (\frac{L}{\sigma_I}) \geq 1.5 \\ 0 & \text{otherwise,} \end{cases} \quad (2.2)$$

where σ_I ($\sim \sigma_Q \sim \sigma_U \sim \sigma_V$) is the off-pulse standard deviation of the total intensity (Everett & Weisberg 2001). The above equation is essentially similar to the ‘baseline subtraction’ technique, where the bias equals $\sqrt{U^2 + Q^2} - \sqrt{U^2 + Q^2 - \sigma_I^2}$.

In general, the uncertainty of the position angle (σ_Ψ) can be derived from

$$\sigma_\Psi = 28.65^\circ \frac{\sigma_I}{\sqrt{Q^2 + U^2}}, \quad (2.3)$$

which is simply an error propagation of σ_U and σ_Q . From their extensive numerical simulations to study the statistics of the linear polarisation, Naghizadeh-Khouei & Clarke (1993) conclude that Eq. 2.3 is accurate only when $L_{true}/\sigma \leq 6$, otherwise the non-Gaussianity in the statistical probability distribution of Ψ becomes significant in estimating confidence interval. The more accurate probability density function of Ψ is given by

$$G(\Psi) = \frac{\exp(-L_{true}^2/2\sigma_I^2)}{\sqrt{\pi}} (1/\sqrt{\pi} + \eta \exp(\eta^2)(1 + \text{erf}(\eta))), \quad (2.4)$$

where $\eta = L_{true} \cos 2(\Psi - \Psi_{true})/(2\sqrt{2}\sigma_I)$ and ‘erf’ is the Gaussian error function. For example, for a 1σ level of uncertainty, one needs to numerically integrate $G(\Psi)$

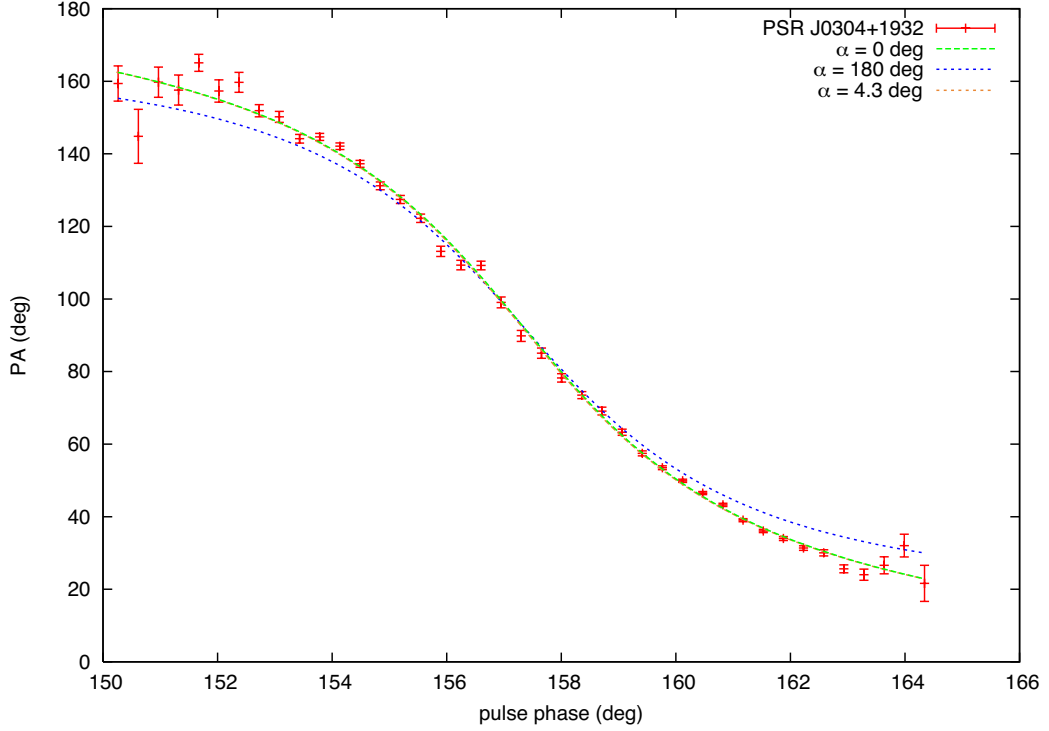


Figure 2.1: The PPA profile of PSR J0304+1932 overlaid with three RVM curves. The *orange* swing is from the LCS’s best fit of $\alpha = 4.3^\circ$. The *blue* and *green* lines are produced using the same slope (c) of -19 , but with $\alpha = 180^\circ$ and 0° , respectively. The *orange* line appears to be indistinguishable from the *green* line.

to encompass 68.26% of the total probability,

$$\int_{-1\sigma_\Psi}^{1\sigma_\Psi} G(\Psi) d\Psi = 68.26\% \quad (2.5)$$

For our work the signal-to-noise limit for Ψ is set to $1.5\sigma_{Ltrue}$ and the pulse width (W) is measured at 5% of peak intensity. Our analysis does not, however, employ Eq. 2.5 even at such low S/N, in which σ_Ψ is underestimated by up to $\sim 5^\circ$ (figure 2a in Naghizadeh-Khouei & Clarke 1993). We believe that this is reasonable, considering that low S/N PPA points are usually located near the edge of a profile, which is the most critical part for the RVM and therefore deserves more weighting in the least- χ^2 (LCS) fitting process.

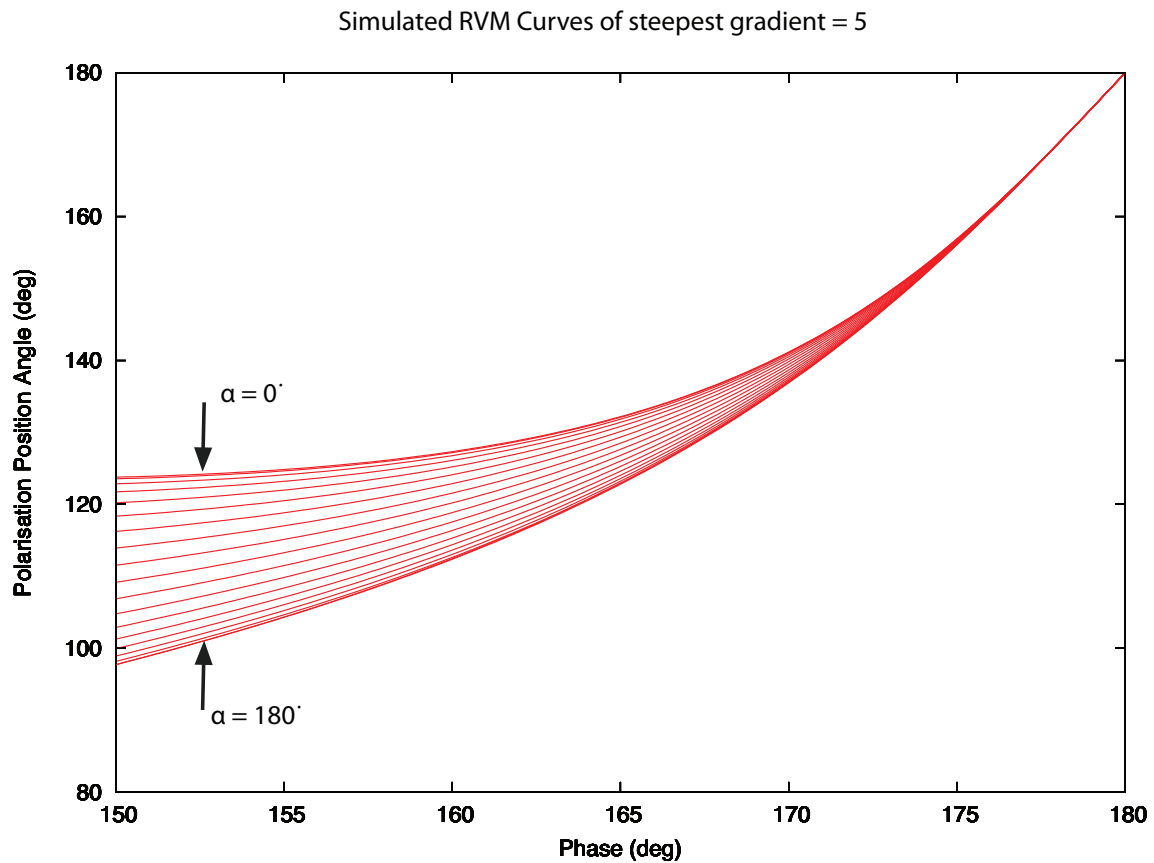


Figure 2.2: With a fixed value of $c = 5$, the simulated RVM lines are of equally spaced $\alpha = 0^\circ, 10^\circ, 20^\circ, \dots, 170^\circ$ and 180° . The coverage of the RVM in the PPA- ϕ space is unevenly distributed, such that the PPA swings become indistinguishable at the extreme α solutions.

2.2 Combined- χ^2 Method

Most of previous works on RVM fitting, e.g. Narayan & Vivekanand (1982); Blaskiewicz et al. (1991); von Hoensbroech & Xilouris (1997a,b); Everett & Weisberg (2001); Jaroenjittichai (2009), are all similarly limited due to the ‘small duty cycle’ or the ‘banana’ problem, as there is not sufficient information on the PPA swing to disentangle the correlation between α and β , resulting in a typical ‘banana-shaped’ χ^2 contour (Fig. 2.3 *top*). Nevertheless, together with ϕ_0 and Ψ_0 , the $\alpha - \beta$ correlation itself can be accurately measured, in which the curve of the banana is described by Eq. 1.17 (see Jaroenjittichai 2009¹’s figure 5.2 (B) for more details).

Another difficulty was noted by Everett & Weisberg (2001) that, occasionally, the resulting α and β are approaching 0° (or 180°). This is called the ‘diverging’ problem and there were many of these cases found in Jaroenjittichai (2009). It is not immediately obvious why the problem occurs because the fitting seems to give a very good χ^2 (including the Monte-Carlo simulation output), regardless of W , c , or S/N of data, or the ‘structure’ of the χ^2 . This is obviously in contrast to conventional pulsar knowledge if the majority of the observable pulsars are aligned rotators. We are confident that this problem is not a software issue, and it is therefore inevitable to conclude that it is about the RVM itself, as will be explained as follows. An example of a diverging solution of PSR J0304+1932 with the best LCS solutions of $(\alpha, \beta, c) = (4.3^\circ, -0.23^\circ, -19)$ is plotted in fig. 2.1 as a *orange* curve. The *blue* line corresponds to an RVM with the same slope $c = -19$ but for $\alpha = 180^\circ$, and $= 0^\circ$ for the *green* curve. It now becomes clear that there is limited coverage of allowed solutions in the PPA-pulse-phase parameter space, i.e. the region between the *green* and *blue* lines, at a fixed c . The problem will occur when there are PPA points outside this permitted region. In the example, there are PPA points at the very leading and trailing parts falling outside the region, on the *green* line’s side (hence $\alpha \rightarrow 0^\circ$, rather than 180°).

To conclude, the diverging problem originates from a contradiction between the central part of the PPA swing, which dictates the slope c , and the sides of the PPA swing, which governs the determination of α . Obtaining a diverging solution simply indicates that the RVM fails to fit the PPA swing, possibly caused by aberration/retardation (Blaskiewicz et al. 1991; Hibschan & Arons

¹<ftp://ftp.jb.man.ac.uk/pub/pjar/Mythesis.ps>

2001), propagation effects (Chapter 3) or interstellar scattering (Li & Han 2003; Karastergiou 2009).

In addition, a simulation, shown in Fig. 2.2, demonstrates that the PPA- ϕ space is unequally sampled in α space. It appears that the PPA points will be more cluttered at extreme values of α . And, importantly, this indeed demonstrates the non-Gaussianity of the RVM equation, in contrast to the PPA error-bars which does not include such non-linearity characteristics. In practice, this suggests that PPA swings of extreme values of α are more difficult to constrain, i.e. requires a higher S/N of the PPAs than those of $\alpha \sim 90^\circ$, in order to obtain a unique solution.

To deal with the difficulties and limitations of RVM fitting, additional assumptions are made in order to put better constraints on α and β . The diverging problem, discussed above, can be easily recognised from the fact that a true aligned rotator is required to have a large W (Eq. 1.20). This effect will be quantitatively combined with the RVM, discussed below. As in Weltevrede et al. (2010), we make an assumption that the full radio beam is illuminated in order to measure W and $\rho(P)$ and utilise Eq. 1.9. However, unlike in Weltevrede et al. (2010), the constraints from the RVM and Eq. 1.9 are combined during the fitting process. We will call it the RVM $_{\rho-W}$ technique, and the total χ^2 is defined as

$$\chi_{total}^2 = \sum_{i=1}^N \frac{(\Psi_i - \Psi_i(\alpha, \beta, \phi_0, \Psi_0))^2}{\sigma_{\Psi_i}^2} + \frac{(W - W_0(\rho_0, \alpha, \beta))^2}{\sigma_W^2} + \frac{(\rho(P) - \rho_0)^2}{\sigma_\rho^2}, \quad (2.6)$$

where W , $\rho(P)$, σ_W and σ_P are the measured pulse width and beam width, and their corresponding uncertainties. Eq. 2.6, which now contains 5 variables, is composed of the original RVM term, and the second and third terms from the constrain from the $\rho - W$ relationship. Nevertheless, results from this combined probability formula are still often suffering from the diverging problem. We therefore adjust the weight of the second and third terms by a factor of N to overcome the influence of the diverging problem. An example of the improvement is shown in Fig. 2.3, where a typical banana-like χ^2 plot from a conventional RVM fit (*top*) becomes better constrained from the RVM $_{\rho-W}$ method (*bottom*).

Because the resulting χ^2 contour usually has a rather complex shape, which indicates a correlation between the fitting parameters (e.g. Fig. 2.3, *bottom*), it

should be better to preserve the information of the χ^2 in terms of probability density functions (PDF) for later analysis, rather than directly measuring the errorbars of α and β from the χ^2 contour. This is essentially the same reason why Jaroenjittichai (2009) studied a Monte Carlo (MC) technique, which also provides a PDF. This technique has already been widely used to calculate the uncertainty of results in pulsar studies and simulations, e.g. Johnston et al. (2005), Kramer & Johnston (2008), and already studied in detail by Jaroenjittichai (2009).

Assuming that the measurements are randomly drawn from the ‘parent’ distribution, the concept of the MC method is to generate a large number of ‘simulated’ measurements ($\mathbf{MC}_{i,i=1,\dots,N}$) which are slightly different from the original dataset (\mathbf{MC}^0), such that the differences imitates the effect of measurement errors. Each \mathbf{MC}_i gives one LCS fitting result (\mathbf{mc}_i). Finally, instead of being estimated from size of the χ^2 surface of \mathbf{MC}^0 , the statistics are evaluated from the distribution of \mathbf{mc}_i (Press et al. (1986)).

In detail, the MC process starts with applying the MC method to a Stokes U and Q profile (\mathbf{MC}^0) to simulate N $U-Q$ datasets ($\mathbf{MC}_{i,i=1,\dots,N}$). The degree of variation in each dataset is based on the off-pulse root mean square of the original profile. Then each \mathbf{MC}_i is converted to a PPA profile with a constant 1° errorbar, which is then fitted with the RVM and gives a solution of α , β , ϕ_0 and Ψ_0 (\mathbf{mc}_i). A statistical analysis is made from the obtained distributions of α , β , ϕ_0 and Ψ_0 values. The median and percentile are used instead of the mean and the root-mean-square because they are more tolerant to complicated non-Gaussian distributions.

Another type of Monte Carlo method is called the Bootstrap (BS) method. It is slightly different from the aforementioned Monte Carlo method in the process of producing synthetic datasets. Suppose that the original dataset \mathbf{BS}^0 consists of n independent data points and one thousand BS dataset ($\mathbf{BS}_{i,i=1,\dots,1000}$) will be simulated. To create each BS dataset, one randomly draws n data points from \mathbf{BS}^0 , viewed as a pool of $(\phi_k, \Psi_k)_{k=1,\dots,n}$. All data points in \mathbf{BS}_0 are allowed to be picked more than once, or otherwise, one will obviously end up with the same dataset to the original. One \mathbf{BS}_i file will randomly contains 63% of the original points, while the other 37% are duplicated. No change is applied to the σ_Ψ which remains fixed to individual Ψ_k , in contrast to the MC method. Then, the processes of fitting and measuring the results follow the same MC steps.

Results from the MC and BS methods applied to the RVM (not the RVM $_{\rho-W}$)

can be found in Jaroenjittichai (2009), where they are shown to provide reasonably consistent results to the LCS method; however, only for well-constrained cases where the diverging problem is not found. Nevertheless, for this work it is difficult to apply the MC or BS methods to the $\text{RVM}_{\rho-W}$ scheme. This is because it is difficult to incorporate the additional variables, $\rho \pm \sigma_\rho$ and $W \pm \sigma_W$ in the MC runs. We instead consider a way to directly convert the resulting χ^2 space to a PDF. Assuming Gaussian statistics of a profile of N PPA points ($\Psi^i \pm \sigma_\Psi^i$, $i = 1, \dots, N$), the probability that a set of (α, β, ρ_0) is the best fit is

$$\begin{aligned} P_{\alpha, \beta, \rho_0}(\Psi_1, \dots, \Psi_N) &= P_{\alpha, \beta, \rho_0}(\Psi_1) \cdot \dots \cdot P_{\alpha, \beta, \rho_0}(\Psi_N) \cdot \\ &P_{\alpha, \beta, \rho_0}(W) \cdot P_{\rho_0}(\rho(P)) \\ &\propto e^{-\chi_{total}^2/2}, \end{aligned} \tag{2.7}$$

where $P_{\alpha, \beta, \rho_0}(\Psi_i)$ is the probability that Ψ_i will be the PPA predicted by the model. The ϕ_0 and Ψ_0 are kept at values which give the lowest χ^2 for individual pairs of α and β . The χ^2 space (we use a 200×200 grid) given from an $\text{RVM}_{\rho-W}$ fit can then be converted into a probability space by the above equation. A PDF of α (or β) is the summation of the probability of all β (or α) corresponding to each α (or β) bin, resulting from a χ^2 grid search as in Fig. 2.3. The PDFs are normalised to a total probability of 1 for further analysis.

2.3 Fitting Routine

Our analysis starts with selecting pulsars with reasonable RVM-like PPA swings from our dataset. The pulse width at 5% of the peak intensity is measured using a Gaussian fits technique developed by Kramer (1994). For this work, the value of k in the $\rho - P$ relationship (Eq. 1.15) is chosen to be $(5.7 \pm 1)^\circ$, which is the averaged value from the results by Lyne & Manchester (1988), Gould (1994), Rankin (1994), and Kramer et al. (1994), as

$$\rho(P) \pm \sigma_\rho = (5.7 \pm 1)^\circ \cdot P^{1/2}. \quad (2.8)$$

The uncertainty in W (σ_w) is an average between $W_{4\%} - W_{5\%}$ and $W_{5\%} - W_{6\%}$, where $W_{x\%}$ is the pulse width measured at $x\%$ intensity level. The σ_w , however, cannot be smaller than 0.35° which is the resolution limit at 1,024-bin sampling. The measured W , σ_w , $\rho(P)$ and σ_ρ are then substituted in Eq. 2.6, in addition to the PPA data points. The resulting $\chi^2_{relative}$ grid of $\alpha - \beta$ is defined as $\chi^2_{relative} = \chi^2 - \chi^2_{min}$, which is converted to a probability of each (α, β) pair as $P_{\alpha,\beta} = e^{-\chi^2_{relative}/2}$ (Eq. 2.7). A PDF of α (or β) is calculated from a summation of the probability of all β (or α) corresponding to each α (or β) bin.

The LCS fitting algorithm is comprised of two fitting algorithms, which are Gridsearch and a downhill Simplex method, to ensure maximum computing efficiency and to avoid local χ^2 minima. First, Gridsearch, which is a simple brute-force search method, scans through all combinations of α and β at a fixed resolution, compromising between speed and accuracy. Each combination of α and β is followed up by the downhill Simplex Method, which is an adaptive-downhill geometric method which is faster but more vulnerable to local minima (Press et al. 1986). The resolution of Gridsearch can be reduced dramatically, especially at $\alpha \rightarrow 0^\circ$ and 180° , due to the correlation of $\alpha - \beta$ in the χ^2 plot, i.e. the banana. Therefore it is more effective to scan through the space of α and the steepest gradient of the S-swing (c) instead (Eq. 1.17).

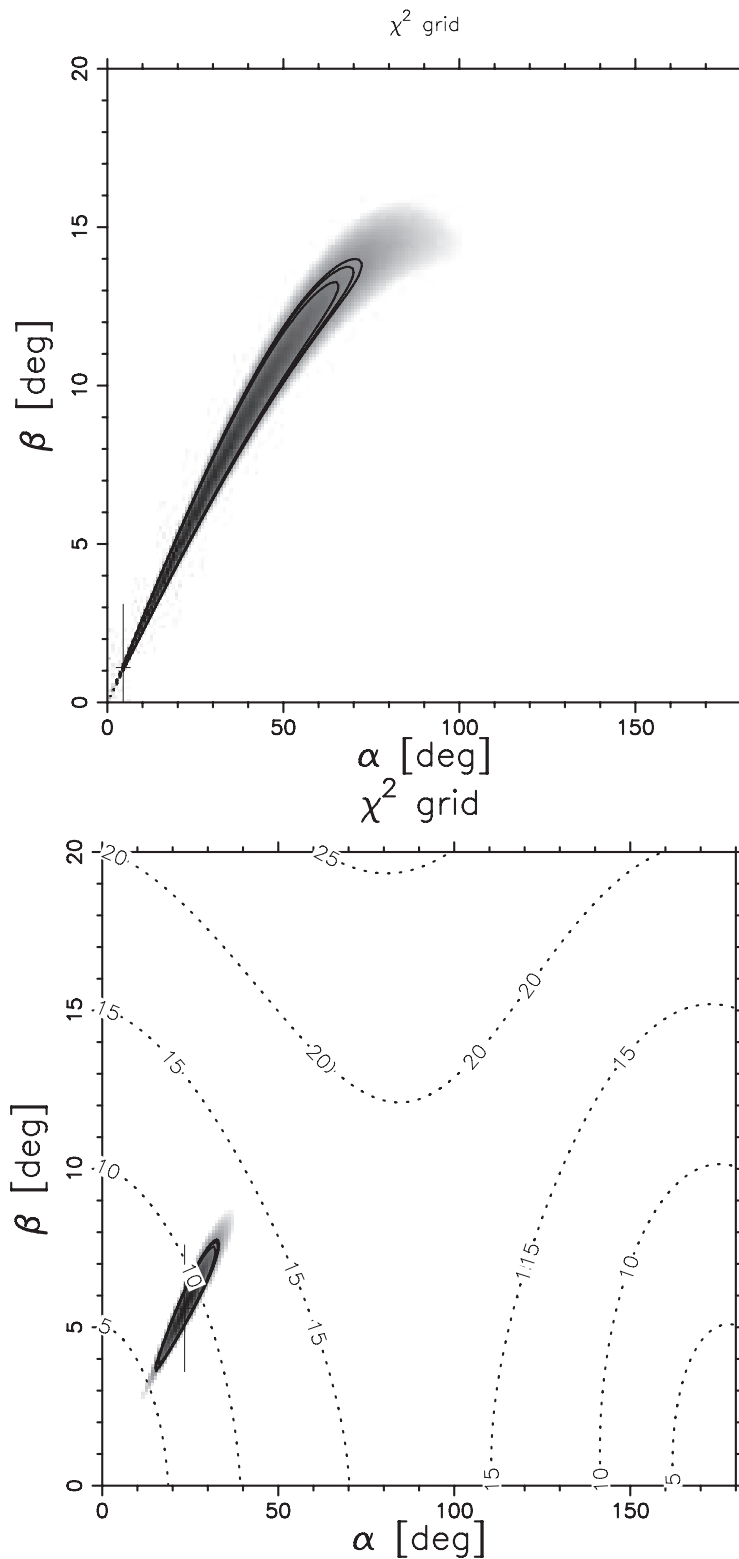


Figure 2.3: (Top) The χ^2 surface from the conventional RVM method, giving a diverging solution at $\alpha \rightarrow 0^\circ$, indicated by the *cross* symbol (PSR B0738-4042). (Bottom) The χ^2 surface from the $\text{RVM}_{\rho-W}$ of the same profile, resulting in a great improvement on the solutions. The three *solid* contours indicate the 1 σ , 2 σ and 3 σ error regions. The labelled *dotted* contours denote the ρ values, which are calculated from Eq. 1.9, using the measured W .

2.4 Results

Tab. 2.1 shows a list of pulsar parameters and the fitting results from the RVM and the $\text{RVM}_{\rho-W}$ methods of 53 profiles from 26 pulsars. All 20 profiles which give diverging RVM fits show great improvements in becoming converged with the $\text{RVM}_{\rho-W}$ technique. The fitting χ^2 maps, pulse profiles and the modelled PPA swings are included in Appendix A.

2.4.1 Interesting Cases

Although a majority of the results are consistent with the conventional dipole field beam model, there are a few cases where the geometry indicated from the RVM conflicts with that from the $\rho-P$ relationship. This inconsistency can be categorised into two types: first, when $\rho(P)$ is too large, such as PSR J0742–2822 and PSR J0835–4510; secondly, when $\rho(P)$ is too small, such as PSR J1057–5226 and PSR J1932+1059.

PSR J0742–2822: we firstly note that it is one of the pulsars known to be profile-switching, such that the trailing half is changing its relative amplitude, correlated with $\dot{\nu}$ (Lyne et al. 2010). As shown in Appendix A, the profiles appear to be comprised of at least three components, which are all highly linearly polarised, however, at high frequency (10 cm) the trailing side appears to be quickly depolarised at the edge. The geometry for this pulsar is problematic because $\rho(P) \sim 14^\circ$ is too large for the measured β , and consequently the $\text{RVM}_{\rho-W}$ implies an orthogonal solution, implying that an interpulse (IP) should be visible. Possible scenarios could be: 1) the IP is not active over the LOS; 2) the calculated ρ is too large, i.e., the chosen k factor is too large; 3) the apparent PPA is distorted to be flatter than the true PPA, meaning the true c is smaller and therefore β is larger, allowing a larger ρ ; 4) the measured $W \sim 15^\circ$ is too small, i.e., the beam is not fully active. The last scenario is rather plausible because the different nature between the leading and trailing halves of the profiles may indicate that a core and only half of the cone is observed. Indeed, Kramer (1994) found that at 1.42 GHz the profile has a very weak trailing component, which indicates a full-beam W of $\sim 24^\circ$, resulting in an α of $\sim 110^\circ$, for which an interpulse is no longer expected.

PSR J0835–4510 (B0833–45): The Vela pulsar’s profile is composed of a bright leading component and a weaker trailing component. At 8.4 GHz, the leading

Table 2.1: The pulsar parameters and fitting results from the RVM and the RVM $_{\rho-W}$; from left to right, PSR name, observing wavelength, the characteristic age, the pulsar's period, α and β from the RVM, $W_{5\%}$, ρ and their errorbars, and α and β from the RVM $_{\rho-W}$ method.

PSR	$\lambda(\text{cm})$	$\tau(\text{Myr})$	$P(\text{s})$	RVM		$W_{5\%}(\text{^\circ})$	$\pm W(\text{^\circ})$	$\rho(\text{^\circ})$	$\pm\rho(\text{^\circ})$	RVM $_{\rho-W}$	
				$\alpha(\text{^\circ})$	$\beta(\text{^\circ})$					$\alpha(\text{^\circ})$	$\beta(\text{^\circ})$
J0631+1036	10	0.044	0.29	121	-5.4	21.4	6.0	10.4	3.4	125	-5.2
	20			110	-6.5	25.7	5.6	10.4	3.4	136	-4.9
J0738-4042	10	3.68	0.37	≈ 0	≈ 0	32.0	0.7	9.1	2.9	24	5.6
	20			58	12.4	34.5	1.1	9.1	2.9	23	5.7
	50			53	12.5	47.8	0.7	9.1	2.9	18	4.7
J0742-2822	10	0.16	0.17	166	-1.6	16.9	0.7	13.7	4.4	99	-6.1
	20			169	-1.3	15.5	0.7	13.7	4.4	-8.1	105
	50			169	-1.3	14.1	0.7	13.7	4.4	-8.1	116
J0835-4510	20	0.011	0.089	112	-7.1	15.8	0.7	18.7	6.0	112	-7.1
J0907-5157	10	2.19	0.25	8	0.8	30.2	1.8	11.1	3.6	41	3.6
	20			43	8.4	34.5	18.3	11.1	3.6	29	6.6
	50			5	1.5	57.7	24.6	11.1	3.6	17	5.3
J0922+0638	10	0.50	0.43	7	0.7	15.0	0.7	8.5	2.7	65	5.0
J1048-5832	10	0.020	0.12	177	0.6	28.5	2.8	15.9	5.1	120	10.6
	50			21	4.6	37.3	5.6	15.9	5.1	41	8.7
J1057-5226	10	0.54	0.2	75	36.2	34.5	1.4	12.6	4.1	159	12
	20			76	35.5	33.4	8.1	12.6	4.1	159	11.9
	50			77	33.4	27.8	0.7	12.6	4.1	153	2.3
J1110-5637	20	4.29	0.56	167	1.6	17.2	1.4	7.5	2.4	137	5
	50			12	1.2	20.7	2.5	7.5	2.4	37	3.7
J1253-5820	20	1.93	0.26	9	0.9	17.6	1.4	11.1	3.6	80	5.4
	50			72	5.3	19.0	2.1	11.1	3.6	85	5.5
J1352-6803	20	8.07	0.63	8	-1.4	27.4	21.4	7.1	2.3	26	-4.3
J1535-4114	10	1.68	0.43	26	2.9	15.8	1.8	8.5	2.7	53	5.4
	20			39	4.4	17.9	1.4	8.5	2.7	47	5.1
	50			72	7	20.7	2.8	8.5	2.7	41	4.7
J1536-3602	20	26.5	1.32	175	0.7	28.1	5.3	4.9	1.6	161	2.5
	50			173	1.2	28.5	3.9	4.9	1.6	162	2.8
J1539-5626	10	0.80	0.24	1	0.2	22.1	2.1	11.4	3.6	40	8.2
	20			3	0.5	24.6	3.5	11.4	3.6	42	7.1
J1641-2347	20	421	1.09	130	-0.5	28.8	9.1	5.4	1.7	158	-0.3
J1645-0317	10	3.45	0.39	28	-0.3	15.5	0.7	9.0	2.9	80	-1.1
	50			163	-0.9	6.7	0.7	9.0	2.9	99	-3.2
J1700-3312	20	4.57	1.36	75	2	13.0	1.1	4.8	1.5	44	1.4
	50			127	1.9	13.7	1.4	4.8	1.5	138	1.6
J1705-1906	20	1.14	0.3	94	-7.7	17.2	0.7	10.2	3.3	94	-7.6
	50			93	-5.5	17.9	0.7	10.2	3.3	93	-5.6
J1733-3716	10	0.36	0.34	151	-5.3	52.0	3.5	9.6	3.1	161	-3.4
	20			175	-0.9	59.8	9.8	9.6	3.1	164	-3.2
	50			180	-0.1	65.0	119.2	9.6	3.1	170	-2.0
J1807-0847	50	90.1	0.16	179	-0.3	26.4	0.7	13.8	4.4	146	-11
J1835-1106	10	0.13	0.17	171	1.4	17.9	6.3	13.7	4.4	89	10
	50			3	0.7	22.9	11.3	13.7	4.4	48	10.3
J1901-0906	20	17.2	1.78	71	6.5	10.9	0.7	4.2	1.3	28	3.2
	50			166	0.9	11.6	0.7	4.2	1.3	142	2.3
J1904+0004	20	18.7	0.14	1	0.5	40.1	17.6	15.0	4.8	25	11.1
	50			9	2.1	35.5	11.6	15.0	4.8	41	8.3
J1917+1353	50	0.43	0.19	13	-1.1	15.1	0.7	12.7	4.1	92	-5.8
J1932+1059	10	3.10	0.23	109	-39.8	17.6	0.7	11.8	3.8	43	-9.3
	50			131	-28.5	19.7	0.7	11.8	3.8	26	-11.7
J2048-1616	10	2.84	1.96	15	-0.5	13.7	0.7	4.0	1.3	35	-1.1
	20			16	-0.5	14.8	0.7	4.0	1.3	32	-0.9
	50			109	-1.8	16.2	0.7	4.0	1.3	151	-0.9

component becomes weaker than the trailing component which suggests that the core and later half of the cone are being observed (Johnston et al. 2006). The amount of PPA aberration shift (Chapter 1) with respect to the peak component seems to support this conclusion well.

Because the Vela pulsar is very bright and hence its σ_{PPA} is very small, the constraint from $\rho(P)-W$ is completely overwhelmed by the RVM solutions, hence the best fit of $(\alpha, \beta) = (112^\circ, -7.1^\circ)$ is exactly the same for the RVM and the $RVM_{\rho-W}$. This solution is comparable with previous fits by Lyne & Manchester (1988) or Rankin (1990). While its $\rho(P)$ is measured to be 19° , the RVM solutions require ρ to be not larger than 11° (Appendix A). The following possibilities are considered: 1) the solutions by $\rho(P)$ and the RVM fit are both correct, but the measured $W = 16^\circ$ is too small, i.e. a part of the beam is not active. The full-width W has to be at least 35° in order to reconcile the solutions; 2) the inferred $\rho(P)$ is too large: it has to be $\sim 11^\circ$ which means k has to be at most 3.3° for the current measured W ; 3) the PPA swing is distorted and no longer represents the RVM geometry: the amount of such effect must be substantial as the steepest gradient (c) has to be -3.4° , instead of -7.5° , in order to obtain larger a β to sustain its $\rho(P)$ of 19° .

Interestingly, there is a sporadic (one in a thousand pulses) third component next to the trailing edge, which will give a full $W \approx 35^\circ$ as required (Johnston et al. 2001). They discussed that if this irregular component is considered to be a part of the full beam, it would suggest that the centre of the beam is no longer at the main peak but shifted toward the trailing weaker component. The fact that this component has its PPA mode orthogonal to that of the main pulse suggests a transition between core and conal components, which is related to different propagating modes (Chapter 3). Nevertheless, this interpretation is inconsistent with the concept of aberration shift of PPA swing and the frequency evolution of the cone/core components earlier by Johnston et al. (2006).

For the second group, the inferred $\rho(P)$ is too small compared to the RVM solutions. It is important to note that both of them have an IP, indicating two possible geometry configurations.

PSR J1057–5226: its main pulse is composed of at least four 100% linearly polarised sub-components, while the IP is only polarised for the leading half of the pulse. The PPA swings of MP and IP appear to be very flat, suggesting that the fiducial plane is not observed. The α configuration of this ‘old young’ (or young

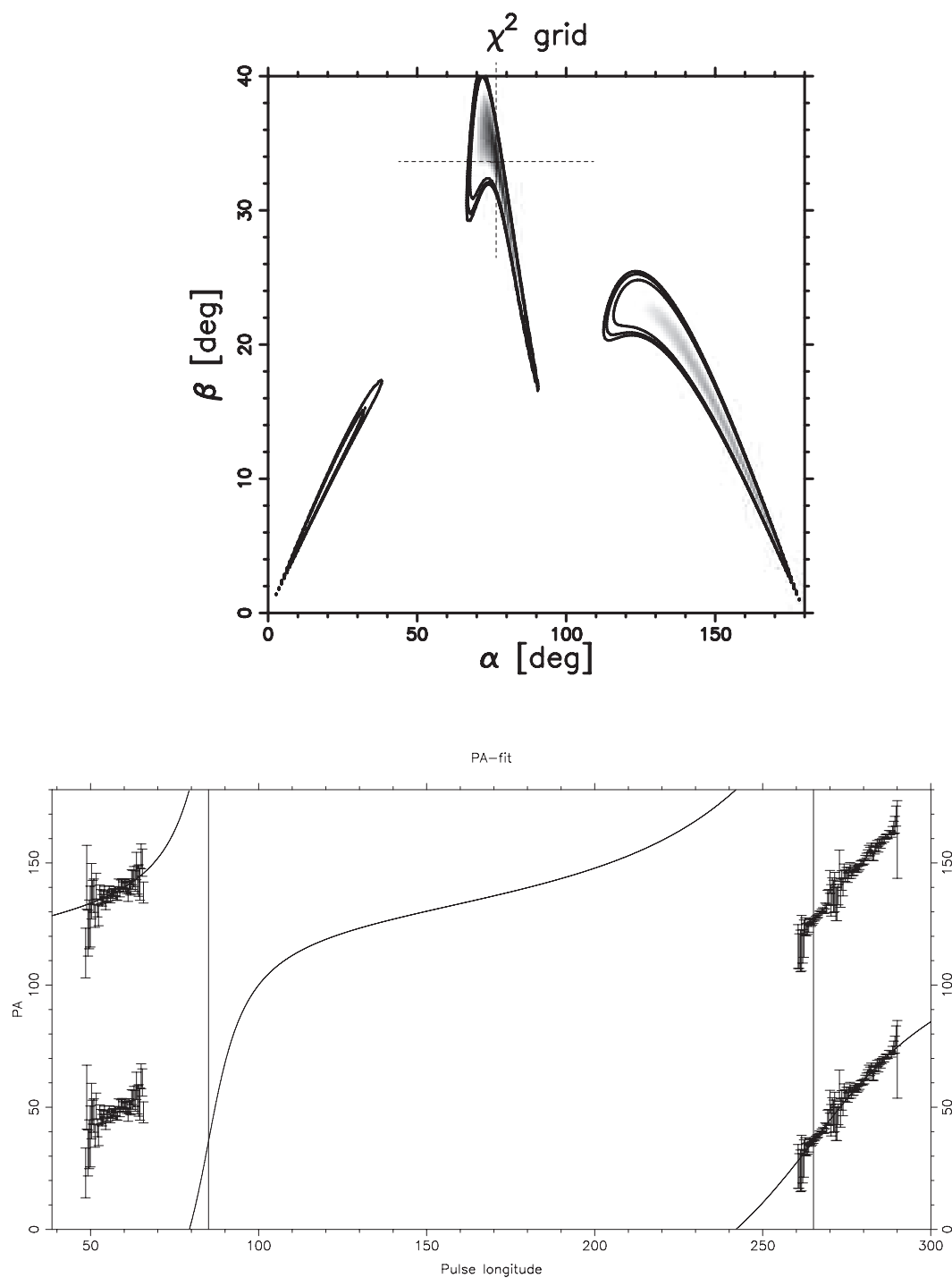


Figure 2.4: The RVM fit of PSR J1057–5226 at 50 cm, see Appendix A for the pulse profile. (*Top*) The χ^2 output, as defined in Fig. 2.3 (*top*). (*Bottom*) The PPA plotted with the best fit solution (*dotted cross*).

old) pulsar has long been debated (recently, Mitra & Rankin 2011). The RVM fit of our data (Fig. 2.4) shows three possible configurations of the geometry—inner and outer LOS alignment and orthogonal—which are all plausible within 3σ levels. However, the pulse profile at 325 MHz by Mitra & Rankin (2011) (their Fig. A3) shows that the PPAs of the IP’s trailing half are present, showing a rather steep swing which indicates a large value of β , in contrast to those of our profiles, which appear to be flat.

As shown in Appendix A, the $\text{RVM}_{\rho-W}$ PPA swings of the fitted α at 10, 20 and 50 cm are all forced to be close to the ‘pole’ solutions because of the fact that W ($\sim 36^\circ$) is too large for the calculated ρ of $\sim 13^\circ$ in order to obtain $\alpha \rightarrow 90^\circ$. Nevertheless, because the $\text{RVM}_{\rho-W}$ method does not take into account the presence of an *orthogonal* IP, its solutions cannot account for the IP which is indeed are inconsistent. Alternatively, instead of changing W , the beam-width ρ can also be increased to bring α close to 90° , which is, however, unlikely because it would require a k value of at least 10° . We also consider the aligned-rotator regime (Fig. 2.5), i.e. using the MP-to-IP $W \sim 200^\circ$ in the fitting process, providing a best-fit of $\alpha \sim 170^\circ$ and $\beta \sim 6^\circ$. Evidently, the fact that no bridge emission is detected within the noise limit (Wang et al. (2006)), lead people to believe that it has an orthogonal configuration.

As discussed by Weltevrede & Wright (2009), the orthogonal solution, however, is also inconsistent in that the expected ρ is at least 1.5 times too large ($W \sim 36^\circ$ compared with $\rho(P) \sim 13^\circ$). Holding onto the RVM’s orthogonal solutions, $(\alpha, \beta) \sim (40^\circ, 30^\circ)$, it is inevitable for them to conclude that the IP component originates from the conventional cone, while the MP must come from a closed-field-lines region above the null line². Interestingly, considering the 325-MHz profile by Mitra & Rankin (2011), the MP and IP components may have different PPA aberration delays, which could lead to a better solution if included in the fit.

PSR J1932+1059: The solutions of α by the RVM (not shown) and the $\text{RVM}_{\rho-W}$ (Appendix A) appear to be consistent at $\sim 40^\circ$, while the β of the $\text{RVM}_{\rho-W}$ is $\sim -10^\circ$, smaller than that of the RVM, $\sim -30^\circ$. The solutions by the RVM are also in agreement with the results obtained by Everett & Weisberg (2001), which also use an LCS RVM-fitting method. As for PSR J1057–5226, a

²Petrova (2009) also proposed a model, explaining the presence of radio components, observed outside the conventional hollow-cone model. See Chapter 5 for more details.

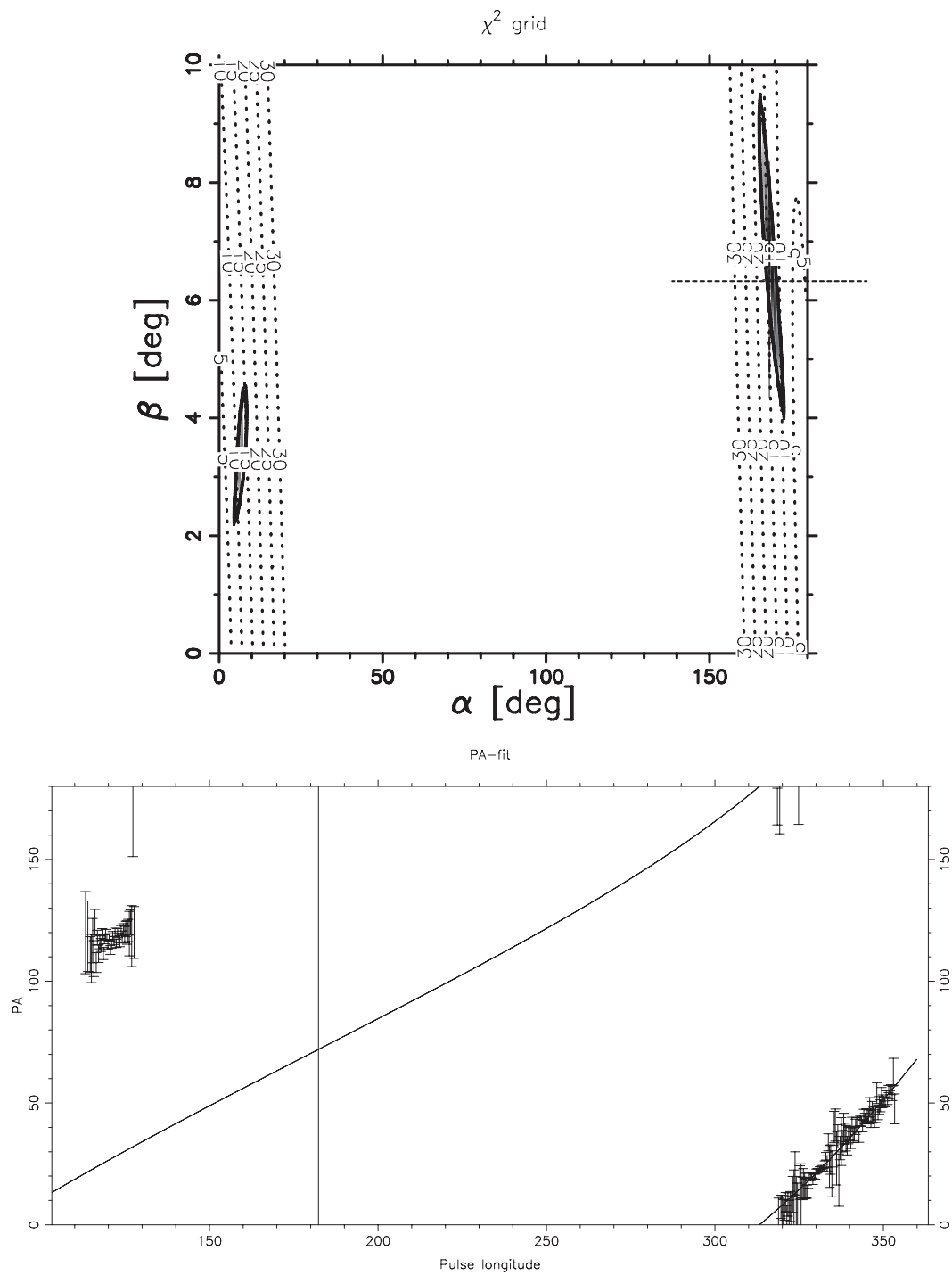


Figure 2.5: The $RVM_{\rho-W}$ fit of PSR J1057–5226 at 10 cm, assuming an aligned configuration of $W \sim 200^\circ$ (see Appendix A for comparison of normal fit, i.e. the W measured from the MP). (Top) The χ^2 output, as defined in Fig. 2.3 (top). (Bottom) The PPA plotted with the best fit solution (dotted cross).

similar inconsistency also arises for this pulsar. The fact that it is an orthogonal rotator, indicated from the MP-IP 180° separation, either requires a smaller W , which implies an emission from the closed-field-line region, or a larger $\rho(P)$, which is, however, unlikely as it requires k to be ~ 2 times larger than typical values.

Because of their similar properties, i.e. 1) having an IP; 2) being highly linearly polarised; 3) having a flat PPA. 4) suggested to have ‘off-the-beam’ emission, PSRs J1057-5226 and J1932+1059 appear to be interesting candidates for supporting Petrova’s model (Petrova 2008a;Petrova 2008b;Petrova 2009) which offers a mechanism for explaining interpulses (Chapter 5).

2.5 Discussions

2.5.1 On the $\text{RVM}_{\rho-W}$ Method

To improve limitations arising from the diverging problem, we included Eq. 1.9 ($\rho - W$ relationship) into the fitting process. In contrast to the RVM method itself, which does not require any assumptions related to the radio beam, the $\rho - W$ equation requires a value for the observed full-beam W and ρ , which need to be measured carefully. The new technique combines the χ^2 from the original RVM term with the additional constraint from the $\rho - W$ equation. The method is then applied to our sample, selected from the same dataset as in Jaroenjittichai (2009). Most cases show considerable improvement and the diverging problem is no longer present. However, there are a few exceptions in which there is an inconsistency between the RVM's and the $\rho - W$'s constraints, as described in the previous section. The exceptions can be put into two groups. The issue in the first group appears to be the underestimation of W . The inconsistency in the second group, which contains two orthogonal pulsars, indicates an underestimated k value in Eq. 2.8, otherwise one has to invoke a 'special' model to explain the off-field-line emission.

To examine how much the calculated α with $\text{RVM}_{\rho-W}$ method relies on the value of $k = (5.7 \pm 1)^\circ$, which translates to an uncertainty in ρ of around 3° for a 100-ms pulsar, and less for slower pulsars, we compare α calculated using ρ from Eq. 2.8 and the case where ρ is smaller by a factor of 2 (α_{half-k}), plotted in Fig. 2.6. Most of α_{half-k} is reduced by nearly the same factor which is represented by the *blue* line. However, the relationship becomes more complicated for $\alpha \rightarrow 90^\circ$ because the $\text{RVM}_{\rho-W}$ also depends on β and W , which become more dominant. A few α_{half-k} remain unchanged, either because their fits are completely dominated by the RVM term, or because their W 's are too large, which minimises the influence of ρ . This test indicates that the dependency of α on ρ (and k) is approximately linear and therefore the uncertainty in the resulting α is on the same level as in k , which is $\sim 18\%$. This uncertainty is, however, small compared to the total uncertainty in the $\text{RVM}_{\rho-W}$.

The diverging problem (Fig. 2.1) is shown to be simply caused by the fact the RVM fails to fit the PPA data, indicating the model's limit. However, it is certainly not because the concept of the RVM is inadequate, as proved to be consistent in many cases (e.g. Kramer & Johnston 2008, Keith et al. 2010), but

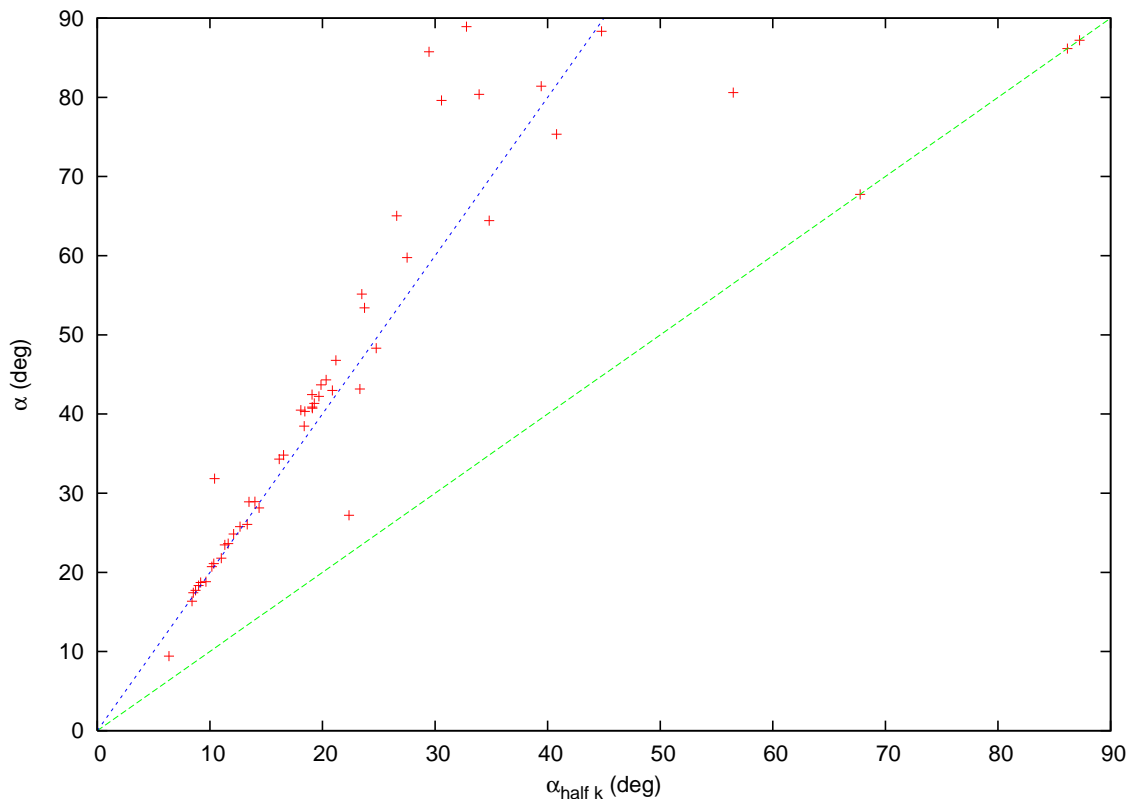


Figure 2.6: A plot comparing α , calculated from $k = 5.7 \pm 1$, with α_{half-k} , in which k is a factor of 2 smaller. The *blue* and *green* lines represent $\alpha = 2\alpha_{half-k}$ and $\alpha = \alpha_{half-k}$, respectively.

rather due to some additional effects which distort the original characteristic RVM PPA swings, e.g. geometrical and propagation effects. We also therefore conclude that the geometry of typical pulsars derived entirely from the best fit of the RVM is *likely to be unreliable* and probably will diverge, irrespective of W or S/N . By including the $\rho-W$ and the $\rho-P$ relationships to the RVM, which was fairly successfully done in this chapter, the derived geometry has been improved. In the next chapter, we explore propagation effects of radio waves in the magnetosphere, as one of the main mechanisms which can alternate the PPA swing from its geometry-related origin.

2.5.2 Beam Alignment

It has been debated whether the inclination angle (α) develops with pulsar's characteristic age (τ) (e.g. Candy & Blair 1983; Lyne & Manchester 1988; Beskin et al.

1988; Gil & Han 1996; Tauris & Manchester 1998; Weltevrede & Johnston 2008a). The α angle plays an important role in, for example, studies of the neutron star population. Also, as will be discussed later in Chapter 6, the recent work by Li et al. (2012a) predicts that the ratio of two $\dot{\nu}$ states (for a situation when there is plasma in the open-field-lines zone can disappear) strongly depends on α (Fig. 6.1).

The angle α has a direct impact on population studies because of the selection effect where the pulsar beam of a certain ρ at different α values covers different area on the pulsar's celestial sphere, which affect its probability of being detected. For example, a pulsar with a wide beam and $\alpha \rightarrow 90^\circ$ will have more chance to be detected than a narrow-beam and nearly aligned pulsar. This selection effect is corrected using the beaming fraction (BF), derived by Tauris & Manchester (1998) as

$$f(\rho, \alpha) = \begin{cases} 2 \sin \alpha \sin \rho & , \alpha > \rho, \alpha + \rho < \frac{\pi}{2} \\ \cos(\alpha - \rho) & , \alpha > \rho, \alpha + \rho > \frac{\pi}{2} \\ 1 - \cos(\alpha + \rho) & , \alpha < \rho, \alpha + \rho < \frac{\pi}{2} \\ 1 & , \alpha < \rho, \alpha + \rho > \frac{\pi}{2} \end{cases} \quad (2.9)$$

This formula assumes a circular beam and does not include a possibility that pulsars can have only one active radio beam.

Tauris & Manchester (1998) collected published α values of several hundreds pulsars from Rankin (1990) and Gould (1994). Despite a large scatter, they found a weak trend of alignment of α as a function of τ , and measured an alignment timescale of 10^7 years.

The $\alpha - \tau$ correlation can also be investigated through indirect observables (e.g. W) or via population synthesis (e.g. Gil & Han 1996; Kolonko et al. 2004; Weltevrede & Johnston 2008a; Young et al. 2010). Young et al. (2010) developed a model of the observed W as a function of τ , which depends on two geometrical parameters, $\alpha(\tau)$ and $\rho(P(\tau))$, because W is inversely proportional to $\sin(\alpha)$ (Eq. 1.9), while $\rho(P(\tau))$ is shrinking with τ due to a growing light cylinder. The model was fitted with the W measured from a large number of pulsars. Despite the rather shallow χ^2 values of the fits, the alignment time scale is measured to be 10^6 years, which is smaller than the typical number (10^7) from other methods. They argued that it is because the process of alignment might not take place immediately after the pulsars are born. They also showed that the initial α (α_0) distribution that can best reproduce the observed α distribution, as measured by

Rankin (1993) and Gould (1994), is the one where pulsars are born with random α .

The population synthesis method may require an assumed parent population (such as the initial pulsars' period distribution) which is then convolved with $\rho(P)$, beam shapes, random viewing angle, and models of α_0 distributions and different model for α evolution. The simulated population of W , P , α or a fraction of IP pulsars can then be compared with observations. The results by Kolonko et al. (2004) suggest that the α distribution, which best fits the α distribution of RAN93, has a local maximum at $\alpha \sim 25^\circ$ and another weaker one at $\alpha \sim 90^\circ$, which is necessary to sustain the rate of IP pulsars. Such a bimodal distribution is interpreted as a competitive mechanism between a progressive alignment and a counter-alignment process. Weltevrede & Johnston (2008a) also compared their simulated population, based on random values of α_0 , and found that too many IP pulsars are predicted, for which possible explanations are given, such as the existence of one-pole orthogonal pulsars, a different $\rho(P)$ law for orthogonal pulsars and a non-random α_0 distribution.

With pulsars with inconsistent solutions (see Section 2.4.1) excluded, the α values of the remaining 39 profiles from 19 pulsars in Tab. 2.1 are included in the following analysis. Having the characteristic age between 10 kyr and 100 Myr, the sample is divided into three age groups, $\tau < 1$ Myr, $1 \text{ Myr} < \tau < 10$ Myr, and $10 \text{ Myr} < \tau$, containing 6, 8, and 5 pulsars, respectively.

Despite the limited number of pulsars in our sample, we attempt to find a correlation between α and τ . The parameter space of PDFs derived in Section 2.2 is reduced by taking α values with respect with the nearest pole, i.e. from 0° to 90° , as opposed to the original 0° to 180° . This would, however, mean that information relating to the sense of a pulsar's rotation will be lost. For example, a question of whether α has a connection with a pulsar's angular momentum vector cannot be tested. If the PDF is too wide, after folding the PDF onto $0^\circ < \alpha < 90^\circ$ there will be an overlap, in which case the highest value of the PDF is chosen. For multi-frequency profiles, their PDFs are the average between those derived at individual frequencies. It appears that the best method to properly combine the PDFs within each group is a highly debated matter of research (Lee, K.J., private communication). We consider two simple methods, which can be considered to be the extremes of the range of possible methods. These methods are multiplying (MP) and adding (AD) the PDFs. Each α bin of the combined

PDF for each group is the product or sum of the probabilities from the PDFs of the members within each group. The total probability of the resulting PDF is then normalised to unity.

The resulting PDFs of the three τ groups, for both the AD or MP methods, and with or without the BF correction, are shown in Fig. 2.7, and their corresponding mean and standard deviation are plotted in Fig. 2.8. We shall first discuss the combining methods to evaluate the significance of the resulting distributions. Resembling the operations of unification (AD) and intersection (MP) in algebra, the two methods present two extremes. The AD method is more tolerant to outliers but results in its wider distributions, while the MP method gives better constrained PDFs but the results can easily be biased by an individual pulsar which has a more constrained fit. We believe that a proper method should lie in between these two extremes, which is possibly well represented by an average sum ($\frac{AD+MP}{2}$). Nevertheless, it should be noted that the accuracy in this analysis is already limited by the small number of pulsars.

Before discussing possible alignment, another feature appears in the BF-corrected version of the AD PDFs (Fig. 2.7), which is the sharp rises at $\alpha \sim 0^\circ$. This stems from the conditions of the beaming fraction in Eq. 2.9, that the beam of aligned rotators cover less area than orthogonal rotators.

Despite the limited numbers of pulsars, the resulting PDFs of the three τ groups indicate a trend favouring progressive alignment with τ , as shown in Fig. 2.7 and 2.8. The finding that the PDFs of the youngest group (*red*) appear to be broader supports earlier works which found that the initial α_0 is random or that young pulsars might have a more complex evolution path, such as the counter-alignment occurring prior to the progressive alignment, which has been discussed in Young et al. (2010).

2.5.3 Averaged Beam Map

Based on the shape of a large number of symmetric pulse profiles, it has been proposed that the structure of the pulsar's emission beam is composed of one or multiple hollow cones concentric with a core component, centred on the magnetic axis (e.g. Rankin 1990, Rankin 1993). However, alternative views exist also. For instance, Lyne & Manchester (1988) argue that there appears to be no common structure and they conclude that the emission region consist of random patches. In this section we attempt to produce an average beam map from our

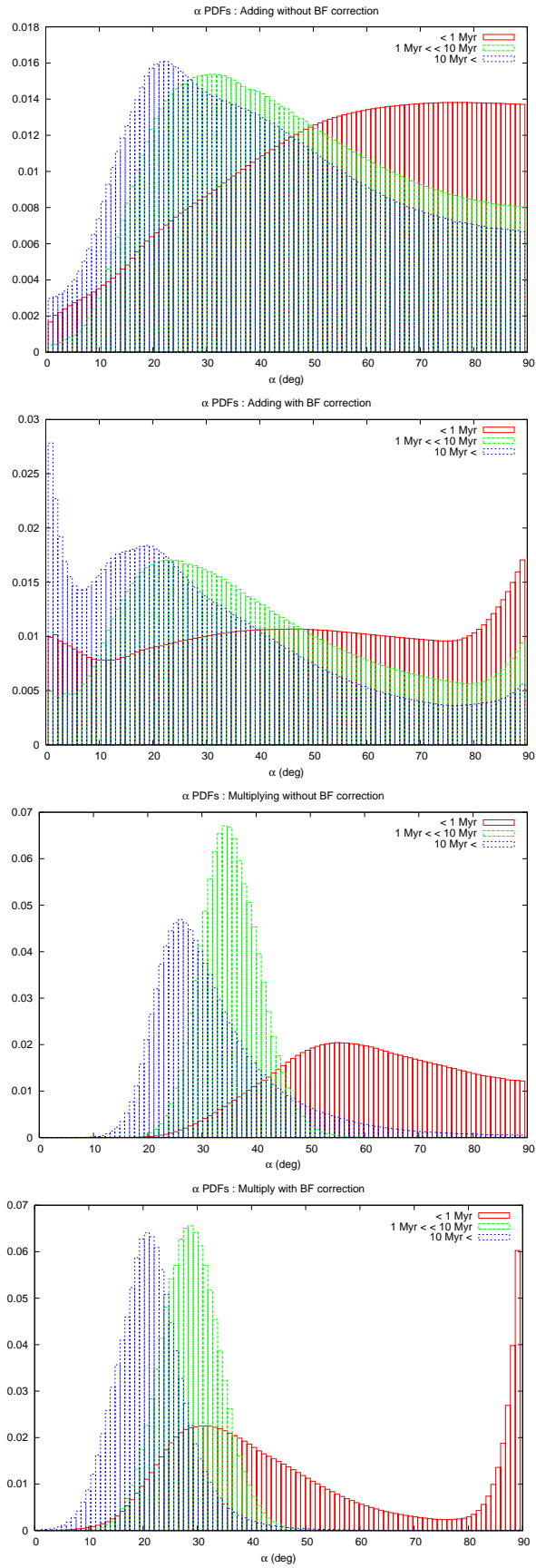


Figure 2.7: The combined α PDFs in three age groups of $\tau < 1$ Myr (red), $1 \text{ Myr} < \tau < 10$ Myr (green), and $10 \text{ Myr} < \tau$ (blue). From top to bottom, the AD version without and with the BF correction, and the MP version without and with the BF correction.

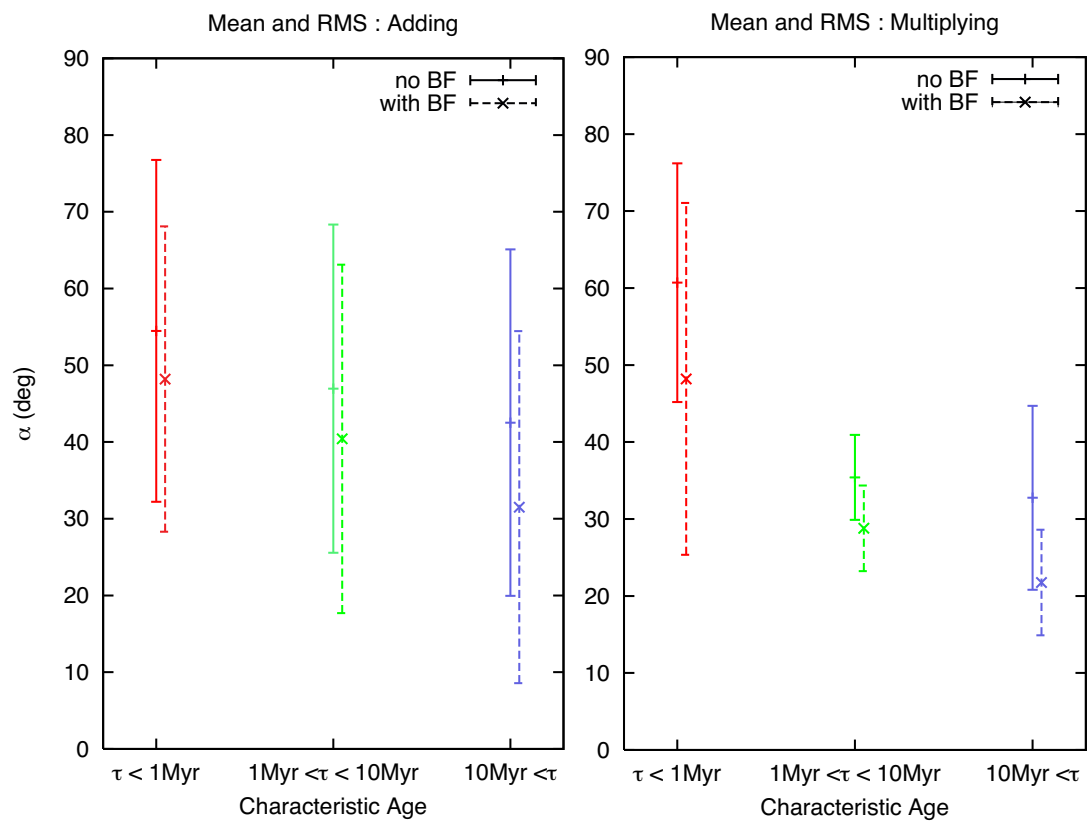


Figure 2.8: The median and 1σ errorbars, measured from results in Fig. 2.7, between three τ groups.

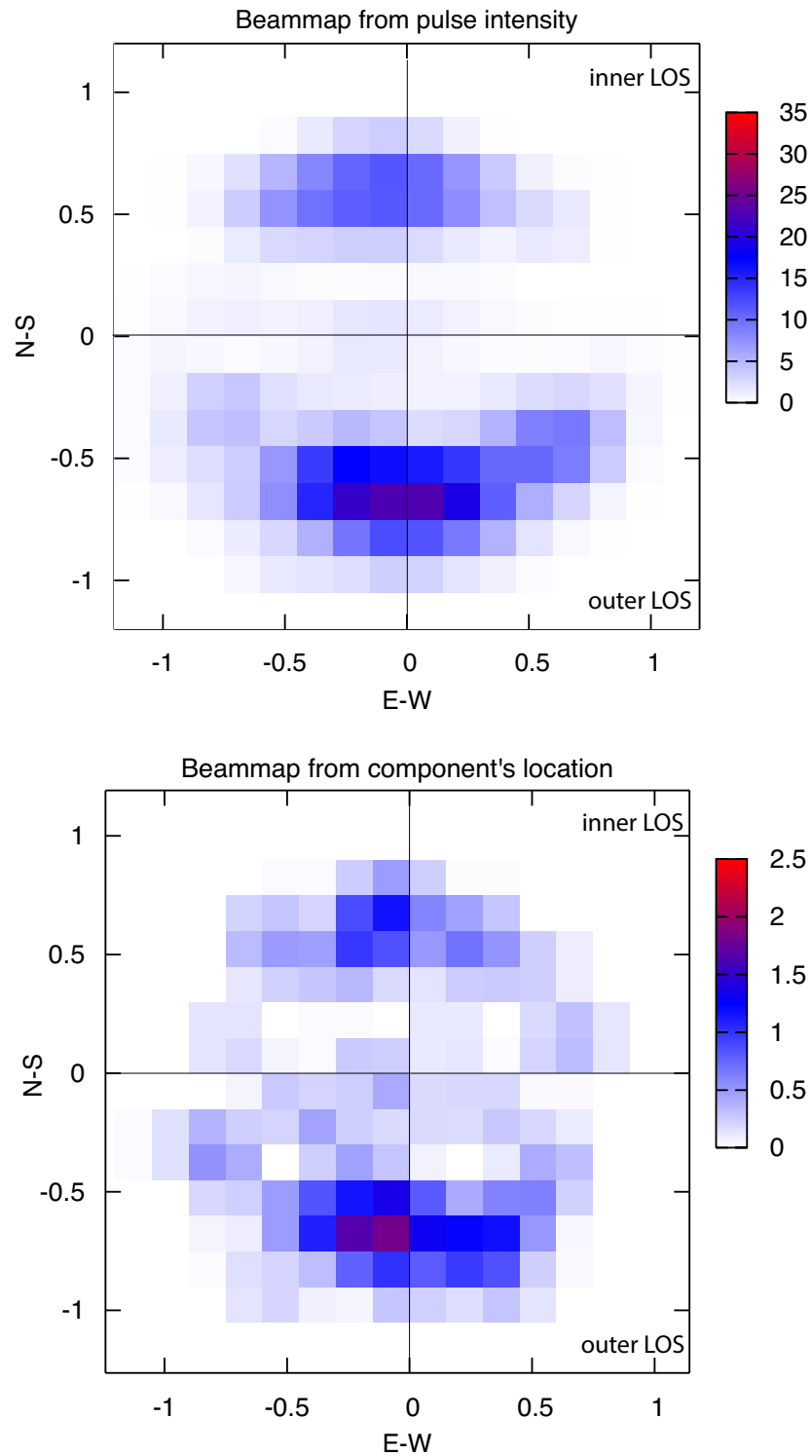


Figure 2.9: The average beam maps. The *top* map is produced by arranging the intensity profiles, accordingly to the measured geometry. The *bottom* map is produced using the counts of the individual sub-component locations. The unit is normalised by ρ .

dataset, using the derived geometry in this chapter, to test if there is any common structure.

The beam maps, shown in Fig. 2.9, are produced by making a 2-dimensional histogram of the intensity profiles (*top*) or the sub-components' location (of the Gaussian-fitted pulse profiles) (*bottom*). For the *East – West*, or longitudinal, coordinate, the pulse profiles are aligned on the map, according to their resulting ϕ_0 and normalised by ρ . Negative and positive sides represent the leading and trailing pulse phase. At this point we neglect the effects of aberration, i.e. assume the centre of the intensity profile is at the same location as the magnetic axis. The *North – South*, or latitudinal, coordinate is represented by the measured β/ρ , where the northern and southern halves of the beam indicate the inner LOS and outer LOS solutions, respectively.

Before being plotted on the average beam map, each profile has its peak intensity normalised to 1 and the measured β is normalised by its ρ , because different pulsars have different P , i.e. ρ . Also, because the LOS path across the beam is not a straight line, depending on α and β , the correct location on the beam map is computed using spherical geometry. To avoid that weak components are suppressed in the intensity map, we also produce a histogram using the locations of the sub-components (ignoring their intensity), which are derived from the Gaussian-component fits of the pulse profiles by Kramer (1994).

We should first note that the maps are biased due to a selection effect that our sample contains only pulsars with RVM-like PPAs and considerably high L . In both versions of the beam map, there appears to be a ring-like structure at radius ~ 0.75 on the beam, accompanied by a possible weak core-structure in the centre. The fact that the core-region is weaker could be because the PPAs of the core component are often very complicated and non-RVM like (e.g. Rankin 1990).

The outer LOS solutions are found to be more populated than the inner LOS case, by a factor of ~ 2 . However, this can be uncertain because the maps are produced by using the best fit solutions (as opposed to the analysis in the previous section which uses the full PDFs information). Often the resulting χ^2 contours from our data cannot distinguish between both types of solutions. A simulation was carried out to confirm that the fitting process and the $\text{RVM}_{\rho-W}$ method itself are not biased towards either of the two types of solutions. Also, because we also found a similar correlation in the calculated results by Rankin (1993) suggests

that there is a larger probability of finding the outer LOS solution than that of the inner LOS. This could imply: 1) either the PPAs are non-RVM-like or have less L on the inner-LOS's half of the pulsar beam, or both (selection effect); 2) on average, the outer-LOS part of the pulsar beam is indeed brighter than the other, due to a physical reason intrinsic to the emission and/or propagation processes.

Lastly, because we ignore the PPA's delay due to the aberration effects; as a result the beam maps appear to be slightly shifted to earlier phase (Eastward). This implies that our results confirm that there is a delay between the PPA swing and the intensity profile, which is suggested to be due to the aberration effect (e.g. Blaskiewicz et al. 1991), rather than being random shifts.

Chapter 3

Modes of Wave Propagation

To gain more insight into the effects of wave propagation in the magnetosphere on the intensity and polarisation of the radio waves, in this chapter we study a recent work of Beskin & Philippov (2012) (hereafter BP12). They have derived a comprehensive model which considers properties of the radio waves after being produced in the radiation zone, propagating higher up, and until they leave the plasma-dense limit at a radius close to the light cylinder. As one of the results, the model predicts a one-to-one correlation between the propagation modes and the temporal coincidence of the signs of the Stokes V profile and the PPA's steepest gradient.

In Section 3.1, we briefly describe essential parts of BP12's model, where results from simulations are presented in Section 3.2. Then in Section 3.3, the above-mentioned predicted correlation is evaluated on a number of published polarisation profiles, based on the assumption that the two propagation modes are each corresponding to the core and conal components of the radio beam. Finally, discussions and conclusions are presented in Section 3.4.

3.1 Theoretical Background

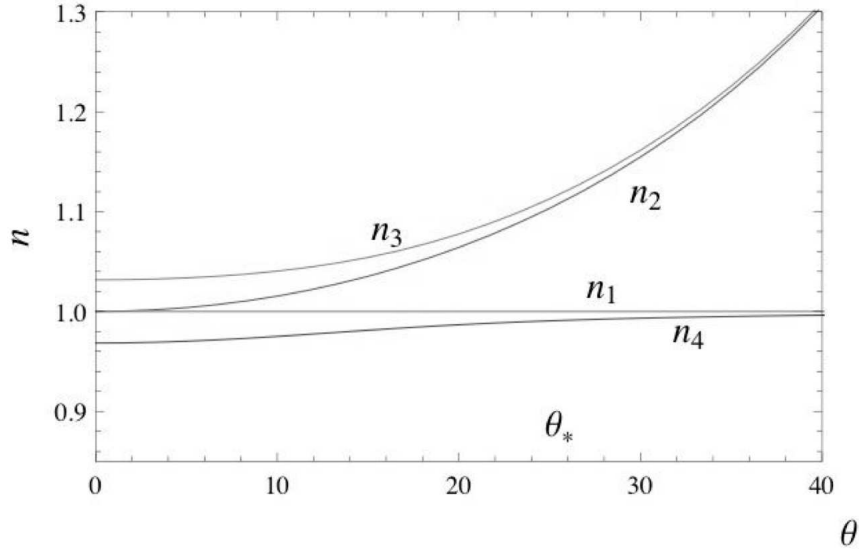


Figure 3.1: The relationship between the refractive indices (n) and the angle between \mathbf{k} and \mathbf{B} (θ), for $A_p \gg 1$. The waves labelled with n_1 ($n \sim 1$) and n_4 ($n \leq 1$) are known as the X- and O-mode waves, respectively (BP12).

In this section, we describe a comprehensive calculation of propagating radio waves in pulsar magnetospheres (e.g. Arons & Barnard 1986) by BP12. Conventional treatments of the propagation of electromagnetic waves in magnetised plasma involve solving the ‘dispersion relation’, in which the natural modes of the possible waves are represented by the refractive indices (n).

Following Beskin et al. (1993) (chapter 6, hereafter BGI93), the derivation starts with a question: what kind of electromagnetic radio waves are ‘permitted’ to propagate in the pulsar magnetosphere, which is assumed to be composed of a relativistic electron-positron plasma in a strong homogeneous magnetic field? Their resulting dispersion relation allows four waves to exist at different limits of plasma density. They consider the dispersion relation further in the limit

$$A_P = \frac{\omega_p^2}{\omega^2} \langle \gamma \rangle, \quad (3.1)$$

where ω is the wave frequency, $\omega_p = (4\pi e^2 n_e / m_e)^{1/2}$ is the plasma frequency, n_e is the particle number density, m_e is the particle mass, and γ is the Lorentz factor. The brackets $\langle \rangle$ denote the averaging over the particle distribution for both

negatively and positively charged particles. In the two extreme limits, $A_P \ll 1$ or $A_P \gg 1$, this A_P factor is an indication of how the plasma density compares to the wave frequency.

The first solution is a wave with $n = 1$ (n_1), which propagates regardless of A_P , i.e. it is present in both limits. In this mode, the wave's $\hat{\mathbf{E}}$ is perpendicular to the $\mathbf{k} - \mathbf{B}$ plane, where \mathbf{k} is the wave vector, indicating propagating direction, and \mathbf{B} is the local magnetic field vector. This means that the wave can travel freely in the extremely strong B field. This wave is the so-called ‘extraordinary’ or the X mode.

In the limit $A_P \ll 1$ (not shown), the same n_1 wave is the only one allowed to propagate and escape the magnetosphere, while the other two waves, which have $n > 1$, are eventually reflected back to the neutron star. In the limit $A_P \gg 1$ (Fig. 3.1), there are two solutions with $n > 1$ (n_2 and n_3), which also cannot escape. The solution n_4 with $n \leq 1$ is known as the ordinary mode or the ‘O mode’, which has its \mathbf{E} is parallel to the $\mathbf{k} - \mathbf{B}$ plane.

In Fig. 3.1, the fact that the refractive index n of the n_4 wave increases towards 1 at large θ (where θ is the angle between \mathbf{k} and \mathbf{B}), indicates that the O-mode wave is strongly refractive at low altitude, i.e. small θ , and it later becomes less refractive as θ grows, i.e. at higher altitude. At $\theta \sim 25^\circ$ ($\theta = \theta_*$), the O-mode wave is approximated to stop being refracted. BP12 derive the altitude which corresponds to θ_* as

$$r_A \approx 10^2 R \lambda_4^{1/3} \gamma_{100}^{1/3} B_{12}^{1/3} f_{\text{GHz}}^{-2/3} P^{-1/3} \text{ km}, \quad (3.2)$$

where

$$\begin{aligned} \lambda_4 &= \frac{\lambda}{10^4} \quad ; \quad \gamma_{100} = \frac{\gamma}{100} \quad ; \\ B_{12} &= \frac{B}{10^{12}} \text{ G} \quad ; \quad f = \frac{f}{10^9} \text{ GHz}, \end{aligned} \quad (3.3)$$

in which $\lambda = n_e/n_{GJ}$ is the multiplicity of the particle number (n_e is the number density and $n_{GJ} = \omega B/2\pi c e$ is the Goldreich-Julian number density (Chapter 1)). For typical pulsars, this altitude appears to be around ~ 1000 km. Another radius, important for studying properties of the polarisation, is the so-called ‘polarisation-limiting radius’ (PLR),

$$r_{PLR} \approx 10^3 R \lambda_4^{2/5} \gamma_{100}^{-6/5} B_{12}^{2/5} f_{\text{GHz}}^{-2/3} P^{-1/5}, \quad (3.4)$$

which represents the boundary above which the plasma density can be considered

to no longer be able to affect the PPAs (Barnard 1986, BP12). The altitude r_{PLR} can range from a few thousands kilometres to close to r_{LC} , which is of order a few tens of thousands of kilometres.

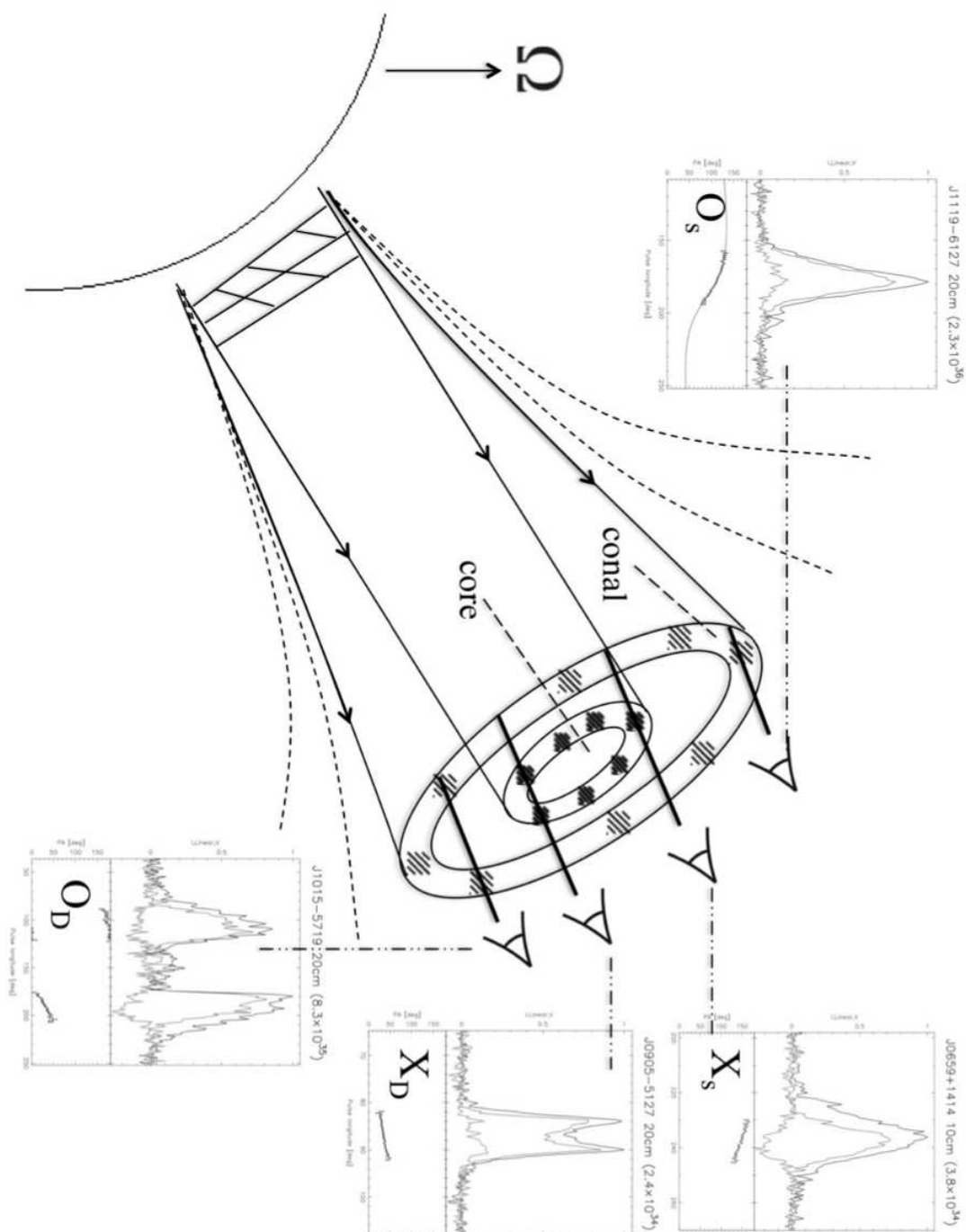


Figure 3.2: Interpretation of the wave-propagation solutions as the cone (the O-mode) and the core (the X-mode) components from the hollow-cone model. BP12's model also predicts a correlation between the polarisation properties and the propagation modes of pulse profiles (see main text).

Because the O-mode is refracted as it propagates in the magnetosphere, while the X mode is not, it can be expected that the two types of waves form a core-cone structure. Consequently, this appears to be consistent with the observations, i.e. the hollow-cone model, where the core component is of the non-refracted X-mode wave and the cone component is of the refracted O-mode wave (Melrose & Stoneham 1977, Arons & Barnard 1986), as sketched in Fig. 3.2. The diagram explains that how different types of profiles, i.e. single or double, and different type of modes, i.e. X or O, are observed depending on different LOS. We will test this prediction in the next section. This model has supporting evidence, for example, the fact that r_A is proportional to $f^{-2/3}$ has two consequences: 1) BGI93 (their section 7.6.2) demonstrated that the calculated power index b in the relation $W \propto f^{-b}$ agrees well with the measurements by Rankin (1983); 2) at high f , there will be much overlapping between the O- and X-mode waves, resulting in the reduction in linear polarisation with f . In addition, the values of k in the ρ - P relationship derived ‘empirically’ from various methods, presented in Chapter 1, appear to be consistent with calculated angular size of the beaming structure of both the X- and O-mode waves (BGI93’s section 7.6.2).

And most importantly, the propagation effect is known to cause the well-known 90° ‘jump’ or the ‘Orthogonal Polarisation Mode (OPM)’ in the PPA swings, when the LOS passes different parts of the beam of different modes (Backer et al. 1976). For example, a pulse profile of PSR J1146–6030 in Fig. 3.6 shows two OPM jumps, which is in general simultaneously observed with an abrupt decrease in L (Stinebring et al. 1984) and often the change of the sign of V .

The model by BP12 is presented as the following. The pulsar magnetosphere can be roughly separated into three separate zones. From the surface outwards there are: 1) the polar gap zone, occupied by highly energetic charged particles which then produce a large number of less energetic pair-plasma particles via the pair production process; 2) the region where those abundant charged particles coherently generate radio waves; 3) the propagation zone where the radiated waves travel, interacting with the plasma medium.

The work of BP12 contains a comprehensive simulation of these zones. Firstly, the initial photon spatial distribution, i.e. radiation pattern, is assumed to be

$$n_e = g\lambda n_{GJ} \quad ; \quad (3.5)$$

Here g is the plasma distribution function and an example is shown in Fig. 3.3. In this figure, the suppression in the centre is due to the assumption that the radio emission originates from the process of curvature radiation, and the field lines are less curved near the magnetic axis.

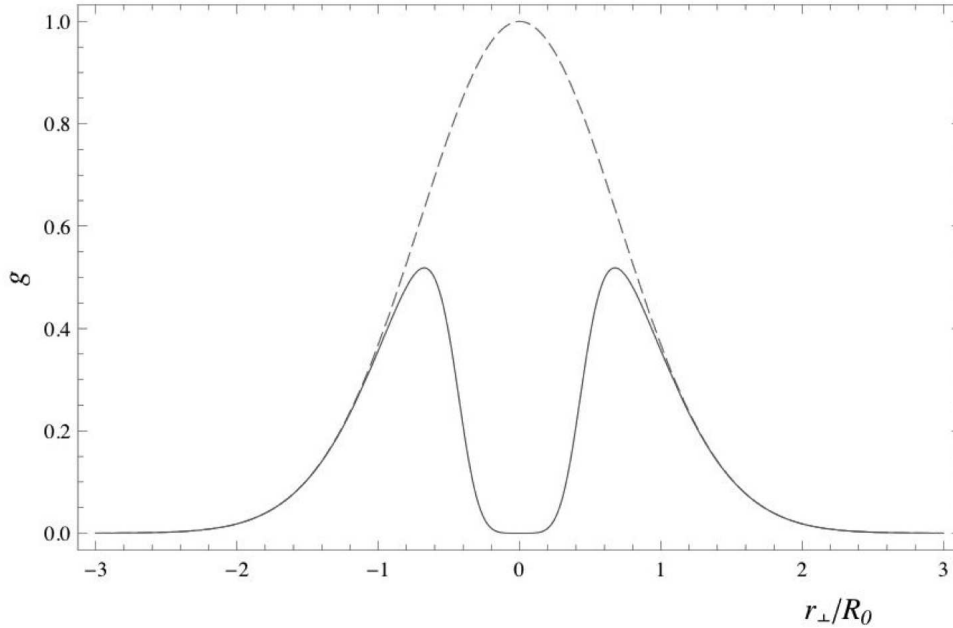


Figure 3.3: Plasma distribution function g for $f_0 = 0.25$ on the polar cap as a function of r_{\perp}/R_0 , which is a dimensionless distance measured from the magnetic axis ($r_{\perp} = 0$) to the edge of the polar cap ($r_{\perp} = 1$).

Both of the outgoing modes are assumed to be generated at the same height ($r_{em} \sim$ a few hundred km), where the initial PPA is also defined according to the RVM, and where the aberration effects (Chapter 1) (e.g. Blaskiewicz et al. 1991; Dyks 2008) are calculated. While X-mode radiation escapes freely, the O-mode wave keeps refracting as long as $r \leq r_A$ and then travels straight upwards. In the propagating zone, the permittivity of the plasmatic magnetosphere is represented by the ‘dielectric tensor’, containing information about how electromagnetic waves propagate. The perturbation on the PPA and the increment of V are calculated from this tensor. The magnetic field model is treated to be composed of two terms, $\mathbf{B} = \mathbf{B}_d + \mathbf{B}_w$, where \mathbf{B}_d and \mathbf{B}_w are the rotating dipole term and the pulsar wind term, respectively. The \mathbf{B}_w term is related to the electric current of the escaping wind, which becomes important for the properties of intermittent pulsars (Kramer et al. 2006, see also Chapter 6). For the results in

the next section, this term is not included as it can be considered to be small, where the simulated profiles remain qualitatively similar, but not quantitatively identical as presented in BP12 (Philippov, S.¹).

BP12 also consider cyclotron absorption, which takes place when the frequency of the radio wave is close to the electron cyclotron frequency $\omega_c = eB/mc$. As a result the intensity of the outgoing wave is attenuated as

$$I_\infty = I_0 e^{-\tau}, \quad (3.6)$$

where I_0 is the initial intensity from the emission region, and τ is the absorption index, mostly related to λ .

One of the important ideas in BP12 is that the magnetic field lines can have a large twist along the ray of propagation, which gives rise to a considerable amount of V . Whether the sign of incrementing V is positive or negative² depends on the direction of the pulsar's rotation vector, indicating the sense of the pulsar's rotation, because different signs of the induced electric field are produced. The sign of the steepest gradient of PPA ($\frac{d\text{PPA}}{d\phi}|_{\text{max}}$) similarly also depends on the direction of the rotation vector, because a PPA swing would be pulse-phase reversed if the pulsar span in the opposite direction. Connected via the pulsar's sense of rotation, the two observables, $\frac{d\text{PPA}}{d\phi}$ and V , are predicted to have their signs dependent on the modes of propagation. Starting from the dielectric tensor, the two possible states are predicted for each combination of the observed $\frac{d\text{PPA}}{d\phi}$ and V , such that one state, identified as the X mode, gives the *same* sign of $d\text{PPA}/d\phi$ and V , and the other solution gives *opposite* signs, recognised as the O mode. This then leads BP12 to propose a way to distinguish the propagating modes, which will be tested in Section 3.3.

¹private communication

²+ V = *left*-hand circular polarisation, and vice versa.

3.2 Observational Consequences

In order to understand the distortion done to the PPA generated according to the RVM at the emission height (r_{em}), we generate a number of simulated profiles³. Note that the following simulations is only for the X-mode wave. We consider various combinations of four parameters: the plasma frequency (f), Lorentz factor (γ), emission height (r_{em}), and multiplicity factor ($\lambda \propto n_e/n_{GJ}$) (Tab. 3.1).

Table 3.1: Combinations of parameters used in the simulations.

f (MHz)	γ	r_{em} (km)	λ
300	50	100	100
1500	100	300	1000
800	300	500	10 000

The inclination (α) and the impact angles (β) are set to 91° and 1° ⁴, while other constants are $B_{\text{surface,pole}} = 10^{12}$ G, $P = 0.7$ s, and $R_\star = 10$ km. The plasma-distribution constant (f_0), which dictates the deficit of particles around the magnetic axis, is set to $0.1R_{\text{polarcap}}$. In terms of resolution, the calculated pulse phase is from -15° to $+15^\circ$, sampled with 15 phase-bins⁵.

Table 3.2: Table summarising how the pulse intensity and the polarisation change with the model’s variables. $\uparrow\uparrow$ (or $\uparrow\downarrow$) signifies a correlation (or anti-correlation) between the effects and the variables. ‘abr.’ stands for the aberration effects which are observed as a delay between the MP and the PPA swing. See text for more details.

	abr.	$\{dPPA/d\phi\}_{max}$	notches	absorption	$ V $
f	$\uparrow\downarrow$	$\uparrow\downarrow$	$\uparrow\downarrow$	$\uparrow\downarrow$	$\uparrow\uparrow/\uparrow\downarrow$ (low/high γ)
γ	$\uparrow\downarrow$	$\uparrow\downarrow$	$\uparrow\downarrow$	$\uparrow\downarrow$	
λ	$\uparrow\uparrow$	$\uparrow\uparrow$	$\uparrow\uparrow$	$\uparrow\uparrow$	$\uparrow\downarrow/\uparrow\uparrow$ (low/high γ)

All of the resulting simulated profiles are presented in Appendix B, where a few examples are shown in Fig. 3.4. Five interesting effects on the PPAs and the pulse profiles are summarised in Tab. 3.2. The PPA delay due to the effects of

³Simulation codes are kindly provided from our collaborators, Beskin, V. and Philippov, S.

⁴As of PSR B1822–09, which will be our case study (Chapter 5)

⁵The resulting profiles look smooth because the ‘interpolation’ plotting option in *Mathematica* software.

aberration, which can be easily recognised, depends primarily on r_{em} , while the dependency on f , γ and λ is accordingly via r_{PLR} (Eq. 3.4), i.e. the higher the PLR altitude, the later the PPAs become fixed, and hence being more distorted. The change in $\{dPPA/d\phi\}_{|_{max}}$ appears to be consistent with the results by BP12 (their table 3). However, because the combination of $\alpha = 91^\circ$ and $\beta = 1^\circ$ has a rather steep swing to begin with, and because of the limitation in the bin resolution, it is rather difficult, in some cases, to recognise the features.

In addition, the PPA's slope is also affected by presence of the 'notches' at both sides (Fig. 3.4, as seen for instance at phase 4° and 9°) which vary as well in amplitude. Similar to the aberration shift, the magnitude of the notches seems to be correlated with r_{PLR} , as with the same dependency on r_{PLR} . Specific causes of this feature are not yet clear and these 'notches' do not appear in BP12. We therefore suspect that it is related to α , which is different from BP12's α ($\sim 45^\circ$), or due to the fact that the contribution of the wind to the \mathbf{B} -field is not included in this simulation. The dependency on α is investigated later.

Development in the pulse profile shape also correlates strongly with r_{em} , as the shape evolves from a sharp single to a clear double type from $r_{em} = 100$ km to $r_{em} = 500$ km (see Appendix B). This is because, for a large r_{em} , there is less distance between r_{em} and r_{PLR} for the structure of the X-mode wave to develop and therefore the profile retains its initial double-type form.

Effects of the cyclotron absorption appear to have a similar relationship to f , γ and λ . However, the amount of absorption strongly depends on λ , where no absorption takes place at all at $\lambda = 100$ and reaches a maximum degree of 25% at $\lambda = 10000$. Consistent with the model's prediction, the sign of V is positive as well as that of $dPPA/d\phi$. However, the profile of $|V|$ is rather puzzling in that its relation to f appears to be both correlating and anti-correlating, depending on the combinations of γ and λ . This is as if the dependency of $|V|$ on the three parameters is somehow a cyclical relationship. The simulated profiles also sometimes show a 'dip' in the V profile (e.g. Fig. 3.4, *right* panels). Potentially this can cause a misinterpretation of an OPM jump for a complicated PPA swing with a rapid variation (i.e. small β) which coincides with such a flip in V .

In general, the results from the simulations indicate that the PPA swing defined at certain r_{em} will be mostly preserved when $r_{PLR} - r_{em}$ is at minimum, i.e. 1) large γ ; 2) small λ ; 3) large f .

As these simulated profiles are of the same geometry, $\alpha = 91^\circ$ and $\beta = 1^\circ$, we

investigate further for any dependency of plasma effects on α . Fig. 3.5 shows the simulated profiles of $\alpha = 15^\circ, 30^\circ, 45^\circ, 60^\circ, 75^\circ$ and 90° , with the other parameters, $r_{em} = 100$ km, $f = 1500$ MHz, $\lambda = 1000$ and $\gamma = 100$, and $\beta = 1^\circ$, and the bin resolution is increased to 30 points over a pulse width of 15° . From the analysis earlier that the plasma effects are mostly governed by r_{PLR} , which is not explicitly related to the geometry, the results in this case are rather unexpected in that the distortions in the simulated profiles heavily evolve with α , especially for $\alpha \leq 45^\circ$. The effects include the pulse-intensity absorption (*dashed* vs. *solid* lines), the aberration shift, and the notches ($\alpha \geq 60^\circ$) and the ‘flattening’ of the PPA ($\alpha \leq 45^\circ$). The sign of V for $\alpha < 90^\circ$ is also altered, indicating that the prediction of the X-mode wave no longer holds; however the relationship between V and the plasma parameters has already been shown to be complicated earlier. The altitude-dependent term in the aberration effects (Dyks 2008) can now be observed in the results as a vertical shift in the PPA swings, at the leading pulse phase, which increases as $\alpha \rightarrow 0^\circ$ (increasing difference between the *solid* and the *dashed* PPA swings in Fig. 3.5). We note that there is no vertical offset introduced by varying the plasma parameters which strengthening the interpretation of the vertical shift to be purely geometric.

Apart from the aberration shift, the distortion effects are understood to be caused by the α -dependency of the co-rotational \mathbf{B} fields, which governs the induced \mathbf{E} and, consequently, the dielectric tensor. It is expected that these simulations should not show any strong correlation with β value, except for the initial emission pattern (Eq. 3.5) which may result in a different pulse shape.

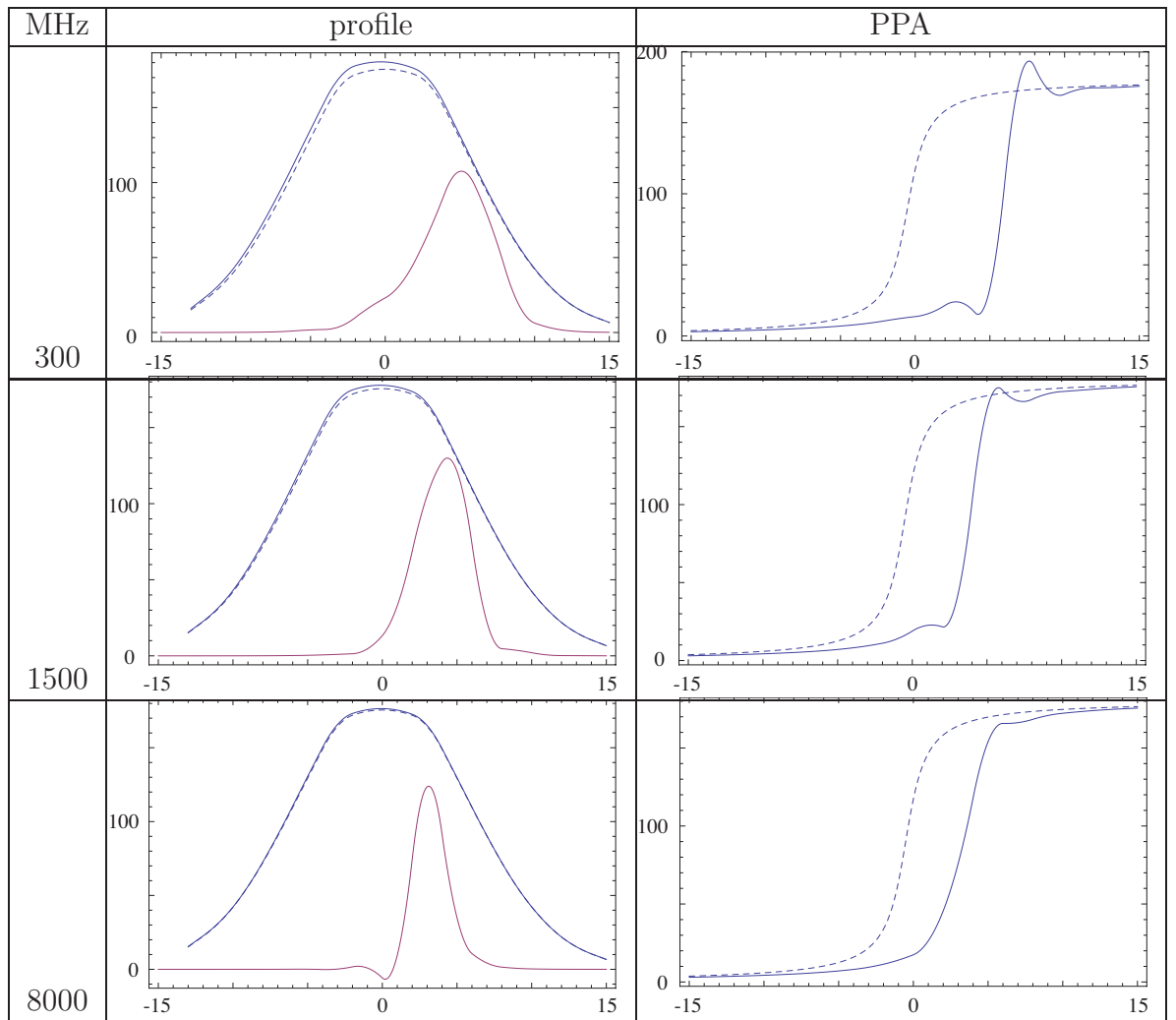


Figure 3.4: Three simulated profiles for $r_{em} = 300$ km, $\gamma = 100$ and $\lambda = 100$. The *left* column shows the pulse intensity before (*solid blue*) and after (*dashed blue*) cyclotron absorption and the Stokes V (*red*). The *right* column shows the perturbed PPA swing (*solid*) and the initial swing (*dashed*), according to the classic RVM.

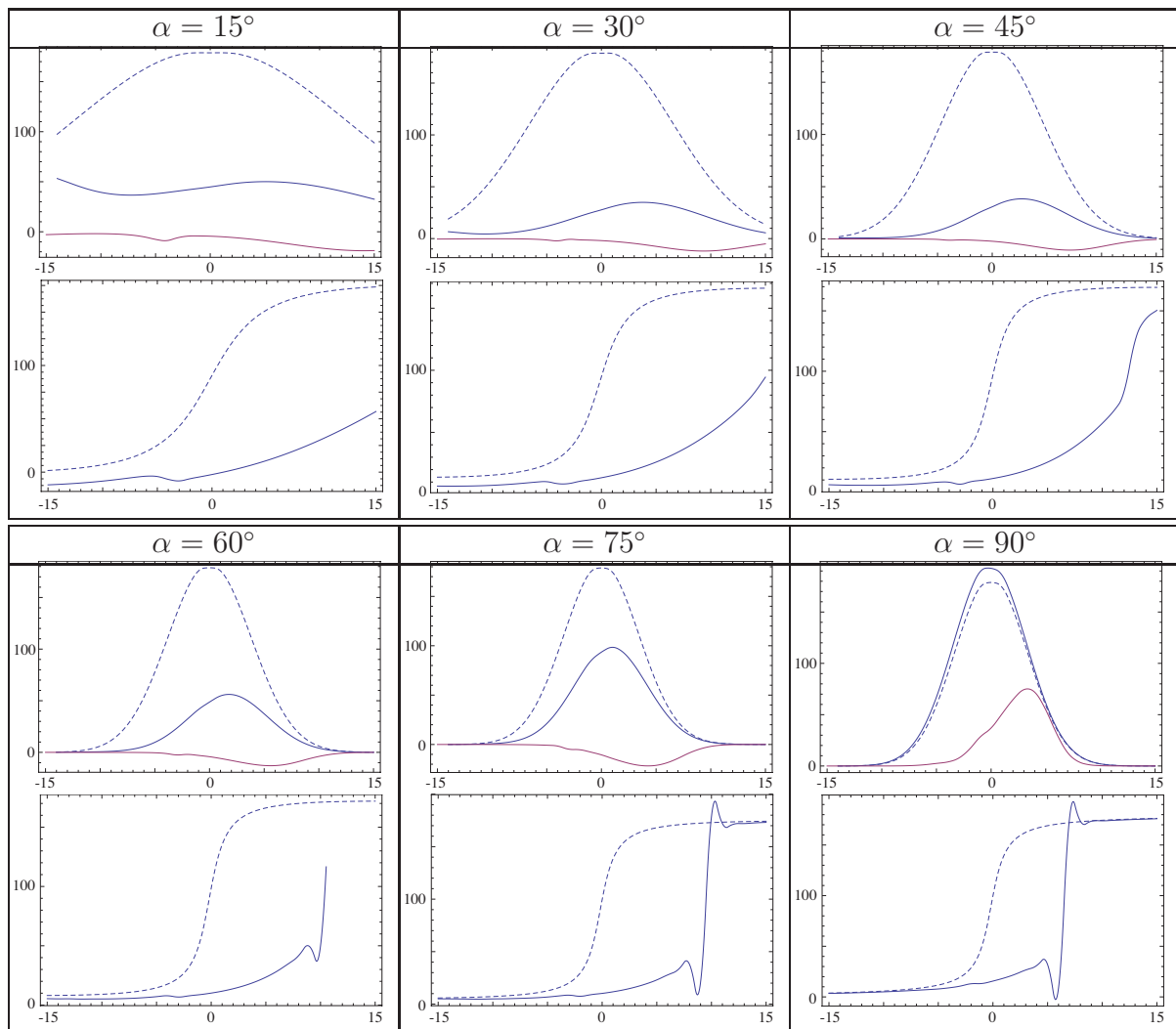


Figure 3.5: Simulated profiles of different α of 15° , 30° , 45° , 60° , 75° , and 90° , while the other parameters are fixed, $r_{em} = 100$ km, $f = 1.5$ GHz, $\lambda = 1000$, $\gamma = 100$ and $\beta = 1^\circ$.

3.3 Prediction versus Observations

The BP12 model provides a method to identify the observed propagation modes from the signs of V and $\{dPPA/d\phi\}|_{max}$, where the pulse-components are identified as the X-mode wave if the signs are the same, and the opposite for the O-mode wave. In this section, we aim to test the prediction based on the hypothesis that double profiles should be conal components, and hence should be related to the O-mode wave. Single profiles can either be related to a core component in the X-mode or in the O-mode, depending on the β value. If this hypothesis is correct, we therefore expect the majority of the profiles identified as the O-mode to be double-type profiles, and the majority of those identified as the X-mode to be single-type profiles. However, we note that, as can be seen in Appendix B for $r_{em} = 500$ km, the X-mode wave can also produce a close-double profile. The polarisation dataset in this section is published in Weltevrede & Johnston (2008a) (hereafter WJ08), which contains 527 profiles, observed at 10 cm (162 profiles) and 20 cm (365 profiles) from 352 pulsars.

Only 105 pulsars have clear enough signs of $\{dPPA/d\phi\}|_{max}$ and V to allow the identification of the modes. The counting statistics are summarised in Tab. 3.3. Out of 105 profiles with the mode identification, 37 profiles ($27X_s+10O_s$) are classified as a single type where 27 of them are of the X mode (70%), and only 10 are of the O mode (30%). This seems to support the model's prediction. As shown in the previous section, the BP12's model can also generate a double-type X profile (X_d) when r_{em} are large enough, which potentially could be the case in PSRs J0630–2834, J0849–6322, J1648–4611 and J1733–3716.

Of the double type, there are 14 and 8 pulsars identified as O_d and X_d , respectively, in which the O_d number is 50% higher than the X_d number. There are also a fair number (14) of double mixed-mode profiles (XO, OX), where their profiles are usually distinct from the O_d and the X_d type, in that their components are closely overlapping, as opposed to a well-separated double.

We now interpret our statistics in terms of a probability of observing different profile types which depends on different values of the impact angle (β). Recalling the values of k in Eq. 1.15 (Chapter 1), for a 1-second pulsar, the beam radius of the conal component is approximately 5° and $\sim 1.23^\circ$ for the core component. This suggests a core:cone occurrence of 20% versus 80%. From the table, the occurrence of the pure X-mode ($27X_s+8X_d$) and pure O-mode ($10O_s+14O_d+4O_{t,m}$) profiles is 55% versus 45%, indicating an excessive number of core-type profiles.

Table 3.3: A table summarising the mode classification. From *top* to *bottom*, the panels are the X-mode-only, the O-mode-only and the mixed-mode profiles. The subscripts s, d and ‘t,m’ refer to the single-, double- and triple (or multi-components)-type of the pulse profiles. ‘?’ represents the case where the $|V|$ of individual sub-component is too weak for determining the mode.

Modes/Types	counts	note
Xs	27	
Xd	8	
Xt,m		
X? or ?X	12	X?, ?X = 10, ?X? = 2
Total X	47	
Os	10	
Od	14	
Ot,m	4	
O? or ?O	8	O?, ?O = 6, ?O? = 2
Total O	36	
XO, OX	14	
OXO		
?X?	4	
XOX	1	
X?X		
?XOXO?	3	
Total mix	22	

Nevertheless, this ratio does not include the mixed-mode group, which can still alter the numbers of the single core and double cone. We believe that the number of our mode-identified samples is not large enough to overcome the primary uncertainty which is the selection effect in the sample itself. For example, it is certainly possible that the core and the conal components can have different degree of polarisation, in which the pulsars will consequently be excluded from the samples if the modes cannot be identified in the first place.

In summary, for simple profiles the statistics seem to favour the prediction that the majority of the double-type are the conal (O-mode) component, and the single-type for the core (X-mode) component, with, however, a considerable number of the O-mode as well. One strong objection to the prediction is a triple-type profile of PSR J1146–6030 at 20 and 50 cm, shown in Fig. 3.6, where the components are identified to be XOX , which is contradictory to the hollow cone picture. In addition to the fact that the sign of V can be different at different frequencies, the large number of the unidentifiable, which are mostly complex profiles, and a few controversial cases indicate that the prediction or the model itself need to be improved further. Nevertheless, the obtained statistics gives us confidence that we can interpret our observations discussed later in the general framework of this model.

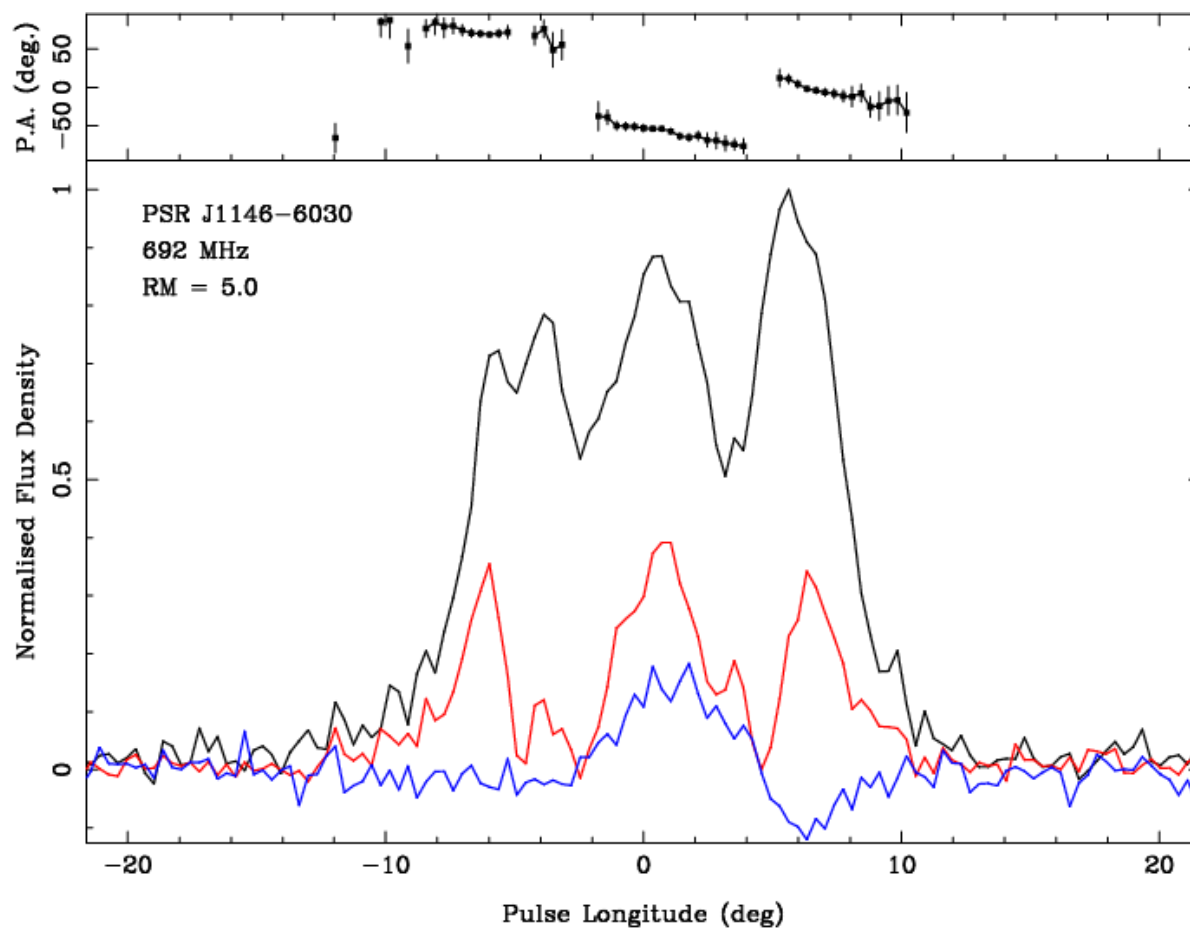


Figure 3.6: The pulse profile of PSR J1146-6030 at 692 Mhz, showing three sub-components, separated by two OPM jumps. According to BP12's predictions, it is classified as XOX and hence contradicts the hollow-cone concept.

3.4 Conclusions

We have explored a propagation model of radio waves in the magnetosphere by BP12, which considers refraction of the two propagation modes, the perturbation on the polarisation due to the twist in the magnetic field lines. The initial characteristic-RVM PPAs and pulse shapes are dictated by geometric variables, e.g. α , β , r_{em} and the primary radiative pattern, while the later propagation effects are mainly dependent on the plasma and wave parameters, i.e. λ , γ , B and f .

The fact that the effects on the simulated profiles, except $|V|$, in Tab. 3.2 are all having similar dependency on the f , γ and λ , indicates that the phenomena are all governed by the same variable, i.e. r_{PLR} . This essentially confirms the validity of the r_{PLR} equation, recalling that the simulated propagation effects are calculated from the dielectric tensor, which has no direct connection to r_{PLR} . We also found that the degree of plasma perturbation is strongly dependent on α , which is understood to be related via the orientation of the magnetic field, relative to the pulsar’s spin vector. This dependency is indeed interesting, because it can be related to the magnetosphere model by Li et al. (2012b), studied in Chapter 6. Nevertheless, for this simulation we only studied the propagation effects of the X-mode wave, which is only half of the story. A further investigation for the O-mode wave is necessary for us to be able to simulate more-realistic mixed-mode pulse profiles for testing with observations. This effort will be done in a later study.

For the profiles with reasonable RVM-like PPA swings and significant V , the statistics of the relation between the mode identification and the profile types appear to favour BP12’s predictions. However, the simulated X-mode profiles in Section 3.2 show a complicated behaviour of V , which fluctuates between different parameter combinations, and hence causes the mode interpretation to change. This suggests that the proposed ‘rule of signs’ is too much simplified—at least for the X mode—and needed to be explored in details and updated to take the response of V into account.

In this chapter, we have shown that the simulated X-mode pulse profiles can be considerably distorted by propagation effects in the pulsar magnetosphere, and, consequently, their PPAs are no longer related to its geometrical origin. However, we learned that the effects is minimal for a situation when, relative to the canonical values: 1) γ is large; 2) λ is small; 3) f is high; 4) r_{em} is small; 5)

$\alpha \sim 90^\circ$. Although, the most apparent distortions on the profiles can be explained by the concept of r_{PLR} , which is governed by λ , γ , f and $B(\alpha)$, it seems to be impractical to improve the RVM to include more fitting parameters, e.g. λ and γ , which does not help constraining the geometry. However, fitting the plasma model to real observations is important in studying the magnetosphere and could be done with exceptional cases where the geometry is well-constrained.

We conclude that methods of obtaining the geometry cannot be improved, at this stage, via including the plasma effects. Instead, we suggest a strategy to somehow combine constraints from various sources, e.g. the RVM, $\rho - W$ relationship, γ -ray light-curve, or the X -ray tori systems, for which additional geometric information is available.

Being aware of the limitations of deriving geometrical information based on the RVM alone is hugely important and needs to be kept in mind when considering the interpretation of observational data. Nevertheless, even though the propagation effects described here seem to make a geometrical interpretation of the data more difficult, we have also seen that the data contain information about the magnetosphere that can be harvested when understanding the effects here. Indeed, we will give an example for this in Chapter 6 when we look at the PPAs of intermittent and moding pulsars, which appear to reveal an interesting effect that allows us to even estimate the plasma density in a pulsar magnetosphere.

Chapter 4

Polarisation Calibration

In this chapter, we explore different methods and techniques for polarisation calibrating the Lovell Telescope system, which will be used for polarisation-calibrate observations of PSR B1822–09, studied in the next chapters.

In early 2009, a new ATNF Digital Filter Bank (DFB)¹ was installed for the Lovell Telescope. It is capable of recording a wider bandwidth (512 vs. 64 MHz) with a much better frequency resolution (1024 vs. 64 channels) than that of the old Analogue Filter Bank (AFB) system, although in practice some part of the bandwidth has to be masked due to Radio Frequency Interference (RFI)² or the part where the system is strongly frequency-dependent. This leaves a usable bandwidth of ~ 320 MHz with ~ 700 channels. Despite great improvements in observing capability, the new setup has not yet been polarisation-calibrated. In addition, a difficulty arises from the fact that reference-signal (‘CAL’) observations had not been done frequently enough to keep up with hardware changes in the system. The DFB system has been providing us with a vast amount of high-quality data, which, after being calibrated, will allow us to not only time pulsars more efficiently, but also to further investigate the radio emission of pulsars.

In the following sections, three methods, which have been successful with other single-dish radio telescopes, are studied and tested. The concept of a linear transformation with the *Jones* matrix is introduced in Section 4.1, while the three methods and their results are presented in Section 4.2-4.4. Method for calibrating a dataset of PSR B1822–09 is described in Section 4.5. All the findings are concluded in the summary in Section 4.6.

¹<http://www.atnf.csiro.au/>

²Man-made radio waves, e.g. radar and mobile phones.

4.1 Mathematical Basis

The purpose of calibration is to take any instrumental effects into consideration to correct observational data. This correction can be described by a Mueller matrix, composed of 7 parameters, i.e., the absolute gain, differential gain, differential phase, and ellipticity and the orientation of the ellipticity of the two feeds (Hamaker et al. 1996; van Straten 2004). Conventional methods of polarisation calibration involve a CAL signal injection into the feed and/or an observation of a well-determined polarisation source, with the assumption that the system's response is linear within the observed frequency band and sufficiently stable between CAL observations.

Starting with a necessary basic formulation (Hamaker et al. 1996; van Straten 2004, 2006), we consider an electromagnetic wave of angular frequency ω , $\mathbf{E} = Ee^{i\Phi(t)}$, written in a Cartesian co-ordinate system as

$$\mathbf{E}(t) = \begin{pmatrix} E_x e^{i\Phi_x(t)} \\ E_y e^{i\Phi_y(t)} \end{pmatrix}. \quad (4.1)$$

Along its path before reaching the data recorder, the wave evolves due to various propagating factors, such as Faraday rotation and instrumental effects, where each effect can be represented by a linear transformation of the form,

$$\mathbf{E}_{\text{obs}}(t) = \mathbf{J}\mathbf{E}(t), \quad (4.2)$$

where \mathbf{J} is a 2×2 -matrix linear operator, known as the *Jones* matrix (Jones 1941).

Upon arrival at the telescope feeds, in the case of Lovell's receiver a circular basis, the incident radio wave is converted into two raw voltage signals. The signals then go through various processes, such as filtering the frequency band, down-conversion and amplification, before being fed to a pulsar filter bank, which is responsible for 'forming' individual frequency channels and individual pulse-phase bins. The information of the wave at this step is represented in the form of the *coherence* matrix,

$$\varrho = \langle \mathbf{E}(t) \otimes \mathbf{E}^\dagger(t) \rangle = \begin{pmatrix} \langle E_x^*(t)E_x(t) \rangle & \langle E_x^*(t)E_y(t) \rangle \\ \langle E_y^*(t)E_x(t) \rangle & \langle E_y^*(t)E_y(t) \rangle \end{pmatrix}, \quad (4.3)$$

where $\langle \rangle$ denotes averaging over the sampling times, and \dagger and \otimes are the Hermitian transpose and the outer product, respectively (Born & Wolf 1999). By forming the coherence matrix (or “detecting” the signal) and doing the averaging, information about the precise form of the electric field is lost, but the data rate is also reduced. The DFB records data in filter-bank format, which can be converted to the Stokes parameters (I, Q, U, V) (e.g. Burke & Smith 2002).

As a final product in his formulation, Britton (2000) is able to include all the necessary propagation and instrumental effects for calibration purposes into a series of linear transformations (Lorentz Group). We will follow his work, however, without digressing into full derivation, but yet being as transparent as possible.

The coherence matrix (ϱ) can be written as a linear combination of Hermitian basis matrices,

$$\varrho = \frac{1}{2} \sum_{k=\hat{\mathbf{i}}, \hat{\mathbf{q}}, \hat{\mathbf{u}}, \hat{\mathbf{v}}} S_k \sigma_k = (S_0 \sigma_0 + \mathbf{S} \cdot \boldsymbol{\sigma})/2, \quad (4.4)$$

where σ_0 is the 2×2 identity matrix, S_0 is the Stoke I , $\mathbf{S} = (Q, U, V)$ in the Stokes Cartesian coordinates $(\hat{\mathbf{q}}, \hat{\mathbf{u}}, \hat{\mathbf{v}})$, and σ are the Pauli spin matrices,

$$\sigma_{\hat{\mathbf{q}}} = \begin{pmatrix} 1 & 0 \\ 0 & -1 \end{pmatrix}, \quad \sigma_{\hat{\mathbf{u}}} = \begin{pmatrix} 0 & 1 \\ 1 & 0 \end{pmatrix}, \quad \sigma_{\hat{\mathbf{v}}} = \begin{pmatrix} 0 & -i \\ i & 0 \end{pmatrix} \quad (4.5)$$

(Britton 2000). And therefore the Stokes parameters can be represented by ϱ as

$$S_k = tr(\sigma_k \varrho), \quad (4.6)$$

where $tr(\mathbf{A})$ is the trace of the matrix \mathbf{A} . Similar to the linear operation in Eq. 4.2, the ‘true’ ϱ (the unperturbed coherency parameter we want to study) transforms as

$$\varrho_{\text{obs}} = \mathbf{J}(\mathbf{E} \otimes \mathbf{E}^\dagger) = \mathbf{J} \varrho \mathbf{J}^\dagger, \quad (4.7)$$

becoming the ‘observed’ or ‘measured’ ϱ , on the assumption that instrumental effects can be described by \mathbf{J} , known as ‘the Jones matrix’. At this stage, the transformation is done on ϱ , however it is inconvenient as astronomers are more familiar with the Stokes parameters, which are scalar time-averaged quantities and have dimensions of power. Therefore, by changing the basis in which ϱ is defined to the basis of the Stokes parameters, the 2×2 Jones matrix now should

be replaced by the (4×4) ‘Mueller’ matrix. It transforms \mathbf{S} as

$$\mathbf{S}_{\text{obs}} = \mathbf{M}\mathbf{S}\mathbf{M}^\dagger, \quad (4.8)$$

and is defined using the notion of Britton (2000) as

$$\mathbf{M} = G(g_0, g_1)\mathbf{B}_{\hat{\mathbf{q}}}(\gamma)\mathbf{R}_{\hat{\mathbf{q}}}(\phi)\mathbf{B}_{\hat{\mathbf{a}}}(\theta_0 - \theta_1)\mathbf{B}_{\hat{\mathbf{v}}}(\epsilon_0 - \epsilon_1)\mathbf{R}_{\hat{\mathbf{a}}}(\epsilon_0 + \epsilon_1)\mathbf{R}_{\hat{\mathbf{v}}}(\theta_0 + \theta_1), \quad (4.9)$$

where the subscript $_0$ and $_1$ represent the signal of the two polarisation feeds.

Before explaining each of the terms, it is important to stress that the transformation of \mathbf{M} is done in the Stokes parameter space. Therefore individual terms in \mathbf{M} do not necessarily have an equivalent physical interpretation (which can also be different between linear and circular feeds), unlike the transformation in Eq. 4.2, which describes the effects on the voltage signal, and hence is easier to relate between the transformation and individual instrumental effects.

Individual terms in \mathbf{M} can be interpreted as corrections made to the Stokes vector (S_0, \mathbf{S}) , by adjusting the magnitude of one of the components (boosting) or rotating the vector itself around one of the basis axes. The scalar G is defined as $\sqrt{g_0 g_1}$, in which g_0 and g_1 represent the amplification (or attenuation or gain) applied to the two voltage signal chains. The boost term $\mathbf{B}_{\hat{\mathbf{q}}}(\gamma)$ is responsible for correcting the amplitude of Q by an amount $\gamma = \ln(g_1/g_0)$. Similarly, $\mathbf{R}_{\hat{\mathbf{q}}}(\phi)$ is a rotation around $\hat{\mathbf{q}}$ applied on \mathbf{S} by the differential phase ϕ . Along the signal path, the two main instrumental effects are: 1) the differential gain, in which the attenuation is done unequally on the two signals; 2) the differential phase, which is a phase delay between the two signal paths.

The last four terms in Eq. 4.9 are often known as the ‘impurity’, ‘leakage’ or ‘cross-coupling’ terms, which describe imperfections of the receiver in the sense that one receptor can pick up the signal which is supposed to be detected by the other receptor only, hence the name leakage. They are described by two scalar variables for each receptor: the ellipticity (ϵ) and orientation of the ellipticity (θ). A good example is the case where the two feeds are not exactly physically orthogonal, which causes a leakage between Q and U and hence a conversion of V into $L = \sqrt{Q^2 + U^2}$, as a circular-polarised will be distorted into an ellipse with major axis determined by ϵ . However, this leakage can also originate from a phase delay, causing the ellipse to rotate by an amount which is determined by θ . Keep in mind that the parameters in Eq. 4.9 depend on observing frequency,

so each individual frequency channel in a data file has their own set of solutions for the Mueller matrix.

4.2 Pre-calibration

In this section, we apply the formalism of Section 4.1 to calculate $\mathbf{B}_{\hat{\mathbf{q}}}(\gamma)$ and $\mathbf{R}_{\hat{\mathbf{q}}}(\phi)$, using the *PSRCHIVE* software ‘*pac*’ (called pre- or *pac* calibration) on two datasets to demonstrate the method. Methods for measuring the leakage terms will be introduced in Sections 4.3-4.4. $\mathbf{B}_{\hat{\mathbf{q}}}(\gamma)$ and $\mathbf{R}_{\hat{\mathbf{q}}}(\phi)$, can be calculated from two constraints derived from a CAL observation: 1) L and V must intrinsically be equal to 100% and 0%, respectively; 2) the PPA has a fixed known value. A CAL observation is made with a signal generated by a noise diode which is injected into the feed of the receiver to quantify some of the properties of the signal path. The software *pac* measures the parameters of \mathbf{M} needed to explain the observed Stokes parameters in the CAL observation. \mathbf{M} can then be applied to pulsar observations, closely in time and, if possible, nearly in the sky-position.

An eighteen-minute pointing on PSR B0740–28 was made on May 9, 2012, in which a reference cal signal was injected for the first six minutes. Before being fed into *pac*, both observation and CAL data are time-integrated, while the frequency resolution is preserved. The CAL signal, shown in Fig. 4.1 (*top*), indicates an excess of V by $\sim 20\%$, while L by $\sim 60\%$, showing that there are significant receiver effects. The *bottom* plots show the solutions of $G = \sqrt{g_1 g_2}$, γ , and ϕ , indicating that the response of the system is highly frequency-dependent, in which both lower frequency band (1350 to 1430 MHz) and higher frequency band (1550 to 1710 MHz) seem to have different characters. Nevertheless, a solution is derived separately for each individual channel. Fig. 4.2 shows the original (*right*) and calibrated profiles (*left*). Compared with a profile by Gould & Lyne (1998), shown in Fig. 4.3 (*top*), the result is consistent; the highly polarised L , the level of V , and the PPA curve, suggesting that the *pac* calibration works rather well. The fact that the pulse shapes of the two profiles are inconsistent is only because PSR B0740–28 is a profile-changing pulsar for which the trailing component switches its relative height at a timescale of ~ 200 days (Lyne et al. 2010).

For the second example, three observations of PSR B0950+08 were made on August 5, 10 and 19. The first observation was calibrated using a CAL file

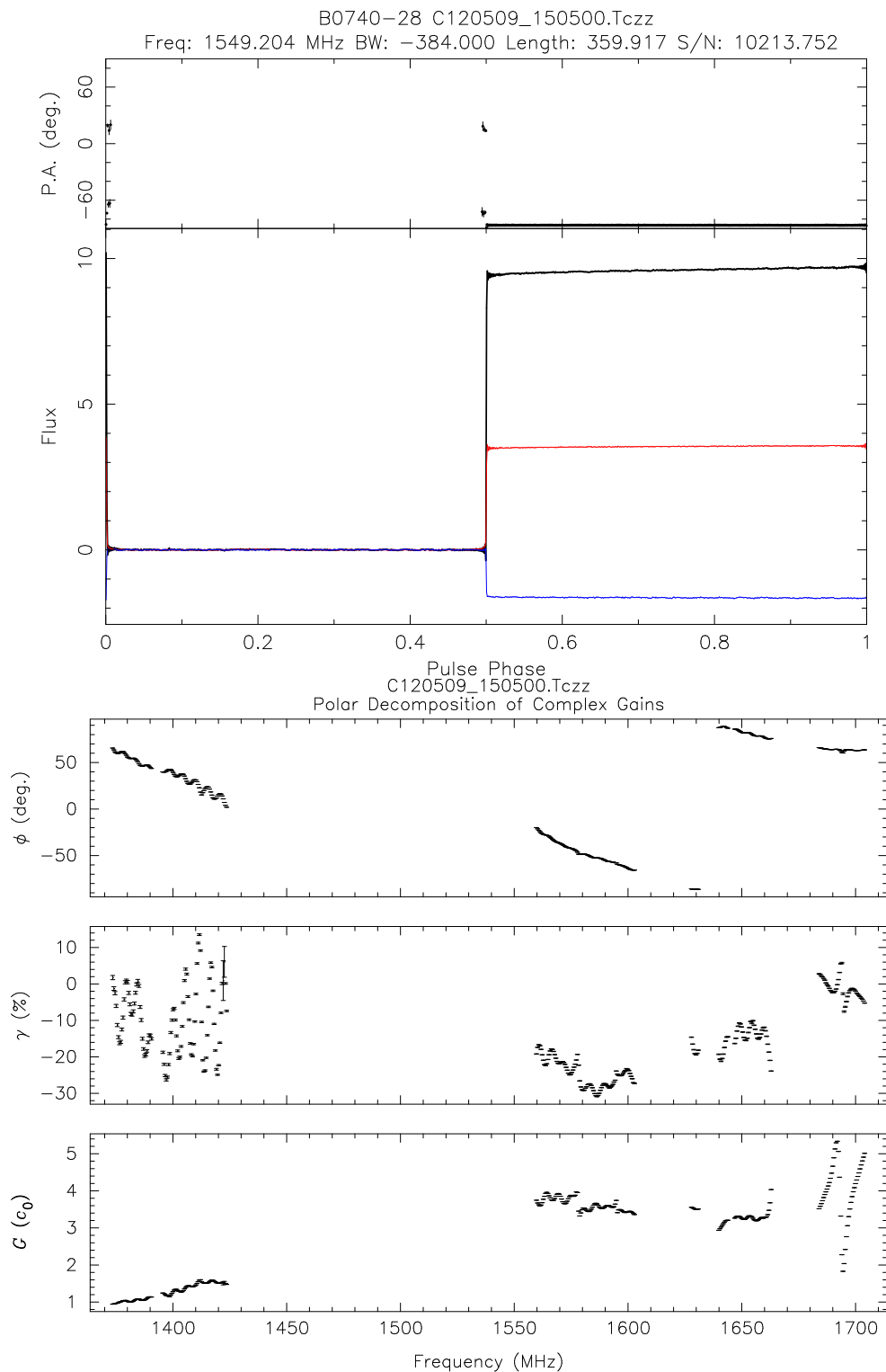


Figure 4.1: The profile and the derived solutions of the CAL observation used for calibrating PSR B0740-28. (*Top*) The PPAs with error bars and the pulse profile are shown on the *top* and *bottom* panels, respectively, where I , L , and V are indicated with the black, red, and blue lines. (*Bottom*) From *top* to *bottom*, the differential phase, the differential gain, and the absolute gain are plotted a function of observing band.

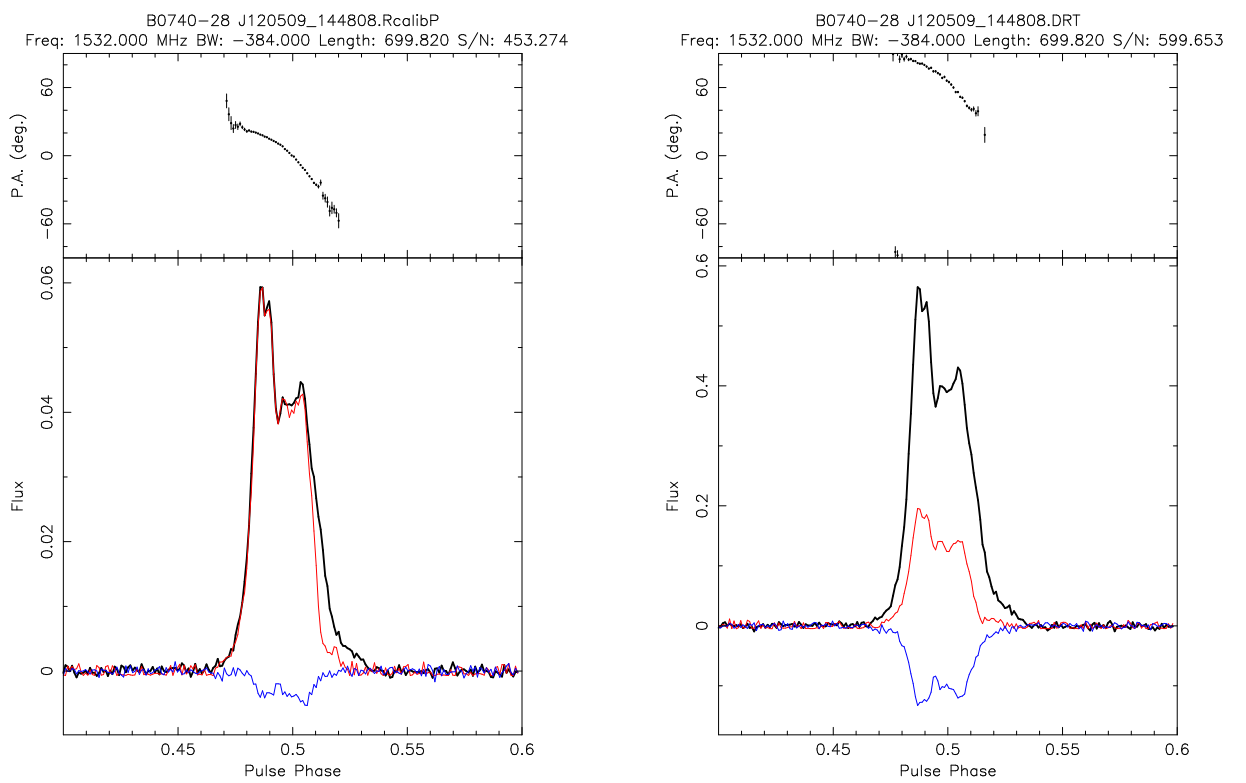


Figure 4.2: The before- and after-calibrated observations of PSR B0740-28 by the *pac* method (*left* and *right*, respectively).

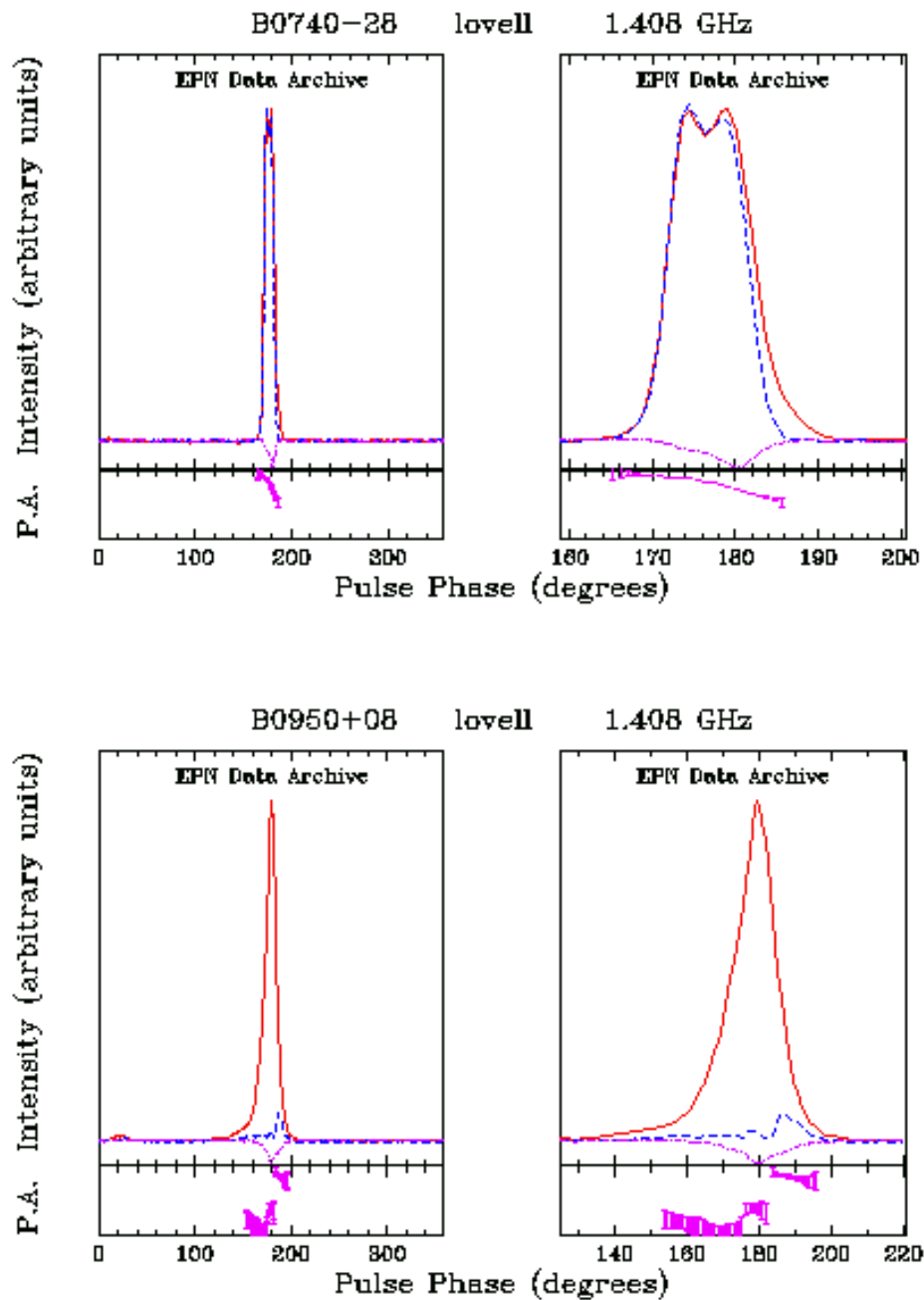


Figure 4.3: Reference profiles at 1.408 GHz for PSRs B0740-28 (*top*) and B0950+08 (*bottom*) by Gould & Lyne (1998). For each plot, in the *top* panels I , L and V are represented by the *red*, *blue* and *magenta* lines. The *bottom* panels show the PPAs with their errorbars. (www.jb.man.ac.uk/research/pulsar/Resources/epn/browser.html)

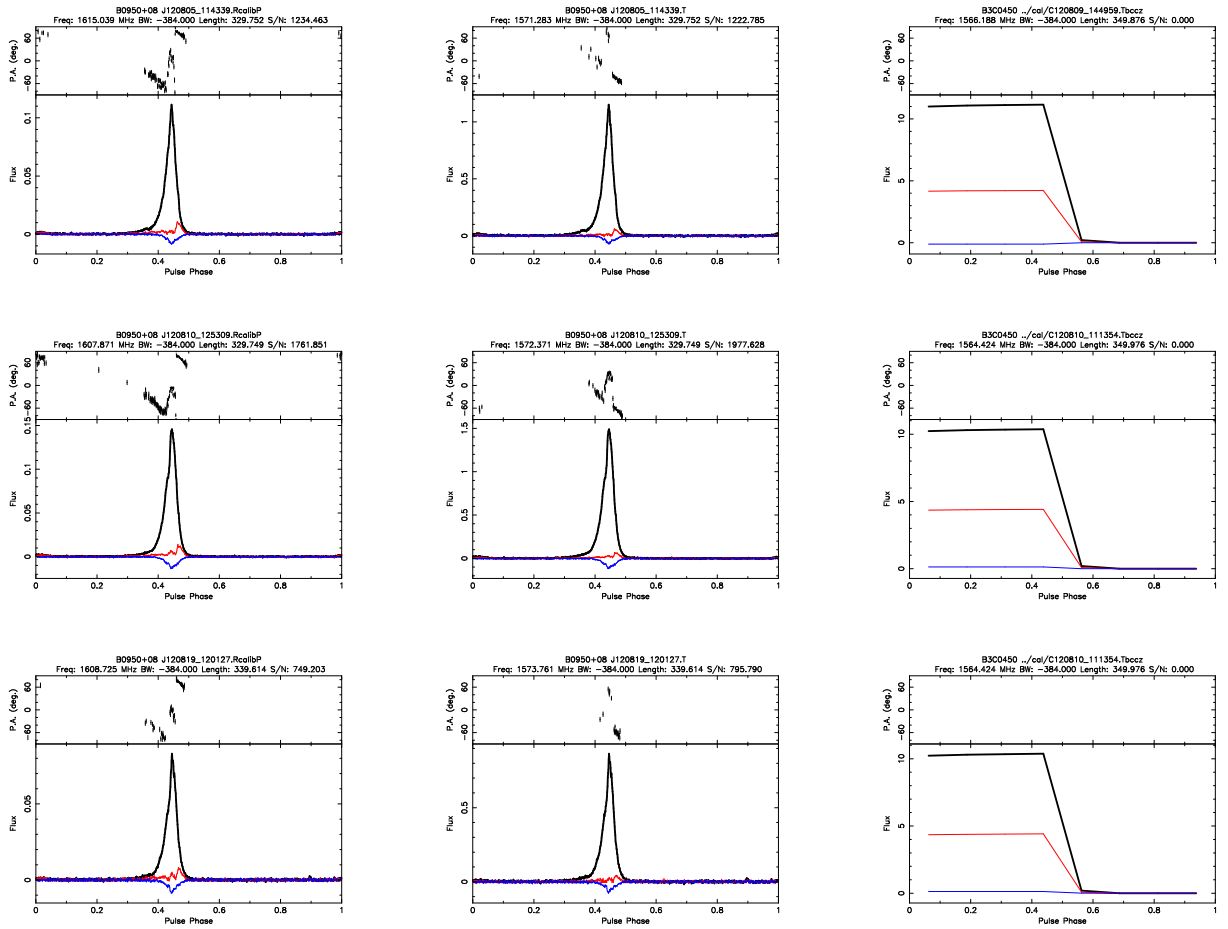


Figure 4.4: Three observations on August 5, 10 and 19 (from *top* to *bottom*) of PSR B0950+08, where the columns are, from *right* to *left*, the applied CAL files, the uncalibrated observations, and the *pac*-corrected profiles. Note that the observation on August 10 and 19 are applied with the same CAL file.

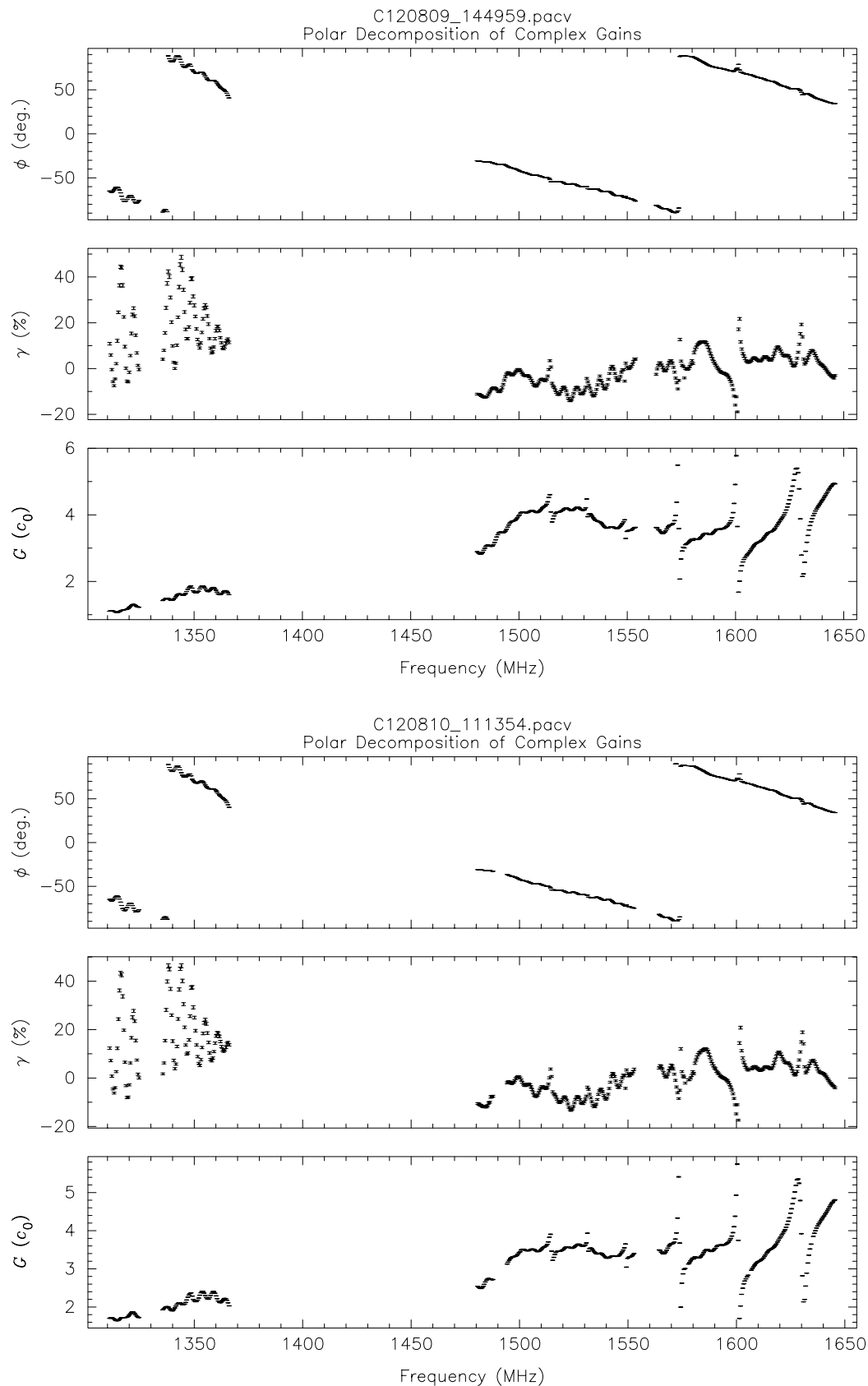


Figure 4.5: The *pac* solutions of the CAL observations shown in Fig. 4.4. Except for a difference in G between $\sim 1480 - 1550$ MHz, the solutions between the two days are identical. Note that these plots show ripples in the high-band part, where the strongly-affected channels are excluded (zapped) from the data.

observed on the 9th of August, and on the 10th for the second and third observations. The results are shown in Fig. 4.4. The two CAL files (*right* column) are sufficiently similar, except the fact that V is changing from $-$ to $+$, although V is close to zero in both cases. The signatures of L and V in the uncalibrated profiles (*middle* column) are moderately similar, while the PPAs seem to have a small offset, possibly due to the change in the parallactic angle³. No significant change appears in the calibrated profiles (*left* column). L and V are slightly increased and the PPA profiles remain in the same three-pieces-two-OPMs configuration, but now the effect of different parallactic angle is corrected for. To examine the difference in the two CAL files more closely, their G , γ and ϕ are plotted in Fig. 4.5, in which the solutions are indistinguishable, except that at ~ 1480 - 1550 MHz G of the first CAL file (*top*) is slightly larger.

Overall, the results are consistent with Gould & Lyne (1998)’s profiles, shown in Fig. 4.3 (*bottom*). However, inspecting each of those profiles carefully, it appears that the signatures of L and V are not exactly identical. This is possibly because the first observation (*top*) is calibrated with a different CAL file than the other two (*middle* and *bottom*) and the system’s response had already changed in between the time when the pulsar the CAL observations were made. The variation could also be due to the fact that the leakage terms cannot be determined from a CAL observation, which can be solved by methods described in the next sections.

After investigating the signal chain, we learned that the attenuation levels are often changing, in both absolute and relative values between ‘left’ and ‘right’ circular (for the circular feeds of the Lovell telescope). The setting is different depending on, for example, the pointing elevation and sky temperature. To understand if different attenuation settings affect polarisation calibration, we performed a test, in which the CAL signal was recorded with different attenuation levels. It appears that the derived values of G , γ and ϕ behave according to our prediction for all the attenuation settings. Nevertheless, it should be emphasised that if the attenuation setting, especially when there is a difference between the two signal chains, is not correctly set, the CAL solution will not represent the state of the system during the observation.

The results of PSR B0740–28 are consistent with the published profiles, in

³See Section 4.3 for explanation about the parallactic angle.

which the CAL observation was made simultaneously with the pulsar observation. For PSR B0950+08, the three calibrated profiles are not in perfectly consistence, which is due to the fact that the system settings were changing within the timescale of those observations.

In summary, we believe that polarisation with *pac* is working rather well for Lovell data, as long as CAL observations are frequently made; however, we are not yet able to identify which process(es) in the signal chains changes the system response.

4.3 Measurement Equation Modelling

To acquire a complete set of solutions to accurately calibrate a system, one must take into account the impurity of the receiver, which is the leakage between the two signal feeds, introduced in Section 4.1. The Measurement Equation Modelling (MEM) technique relies on the fact that the orientation of the source (or plane of linear polarisation) with respect to the feeds of altitude-azimuth telescopes is changing with time. In other words, the feed angle is rotating about the line of sight (LOS) determined by the parallactic angle. A model of the ‘expected’ Stokes parameters as a function of the parallactic angle can be constructed. Used in many polarisation studies (e.g. Stinebring et al. 1984; Xilouris 1991; Johnston 2002), the MEM technique has been used as a standard calibration method for pulsar observations at the Parkes telescope. van Straten (2004) incorporated this technique into the *PSRCHIVE* package (*pcm-MEM*), in which the parameter \mathbf{M} from Britton (2000) (Eq. 4.9) was implemented. The model describes the coherence matrix as a function of the parallactic angle (Φ) as

$$\varrho'(\Phi) = \mathbf{M}\mathbf{R}_{\hat{\nu}}(\Phi)\varrho\mathbf{R}_{\hat{\nu}}^{\dagger}(\Phi)\mathbf{M}_B^{\dagger}. \quad (4.10)$$

This is interpreted as the observed signal (ϱ') being equal to the intrinsic signal (ϱ) which has been through the rotation due to the parallactic angle ($\mathbf{R}_{\hat{\nu}}$) and the instrumental effects (\mathbf{M}).

Let M be the number of pulsars observed. Considering N_m independent observations of the m th pulsar, where each observation measures $(S' \pm \sigma)_{k,m,n}$ (defined in Eq. 4.4). ϱ'_m in Eq. 4.10 can be rewritten as $\varrho'_m(\mathbf{x}; \eta)$. Here \mathbf{x} represents the vector of independent variables that constrain the model, which is a function of Φ , and η is the vector containing the instrumental scalar parameters in Eq. 4.9, which are g_0 , g_1 , ϕ , θ_0 and θ_1 , and ϵ_0 and ϵ_1 , and also the ‘true’ Q , U and V of the signal (ϱ_m). Then, the merit function can be defined as

$$\chi^2(\eta) = \sum_{m=1}^M \sum_{n=1}^{N_m} \sum_{k=0}^3 \frac{[S'_{k,m,n} - S'_{k,m}(\mathbf{x}_{m,n}; \eta)]^2}{\sigma_{k,m,n}^2}, \quad (4.11)$$

where $S'_{k,m}(\mathbf{x}_{m,n}; \eta) = \text{tr}[\sigma_k \varrho'_m(\mathbf{x}_{m,n}; \eta)]$ are the predicted Stokes parameters according to $\mathbf{x}_{m,n}$ (van Straten 2004).

van Straten (2004) also presented an example where he applied the routine

in practice by using observations of PSR B0437–4715, and the flux-reference source Hydra A, to calibrate the centre element of the Parkes 20-cm multi-beam receiver. Fig. 4.6 (*top*) shows 97 sets of the Stokes parameters (taken with a 64 MHz bandwidth, filtered to 256 channels, and sampled to 2048 phase bins) and their best-fit model, as a function of Φ . Note that for each observation 65 data points centred at the pulse’s peak are selected for the fitting. The corresponding solutions (*bottom*) suggest that the method works well, helped by the fact that it not only uses the pulsar observations, but also additional constraints from the noise diode (CAL signal) and an un-polarised source (Hydra A).

To apply the *MEM* method to the Lovell-DFB system, four observations of PSR B0355+54, covering a wide range of Φ , were made on August 9 and 10, 2012. We used a *PSRCHIVE* software *pcm* by van Straten et al. (2012) in *MEM* mode. The routine starts by creating a CAL database, containing available noise diode observations. *pac* and *pcm* can choose a most appropriate file, in terms of minimising differences in, for example, the bandwidth, the start time and the coordinates of the pointing, between the pulsar and CAL observations. The first-order calibration by *pac* (Section 4.2) is applied to the uncalibrated files, producing the pre-calibrated files (with an extension *.calibP*). As shown in Fig. 4.7 (*top*), these *.calibP* files are very similar, assuring that the *pac* calibration worked rather well. They are then added together to make a high signal-to-noise template file (*bottom*), which is used by *pcm* to select a proper region (centered on the pulse’s peak, in general). This region can also be set manually. The template’s PPA is slightly shifted up compared to the *.calibP* files, because it is corrected for Faraday rotation.

The calibrated results of the four observations are shown in Fig. 4.9, which appear to be corrupt, and the best χ^2 and fitting solutions are shown in Fig. 4.11–4.14 (*red*) as a function of frequency band. It is obvious that the issue is caused by a few very bright frequency channels, which occur sporadically within the band (from calibration to calibration) but they are the same channels for each profile (Fig. 4.9, *bottom*). These channels seem to have no correlation with other parameters, except having extremely large χ^2 values, which suggests that the fit failed to converge. However, we managed to remove them from the uncalibrated observations prior the fitting, for which the recovered profiles are shown in Fig. 4.10. Note that it makes no difference whether they are removed before or after calibration, as each frequency channel is fitted separately.

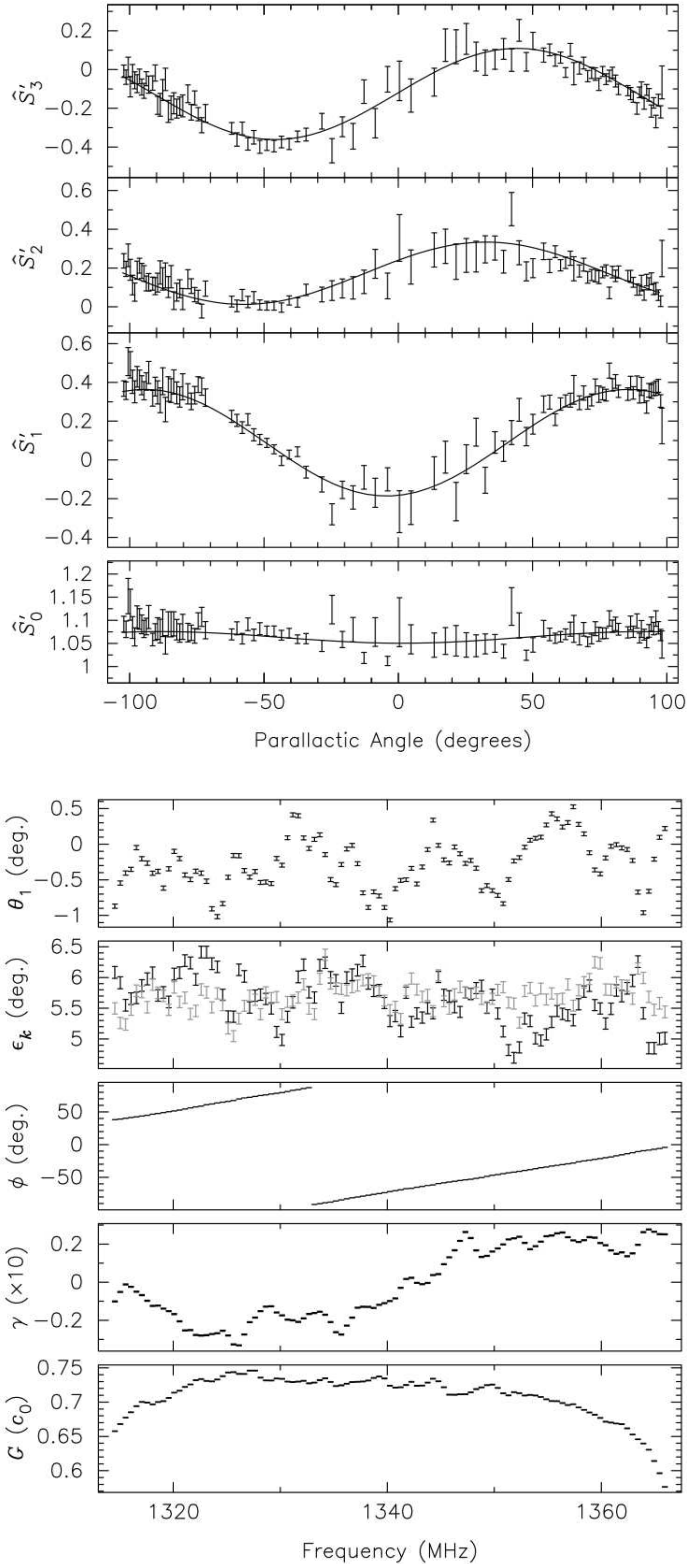


Figure 4.6: Example of the MEM method by van Straten (2004) applied on Parkes data. (*Top*) A plot of the observed and fitted Stokes vectors ($\hat{S}'_0, \hat{S}'_1, \hat{S}'_2, \hat{S}'_3$) as a function of Φ . (*Bottom*) The corresponding best-fit model parameters as a function of frequency, which are (from *bottom to top*) the absolute gain G , the differential gain γ , the differential phase ϕ , the ellipticity of the receptors ϵ_k , and the ellipticity's orientation of receptor 0 relative to receptor 1 θ_1 (equivalent to $\theta_0 - \theta_1$ in Eq. 4.9).

The facts that the best fit has a very high reduced- χ^2 (average ~ 300 , see Fig. 4.11 (*top*)) and that the calibrated profiles appear to be corrupt (Fig. 4.9 (*top*)) indicate an unsuccessful convergence of the fit. We suspected that the very high χ^2 value was related to the absolute gain as it seems to be inversely proportional to the χ^2 , which later is proved to be the case as shown below. Hence, employing a similar process, the four observations are fitted again with the same CAL files, but with their absolute gains forced to be 1. The new fitting solutions (*green*) are shown in the same Fig. 4.11-4.14. The reduced- χ^2 now decreases to an average of 27 (Fig. 4.11, *top*), from which the absolute gain is correctly resolved to 1 (Fig. 4.11, *bottom*), while the rest of the parameters do not noticeably change. This suggests that there is an issue with the absolute gain as derived from the CAL signal of the Lovell.

The recovered profiles (Fig. 4.10) are fairly consistent with those using the *pac* method (Fig. 4.7); however, they are not exactly similar, for example, L of the middle component of observation J120810_032124 (*bottom-left*). Despite being less constrained, the solutions by the *MEM* method are reasonably consistent with those by the *pac* method. For the leakage terms, solutions of $\epsilon_{0,1}$ and $\theta_{0,1}$ (Fig. 4.13, 4.14) appear to spread over a range of $\sim \pm 7^\circ$ around zero with errorbars of $\sim 20^\circ$ (not shown). Despite having large uncertainties, we at least now know that the leakage terms should be, on average, close to zero. It is also apparent that both $\epsilon_{0,1}$ and $\theta_{0,1}$ show a strong frequency dependence at ~ 1520 MHz. To test if the polarisation calibration was done correctly, the PPA points of the leading component (with $\sim 100\%$ L) are plotted as a function of frequency (Fig. 4.15-4.16), in which there is no evidence of any frequency dependence. This is what is expected, given that profile evolution of pulsars is in general relatively slow as function of frequency. Therefore most frequency dependence of the pulsar signal is expected to disappear after calibration.

Despite the issue where the fits of a few channels do not converge, we believe that the *MEM* technique should be more robust than the *pac* method as it requires fewer assumptions, e.g. the properties of the injected CAL signal. Although one may plan to try this method again with more observations, better Φ coverage, and with less time gap between observations, there is still a problem, as suggested in the previous section, in that the resulting solution will only describe the system at that period of time. It seems that we need a better strategy to handle unstable systems, e.g. the *MTM* method (next section).

4.3. MEASUREMENT EQUATION MODELLING

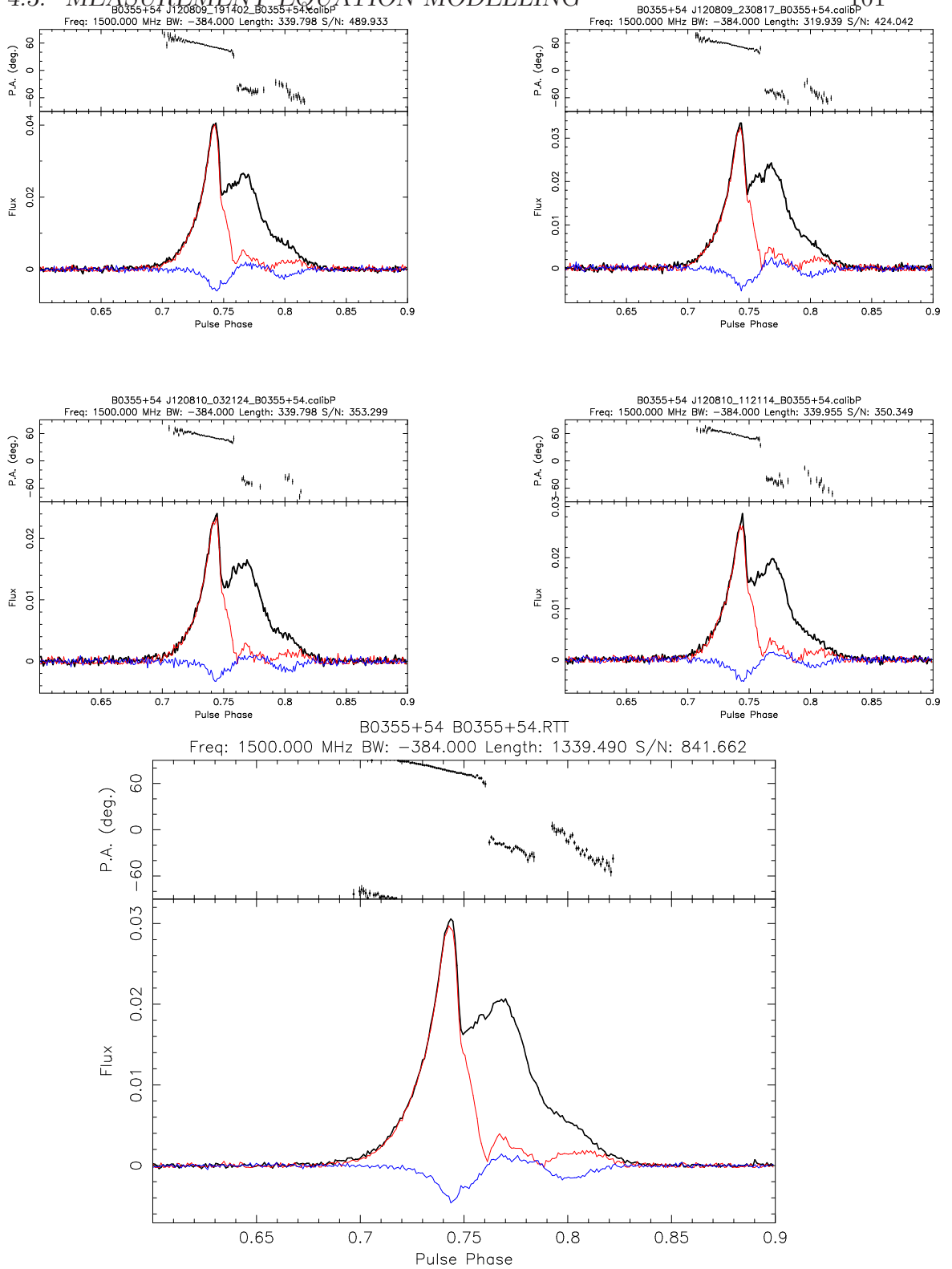


Figure 4.7: (Top) Four *pac*-calibrated profiles of PSR B0355+54. (Bottom) A template made from adding those four calibrated observations, which is the only required input for *pcm* to select the fitting region.

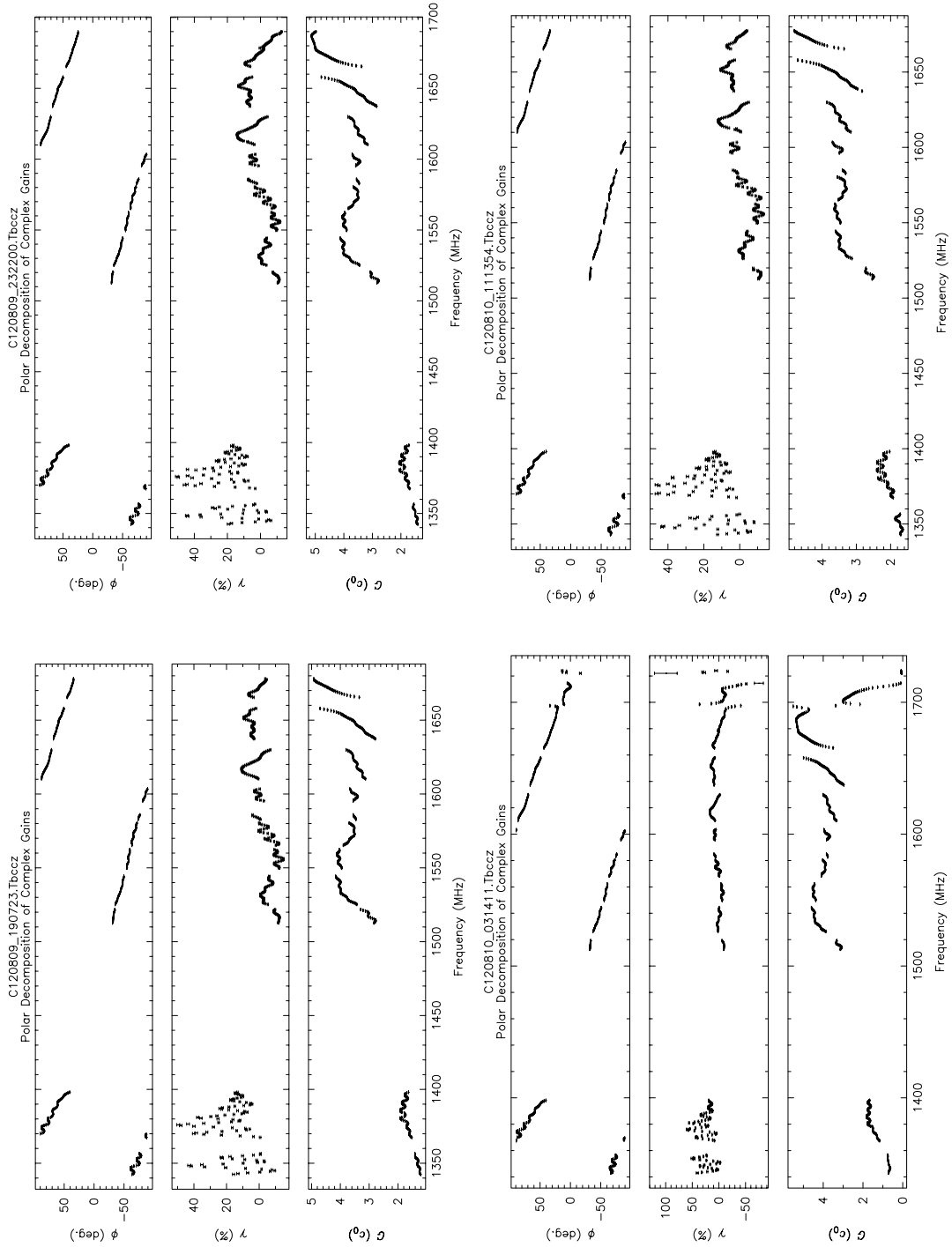


Figure 4.8: Four receiver solutions derived from CAL files used for calibrating the four observations of B0355+54 in Fig. 4.7. Despite the different scales of the axes, the solutions are rather stable over the two days of observations.

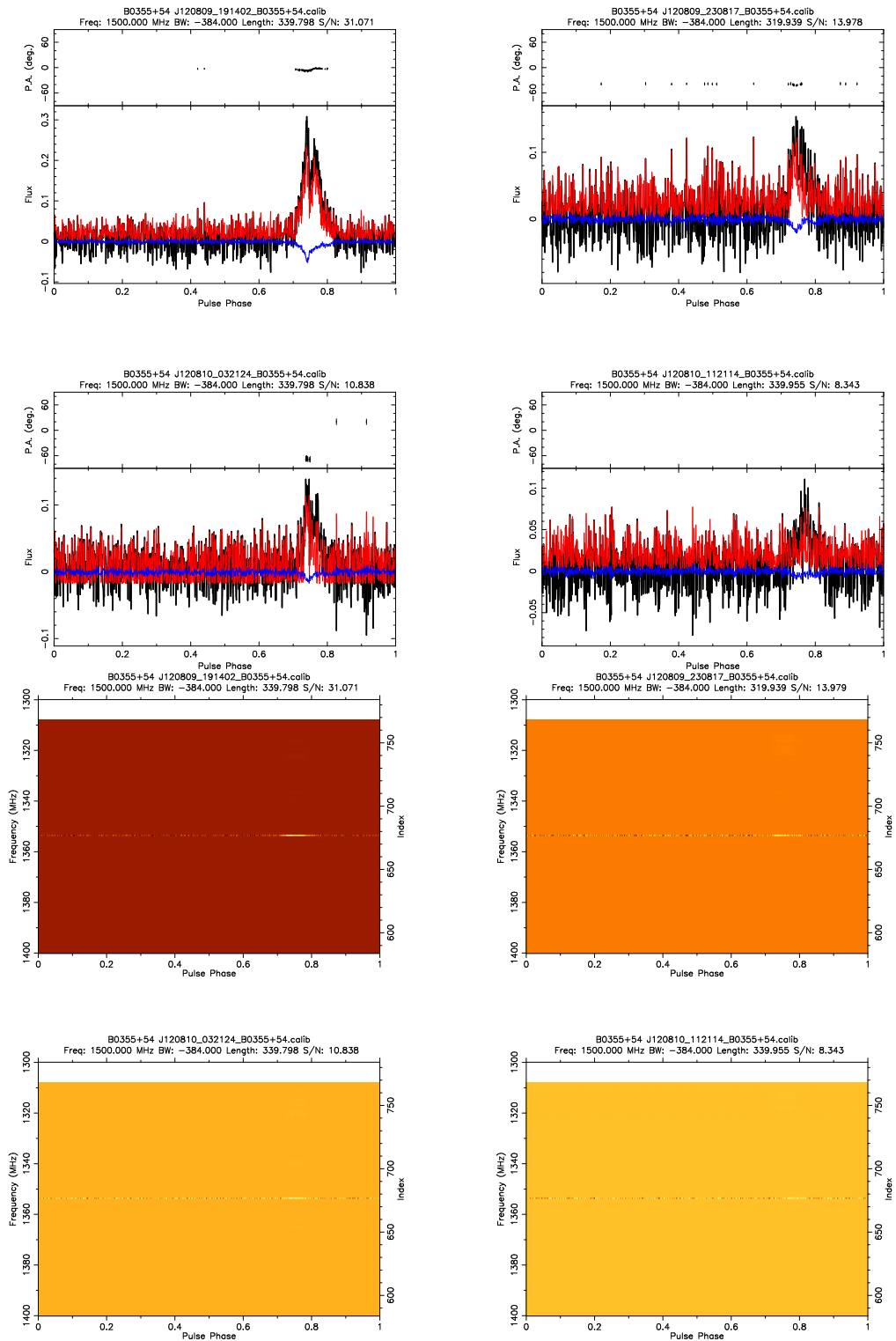


Figure 4.9: Unsuccessful calibration by *pac*. Calibrated profiles from the *MEM* method (*top*) and the pulse phase vs. frequency band plots (*bottom*). See next figure for the recovered profiles.

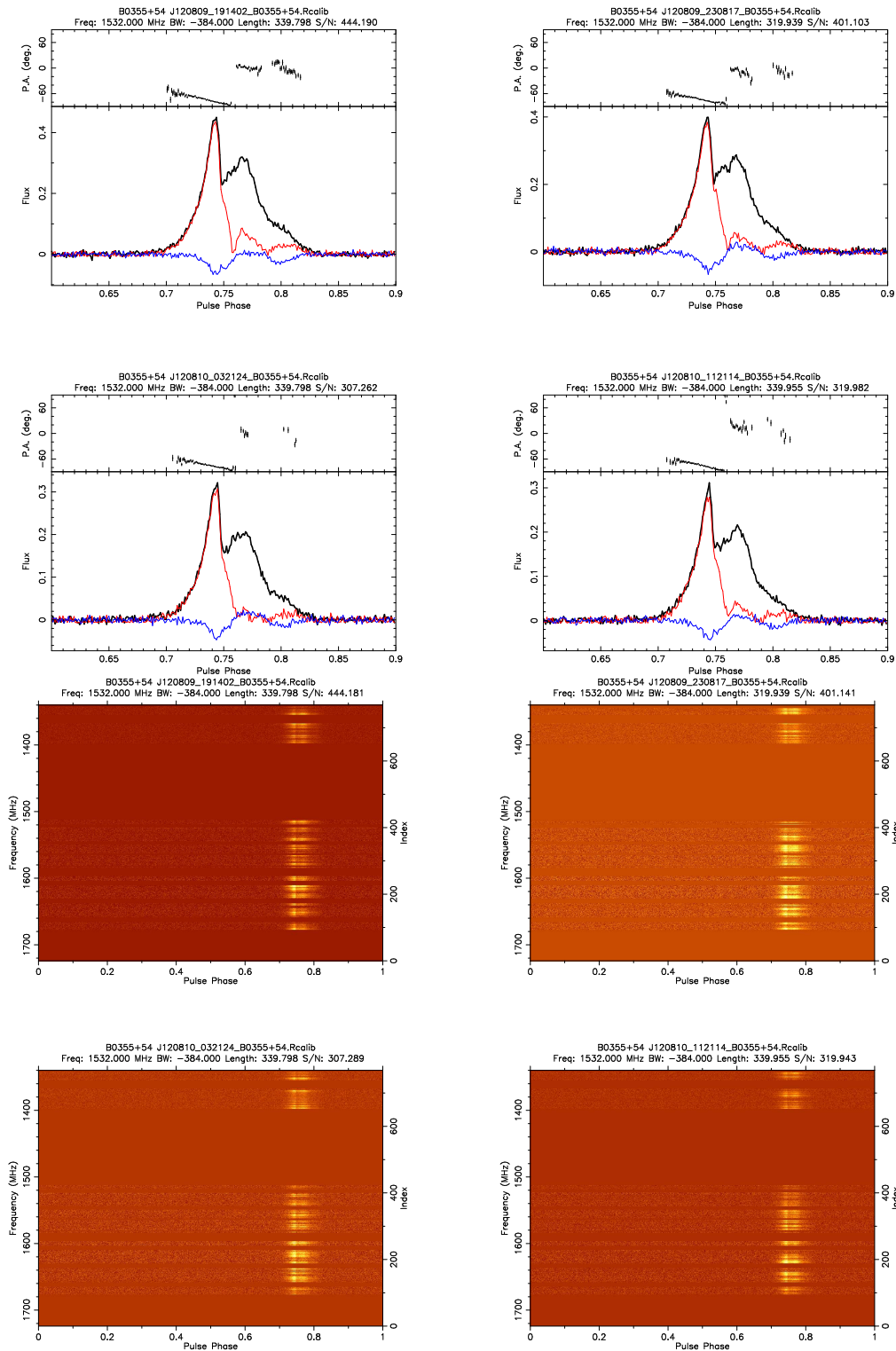


Figure 4.10: As in Fig. 4.9, but with bad channels removed from the uncalibrated data before the fitting process.

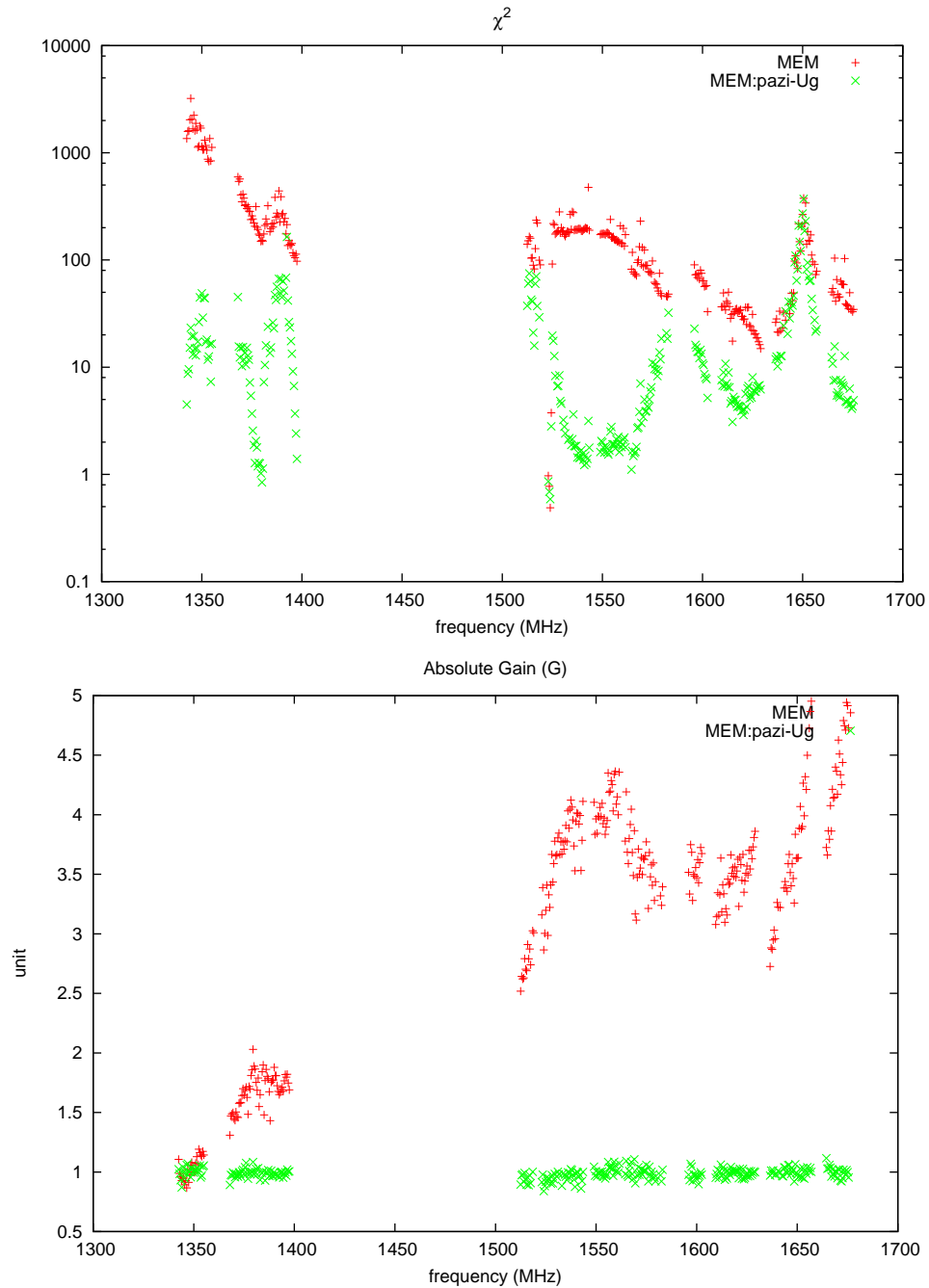


Figure 4.11: As a function of frequency band, the best fit's reduced- χ^2 and G are plotted in the *top* and *bottom* figures, respectively. The *red* and *green* points correspond to the normal *MEM* method and the case where G of the input CAL file is manually set to unity.

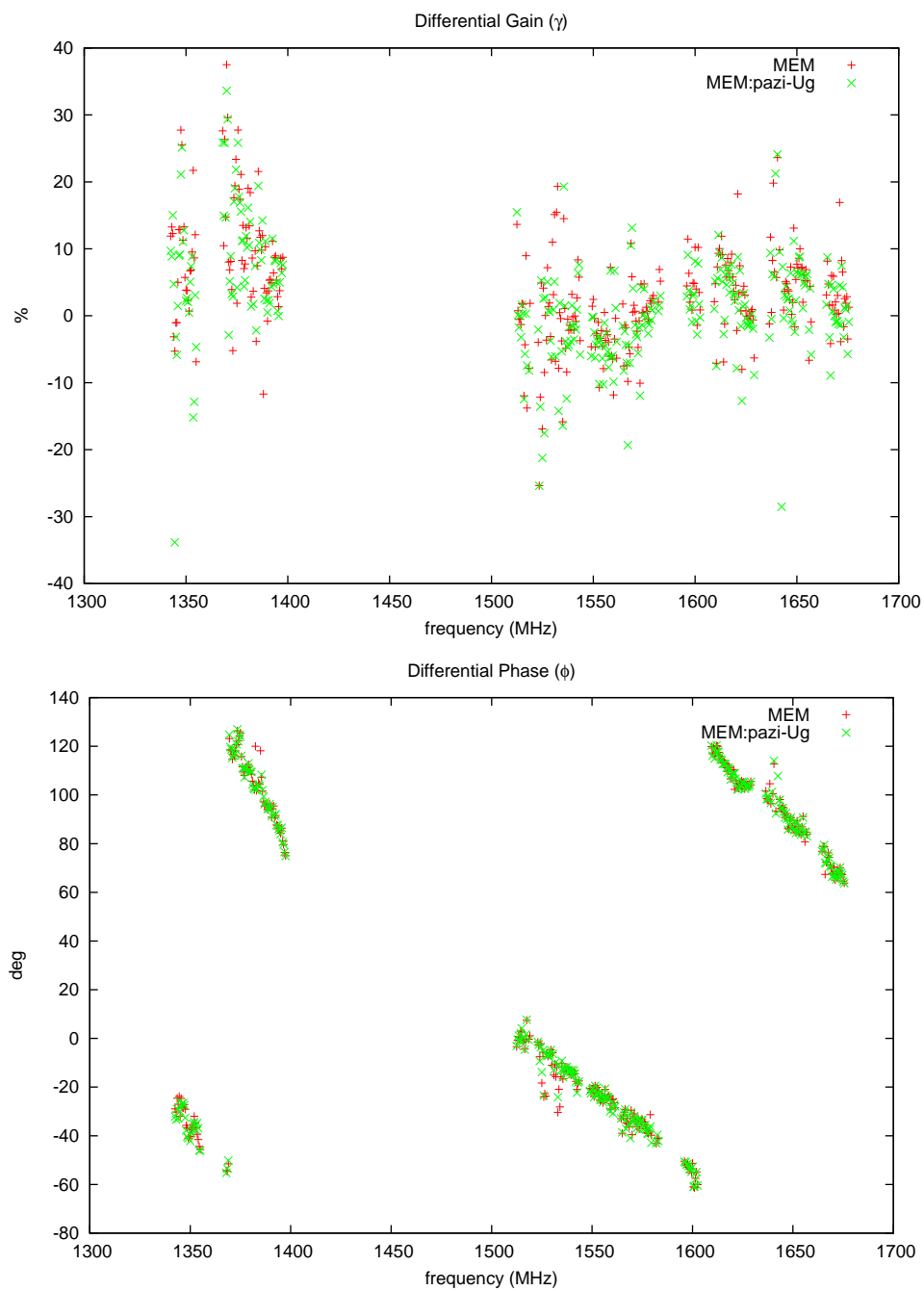


Figure 4.12: As in Fig. 4.11, but for the differential gain (*top*) and differential phase (*bottom*).

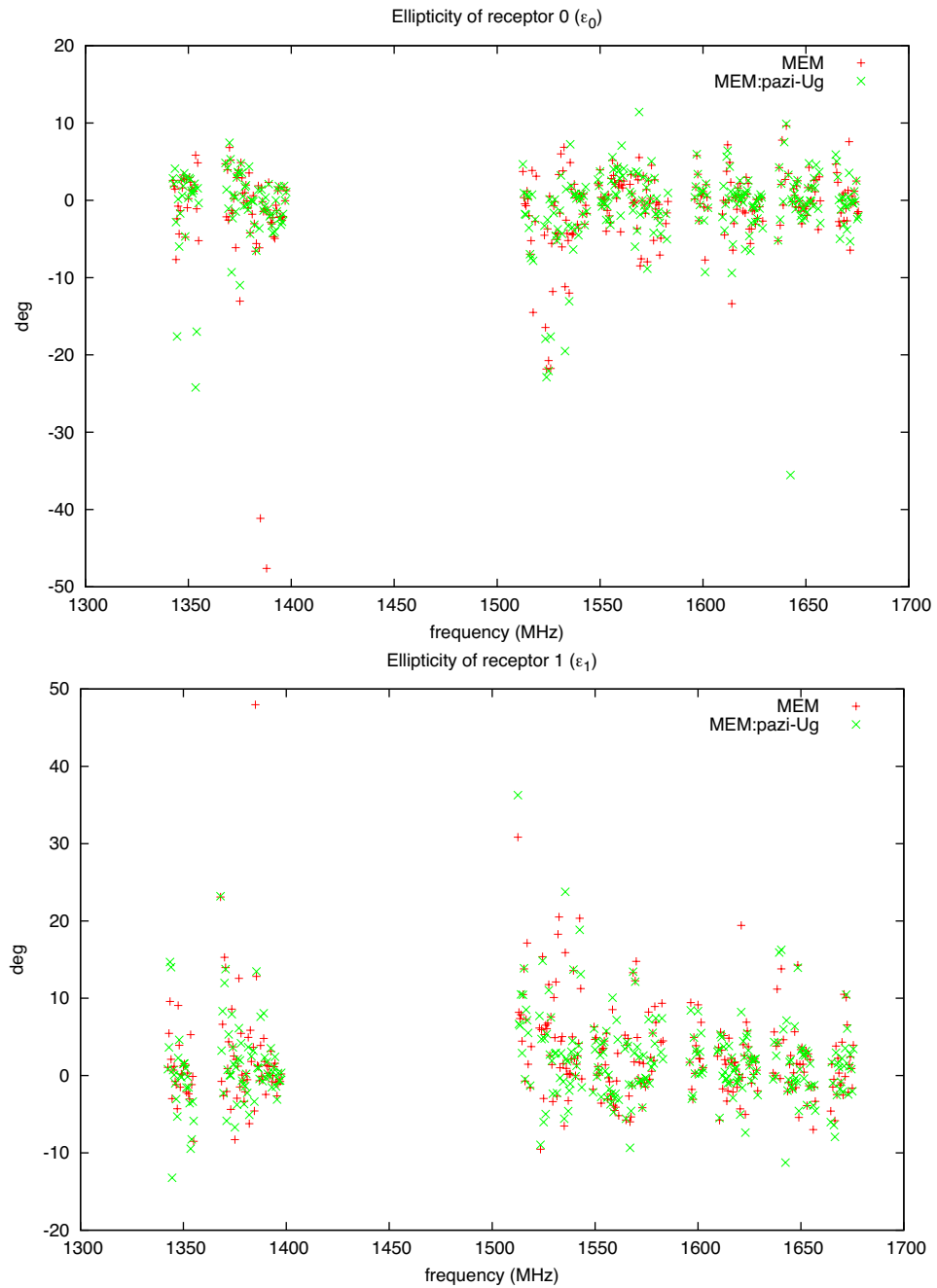


Figure 4.13: As in Fig. 4.11, but for the ellipticity of the receptors 0 (*top*) and 1 (*bottom*).

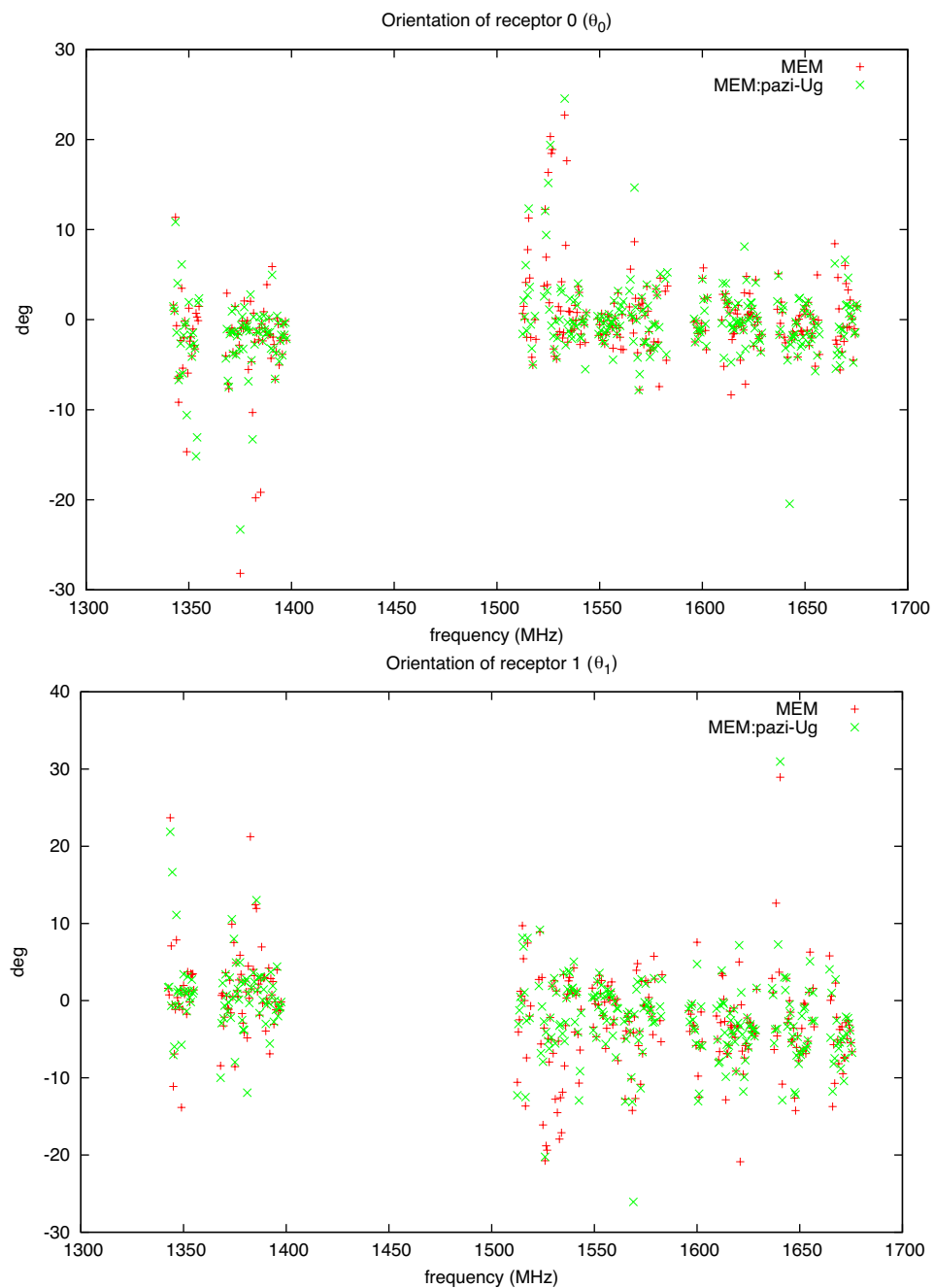


Figure 4.14: As in Fig. 4.11, but for the orientation of the ellipticity of the receptors 0 (*top*) and 1 (*bottom*).

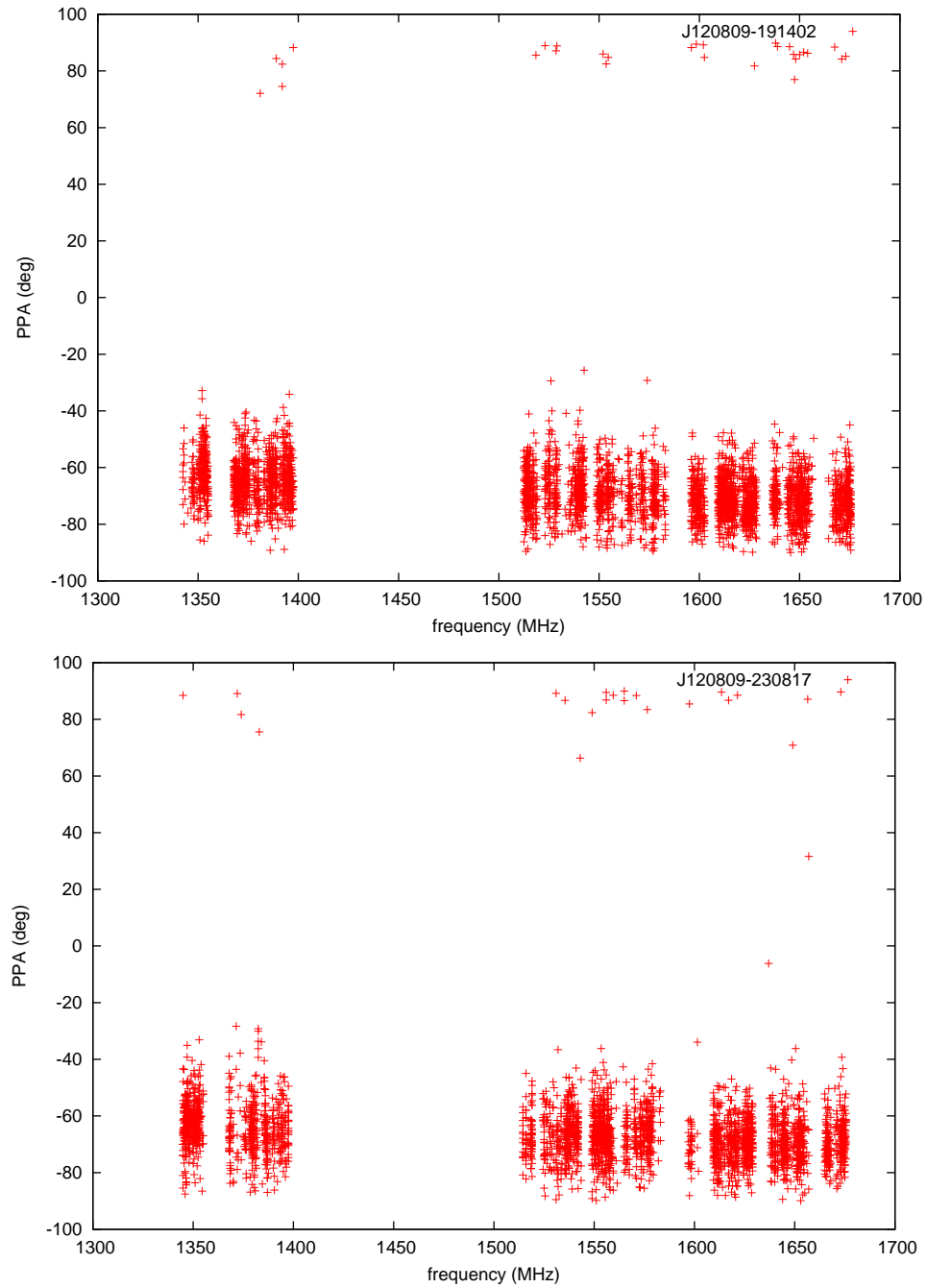


Figure 4.15: The PPAs points of the highly-polarised leading component of the calibrated profiles, observed on August 9, plotted as a function of observing frequency.

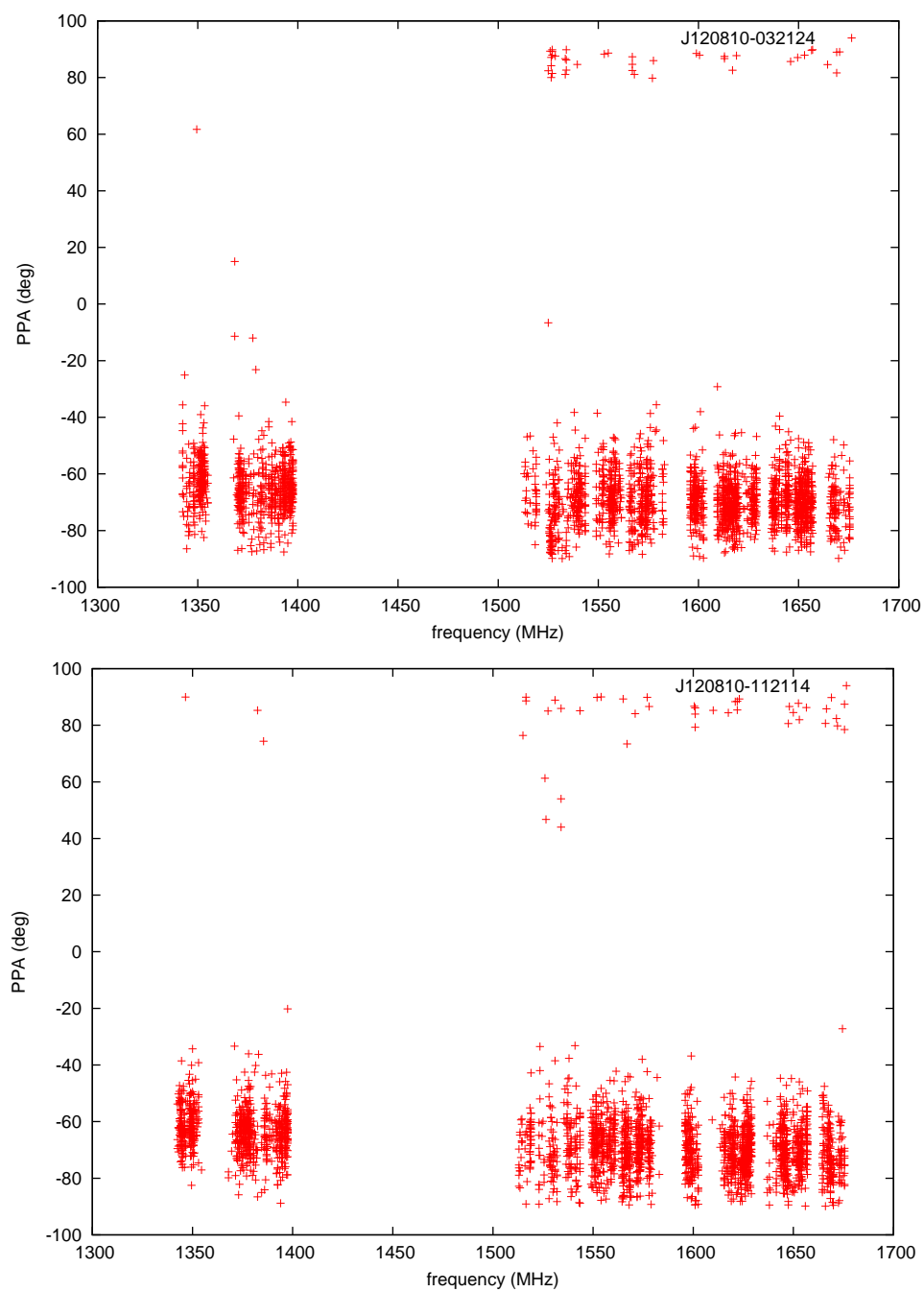


Figure 4.16: As in Fig. 4.15, but for the observations on August 10.

4.4 Matrix Template Matching

van Straten (2006) presents a template matching technique, in which he shows that, for a number of millisecond pulsars, the time of arrival measured from the polarimetric profile can provide better precision than that measured from the conventional total intensity profile, given that the system is well calibrated. Alternatively, the method can also be used to calibrate the data itself, by fitting the observed polarisation profile with a high-S/N template, which is usually created by adding many well trusted calibrated (with different calibration methods) observations. The main advantage of this *MTM* method is that it is based purely on a template matching technique, which requires no input from a CAL observation, making it is possible to calibrate observations in which no CAL observations are available. This suits the present situation with the Lovell telescope well, where CAL observations are not performed frequently enough to keep up with the change in the hardware configuration.

The coherence matrix, (ϱ) , which is defined in Eq. 4.4, is rewritten as a function of discrete pulse phase, ϕ_n , where $0 \leq n < N$ and N is the number of intervals (bins) into which the pulse period is evenly divided. The observed polarisation profile (ϱ') is modelled as

$$\varrho'(\phi_n) = \mathbf{J}\varrho_0(\phi_n - \varphi)\mathbf{J}^\dagger + \varrho_{DC} + \varrho_{\text{noise}}(\phi_n), \quad (4.12)$$

where φ is a shift in pulse phase of the template $\varrho_0(\phi_n)$ with respect to the observed profile, \mathbf{J} is the same Jones matrix defined in Eq. 4.9, ϱ_{DC} is the DC offset between the two profiles, and ϱ_{noise} is the system noise term. The discrete Fourier transformation of Eq. 4.12 is

$$\varrho'(f_m) = \mathbf{J}\varrho_0(f_m)\mathbf{J}^\dagger \exp(-i2\pi f_m\varphi) + \varrho_{\text{noise}}(f_m), \quad (4.13)$$

$$\chi^2(\varphi) = \sum_{m=1}^{N/2} \sum_{k=0}^3 \frac{[S'_k(f_m) - \text{tr}[\sigma_k\varrho'(f_m)]]^2}{\zeta_k^2}, \quad (4.14)$$

where ζ_k^2 is the rms of the noise in each spectral channel. The strategy to use the *MTM* method for calibrating older observations is to first select a set of prototype pulsars which were observed frequently and can be calibrated (via different methods) at the present, and make a high-S/N template for each of

them. Then, for individual pulsars, those templates are used to calibrate older observations, in which we can ideally derive a series of solutions of the system response in the past.

The *MTM* method is implemented as another option in *pcm* by van Straten (2006). We tested this method with the same three August observations derived in Section 4.2 (Fig. 4.4), by following the *PSRCHIVE* manual page⁴. The three *pac*-calibrated profiles are combined to create a high-S/N template, shown in Fig. 4.17. With this template, the *MTM* method is then applied to two datasets, which are the same raw profiles (before *pac*-calibration) used to make the template itself (or the ‘self-test’) and an observation made on July 1.

Shown in Fig. 4.18, calibrated profiles from the self-test are reasonably consistent with the template and with their own *pac*-calibrated versions. Comparing to solutions derived from the CAL files (Fig. 4.4), this method is able to recover most of the solutions (Fig. 4.19), although one would expect better because the template is essentially fitting itself. The reduced- χ^2 is shown in Fig. 4.20 (*top*), which has an average of ~ 0.6 with a small number of channels sporadically occupying different values. On the other hand, however, this might be excusable as the template itself is made of three profiles observed at different epochs, and therefore may cause the fitting solutions to be imperfect.

Although solutions of $\theta_{0,1}$ and $\epsilon_{0,1}$ (Fig. 4.20, *bottom*) appear to be very well constrained, they are indeed artefacts because the information in this test is already limited by the CAL file used in making the template in the first place.

Another test of this *MTM* method was made on a July observation of the same pulsar, and with the same template. In that period of time (July) no useful CAL observation is available. As shown in Fig. 4.21 and Fig. 4.22, the results suffer of a similar problem as in the *MEM* method, where a few individual channels are corrupt (*top – left*). When these channels are manually removed, the final profile (*top – right*) are still in disagreement with the template (*bottom – right*). The *bottom – left* profile is the uncalibrated original profile.

The best-fit solutions, shown in Fig. 4.23 (*top*), appear to be barely resolved, particularly for ϕ which is normally shown to have a smooth and linear relation with frequency band (e.g. Fig. 4.19). There is a vaguely familiar trend for G and γ . Despite these results, the leakage terms $\theta_{0,1}$ and $\epsilon_{0,1}$ (*bottom*) are interestingly statistically small, i.e. close to zero and equal for both ‘left’ and ‘right’ signal

⁴<http://psrchive.sourceforge.net/manuals/pcm/>

chains (*red* or *black*), except for the ~ 1530 and ~ 1610 MHz parts of the band. Similarly, the resulting reduced- χ^2 values (Fig. 4.24) are surprisingly close to one, with the exceptions at 1550 and 1630 MHz. The convergence problem reminds us of the ‘diverging problem’ described in Chapter 2: that, while the χ^2 value indicates a well-constrained fit, the solution itself appears to be wrong. This, therefore, leads us to inevitably conclude that the constructed model, for some reasons, is unable to realistically describe the data and more investigation is required.

The *MEM* technique only requires a high-S/N template, made from well-calibrated observations, with no requirement of CAL observations, making it suitable for unstable observing systems. Unfortunately, it was shown that we have not been able to properly apply this technique to the Lovell system yet. This technique is capable of using the necessary template created with calibrated observations from different hardware setups or even different telescopes, e.g. EPN database⁵; however, difficulty will arise when dealing with different header information and data formats. Nevertheless, it is important to note that this method anticipates a constant character for the pulse profile, which has been shown to not always be the case (e.g. Lyne et al. 2010). Indeed, it is these changes in pulse profile which will interest us most for the rest of this thesis.

⁵<http://www.jb.man.ac.uk/research/pulsar/Resources/epn/browser.html>

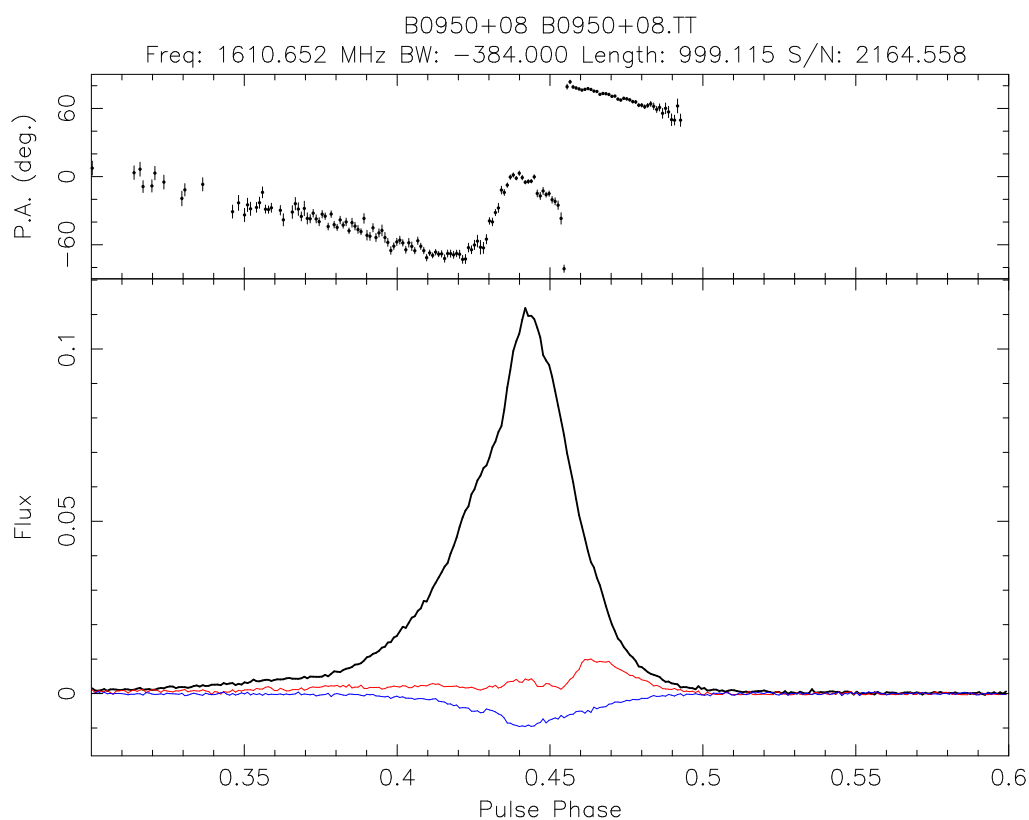


Figure 4.17: The template of PSR B0950+08 from combining the three *pac*-calibrated profiles in Section 4.2, which is used for the *MTM* method.

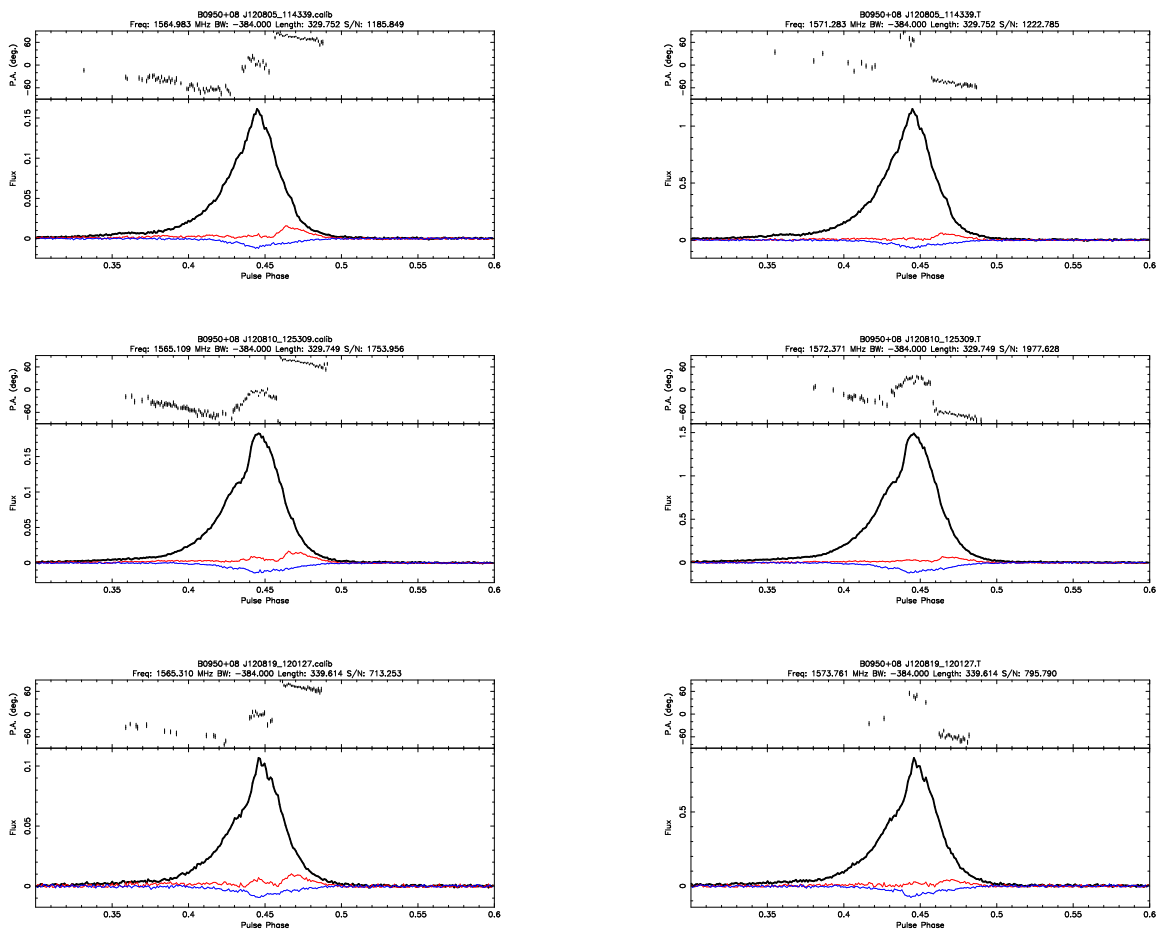


Figure 4.18: Results from the self-calibrating *MTM* test (*left* column), compared to the uncalibrated profiles (*right* column).

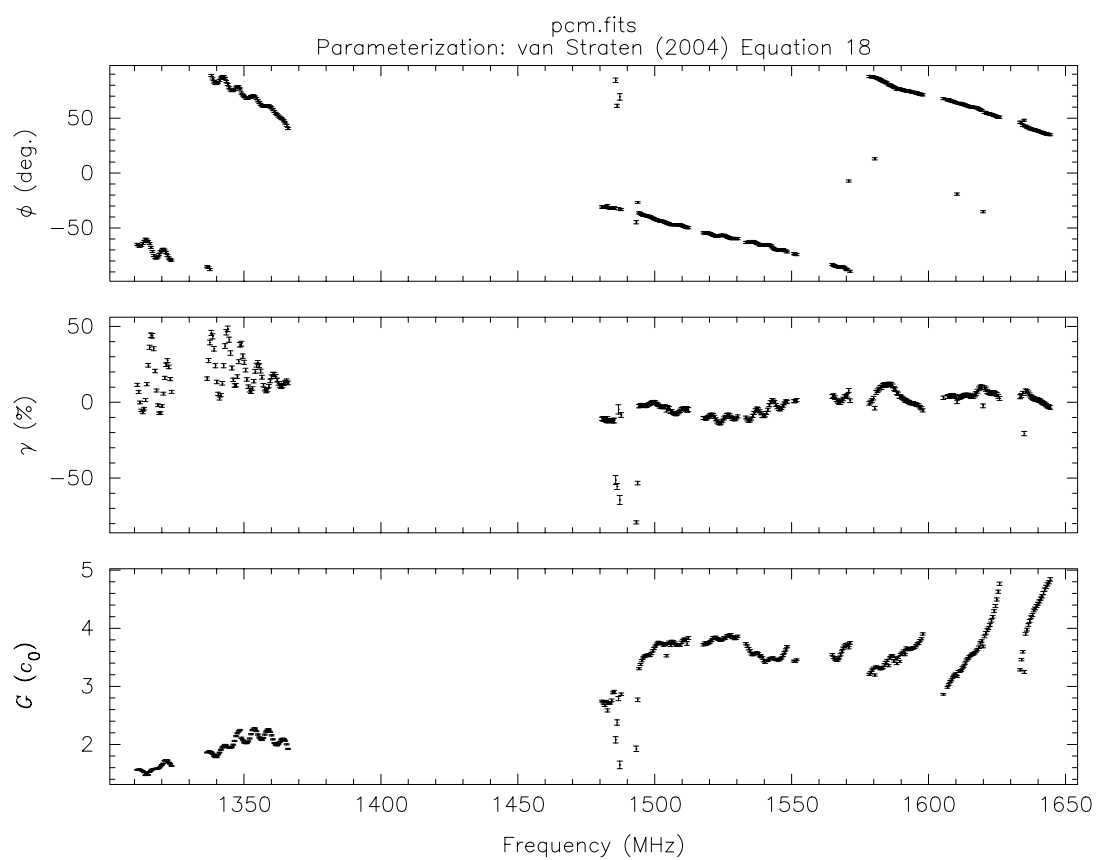


Figure 4.19: The derived G , γ and ϕ from the self-calibrating *MTM* test.

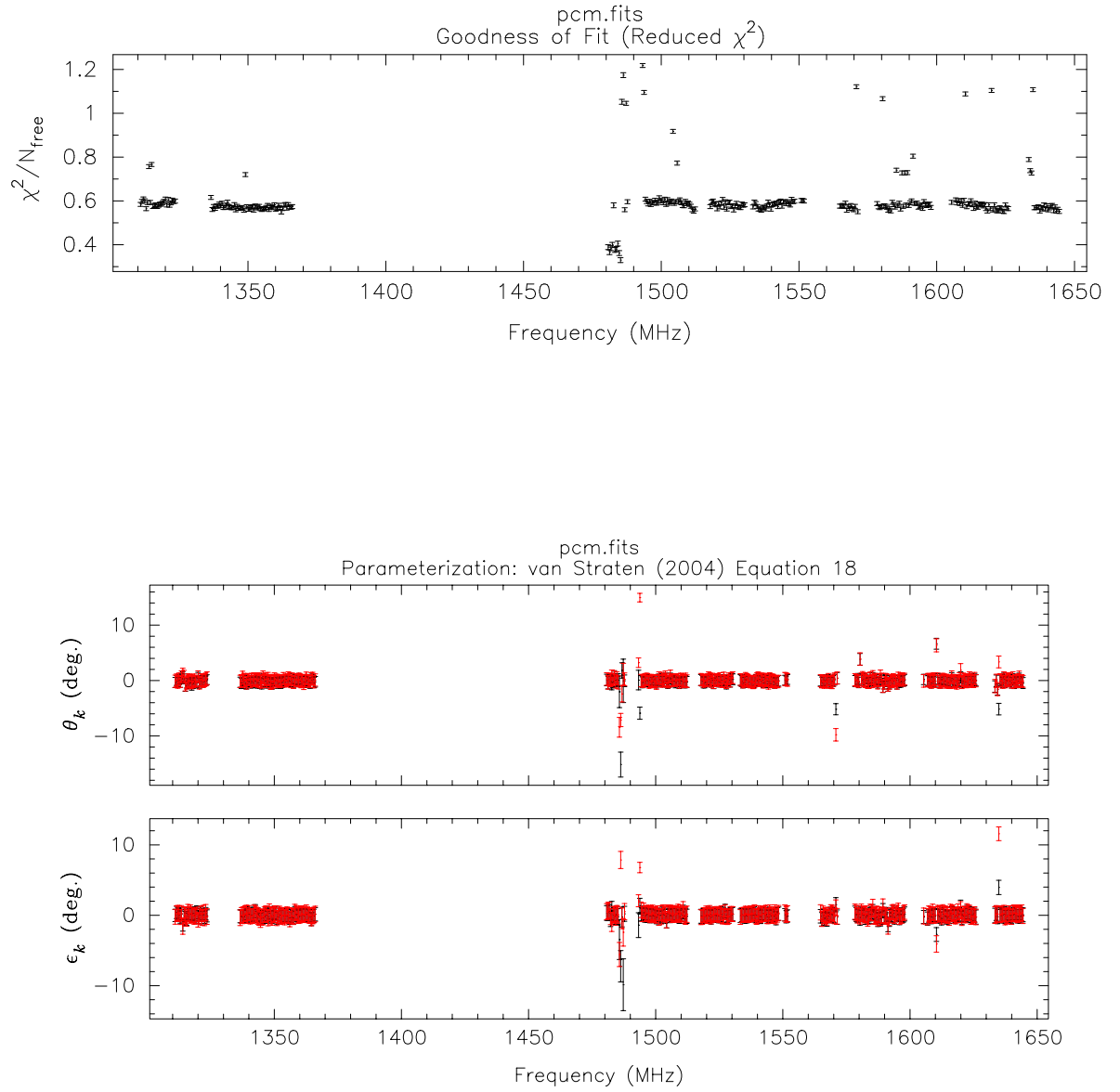


Figure 4.20: (*Top*) The reduced- χ^2 from the self-calibrating *MTM* method. (*Bottom*) And the derived $\theta_{0,1}$ and $\epsilon_{0,1}$.

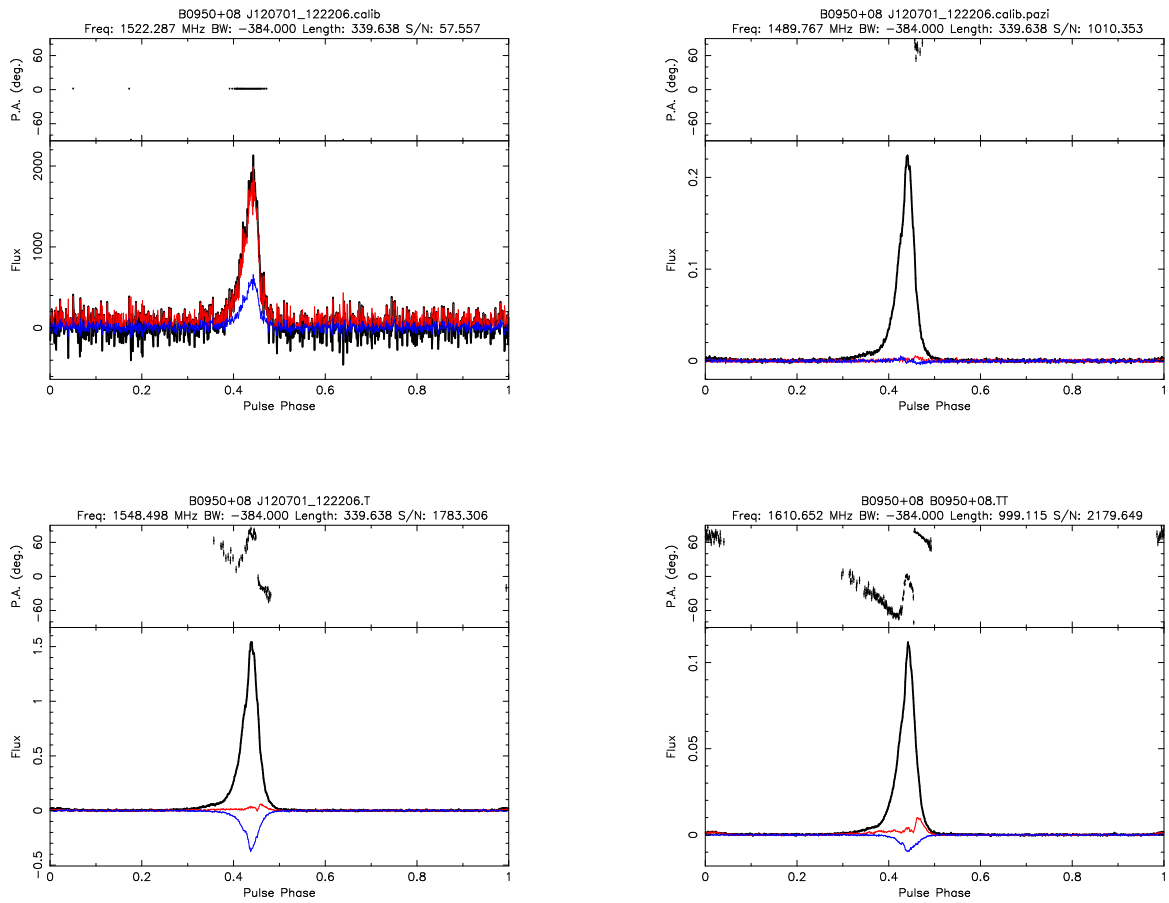


Figure 4.21: Applying the *MTM* method with the observation in July (*bottom-left*) with the template (*bottom-right*), the output profile appears to be unsuccessful (*top-left*), in which the result can be recovered (*top-right*) with the corrupted channels (see next figure) are removed.

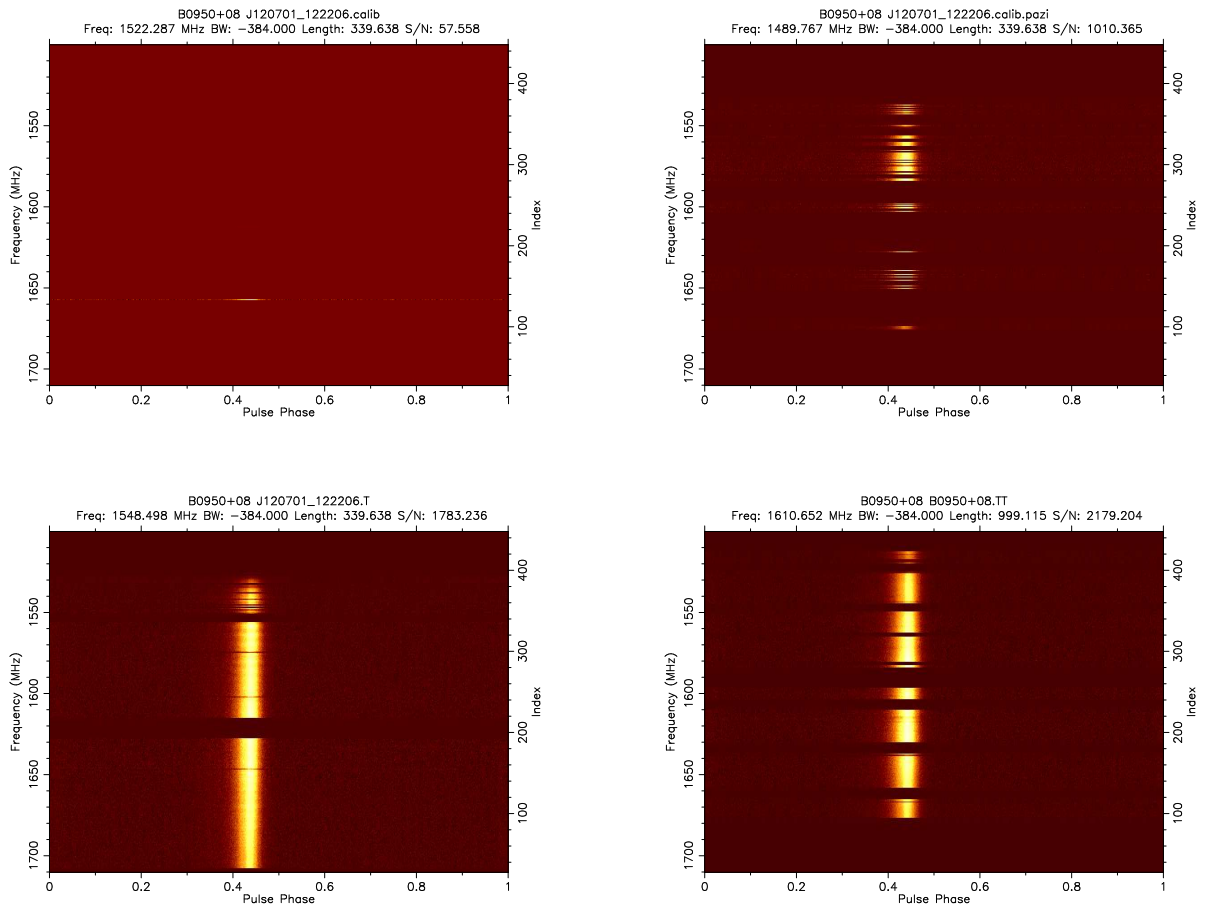


Figure 4.22: As in Fig. 4.21, but plots of frequency channels vs. pulse phase, in which the frequency axis is zoomed into the high-frequency part of the band.

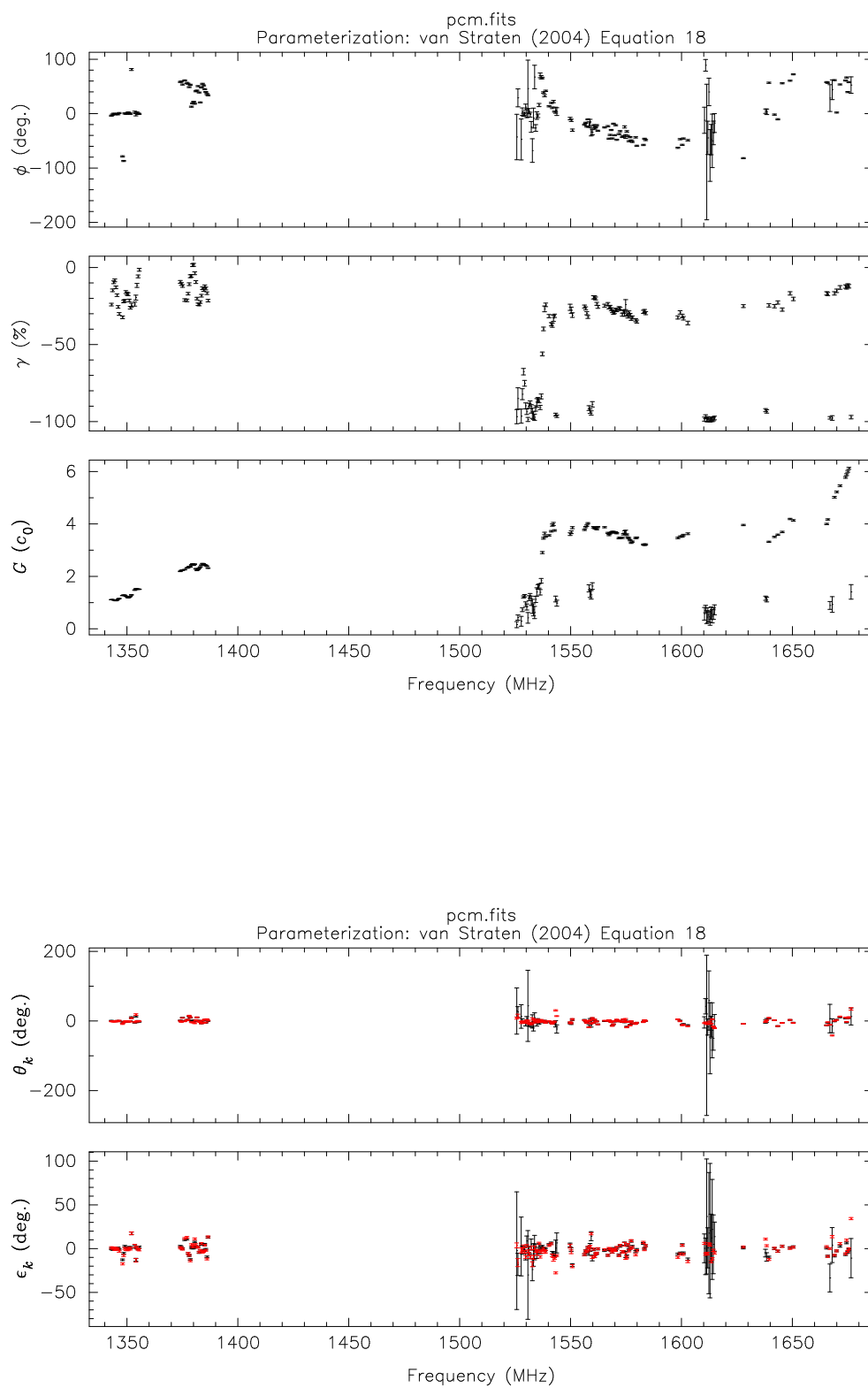


Figure 4.23: Solutions from the *MTM* method on the July observation. (*Top*) G , γ , and ϕ . (*Bottom*) $\phi_{1,2}$ and $\epsilon_{1,2}$.

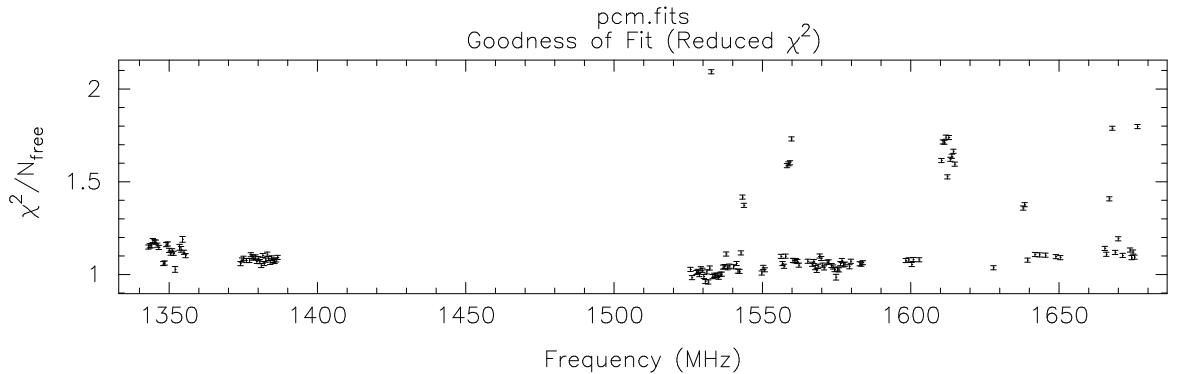


Figure 4.24: The reduced- χ^2 from the *MTM* method on the July observation.

4.5 Polarisation Calibration of PSR B1822–09

Having studied and tested various polarisation calibration techniques in the previous sections, we now move our attention to PSR B1822–09. Despite the conclusions that the available calibration methods all have their own issues with the current observing system, we believed that, with the *pac* method and sufficiently good CAL observations, a proper polarisation calibration can be made at a reasonable level of confidence for this pulsar.

Twelve 40-minute observations of PSR B1822–09 were made between May and September 2012 and eight CAL observations are available in that period of time. Following a similar process as in Section 4.2, the data is calibrated and the results are shown in Fig. 4.25 and 4.26. A few observations seem to be noisier than the rest, which is possibly due to scintillation, however the polarisation is consistent for these observations. Similar to what we did with the *MEM*'s results we confirmed that the PPAs of those calibrated profiles are independent of frequency for ten of the twelve observations (Fig. 4.27-4.29). Two observations will be ignored because their PPAs express some frequency dependence, which we can attribute to hardware changes.

These ten polarisation calibrated observations were processed for mode-switch behaviour study in the next chapter.

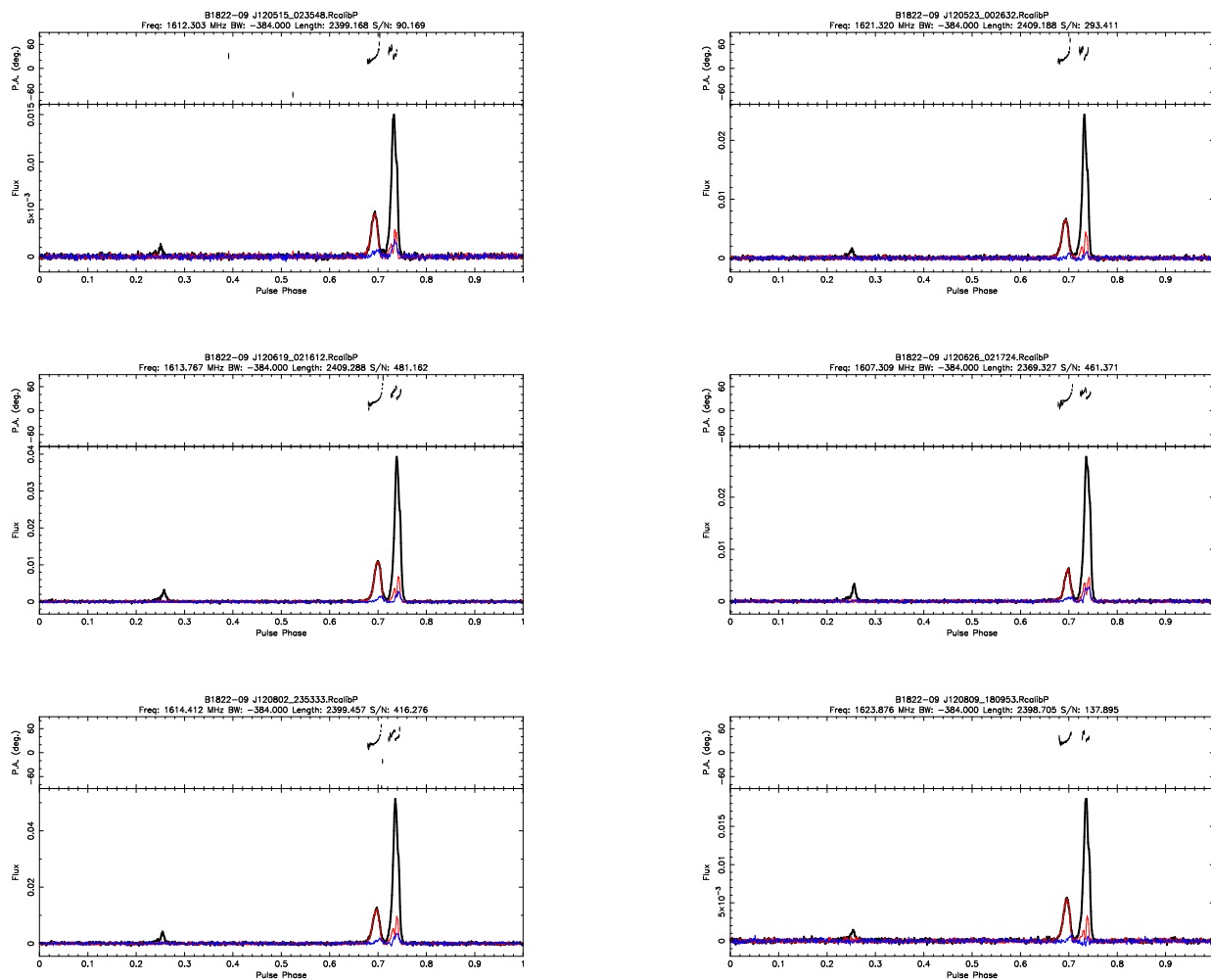


Figure 4.25: Calibrated with the *pac* method, ten 40-minutes observations of PSR B1822-09. From *left to right* and *top to bottom*, the date of observations are May 15 and 23, June 19 and 26, and August 2 and 9. Continued with next figure.

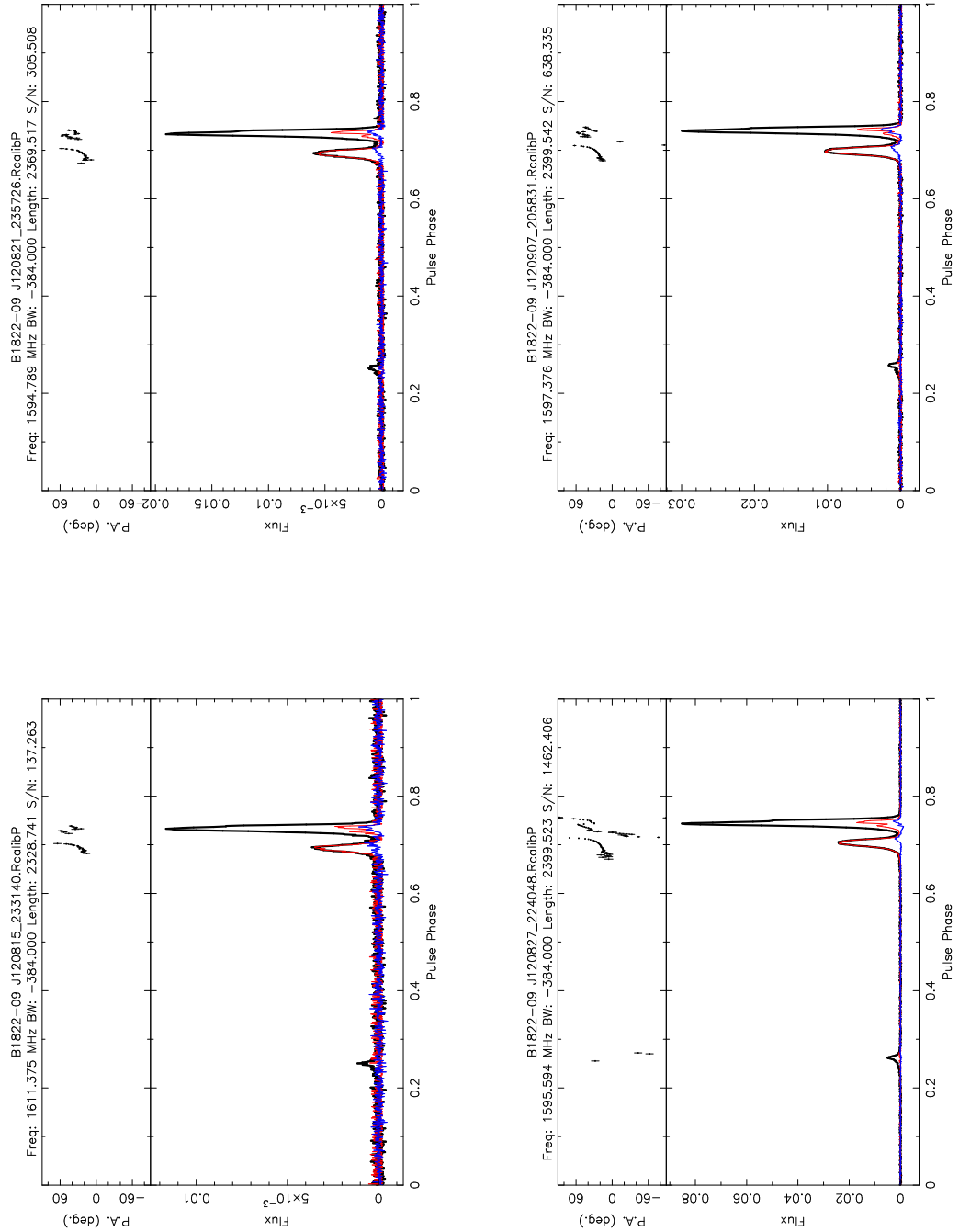


Figure 4.26: Continued from Fig. 4.25. Horizontally from *left* to *right* and *top* to *bottom*, observations on August 15, 21, and 27, and September 7.

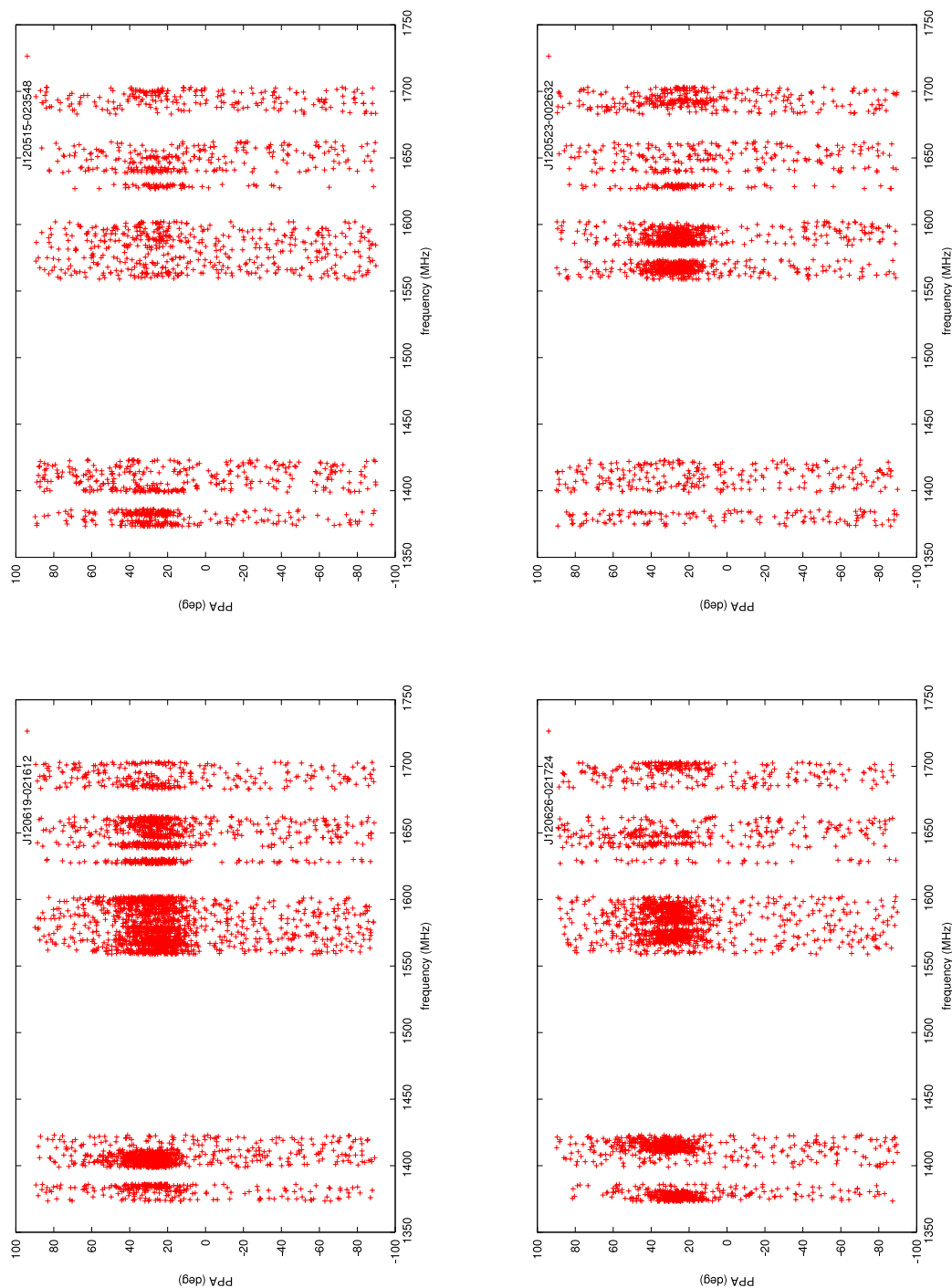


Figure 4.27: To find any evidence of frequency dependency, the PPA points of the calibrated profiles are plotted, in order of observing date from *left to right* and *top to bottom*. Continued with next two figures.

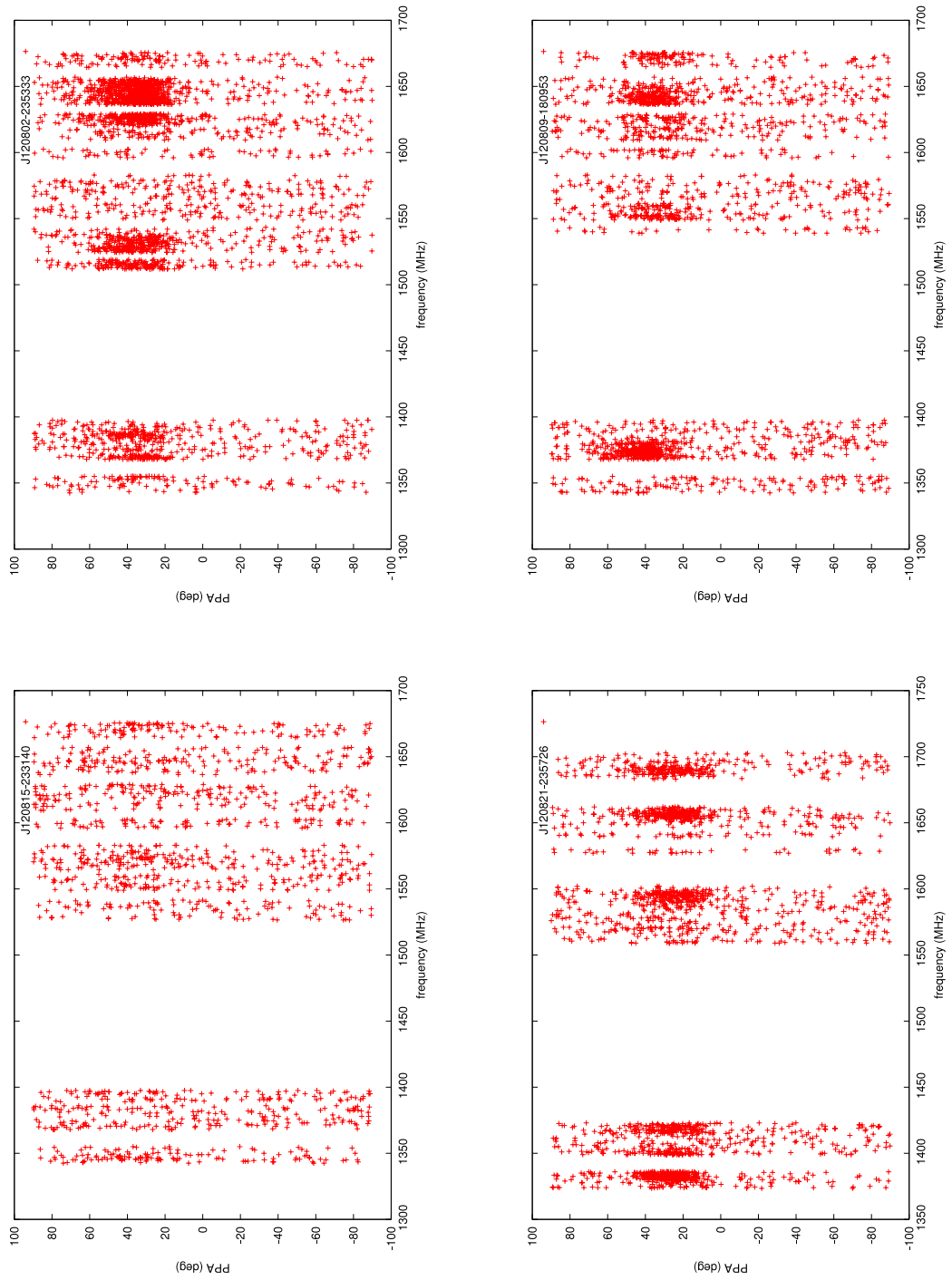


Figure 4.28: Continued from Fig. 4.27, and to next figure.

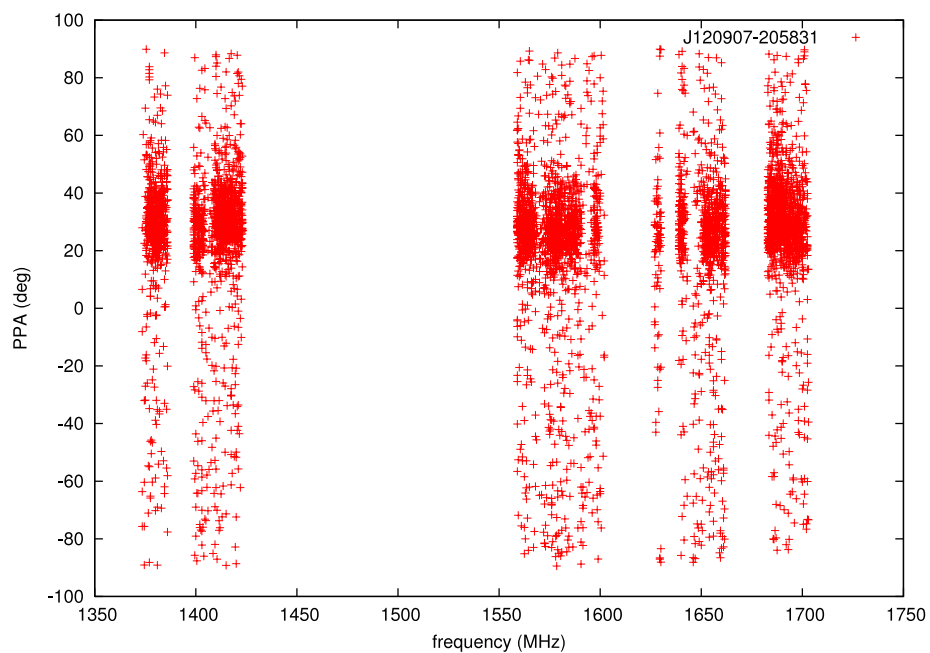
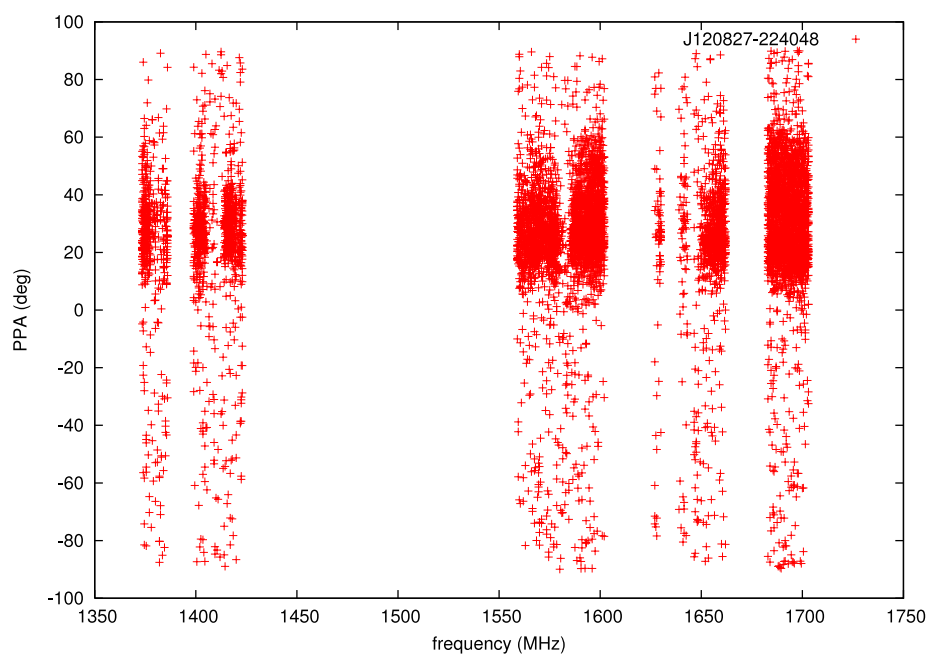


Figure 4.29: Continued from Fig. 4.28.

Table 4.1: (*Left to right*): the observation date, observing frequency, integration time, signal to noise and CAL observation date of the PSR B1822–09 dataset.

Number	Date (Y-M-D)	f (MHz)	Length (s)	SNR	CAL (Y-M-D)
1	12-05-15	1532	2399	301.52	12-05-16
2	12-05-23	1532	2409	191.70	12-05-16
3	12-06-19	1532	2409	661.17	12-06-19
4	12-06-26	1532	2369	513.16	12-06-25
5	12-08-02	1532	2399	467.76	12-08-09
6	12-08-09	1532	2398	137.81	12-08-09
7	12-08-15	1532	2328	114.83	12-08-10
8	12-08-21	1532	2369	372.01	12-09-20
9	12-08-27	1532	2399	1678.4	12-09-20
10	12-09-07	1532	2399	1228.1	12-09-20
11	12-09-13	1532	2398	160.85	12-09-20
12	12-09-21	1532	2398	2612.6	12-09-20

4.6 Summary

Concepts of polarisation calibration can be categorised into two categories: 1) those using a well known source, i.e. a CAL signal (*pac* method) or a template of the pulsar (*MTM* method); 2) those using a model which links the observed polarisation (Stokes parameters) to additional variables, i.e. the parallactic angle (*MEM* method) and the *RM* technique (Edwards & Stappers 2004), in which the rotation of the linear polarisation plane is caused by Faraday rotation, instead of the parallactic angle.

We have shown that each of those methods has their own advantages and issues. For the Lovell Telescope, there is an indication that the system response can sometimes change on a timescale of a day and the CAL signal has not been observed frequent enough, and that the CAL signal may have additional factors which are not included into the assumptions of the model, e.g. standing waves in the system. To deal with this problem, we hope to record the CAL signal more often in the future.

Being very less stable, our system proves the *MEM* technique to be insufficient at times, although it seems to be working robustly for most of the time. The *MTM* technique, which we hoped to be the method to calibrate old observations with no CAL file available, is shown to be not working properly yet as it fails to provide a credible solution (particularly ϕ) for the majority, if not all, of the

frequency channels, despite having a very low χ^2 value.

The best way to proceed to calibrate the dataset of PSR B1822–09 was to use the *pac* method with, fortunately, sufficiently good CAL files. The calibrated profiles are found to be consistent, providing us the opportunity to make a reliable polarisation study of this pulsar in the following chapters.

Chapter 5

A Study of PSR B1822–09

PSR B1822–09 is one of the most interesting pulsars. It has several peculiar features observed in one package: switching between two stable profiles (or ‘mod-ing’), a 100% linearly polarised precursor (PC), mode-preferential subpulse periodicity, a 180°-separated interpulse (IP), and the correlation between profile-switching behaviour and the pulsar’s spin variability. Recently, this pulsar has been shown to have its mode-switching character correlated with its spin evolution (Lyne et al. 2010). In terms of strategic importance, it represents a population of mode-switching pulsars where the process of the mode switching is still a mystery. Comparing its properties to relatively better understood intermittent pulsars may lead to a more complete knowledge of these instabilities.

Via the knowledge and techniques harvested in Chapters 2 and 3, we aim to study differences between properties of the switching modes in terms of the classic hollow-cone model, the polarisation modes of wave propagation, and subpulse modulation. We also discuss whether a model by Petrova (2008a,b, 2009) can explain our findings. Long-term variation of the pulse profile and switching statistics are also investigated, making further implications for Lyne et al. (2010)’s results.

5.1 Known Characteristics

PSR B1822–09 ($P = 0.769$ s, $\dot{P} = 5.25 \cdot 10^{-14}$) is a relatively young pulsar with a characteristic age 2.3×10^5 years, due to its relatively high \dot{P} relative to its P . Being discovered in the first ten years of the pulsar era, it was first identified

to have an interpulse by Cady & Ritchings (1977) and later to have two different ‘averaged’ profiles and sub-pulse modulation characteristics by Fowler et al. (1981) (hereafter FWM81). Its pulse profile was found to switch dramatically every few minutes, and the subpulse periodicity was also found to change during the same switching (FWM81; Gil et al. 1994 (hereafter GJK+94); Backus et al. 2010 (hereafter BMR10)).

The two modes are known as the ‘B’urst mode and the ‘Q’uiet mode (Fig. 5.1). In B mode (*left* column) the pulses are approximately three times brighter and possess a $\sim 100\%$ linearly polarised PC at 15° prior to the main pulse (MP). GJK+94 showed that both the component’s width and the separation to the MP are independent of frequency from a few hundred MHz to ten GHz. They also found that the PC is made of burst-like ($\leq 300 \mu\text{s}$) and highly polarised emission, which is very distinct from regular polar-cap character of the MP emission ($\sim 600 \mu\text{s}$).

During the Q mode (*right* column of Fig.5.1, more clearer in Fig. 5.7), the pulsar’s MP becomes narrower and an IP appears at around half the rotation, instead of the PC. Also, the MP and the IP are coherently modulating on a pulse-to-pulse timescale with a periodicity of ~ 40 times the pulsar’s spin period (P). The correlations of the IP, in both mode-switching (FWM81) and subpulse modulation (GJK+94, BMR10), creates a predicament where if the pulsar is an orthogonal rotator, supported by the almost-half-rotation MP-IP separation, then one would be left with a question of how the radiation from the two opposite magnetic poles are in such a precise synchronisation. In addition to a few other similar cases (e.g. Weltevrede & Wright 2009), this has led astronomers to believe in the possibility of global change in the pulsar magnetosphere on very short timescales.

PSR B1822–09 has also been searched for X-ray/gamma-ray pulsation, but no detection has yet been made (e.g. Brown & Hartmann 1993). Nevertheless, it was shown by Alpar et al. (1995) to have X-ray luminosity consistent with the limit of a conventional cooling process of neutron stars. Interestingly, its mode-switching partner, PSR B0943+10, has recently been reported to have X-ray pulsations detected during the pulsar’s Q mode which appears to be exclusively thermal emission, while in the B mode the pulsar expresses a non-pulsing non-thermal radiation (Hermsen et al. 2013).

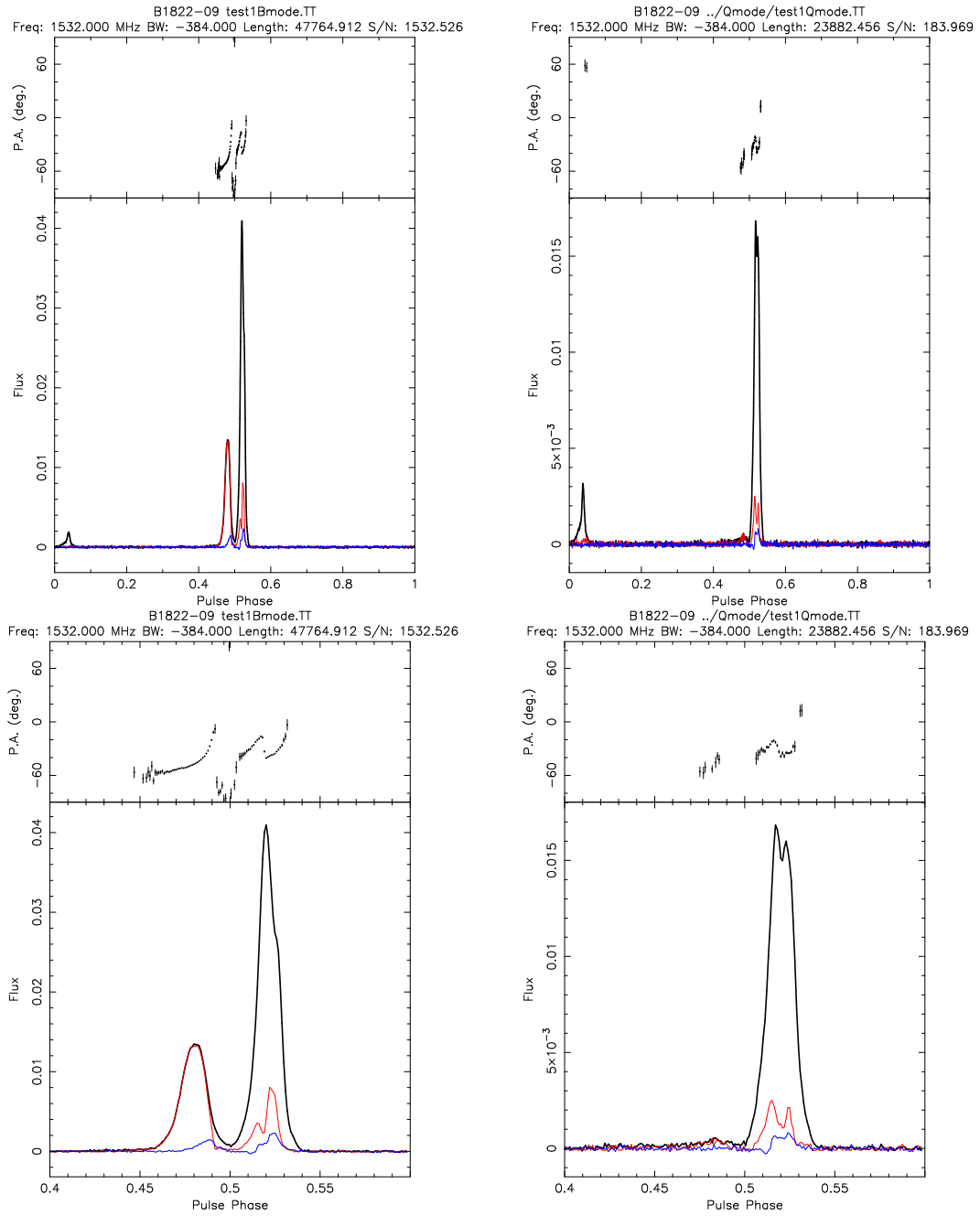


Figure 5.1: The averaged mode-separated profiles of PSR B1822-09 in the *top* plots, showing full pulse-phase, and in the *bottom* plots, the zoom-in. They are added from ten 40-mins observations. The *left* and *right* columns are of the B- and Q-mode profiles, respectively. For each plot, the *top* panel shows the polarisation position angle (PPA) swing and the *bottom* panel shows the pulse profile where the *black*, *red* and *blue* lines correspond to the total intensity, degree of linear and circular polarisation, respectively.

5.1.1 Petrova’s Model

Another route to avoid invoking the instantaneous global change in the pulsar magnetosphere of the supposedly orthogonal geometry of PSR B1822–09 is to assume that the PC and IP can originate from the same polar cap region, as of the MP, but due to some mechanism they are detected outside the normal pulse window. Dyks et al. (2005) proposed an idea of a single-pole geometry which, however, still requires α to be close to 90° , and can account for the anti-modal-occurrence of the PC and IP. This is possible by postulating that they both originate from the emission region above the magnetic pole responsible for the MP. In the B mode a forward coherent radio emission with some specific direction is observed as a PC prior to the MP—which is from another region, but of the same magnetic pole—at phase $\sim 0^\circ$, and in the Q mode a backwards emission is detected as an IP when the same magnetic pole is at phase $+180^\circ$. Without much detail in the physics of such radiation, it is certainly an interesting thought. Nevertheless, this scenario would require a specific line-of-sight (LOS), depending on the mechanism, and the condition that the emission from the ‘other pole’ cannot be seen or is not active.

Petrova (2008a,b, 2009) adapt this idea into a more realistic physical model, involving longitudinal and transverse magnetised scattering of the propagating radio photons off the escaping plasma particles, in order to allow such emission to be observed outside the MP’s window, as ‘interpulse’ components. She demonstrated that due to a very high brightness temperature of pulsar radio emission, the induced scattering of radio photons off the outflowing plasma particles can be significant inside the pulsar magnetosphere. This process is possible on the condition that the radio frequency in the particle’s rest frame (ω) is much less than the electron gyro-frequency $\omega_G(\propto B)$. Such condition can be met at the altitude above the emission zone, in which the coherent effects of plasma still strongly dominate, but not too far off to the light cylinder, where $B \propto r^{-3}$ is decreasing rapidly and the cyclotron resonance takes place when $\omega \sim \omega_G$, resulting in the absorption of the emission.

The scattering process in the presence of strong magnetic fields is shown to be divided into two limits, depending on the strength of B and also the states of the incident waves. In the first regime where B is ‘super-strong’, the motion of the scattering particles is tightly confined to the magnetic field lines, in which they only interact with waves polarised parallel to the electric-magnetic plane

(the O-mode). This is known as ‘longitudinal scattering’. The resulting outgoing wave, which is composed of pure O mode, propagates approximately along the magnetic field lines (and the particle’s velocity) at that scattering point. And if the field lines at that point happen to coincide with the LOS, those scattered photons can then be observed. Rotational aberration (Chapter 1), due to the fact that this process takes place at higher altitude than the typical polar cap emission, means the scattered component is then expected to appear prior to the MP by $r_s/2R_{LC}$ rad, where r_s and R_{LC} are the scattering altitude and the light cylinder radius, respectively. The fact that most PCs have an extremely high L and their location prior to the MPs (hence the name), is a strong evidence supporting this model as only the O mode is expected to be scattered.

In the other regime where B is moderately strong and the condition $\omega \ll \omega_G$ still holds, the motion of the particles can have a certain amount of transverse component, as opposed to a complete longitudinal scattering in the first case, which can interact with the orthogonal mode of the incident wave (the X mode). The outgoing of this ‘transverse scattering’ is calculated to be mostly permitted in the anti-parallel direction to the particle’s velocity, in which the resulting ‘backwards’ emission originates at the rotational phase $+180^\circ$. This wave is, however, required to be able to propagate downwards and across the magnetosphere, suggesting that it is unlikely to be 180° separated from the MP. It can be understood that the efficiencies of the two scattering regimes are competing, depending on ω and ω_G , hence also B and r_s , and therefore the outgoing wave from this regime can be a mixture of both the O and X modes. Unlike the longitudinal scattering, which requires a more stringent condition, such that B must be extremely high but not too close to the radio-emission zone, in general the transverse scattering should be more common and takes place at the altitude close to R_{LC} .

PSR B1822–09 is a good case, as it has both the PC and the IP, to be discussed with Petrova’s model in Section 5.4.3.

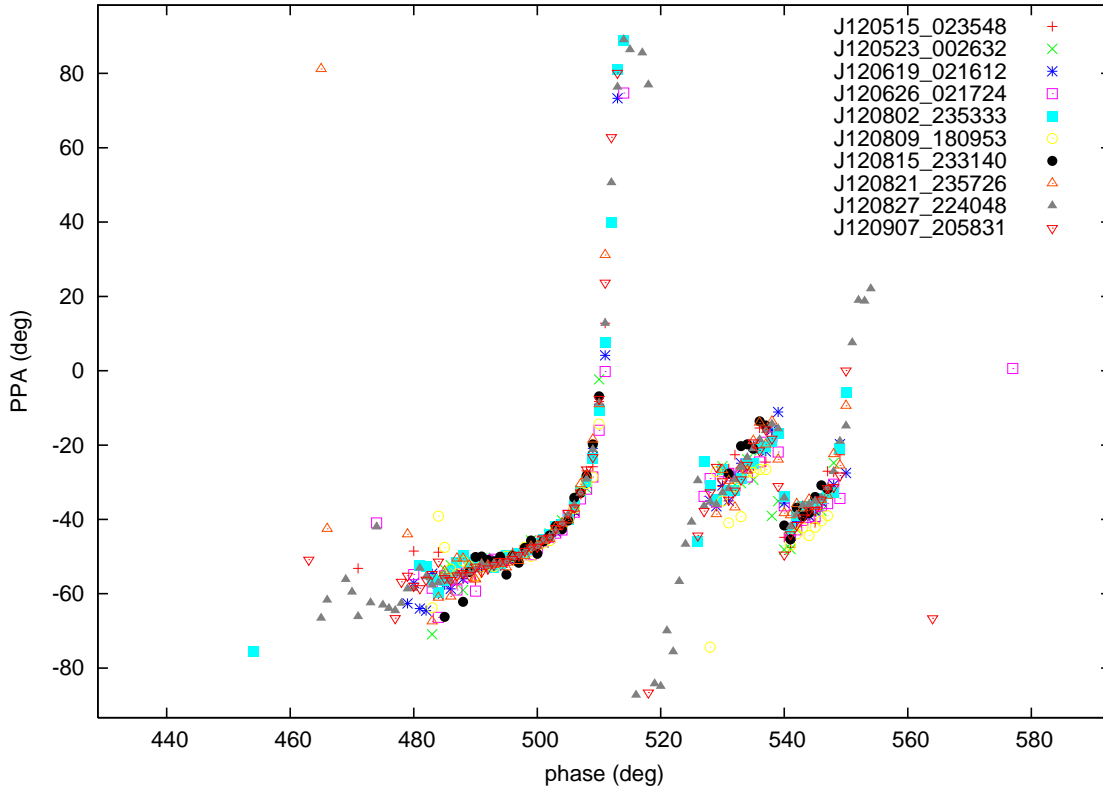


Figure 5.2: An overlay plot of the PPAs swings of the ten observations of PSR B1822-09 after being aligned in phase and PPA value.

5.2 Observations

PSR B1822-09 has long been one of the the most common objects to be observed with the Lovell telescope (at least after Cady & Ritchings (1977) conducted a pulsar survey with simultaneous 327, 408, and 610 MHz observing frequency, in which its IP was identified). In this work, we have access to the AFB data (since 1995) and observations done with the new DFB, installed in 2009. Ten 40-minute sessions were also carried out from May to September 2012, where the data were sampled at $750 \mu\text{s}$ and recorded by the DFB (10-second sub-integrations) and by the *ROACH* board (single-pulse) in *PSRFITS*¹ format centred at 1532 MHz with a bandwidth of ~ 384 MHz (after RFI rejection). The dataset were calibrated with available *CAL* observations using the *pac* method, as presented in Chapter 4.

¹<http://www.atnf.csiro.au/research/pulsar/psrfits/index.html>

The *ROACH* board has an advantage over the DFB that it is capable of coherently de-dispersing and recording single-pulse data, which was deployed for the *LEAP* project². It has been piggybacking the signal chain, providing a rich amount of single-pulse data which is, unfortunately, not yet properly calibrated. For this work, we look into one single-pulse dataset of PSR B1822–09 to investigate its sub-pulse modulation behaviour, and, using a very narrow part of the bandwidth, the PPAs of individual pulses are also studied.

To be able to measure any subtle differences between the profiles of the two modes, the ten DFB observations have to be in good alignment in pulse phase and in position angle. The phase alignment is done by cross-correlating the profiles, using the command *pas* from *PSRCHIVE* package. The profiles are manually put together, by minimising the vertical offset of the PCs' PPA swings, which is very accurate because they are highly polarised and well-defined. To align the PCs' PPAs, we first measure the reference point, which is Ψ_0 in Eq. 1.10, of individual PCs' PPA swing by making an RVM fit with a fixed $\alpha, \beta = 90^\circ, 1^\circ$ to solve for just the best offset value (ϕ_0, Ψ_0) . Fitting the RVM for just the offset can be done very accurately, in contrast to fitting for all four parameters. Then the vertical offset between the individual observations can be calculated and the PPAs are shifted accordingly. However, because there is no practical way to do so with *PSRCHIVE* package, the process was done by applying the Faraday correction at different centre frequencies, which will rotate the $U - Q$ plane accordingly, and change the PPA value by

$$\Delta\Psi = \left(\frac{c}{f}\right)^2 \cdot RM, \quad (5.1)$$

where $RM = 65.2 \text{ rad/m}^2$. Fig. 5.2 demonstrates a very good alignment of the PPA profiles.

Before moving to the process of making mode-separated profiles, it is interesting to discuss an important point: whether the *mode separation* or the *alignment* should be done to each observation first. Ideally, the horizontal and vertical offsets can be caused by various reasons, which however affect all parts of the profile and both modes equally. This means it is not advisable to do the mode separation to the observations first and then align each of the modes individually, i.e. with different offsets to each mode of the same observation. However, there is an

²<http://www.epta.eu.org/leap.html>

exception when the points of reference themselves, which are the pulse intensity profile and the PC's PPAs, dependent on the modes, which are what we are trying to find in the first place. Therefore, if one of the modes of any mode-switching pulsar is expected to have different, for example, component locations or PPA swings, it is better to separate the modes before making the alignment, to be able to clearly detect such differences. Nevertheless, we have investigated this point and compared the final aligned-and-mode-separated profiles from both scenarios, which are indistinguishable.

Our criteria for separating the modes by eye are: 1) the B-mode state of the pulsar is identified when the PC and the MP are simultaneously at their peak amplitude; 2) the Q mode is confidently identified by its unique 'hair-comb' modulation feature (e.g. Fig. 5.13), as well as the appearance of the IP and that the main pulse intensity is weaker. This will leave a 'transition zone', which is indeed excluded, of approximately a few 10-second sub-integrations, which is accounted to be on an average $\sim 20\%$ (including RFI mitigation) of the total 40 minutes' observing time from our dataset.

5.3 Results

This section is organised into the results from: 1) comparing the mode-separated pulse profiles at different frequencies; 2) single pulse behaviour; 3) long-term variation, in connection with the pulsar’s spin stability.

5.3.1 Mode-separated Pulse Profiles

Ten polarisation-calibrated observations are phase-and-PPA-aligned and mode-separated into the B-mode and Q-mode profiles, as shown in Fig. 5.3-5.6. The B-mode profiles (*top*) remain fairly consistent in terms of the B mode’s main features, such as the highly polarised PC and the OPM in the MP, while the Q-mode profiles (*middle* and *bottom*), having lower S/N due to the fact that it is a weaker mode (which is however also dependent on the fraction of mode duration), show a double-type shape of the MP and a narrow IP with a weak leading edge. Variations in relative components’ amplitude between these observations, spanning over four months, are discussed in Section 5.3.3.

After summing all data together, the resulting B- and Q-mode profiles (Fig. 5.7) are consistent with results of similar observing frequencies from FWM81 and GJK+94. In B mode, the pulsar shows the usual highly polarised PC, and the MP, which is composed of a core and a weak trailing component. In the Q mode, the unpolarised IP (Fig. 5.8) becomes more prominent and the MP changes its shape to a close double, in which the trailing component is at the same location as that of the B mode. Despite being confident that the separation was successful, it appears that there are signs of contamination between the separated profiles, i.e. a weak IP can be seen in the B-mode profile, and vice versa for the PC in the Q mode, which is consistent with the results by GJK+94, although their criterion for B-mode is whenever the PC is active.

Despite the drastic changes of the pulse profiles, the PPAs of the two modes are *roughly* identical (Fig. 5.7, *top*), which is also in agreement with FWM81’s 1720 MHz profile. The PC is strongly linearly polarised, which becomes rapidly depolarised at pulse phase $\sim 176^\circ$, coincidentally with increasing V . The PC’s PPAs show an RVM-like swing, while the MP’s PPAs break into three pieces (hereafter as component 1, 2 and 3), in which both the separation in the PPAs are $\sim 20^\circ$.

Looking at the PPAs more closely into the MP region to investigate how they

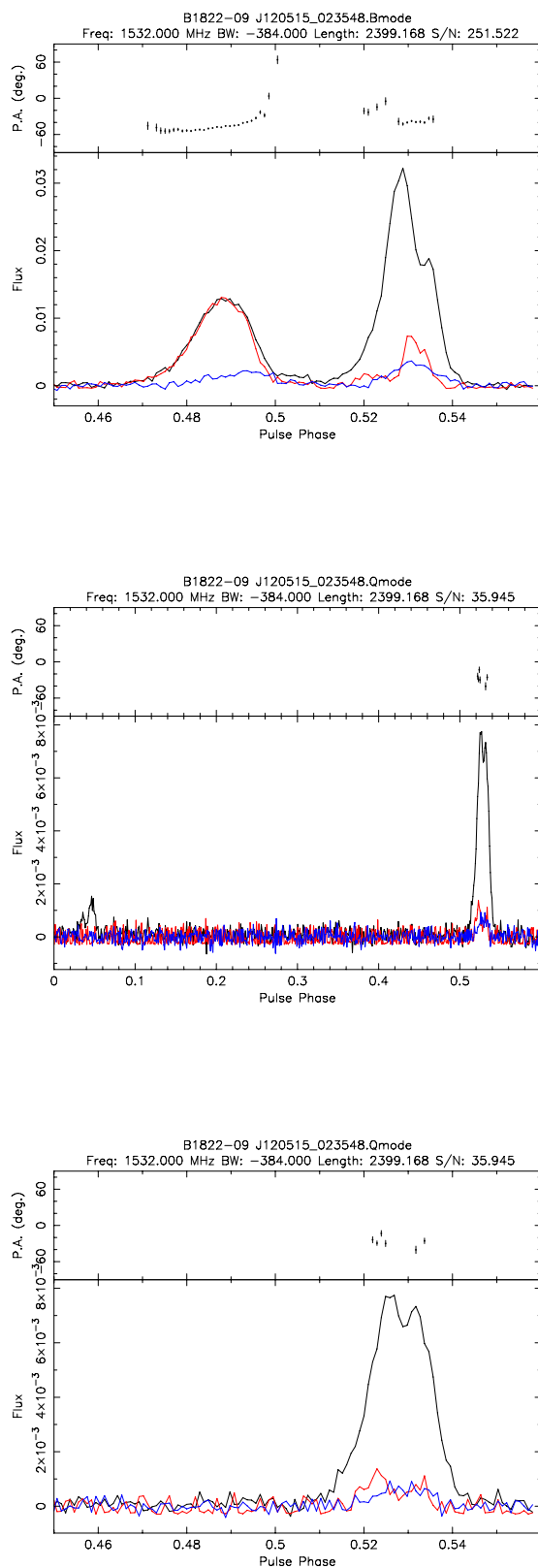


Figure 5.3: (top to bottom) The profiles of the B mode, Q mode and Q mode zoom-in, after the alignment process of observations *J120515-023548* (meaning the observation was on the 15th of May 2012 at 0235 hour and 48 seconds).

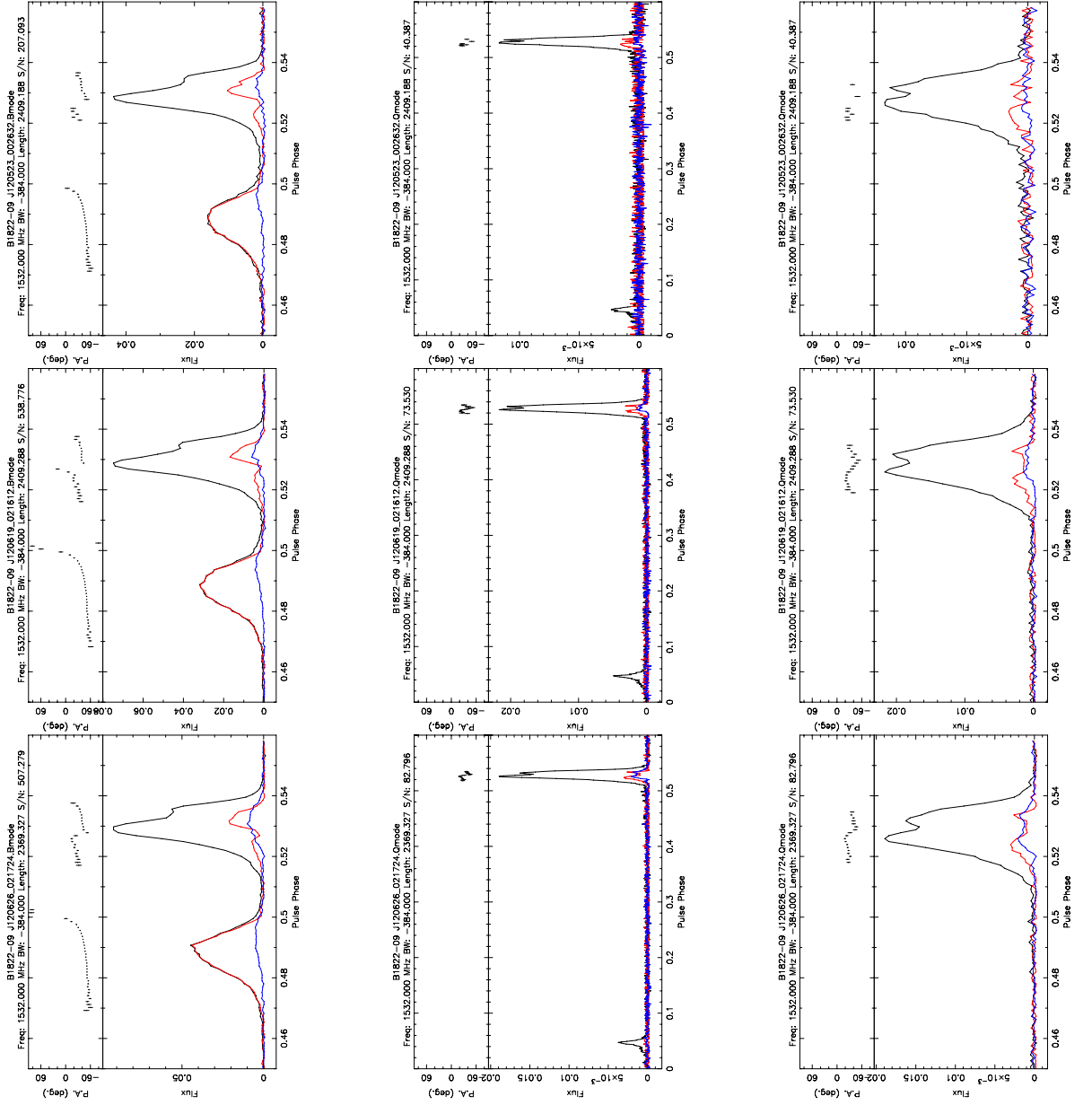


Figure 5.4: As in Fig. 5.3, for observations *J120523-002632*, *J120619-021612*, *J120626-021724*.

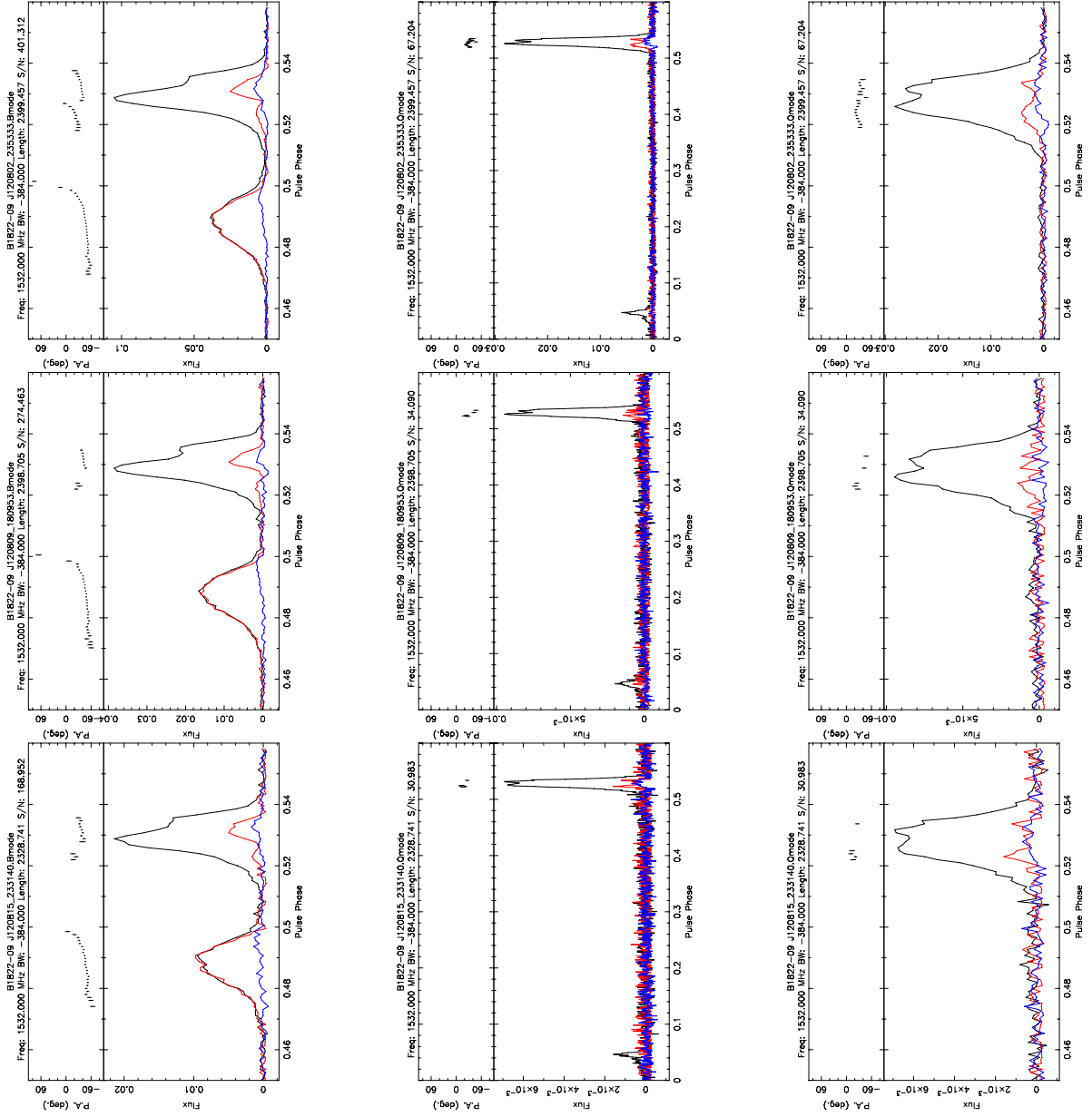


Figure 5.5: As in Fig. 5.3, for observations *J120802-235333*, *J120809-180953*, *J120815-233140*.

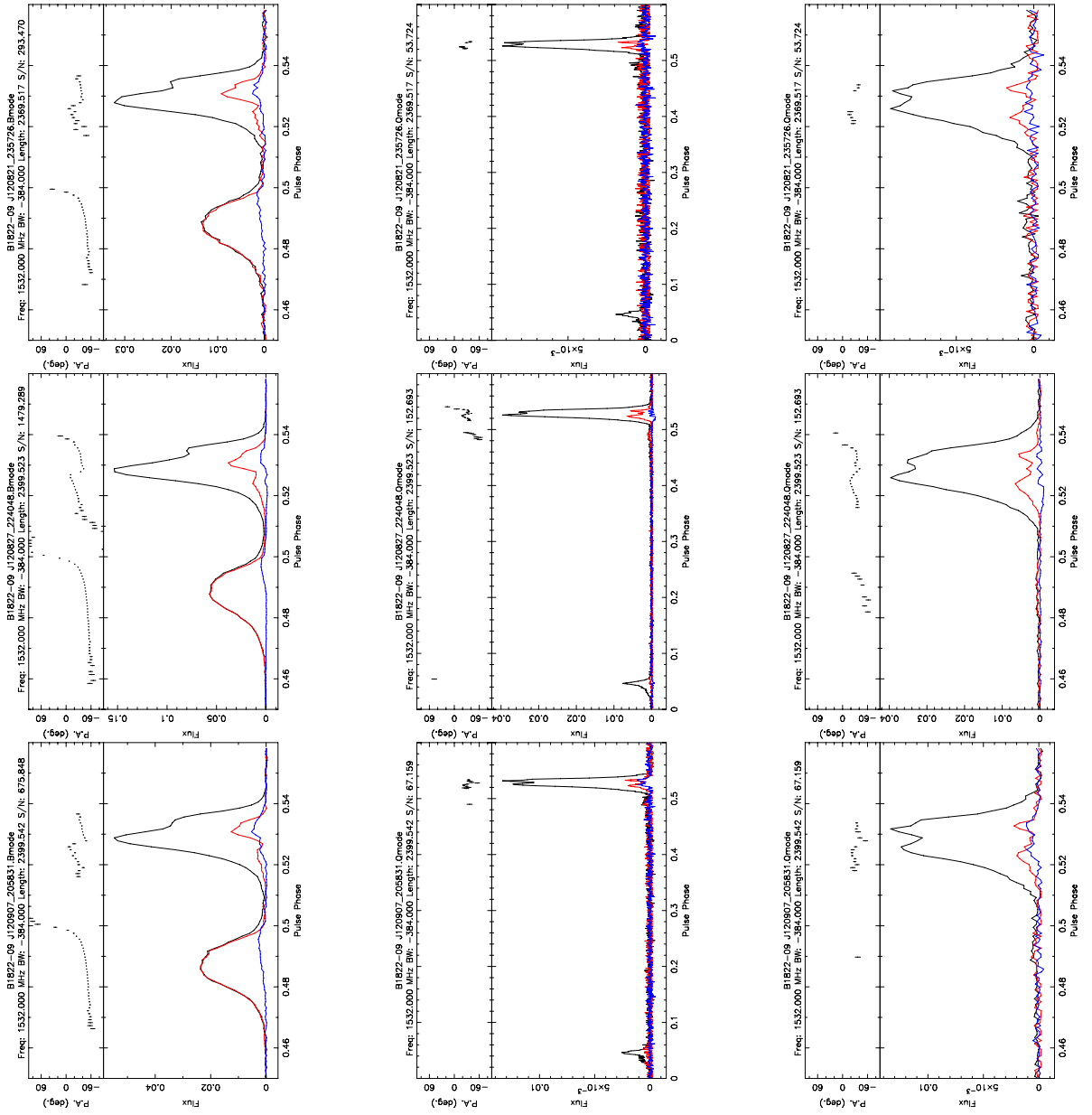


Figure 5.6: As in Fig. 5.3, for observations *J120821-235726*, *J120827-224048*, *J120907-205831*.

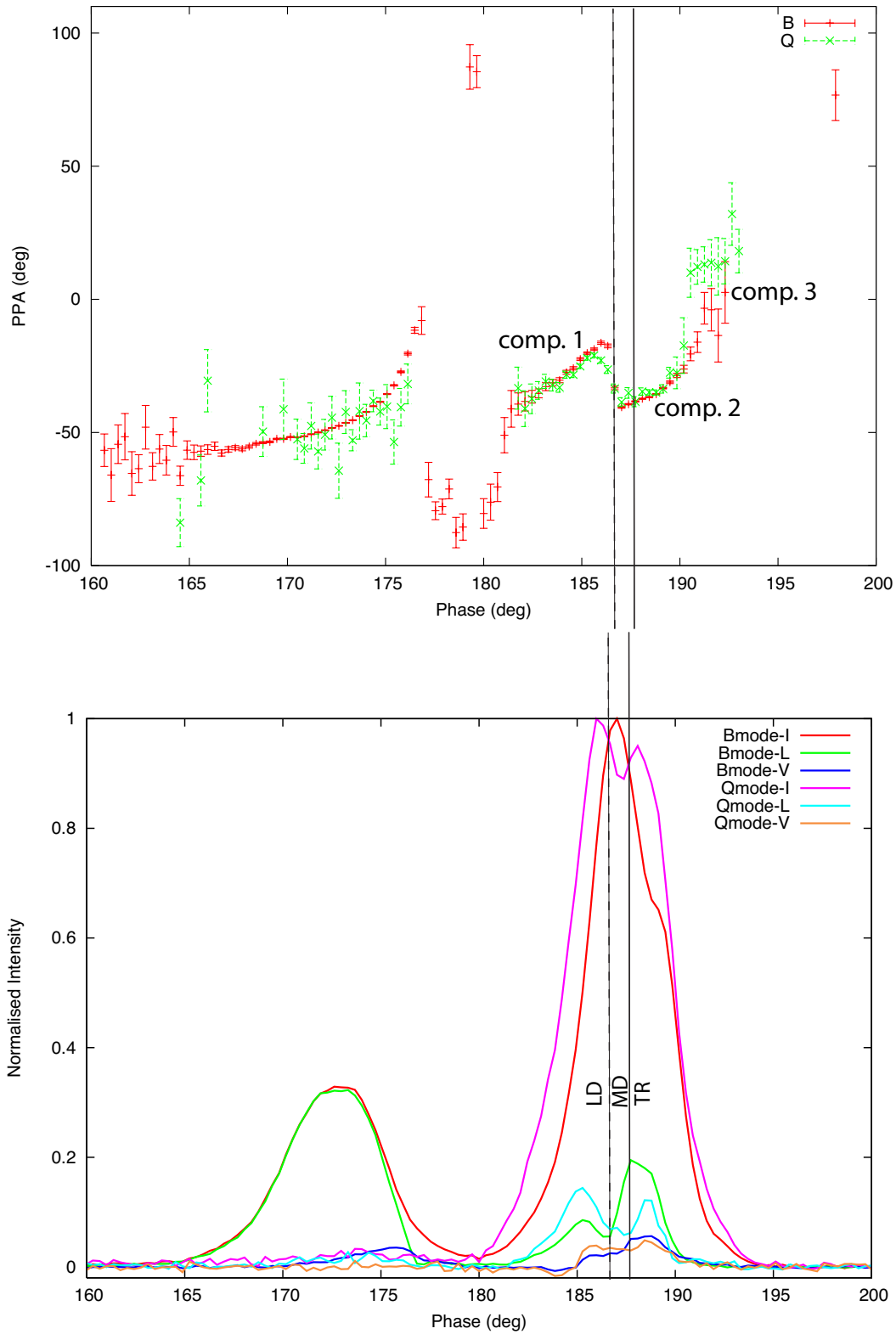


Figure 5.7: Overlay plots of the PPAs and MPs of the two modes. (*Top*) The PPAs of the B mode (*red*), Q mode (*green*). Each component of the PPAs will be referred to as component 1, 2 and 3, from left to right. (*Bottom*) The normalised intensity I , L , and V of both two modes. The two vertical lines denote the mid-point location between the leading (LD), the middle (MD) and the trailing (TR) components, which however are not necessarily related to the PPA components.

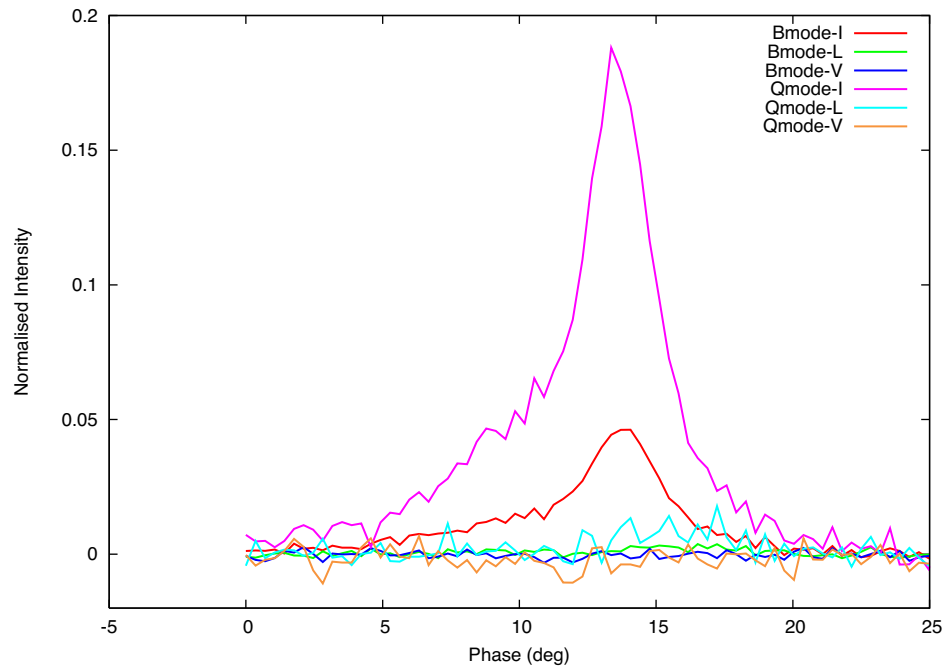


Figure 5.8: As in Fig. 5.7 (*bottom*), but for the IPs.

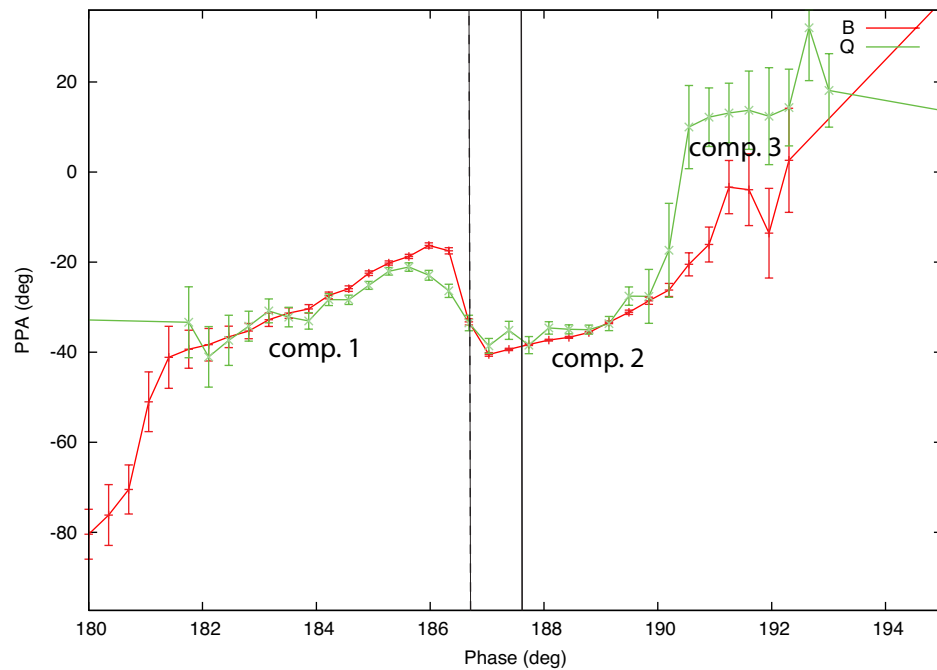


Figure 5.9: As in Fig. 5.7 (*top*), but magnified in the main pulse's region. It is to emphasise the very subtle difference in the PPAs.

relate to L and the sub-components of the MPs, the two vertical lines are drawn on the *bottom* plot accordingly to the mid-point between the leading (LD), middle (MD) and the trailing (TR) sub-components, in which they happen to be located close³ to the pulse locations where the decrease of L occurs for both modes. Including the same vertical lines on the *top* figure, the first overlapping (*dashed* line) appears to correspond to the main jump, and the remaining small deviation can still be seen at the second overlap (*solid* line).

Zooming closer, Fig. 5.9 shows a subtle-but-significant deviation of the Q-mode's PPA (*green*) from the B-mode's (*red*), that it starts off being noticeably below the B-mode's (between phase 184° and 186°) and then quickly departs for the jump at $\sim 186^\circ$, corresponding to the LD component of its MP, causing the jump to be more continuous than the B mode's. It then reunites the B-mode's again at the point where the L first decreases (*dashed*). In component 2 it appears to be slightly above, although less significant, in which the offset becomes more prominent at the transition to component 3. The two separations between components 1 and 2, and 2 and 3 similarly appear to be $\sim 20^\circ$. These findings shall be proved to be important clues to understanding this pulsar's emission beam, in later discussions.

For multi-frequency analysis, apart from published profiles by FWM81, GJK+94, and BMR10, we are kindly provided with another two average profiles of PSR B1822–09 at 325 MHz and 600 MHz, observed with the Giant Metrewave Radio Telescope (GMTR)⁴ and the Parkes Telescope⁵, respectively (Johnston, S. *private communication*). Note that they are not mode-separated profiles.

First, we look at the published results at 325 MHz by BMR10 (Fig. 5.10). Comparing BMR10's B- and Q-mode profiles (their figure 8) with our results, it is astonishing to find that the pulse shapes of the MPs appear as if they are being reversed between 1532 and 325 MHz, i.e. the B mode's MP at 1532 MHz resembles the Q mode's at 325 MHz, and vice versa, while the rest of the mode-depending characteristics remarkably remain the same. And the main OPM jump in the profiles also appears to be at the same location, which is in between the leading and the middle components, for both modes *and* both frequencies.

The overall trend of the PPA swings at 325 MHz is consistent between the modes and with the 1532 MHz profiles. Assuming that the PPA jump at 325 MHz

³with pulse phase resolution at $360^\circ/1024 \sim 0.3516^\circ$.

⁴<http://gmrt.ncra.tifr.res.in/>

⁵<http://www.parkes.atnf.csiro.au/>

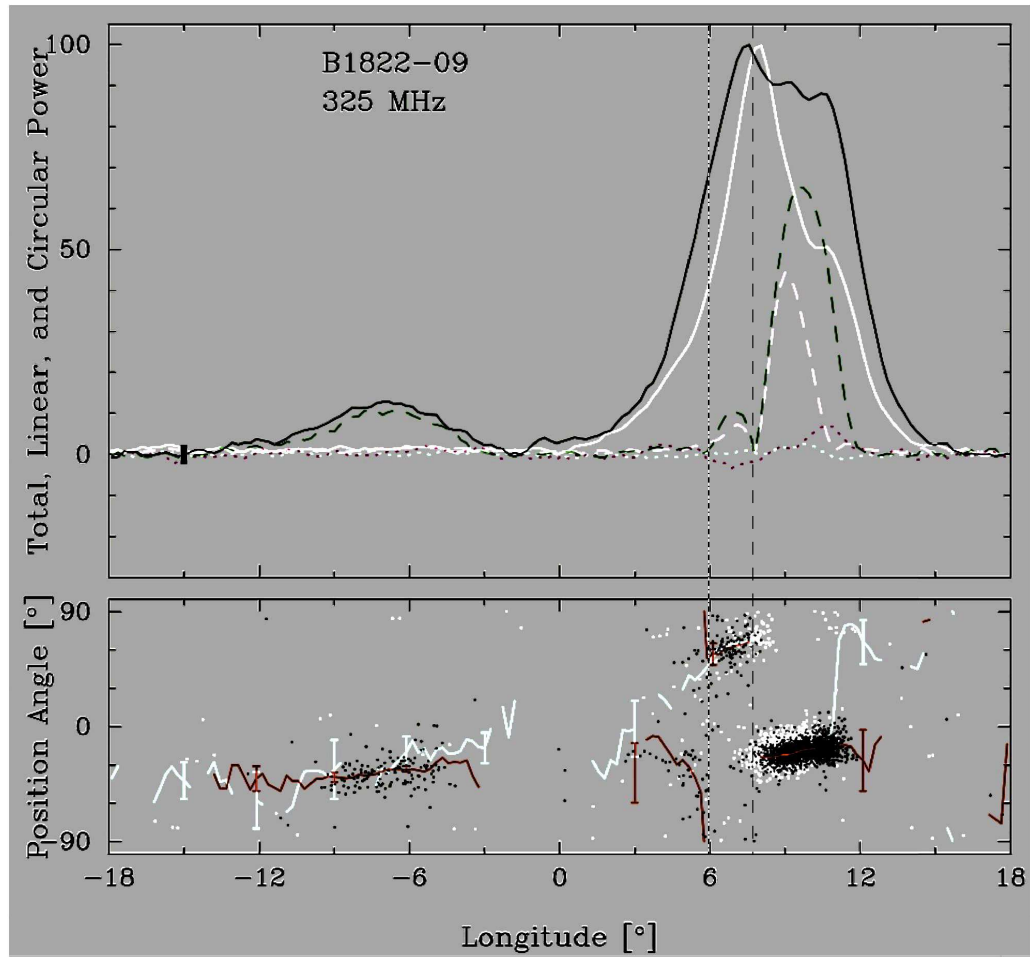


Figure 5.10: Adapted from BMR10’s figure 8, this overlay diagram displays a few delicate differences and similarities between the modes. In the *top* panel, the pulse intensity I , L and V of the B mode are denoted with the *black*, *dashed-green* and *dotted-red* lines, where those of the Q mode the lines are *white*. In the *bottom* panel, the *red* line and *black* dots correspond to the average and individual PPAs of the B mode, and *white* for the Q mode. The *dotted* and the *dashed* vertical lines reference locations of the leading OPM and the main OPM, respectively.

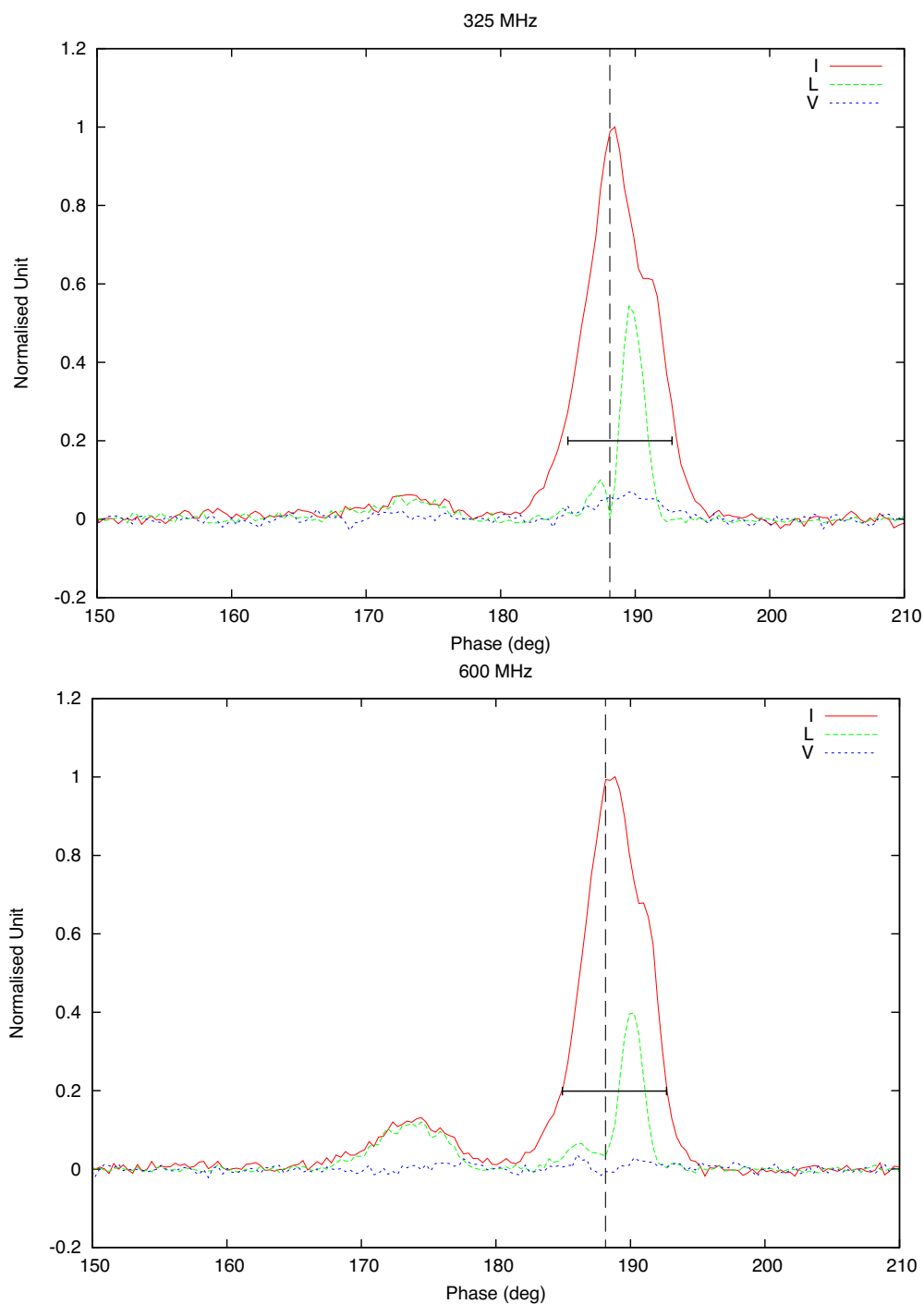


Figure 5.11: The averaged profiles of the *GMRT* observation (325 MHz, *top*) and the *Parkes* observation (600 MHz, *bottom*), which are phase-aligned according to the OPM jumps, indicated by the vertical lines. The horizontal line in the *top* plot, which has the same width of that in the *bottom* plot, is drawn for pulse-width comparison.

is the same jump at 1532 MHz, components 1, 2 and 3 at 325 MHz are recognised at pulse phase $\sim 7^\circ$, $\sim 10^\circ$ and $\sim 12^\circ$, respectively. It is apparent that the PPA jump at the 325 MHz has a larger separation of $\sim 90^\circ$, which is the expected value for a genuine OPM, while the jump at 1532 MHz is only $\sim 20^\circ$. The fact that components 2 of both frequencies remain fixed relative to the PC's PPAs indicates that it is indeed component 1 which appears to shift with frequencies.

To be certain, Fig. 5.10 shows the overlay of the B- and Q-mode profiles adapted from BMR10's figure 8, showing the pulse intensity (*black* and *white* for the B and Q mode) and L (*green* and *white* for the B and Q mode) on the *top* panel, and the average PPA swings and individual PPA points (*black-red* for the B mode and *white* for the Q mode), on the *bottom* panel. It is now apparent that the centre of the Q-mode MP is not aligned with the core component of the B-mode MP. Interestingly, the OPM jump, which is at the same phase in both modes, takes place at the overlap point between the LD and the MD (*dashed* vertical line), similarly at 1532 MHz. The signature of L appears to be simple, in which it is separated into the low- L and the high- L parts by the OPM jump. There is also a trace of another two OPM jumps, located at phase $\sim 5^\circ$ and $\sim 11^\circ$, where the latter corresponds to the split between our components 2 and 3.

The differences in the PPAs of the B and Q mode are also apparent and are consistent to those at 1532 MHz profiles. In the B mode the OPM jump is more instantaneous than that of the Q mode, as there is more overlapping of the *white* dots at pulse longitude of the vertical *dashed* line. Also, although not so strongly, component 3 of the Q mode is located at higher PPA values than that of the B mode, at phase $\sim 12^\circ$.

We now turn our attention to study how the relative amplitudes between the MP, PC and IP of the two modes behave at different frequencies. Firstly, we shall recall Fig. 5.7 again to introduce some nomenclature. The core-shoulder-type of the B-mode MP is defined to consist of the MD_B and the TR_B and that the double-type of the Q-mode MP is defined to comprise the LD_Q and the TR_Q .

Tab. 5.1 contains the peak amplitude of the PC and IP measured relative to the pulse peak (A_{PC} and A_{IP}), of each mode, where a_{MP-B}/a_{MP-Q} is the relative pulse peak between the B- and Q-mode profiles. It appears that the value A_{PC} of the B mode (A_{PC-B}) increases with frequency, and the value A_{IP} of the Q mode (A_{IP-Q}) decreases with frequency. These results are consistent with the work of

GJK+94 (their figure 12), that the PC becomes brighter with frequency and the opposite for the IP. However, note that their multi-frequency analysis was done on average, i.e. not mode-separated, profiles. Evidence of contamination between the PC and the IP across their associated modes is also present, in Fig. 5.7 and GJK+94's work. Recently, Latham et al. (2012) (hereafter LMR12) conducted an 8-hour observation with the GMRT and found that there are indeed occasions where both the IP and PC are present simultaneously. Nevertheless, this analysis is based on a rather rough simple reading with a scale ruler for measurements of BMR10, GJK+94's and FWM81, so a flux density measurement will be preferable as it is less dependent on the noise level, and also better at representing the pulse energy.

Table 5.1: The relative amplitude of the PC and IP in both modes, which is normalised to its associated MP's peak. a_{MP-B}/a_{MP-Q} is the amplitude ratio of the MPs' peak between the B and Q mode. The symbols - and ~ 0 mean not available for measurement and available but no detection, respectively. \sim indicates a noise-dominated detection. And \dagger denotes the non-mode-separated profiles' values.

A_{PC-B}	A_{IP-B}	A_{PC-Q}	A_{IP-Q}	a_{MP-B}/a_{MP-Q}	Ref.	f (MHz)
0.12	-	~ 0	-	-	BMR10	325
0.35	0.02	~ 0.03	0.17	3.5	GJK+94	1408
0.33	0.04	~ 0.03	0.19	2.4	Fig. 5.7	1532
0.35	-	~ 0.01	-	1.7	FWM81	1620
0.40	~ 0.1	~ 0.01	~ 0.12	5.6	GJK+94	4750
$\sim 0.06^\dagger$	-	$\sim 0.06^\dagger$	-	-	GMRT	325
0.11^\dagger	-	0.11^\dagger	-	-	Parkes	600
$\sim 0.4^\dagger$	-	$\sim 0.4^\dagger$	-	-	FWM81	2650

The 325-MHz GMRT and the 600-MHz Parkes profiles are aligned with respect to their central OPM and their component 2, as shown in Fig. 5.11 and 5.12. It seems that the Parkes profile (600 MHz) holds the key in the transition of the MPs between the 325 MHz and 1532 MHz. However, assumptions are first made in order to determine the B-mode proportion of the profile, before the MP's shape can be inferred through pulse width measurements. Assuming that A_{PC-Q} is negligible, the B-mode proportion for an average profile can be approximated

from the amplitude of the PC relative to MP (A_{PC} ⁶) as

$$\frac{T_B}{T_{\text{total}}} \approx \frac{A_{PC}}{A_{PC-B}}, \quad (5.2)$$

where T_B/T_{total} is the fraction of B-mode time and A_{PC-B} is the relative amplitude of a B-mode template. For the GMRT profile (Fig. 5.11, *top*), A_{PC} is measured to be ~ 0.06 , while A_{PC-B} is ~ 0.12 , given by BMR10's B-mode profile. The B-mode time for the GMRT observation is then inferred to be $\sim 50\%$. Due to the lack of a B-mode template at 600 MHz, the A_{PC-B} is taken from the 325-MHz template; the A_{PC} has a value of ~ 0.11 , indicating as an almost total dominance of the B mode during the observation.

Table 5.2: Similar amplitude measurements as in Tab.5.1: the sub-components and the linear intensity (L) are measured relative to their own modal MP's peak. The symbol * denotes that the L is measured from FWM81's 1720 MHz average profile. † emphasises the MP's shapes reversal at 325 MHz between the modes.

LD_Q or MD_B		TR_{BorQ}		Ref.	f (MHz)
$A_B(L_B)$	$A_Q(L_Q)$	$A_B(L_B)$	$A_Q(L_Q)$		
1.00 (0.10)	1.00 (0.08)	<u>0.88</u> (0.65)	0.51 (0.45)	BMR10†	325
1.00 (-)	0.93 (-)	0.62 (-)	<u>1.00</u> (-)	GJK+94	1408
1.00 (0.09)	1.00 (0.16)	0.65 (0.20)	<u>0.95</u> (0.12)	Fig. 5.7	1532
1.00 (0.08*)	1.00 (0.08*)	0.55 (0.13*)	<u>0.73</u> (0.13*)	FWM81	1620
1.00 (-)	1.00 (-)	0.30 (-)	<u>0.55</u> (-)	GJK+94	4750
1.00 (0.11)		0.61 (0.55)		GMRT	325
1.00 (0.07)		0.68 (0.40)		Parkes	600
1.00 (≤ 0.05)		~ 0.7 (~ 0.1)		FWM81	2650

We now turn our attention to study the relative amplitudes (A) and the degree of linear polarisation (L) of individual sub-components of the MP, i.e. LD, MD and TR, of both modes at different frequencies (Tab. 5.2). For both A and L , the values are measured relative to the MP's peak. Furthermore, we emphasise that the profiles are swapped at 325 MHz and higher frequencies, such that at the higher frequencies the Q mode shows a double MP, while at 325 MHz the B mode shows the double-type profile, and the opposite for the other profile.

The TR component of the double type (LD-TR), which includes the $TR_B^{325\text{MHz}}$

⁶Emphasise that A_{PC} is of an average profile, while A_{PC-B} , A_{IP-B} , A_{PC-Q} and A_{IP-Q} are of mode-separated profiles.

and the TR_Q at other frequencies, appears to have its relative amplitude decreasing with frequency (*underlined* in Tab. 5.2) as 0.88, 0.88, 1.00, 0.95, 0.73, 0.55 from 325 MHz to 4750 MHz. For the MD-TR type, a somewhat different relation is present as 0.51, 0.62, 0.65, 0.55, 0.30 from 325 MHz to 4750 MHz (*bold*). The degree of linear polarisation (L) is very high at 325 MHz before quickly decreasing to $\leq 20\%$ at frequencies ≥ 1500 MHz for both TR_B and TR_Q . The measured A and L for the 600MHz profile, which is believed to be a pure B-mode observation, is also consistent with these trends.

For the GMRT profile, the measured A of 0.61 is much closer to $A_Q^{325MHz} = 0.51$ than $A_B^{325MHz} = 0.88$, which seems to contradict our previous conclusion that this observation is dominated by the B mode. Or, in other words, it is suspicious that the characteristic shape of the MP does not resemble the B-mode template (MD-TR), but rather is Q-mode-like (LD-TR), despite its W being wider. This raises a few concerns about our assumptions for Eq. 5.2, such as whether the profile reversal at 325 MHz is permanent, and whether A_{PC} is time-dependent, which will be addressed in subsection 5.3.3.

For the MD_B or LD_Q components, it seems that in general they are the brightest components for each of their respective modes, except for the $LD_Q^{1408MHz}$ in which the amplitude is slightly weaker. Including the GMRT and Parkes profiles, their degree of L is approximately 10% on average, which is also less than L of the TR.

Comparing L of each component-type and also between the modes from the 325 MHz and 1532 MHz profiles, which only have mode-separated L available, we found the following relations. By considering the difference in the ‘profile shapes’, it appears that the leading component (LD) of the double-type profile (LD-TR) (which are the B-mode LD at 325 MHz and the Q-mode LD at 1532 MHz) will have a larger L than that of the MD of the core-shoulder (MD-TR) type (which are the Q-mode MD at 325 MHz and the B-mode MD at 1532 MHz), regardless of the emission modes. On the other hand, if we consider the ‘emission modes’, it appears that the TR component of the B-mode profile will have a larger L than that of the Q-mode profile.

As pointed out earlier about the difference in component 1 between BMR10’s 325 MHz and the 1532 MHz profiles, Fig. 5.12 includes the PPAs from the GMRT, the Parkes, and our profiles. The PPAs of the GMRT observation, which is also at 325 MHz, are consistent with BMR10’s templates in that their component

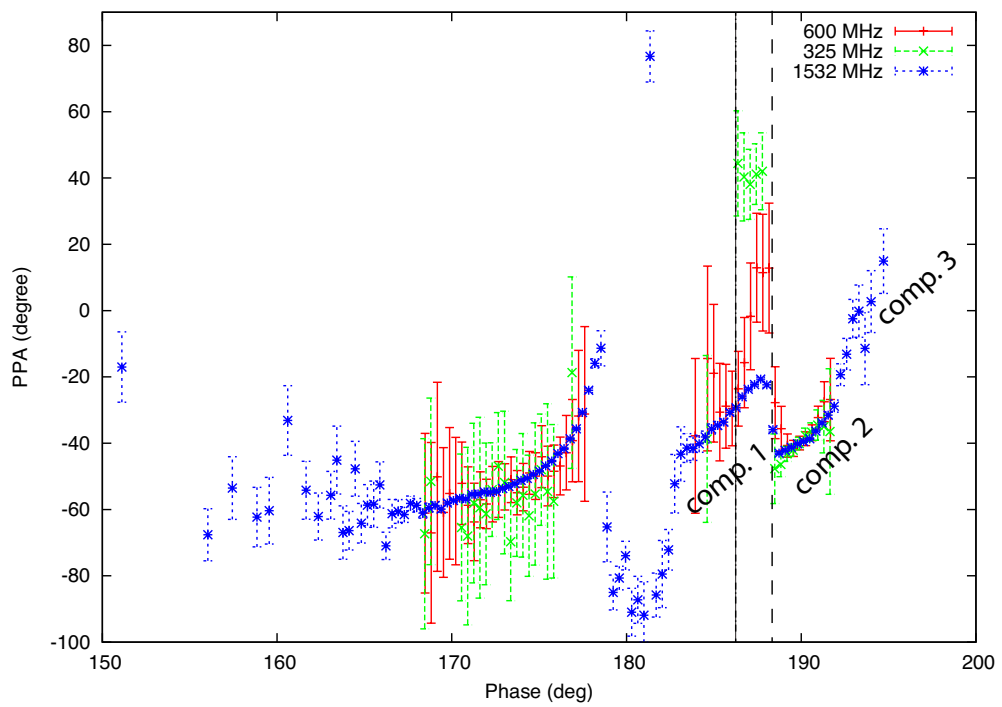


Figure 5.12: The PPA swings of the Parkes (*red*), the *GMRT* (*green*) and the 1532 MHz (*blue*). The profiles are aligned with respect to the main OPM (*dashed* vertical line), while the *dashed-dotted* line represents the leading OPM of the 325 MHz PPAs.

1 values are similarly only half of those at 1532 MHz, which is due to another OPM located a few degrees prior, indicated by the vertical *dashed-dotted* line. The 600 MHz component 1 is overlapping with the 1532 MHz at the early part before diverging to be in between the 325 and 1532 MHz. Due to the lack of data quality, it is not yet conclusive if the pulse phase in between the vertical lines is the only region affected by this frequency dependence.

Despite being limited in between 325 and 1532 MHz, or including 4750 MHz in some cases, the findings in this subsection strongly suggest that the pulse intensity and the polarisation properties react to the mode-switching mechanisms differently, depending on observing frequency.

5.3.2 Single-pulse Analysis

In this subsection, we investigate further the pulse-to-pulse characteristics of the two modes, which allows us to study the sub-pulse modulation of the Q mode, the flux variation in the sub-components, and the PPA of individual pulses. However, first we demonstrate the mode switching behaviour in a series of the 10-second sub-integrations from one of our 40-minute observations (Fig. 5.13 *top*), showing five sequences of each mode. Interestingly, comparing to GJK+94’s finding that the MP-PC separation doesn’t evolve with frequency, the PC appears to also drift over time to an earlier pulse phase, as shown in Fig. 5.13 at the beginning of the first and last occasions. At the end of the B mode, the PC seems to shut off rather rapidly and, occasionally, simultaneously to the MD component, while, however, sometimes delayed, coinciding with the TR instead. For the Q mode, in which the IP can be barely seen to be anti-correlated with the PC’s occurrences, we zoom in closely to the first Q-mode appearance (*bottom*) which demonstrates the $\sim 46P$ ‘hair-comb’ modulation feature in the MP (GJK+94; BMR10), which will be studied in detail with the single-pulse dataset later.

The *ROACH* dataset, which was piggybacking on the same observation (Fig. 5.13) and contains ~ 3900 pulses, was polarisation-calibrated with the *pac* method using the same CAL session, in which however the resulting polarisations seem to have a larger frequency dependence relative to the DFB results. Examples of individual pulses are shown in Fig. 5.14 and Fig. 5.15 for the B and Q mode, respectively. Although the y-axis is scaled differently for each pulse, there seems to be no clear distinction between pulses of the B and Q modes, except the presence of the PC. There is also a likely correlation that the MD pulses are more

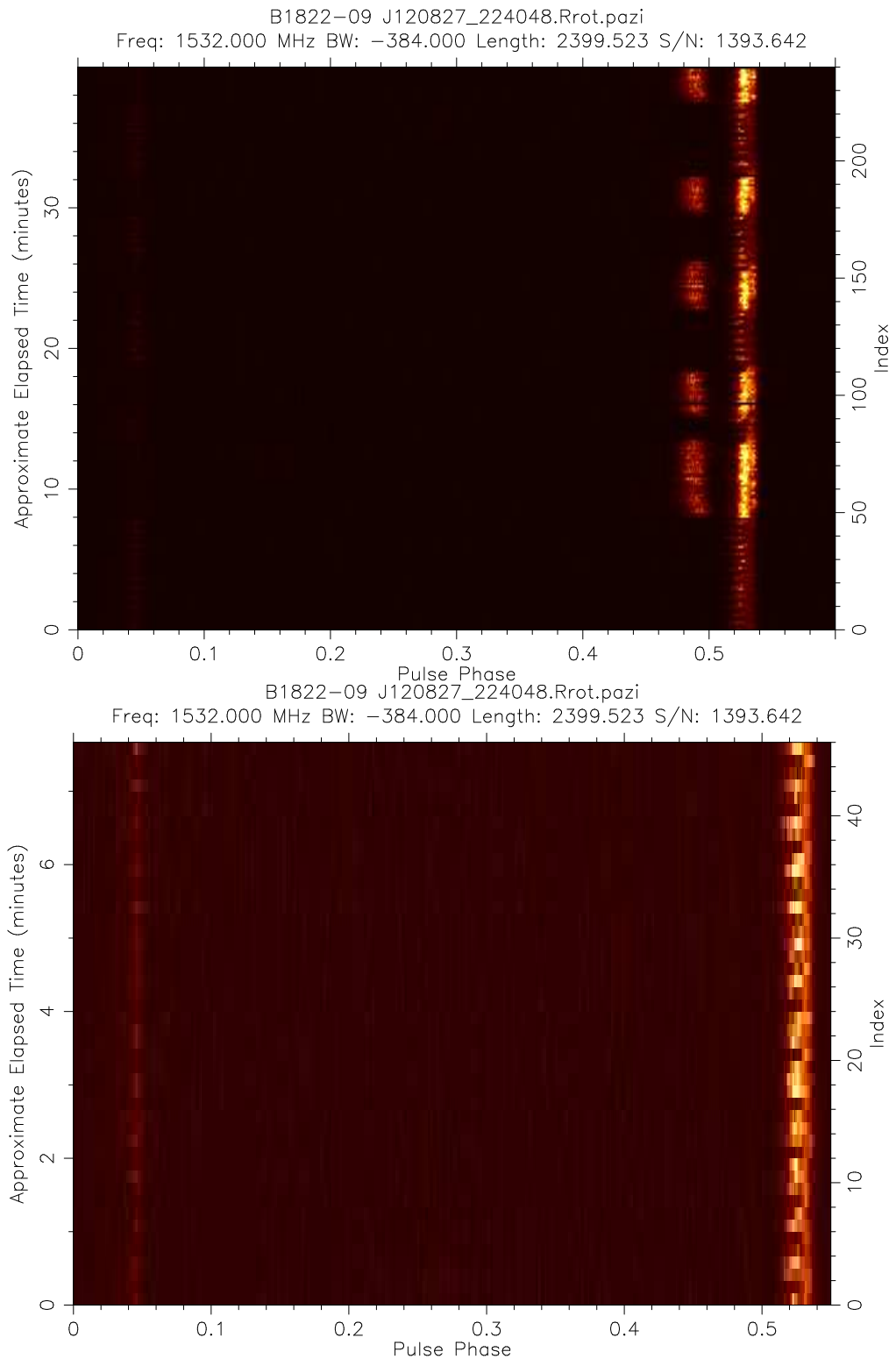


Figure 5.13: (top) A plot showing a series of 10-second sub-integrations of the forty-minute observation (*J120827-224048*). (bottom) A zoom-in to the first 8 minutes, demonstrating the ‘comb-like’ feature and the IP of the Q mode.

likely to be brighter than others, as indicated with * (which can be seen from the noise level). Therefore, we are led to suspect that it is not correct to believe that the two modes are completely different in emission character as discussed in the last subsection, but rather have a probability of certain kinds of pulses being drawn from the parent distribution. Pulses of the PC are shown to be strongly polarised, however, *not all* of the pulses with the PC is as spiky (or ‘rain’-like) as claimed by GJK+94 and BMR10, (indicated with †), which could be due to the limitation in our sampling time ($0.769 \text{ s}/1024 \text{ bins} = 750 \mu\text{s}$). Later we will investigate further the flux distribution of individual sub-components, but first we study the acclaimed sub-pulse periodicity.

After being mode-separated, the same *ROACH* observation was used to calculate phase-resolved fluctuation spectra (PFS), using a method described in Weltevrede et al. (2012), employing a 512-point FFT, as shown in Fig. 5.16 and Fig 5.17 for the Q and B mode, respectively. The Q-mode PFS (Fig. 5.16, *top*) shows a periodicity at around $1/0.0216 = 46.2P$, while the peak frequency at 0.002 cycles/period corresponds to fluctuation power caused by mode switches. This $46.2P$ modulation is only active on the leading part of the MP, or the LD component, and was seen as the ‘hair-comb’ feature. There appear to be surrounding sidebands which are measured from 0.0197 to 0.0245 cycles/period, reflecting a range of approximately $\pm 5P$ around $46.2P$, in which the separation seems to be larger than the spectral resolution. Nevertheless, there is no reason why this modulation has to be at a precise frequency. Such periodicity and the sidebands can also be found for the IP (*bottom*), although with a weaker amplitude by around a factor of 2. There seems to be also another modulation in both the MP and IP at $\sim 1/0.062 = 16P$.

For the B-mode PFS (Fig 5.17, *top*), there is no strong modulation found on the MP nor the PC, however, the zoom-in plot (*bottom*) shows a possible indication of the $11P$ periodicity claimed by FWM81 and GJK+94 at the frequency ~ 0.09 cycles/period. Also, the power seems to split into two locations which correspond to the locations of the MD and the TR components, indicated by the vertical arrows. This indeed demonstrates that the MP is composed of two pulse windows for the MD and the TR, which is therefore reflected as a core-shoulder shape in the average profile.

Now we investigate further the peak’s location, the flux distribution and the polarisation of individual pulses.

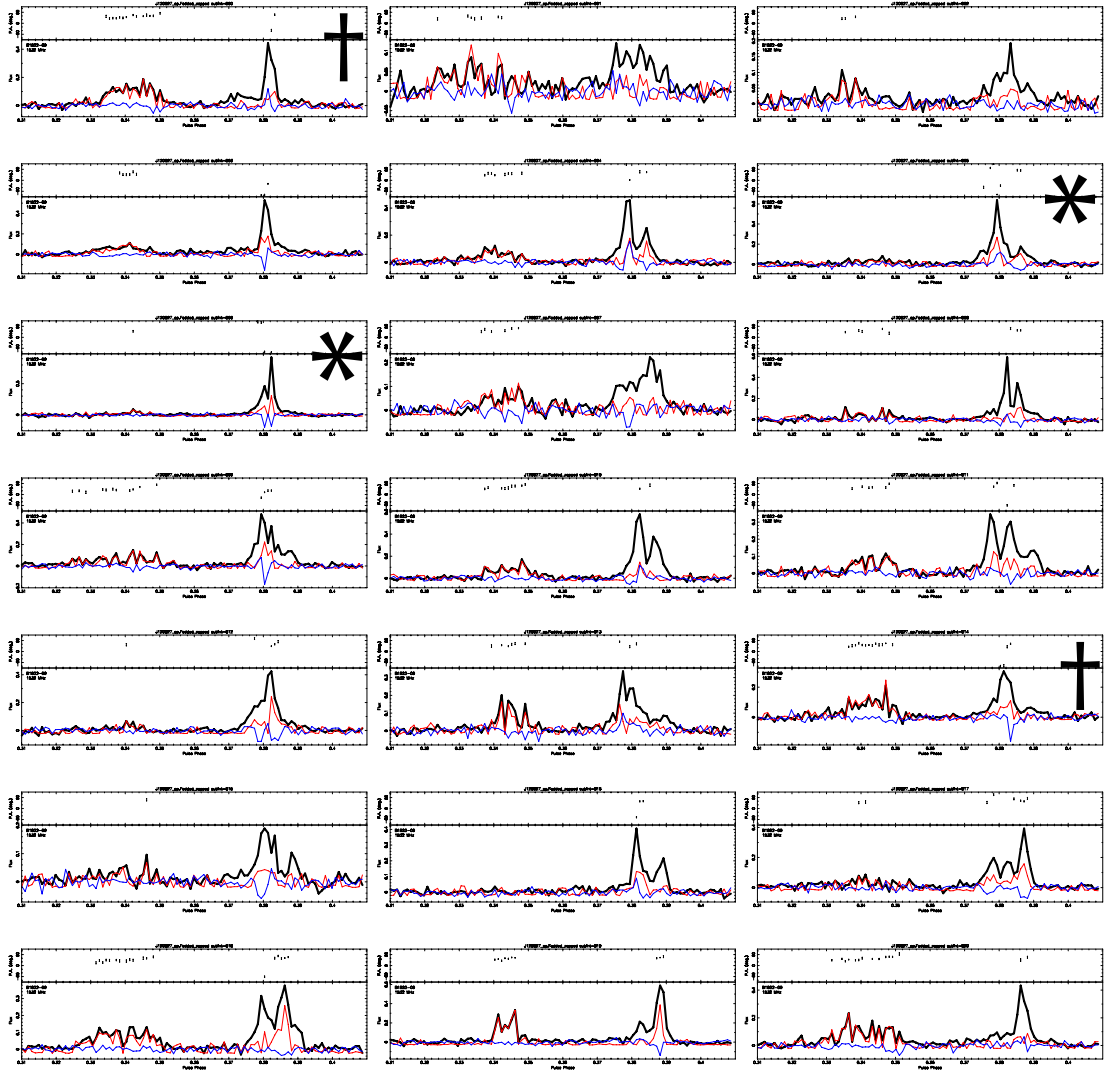


Figure 5.14: (*left to right, top to bottom*) An example of pulse sequence during the B mode from pulse number 800 to 820, from the same observation. The symbol * indicates MD-dominated pulses which seem to be brighter (from the noise level) than other types. The symbol † indicates pulses with the PC which shows no micro-structure; however not true for all pulses with the PC. See text for more description.

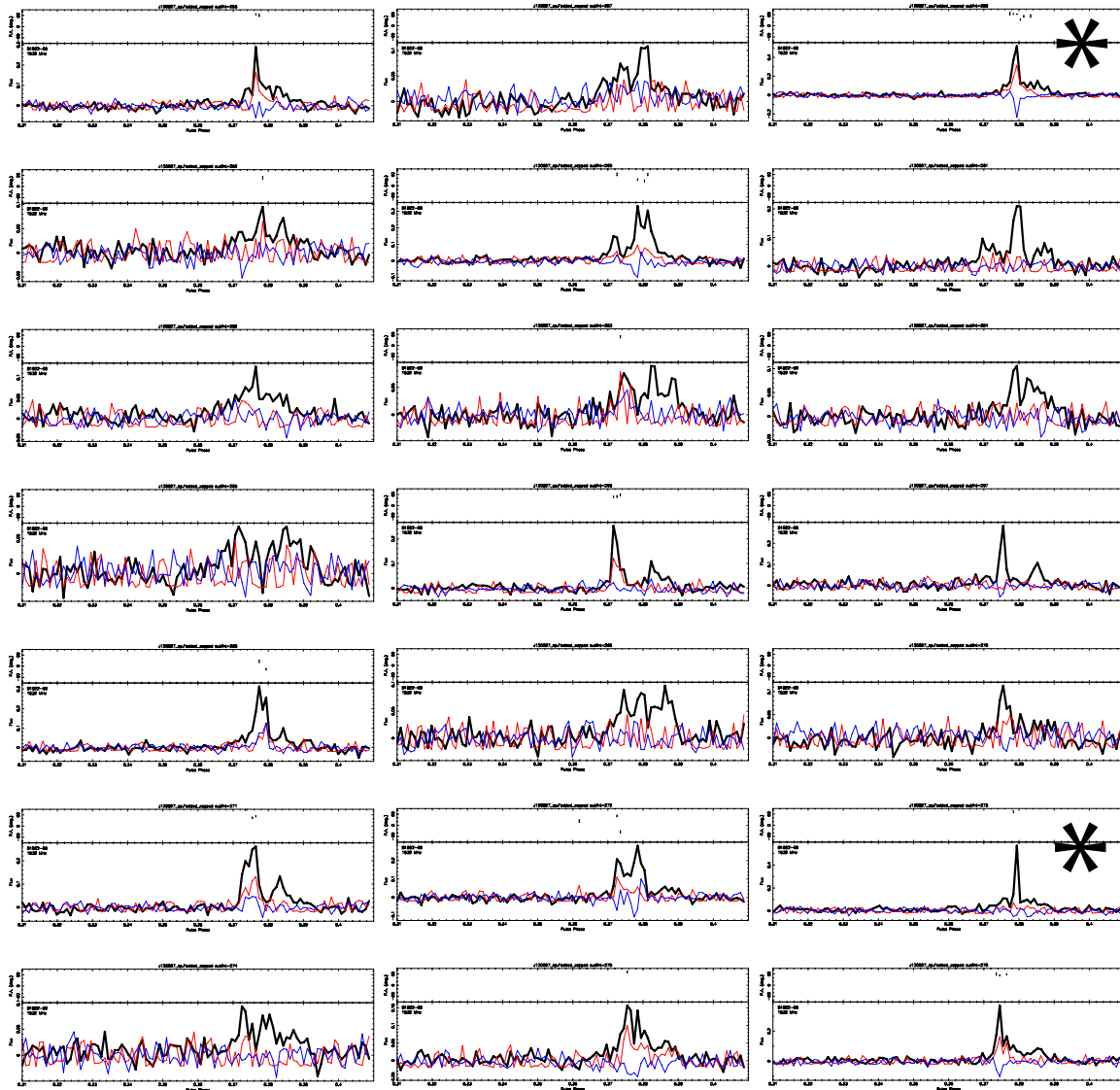


Figure 5.15: (*left to right, top to bottom*) An example of pulse sequence during the Q mode from pulse number 249 to 269, from the same observation. See text for more description.

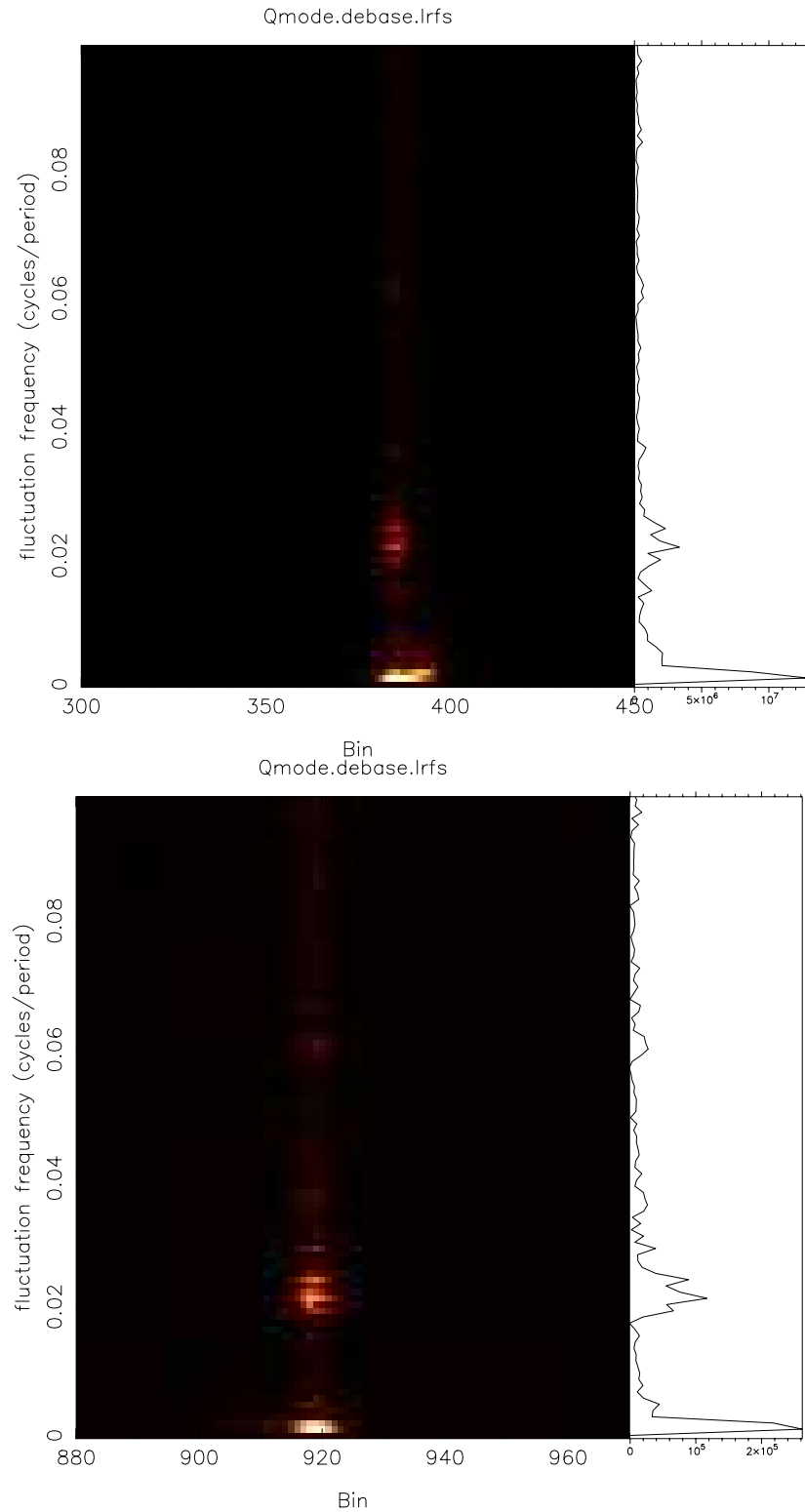


Figure 5.16: Phase-resolved fluctuation spectrum of the Q mode's MP (*top*) and the IP (*bottom*). Amplitude of the spectrum integrated over pulse phase is shown on the *right* panel.

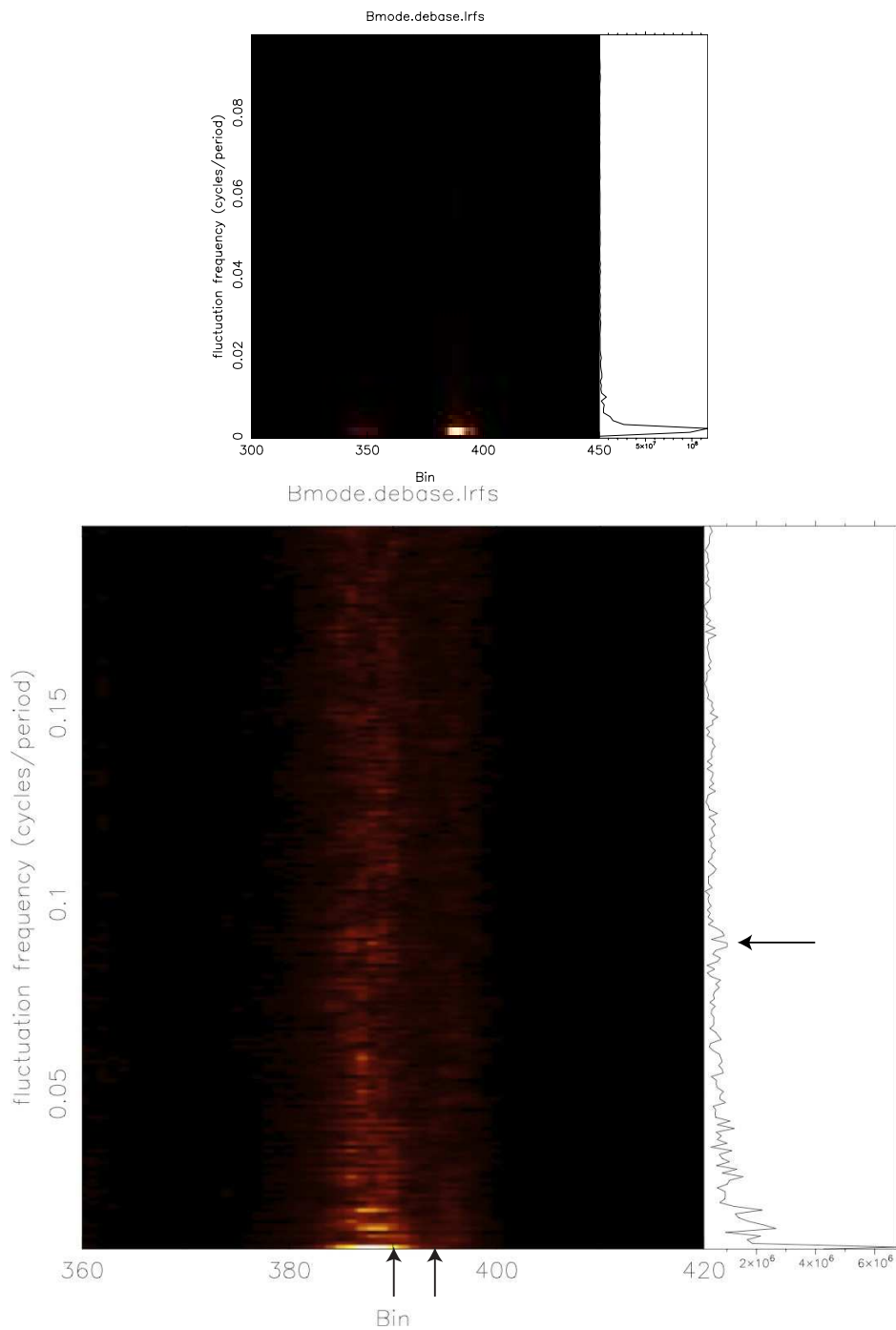


Figure 5.17: Phase-resolved fluctuation spectrum of the B mode's MP (*top*). The *bottom* plot is the zoom-in and contrast-adjusted version of the MP region, to demonstrate a difference in character between the MD and the TR component, denoted by the two *up* arrows. The *left* arrows signify a sign of what could have been identified as the $11P$, claimed by FWM81, at frequency of ~ 0.09 .

The location of individual pulse peaks is measured from the same *ROACH* dataset and plotted in Fig. 5.18, where the *bottom* plot shows a zoom-in and contrast-tweaked version. For each pulse, the location of the strongest peak was recorded. More significant than the off-pulse noises, there seems to be $\sim 1\%$ of the time where emission at the IP location is the strongest (*green* line). The modulation behaviour seen from the DFB data (Fig. 5.13) is now even more evident. The pattern from the Q-mode modulation is strikingly apparent on the LD and the TR part of the MP. The pattern of the TR part cannot be observed in the PFS plot, indicating that the modulation power must be low. The drift of the PC is also visible at pulse number ~ 700 . The delay of the TR component during the B mode can also be seen at pulses ~ 1100 and ~ 1500 , where the TR becomes the strongest component after the MD's emission has ceased. This delay at both locations is approximated to be around $40P$, which is interestingly close to the measured $46.2P$ modulation of the Q-mode MP-IP. Interestingly, the TR during the B mode appears to be rather distinguishable from the MD pulses, seen as a horizontal band from pulse number 600 to 1000.

Considering the pattern in Fig. 5.18 (*bottom*), the pulses are categorised into the LD, the MD and the TR groups, in which the three thick markers on the y-axis indicate the selective ranges. Individual average profiles are shown on the *top* panels of Fig. 5.19, and the overlay plot on the *bottom* panels. In general, the pulse shapes are as expected in that the LD possesses very little of the PC, while the MD and TR promptly show the PC, however, note that this TR profile is a combination of the TR_B and TR_Q , which might have different characteristics. There seems to be no significant difference in the PPA swings.

The measured peak flux (A) and the flux density integrated over pulse longitude (S) are shown in Tab. 5.3. Note that S is *not* the flux density of individual components, but rather of the whole MP window. It appears that the pulses in which the LD have larger values of A and S than those of the MD and TR by approximately a factor of two ($\bar{A}_{mp}6.41$ versus 3.23 and 3.51 and $\bar{S}_{mp}70.1$ versus 30.9 and 37.5). For the MD and TR components, the values seem to be very similar for the PC and IP ($\bar{A}, \bar{S}_{PC/mp}$ and $\bar{A}, \bar{S}_{IP/mp}$). However, no significant conclusion shall be made from these numbers, especially for the MD and TR as they are present in both modes, due to the fact that pulses in these three groups are not mode separated, which will be done in the following.

In arbitrary units, the flux density (S) of the MP, PC, and IP components

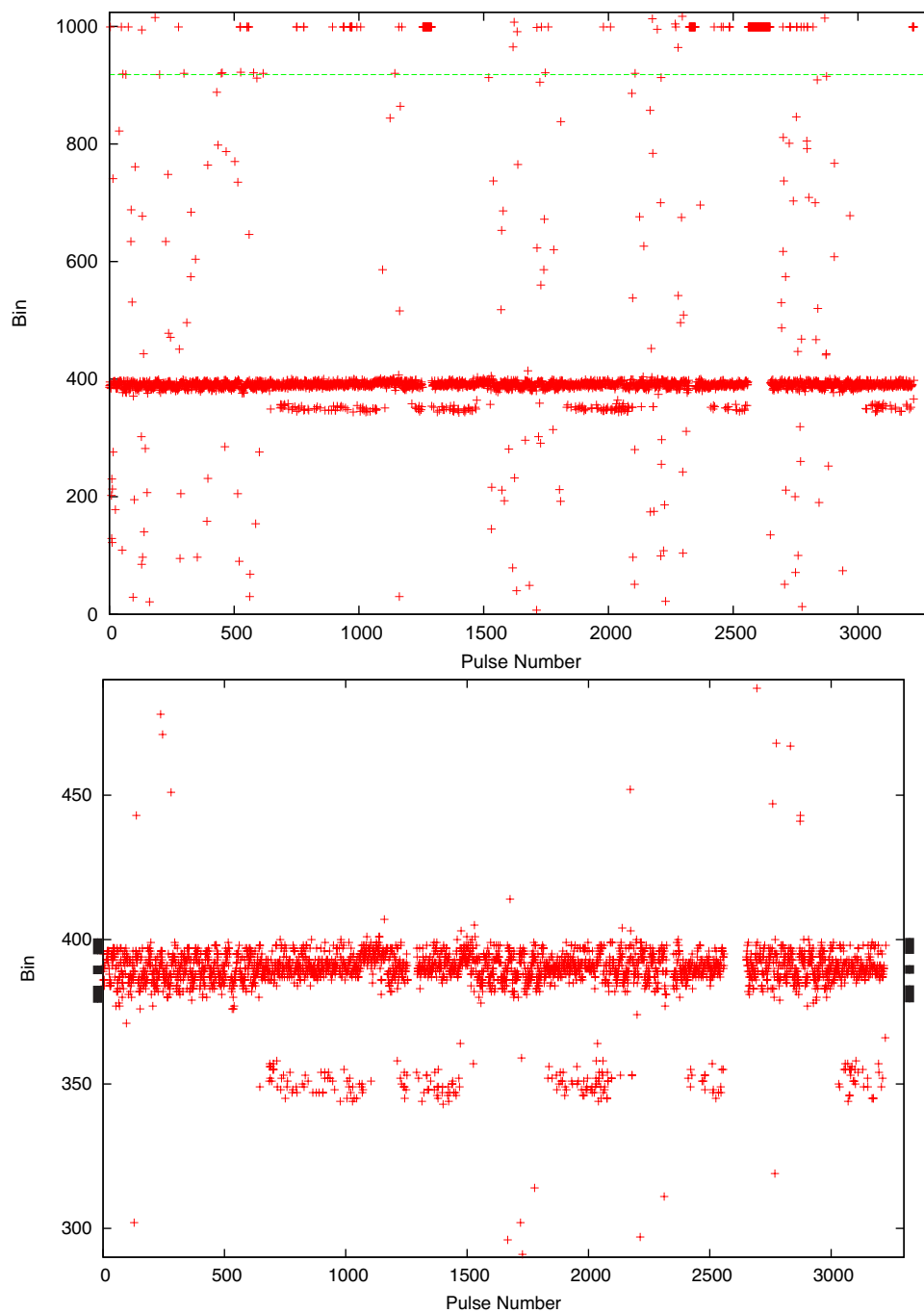


Figure 5.18: (*top*) A series of the sub-components' peak locations. The *green* horizontal line indicates pulse bin where the IP is expected. (*bottom*) Zooming into MP-PC region. The three thick markers represent the pulse ranges for sub-components' selection.

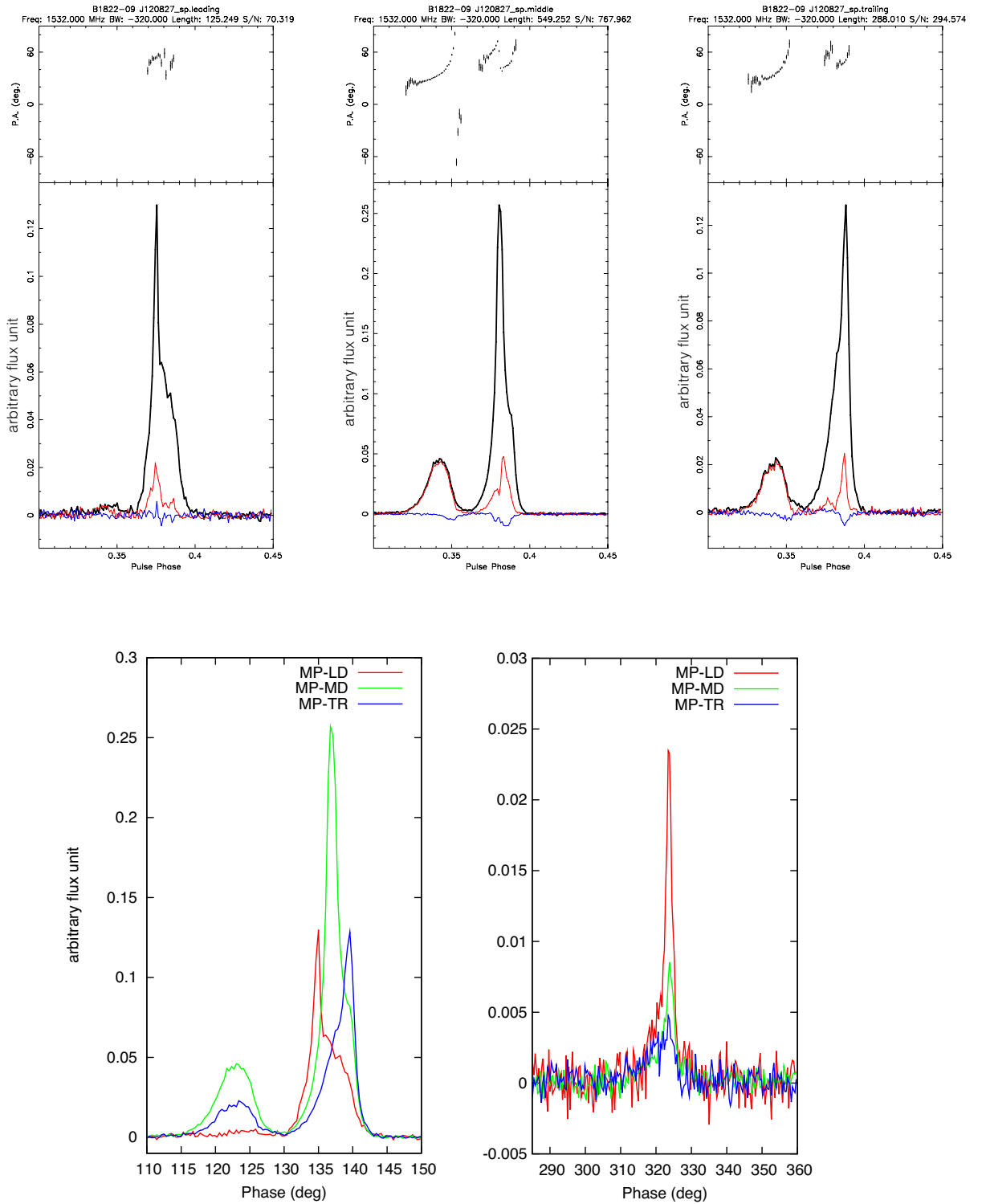


Figure 5.19: (*Top*) The resulting average profiles of each group, from left to right, the leading (LD), middle (MD) and trailing (TR) types. (*bottom*) The overlay plots in relative intensity of the MPs (*left*) and the IP (*right*).

Table 5.3: The measured amplitude (\bar{A}) and the flux density (\bar{S}) of the main pulse (mp) of the pulses categorised as the LD, MD and TR types, and also their PCs and IPs. N is the number of pulses in each type between the modes and the mean value of the flux density distribution (Fig. 5.20) is indicated with M . \bar{A} and \bar{B} are normalised by $N/10000$.

	LD	MD	TR			
A_{mp}	6.41	3.23	3.51			
$\bar{A}_{PC/mp}$	0.32	1.76	1.60			
$\bar{A}_{IP/mp}$	1.76	0.32	0.24			
\bar{S}_{mp}	70.1	30.9	37.5			
$\bar{S}_{PC/mp}$	0.74	3.54	3.13			
$\bar{S}_{IP/mp}$	1.71	0.44	0.54			
Modes	B	Q	B	Q	B	Q
N	9	186	466	308	108	248
M	(2.7)	1.2	3.0	1.2	2.7	0.6
σ_M	(1.1)	0.6	0.9	0.7	0.8	0.4

are measured for individual pulses. The resulting S is then categorised according to in which sub-component group, i.e. LD, MD or TR, the pulse is. The pulses in each group are also separated into the B and Q modes with the same criteria as the DFB dataset. A total of six histograms are shown in Fig. 5.20 and Tab. 5.3 summarises the number of pulses (N) and the mean value (M) of the distributions.

In the B mode (*left* column), despite the fact that the MD (*middle*) pulses are approximately a factor of five more populated, its distribution is found to be similar to that of the TR (*bottom*) pulses, where the TR's M is slightly weaker by $\sim 10\%$. Despite the limiting number of only nine, scattered from 1 to 4 units, the LD pulses (*top*) also have a mean of ~ 2.7 , close to that of the TR.

For the Q mode (*right* column) the distributions of the LD and MD pulses are relatively similar with $M \sim 1.2$, comparing to that of the TR which has an M of ~ 0.6 . Nevertheless, this can be understood as being because the underlying structure of the Q mode's MP which is double, not triple, and the middle region is essentially a combination of the brighter leading cone and the trailing cone. Therefore the distribution of the MD should resemble more that of the LD than TR.

Comparing the sub-component types between the modes, it is consistent that the B-mode pulses are on average a factor of ~ 2.5 times brighter, and also the fact

that the TR of both modes clearly have different energy distributions, possibly related to the shift in the PPA component 3.

The same flux density measurements (S) of the PC, IP and MP are also plotted with the pulse series in Fig. 5.21 and 5.22. During the Q mode, the MP expresses the ‘haircomp’ feature, modulating as well with the IP component (e.g. at pulse ~ 1600), while during the B mode it seems to turn into and out of the ‘bright’ mode rather gradually and with a well-defined flux level. The flux level of the PC’s is much more instantaneous in the B mode (see next figure). The burst-like emission of the PC is observed to be highly fluctuating, in which pulses can be as bright as the MP and also can sometimes be as weak as the Q mode’s noise level. Comparing its modal intro and outro, especially the second and third B-mode onset, the PC appears to become gradually active, relative to its cessation which ends rather abruptly. There also seem to be occasions where the emission from the PC and MP simultaneously completely ceases, or ‘nulls’, for example, at pulses ~ 780 and ~ 2450 , in Fig. 5.21 and Fig. 5.22.

To avoid the calibration issue which results in the PPAs to be frequency-dependent, a narrow frequency band from 1580 – 1586 MHz is selected to create PPA histograms, shown in Fig. 5.23, in which each count is weighted by one over the PPA’s errorbar squared. Their average PPA swings (*red* and *blue* for the B and Q mode) are very well consistent with the all-in average profiles in Fig. 5.7. The two vertical lines indicate the mid-point between the sub-components, which still also coincide with the decreases in L . Most importantly, we can now observe how an average PPA swing is formed from single pulses. For the B-mode PPA, it is now very apparent that there are two disconnected PPA lines, which are overlapping at the pulse window of the LD and MD, and it is this region where the averaging causes the OPM to be less than 90° . The intensity of the histogram also demonstrates that the majority of the B-mode pulses are of the MD and TR types. Despite having less S/N, the Q-mode histogram shows the underlining PPA to be rather similar to the B-mode histogram, within the noise limit. If the actual PPAs of both modes are indeed identical, then this would suggest a possible explanation for the differences between the B- and Q-mode PPAs, as presented in Fig. 5.9, being simply due to the fact that L of the two modes are ‘accented’ at different locations. The L in the B mode is strongest at the trailing half of the MP because there is very little overlapping between component 1 and 2, and hence its jump is more instantaneous, although still not a perfect 90° . On

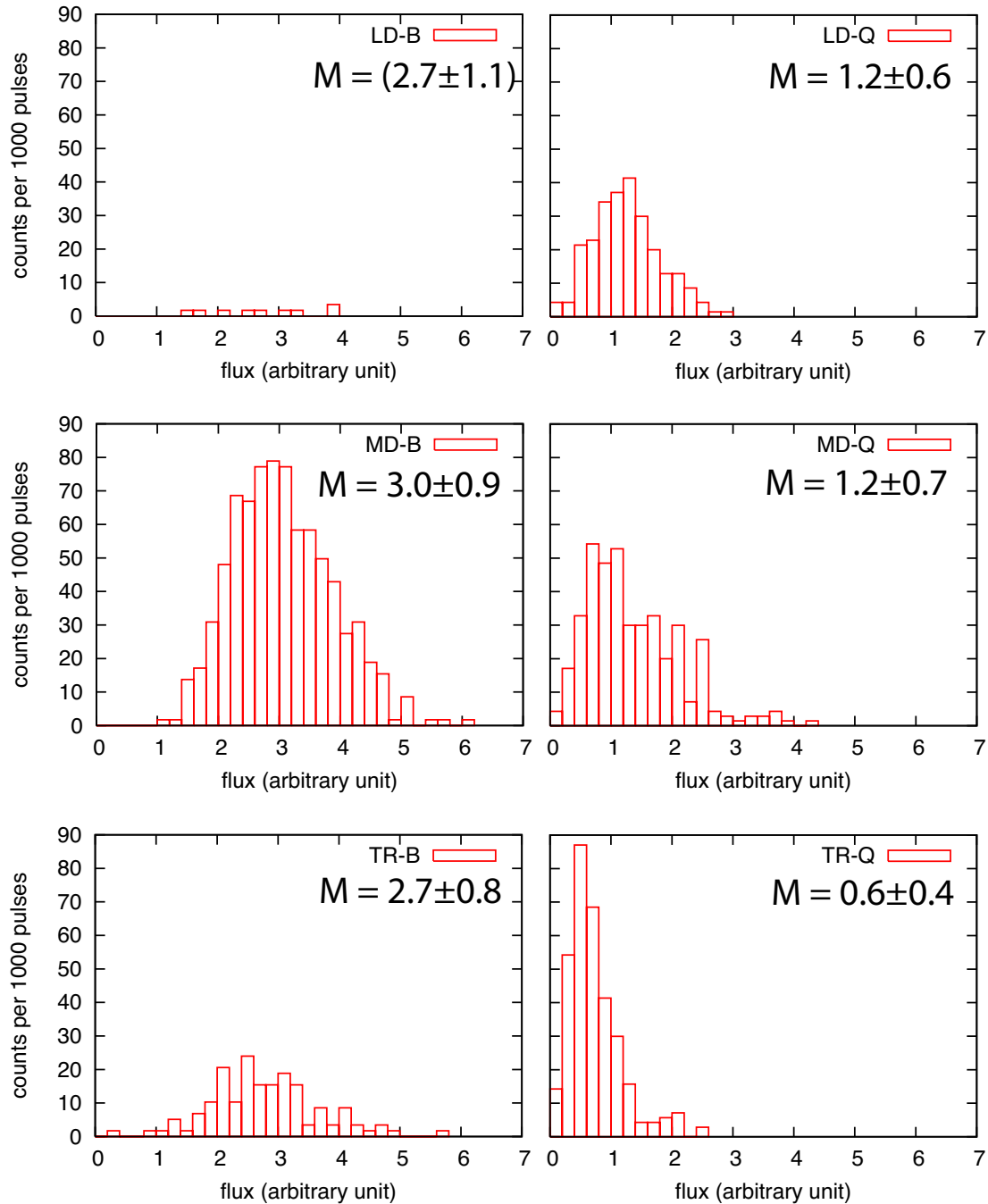


Figure 5.20: Histograms of the MP flux density of the B mode (*top*) and the Q mode (*bottom*), separated into which group the peak sub-component belongs to. The counts are normalised to 1000 pulses.

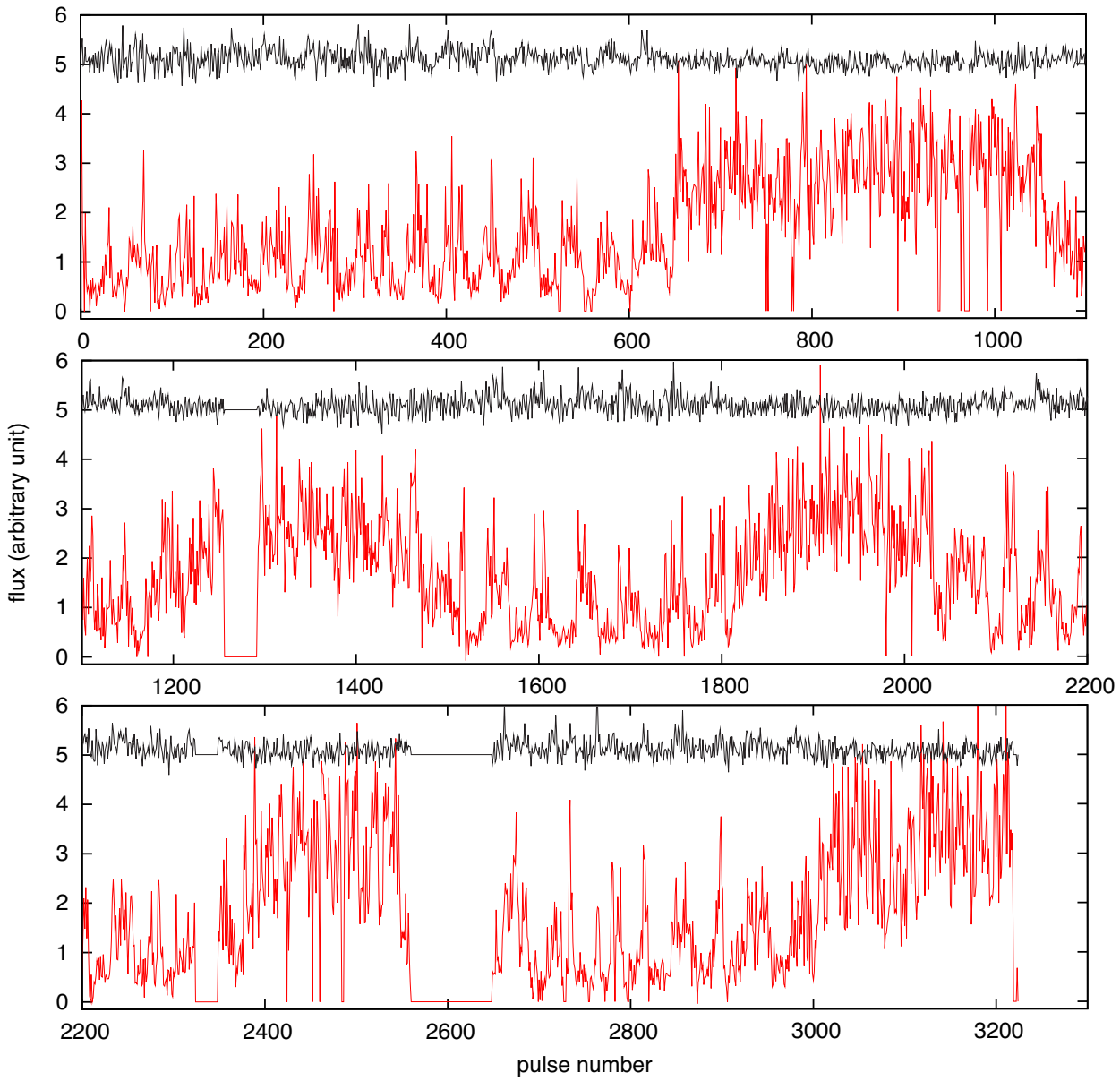


Figure 5.21: From top to bottom panels, the pulse sequence of the MP's (*red*) and the IP's (*black*, +5 unit) flux density.

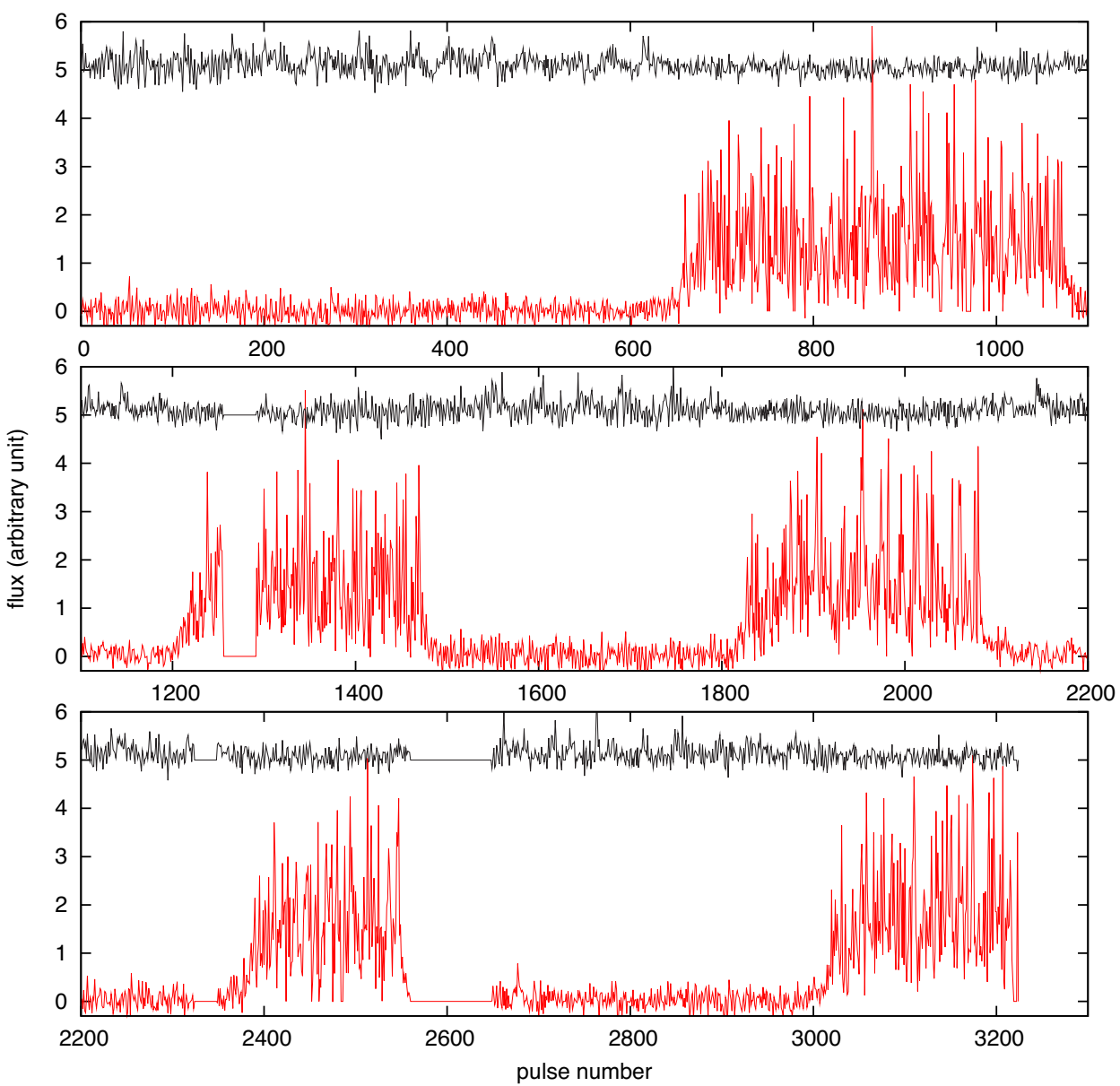


Figure 5.22: From top to bottom panels, the pulse sequence of the PC's (*red*) and the IP's (*black*, +5 unit) flux density.

the other hand, the Q-mode's polarisation is strong at the leading part of the pulse in which there is more in the 'PPA overlapping zone', and therefore results in a flatter PPA. We are unable to speculate if the same explanation also accounts for the deviation in component 3.

To demonstrate whether the two overlapping PPA trends are actually the steepest-gradient point of an RVM swing, we carried out an RVM least- χ^2 fitting on all the single-pulse PPA points of both the B and Q modes, assuming that the steepest-gradient point is around the jump and the solution should be close to an orthogonal rotator. As usual for RVM fitting, the fit is barely constrained within a 1σ limit; however, we chose an orthogonal solution of $\alpha/\beta = 86^\circ/1.8^\circ$, which is plotted as a *green* curve on the *top* and *bottom* panels of Fig. 5.23.

While the curve is positioned to fit component 2 rather well, it is however slightly too steep for component 1. This indicates that only the trend of the PPAs itself cannot be perfectly described by the RVM. The PPA swing at the leading side is too shallow to sustain its large value of the gradient seen at later phase, i.e. an RVM swing cannot be flat and steep at the same time. Including the frequency-dependent shift of component 1 (fig. 5.12) into consideration, it is fairly conclusive that the steepest gradient could not have taken place here, and also because otherwise this would lead to a negative aberration shift.

Reconsidering the component-2-to-3 jump (Fig. 5.9), it seems rather plausible for the rise in component 2 to 3 of the B mode to correspond to the steepest point of an RVM, which is also well consistent with the aberration shift constraint. However, it is unclear if this is true for the Q mode's component 3 which departs abruptly from its component 2, which will be hard to fit with the RVM.

For the PC, shown in Fig. 5.24, it appears to consist of one single propagation mode, i.e. no OPMs, which, however, could be either the X or the O mode. Again, this evidence supports the distinction between the PC's and the MP's origin as the scattered PC emission should consist of a single polarisation mode. Broadening of the PPA points is also a very interesting feature to study, as it should roughly reflect the condition of plasma in the propagating zone (Chapter 3). As in this case, given the very narrow frequency band of only 6 MHz, we believe that polarisation calibration issues for this pulsar with an RM of ~ 65 rad/m² should have very limiting influence on the broadening.

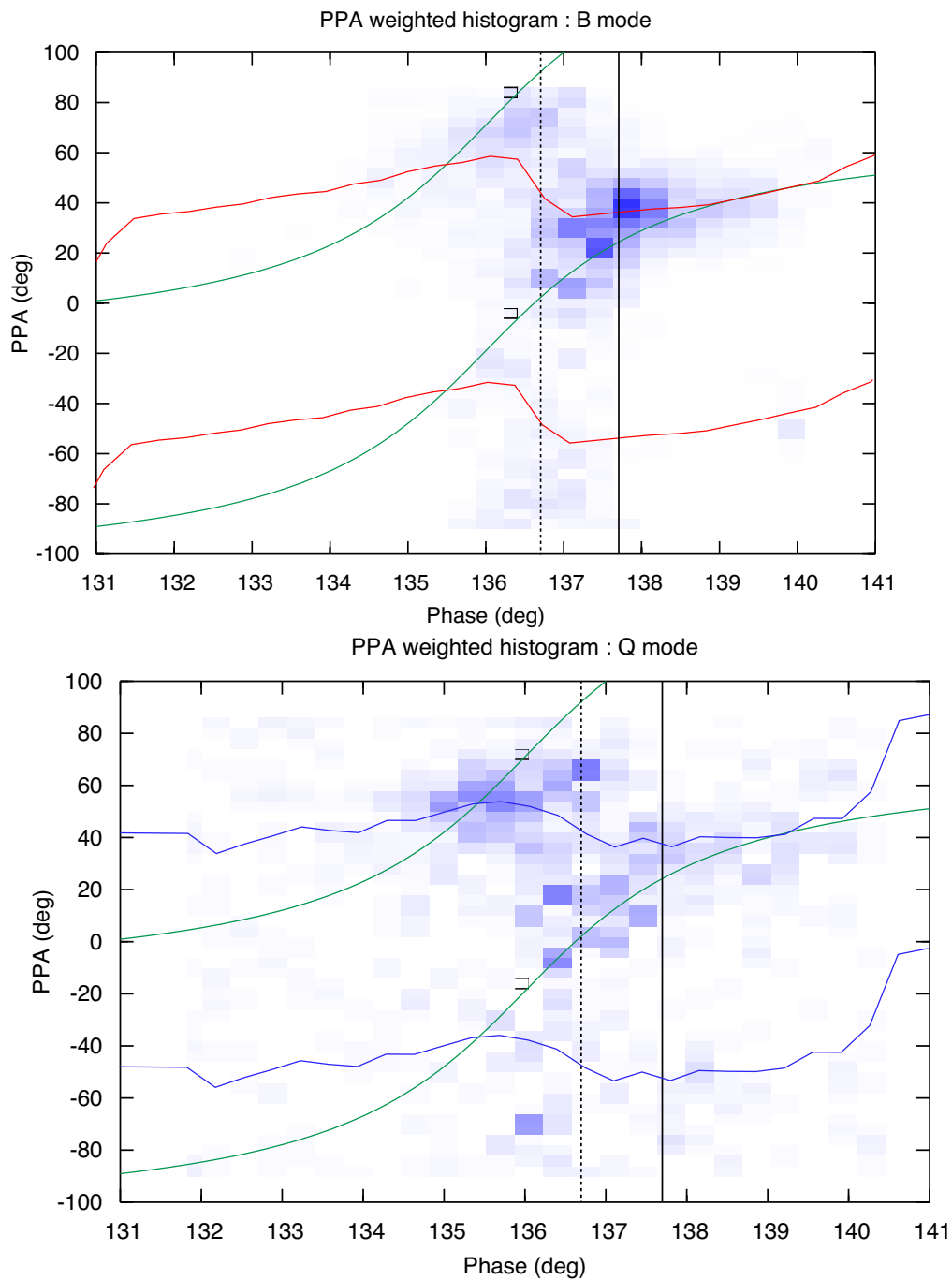


Figure 5.23: The PPA histograms of the B mode (*top*) and the Q mode (*bottom*) with their average PPA swings (*red* and *blue*). The counts are weighted by each individual PPA's errorbars. The *green* line is the proposed RVM swing of $\alpha/\beta = 86^\circ/1.8^\circ$. The two vertical lines denote the two locations as in Fig. 5.7.

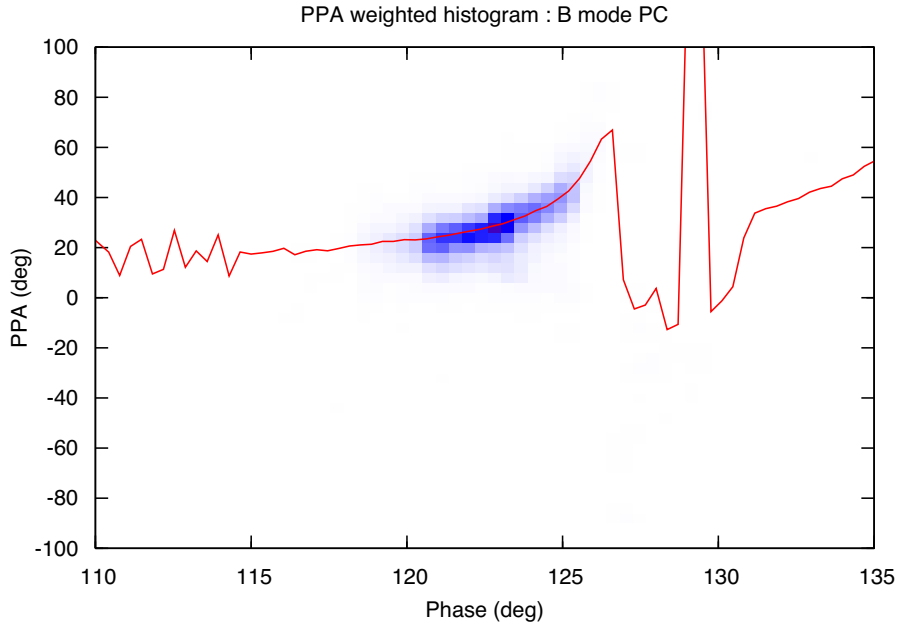


Figure 5.24: The PPA histogram of the B mode’s PC and the average PPA swing (*red*).

5.3.3 Modal Statistics

It has been shown in the work of Lyne et al. (2010) that for a number of pulsars the rate of change of a pulsar’s spin ($\dot{\nu}$) appears to be related to the change in the pulse’s shape. For PSR B1822–09, the shape parameter, which is represented by the relative PC amplitude of an average—i.e. not mode-separated—profile (A_{PC}), seems to be correlated with $\dot{\nu}$ strongly at MJD of 51100 and 52000 (Fig. 5.25). The fact that the correlation is not perfect over the course of a 15-year dataset could be due to the following reasons.

Firstly, the switching timescale, ~ 4.5 mins/switch, is much shorter than the time for measuring the change in $\dot{\nu}$. This suggests that only extreme changes, can be observed, while small, subtle variations are harder to measure. Secondly, it is *not* certain that the measured A_{PC} of average profiles, which is used to infer the portion of time the pulsar is in B mode, is a proper representation of a pulse-shape- $\dot{\nu}$ correlation.

Tab. 5.4 summarises modal statistics from twelve observations⁷, collecting a

⁷Two observations were added later, which are not included as a part of the B- and Q-mode templates. However, no significant changes in the A_{PC} are observed after adding them.

Table 5.4: Mode-switching statistics of twelve 40-min observations. (exc.) means excluded from the B- and Q-mode profiles, which includes RFI rejection and pulses during transitions between the modes.

statistics	number	unit
observation	12	40-mins each
total	37344	pulses
RFI (exc.)	9743	pulses
switches	106	times
transition (exc.)	4141	pulses
B: total pulses (percentage)	8290 ($T_B = 35\%$)	pulses
Q: total pulses (percentage)	15170 ($T_Q = 65\%$)	pulses
B: average time/switch	2	mins
Q: average time/switch	3.67	mins

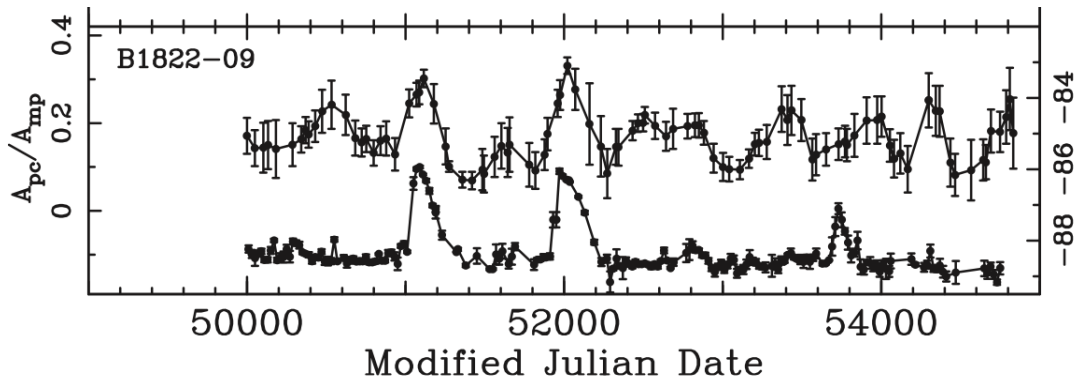


Figure 5.25: The plot by Lyne et al. (2010), showing the measured A_{PC} (left axis) and the spin-down frequency in a unit of 10^{-15} Hz/s (right axis), over a length of ~ 5000 days.

total of over 37000 pulses, in which ~ 13800 ($9743+4141$)⁸ pulses are excluded from the B- and Q-mode profiles, due to the RFI and the modal ‘transition’ zone, respectively. The remaining pulses are accounted for by 8290 pulses in the B mode and 15170 in the Q mode. On average, the pulsar switches once every 4.5 minutes ($(12 \times 40)/106$). The average modal time of the B mode is ~ 2 minutes, and ~ 3.7 minutes for the Q mode, from 53 occasions of each.

Fig. 5.26 shows the variation in the PC/MP and IP/MP ratio of both the B and Q modes, however, note that the errorbars of the three lines are not included

⁸This is only approximated on an average of a transition region of around 3 bins, i.e. 30 s. Can easily find out how many exactly later!

because they are already larger than the magnitude of the variation. Focusing on the PC lines (*red* and *magenta*), it appears that the lines are anti-correlated before month eighth, and strangely become correlated afterwards. The anti-correlation can be understood in terms of the contamination of the Q mode by the PC component. However, the strong correlation after the eighth month can only imply that the MP has become weaker relative to the PC, and similarly relative to the IP. Despite the large errorbars, this plot demonstrates that the relative strength of the PC component is not absolutely stable. We also note that there is no correlation between the apparent variation in the PC/MP ratio and the measured spin-down over this period of time.

It also appears that the relative amplitude of the PC of the B-mode observations (A_{PC-B}) is anti-correlated with the duration of the B mode of each observation. What could be said is that the amount of ‘budget’ energy for the B-mode PC is limited, so that if it is very bright, relative to the MP, the B mode duration will not last long (Fig. 5.27 *top*). Nonetheless, the ratio of total pulse flux per pulse, i.e. MP+IP+PC, of the B mode to the Q mode is shown in Fig. 5.27 (*bottom*), resulting in one of the observations in late June having the B mode’s power surpassed the Q mode by a factor of ~ 30 .

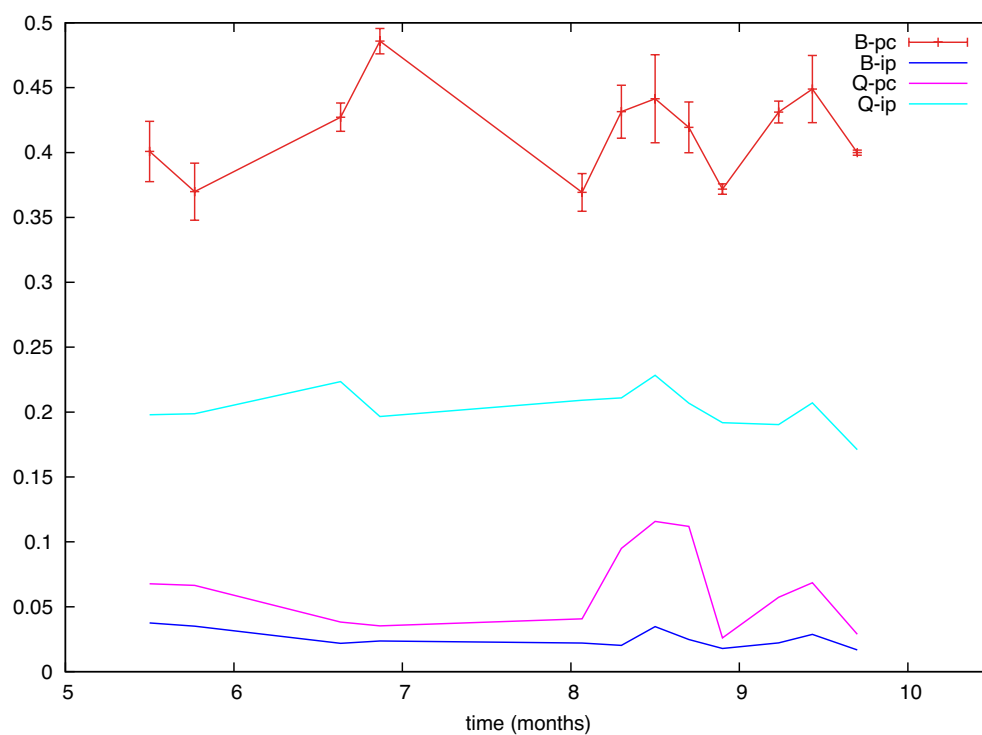


Figure 5.26: The normalised relative amplitudes of the PC and IP of both the B- and Q-mode profiles (A_{PC-B} , A_{IP-B} , A_{PC-Q} and A_{IP-Q}). The errorbars are not plotted on three of the four curves because they are very large.

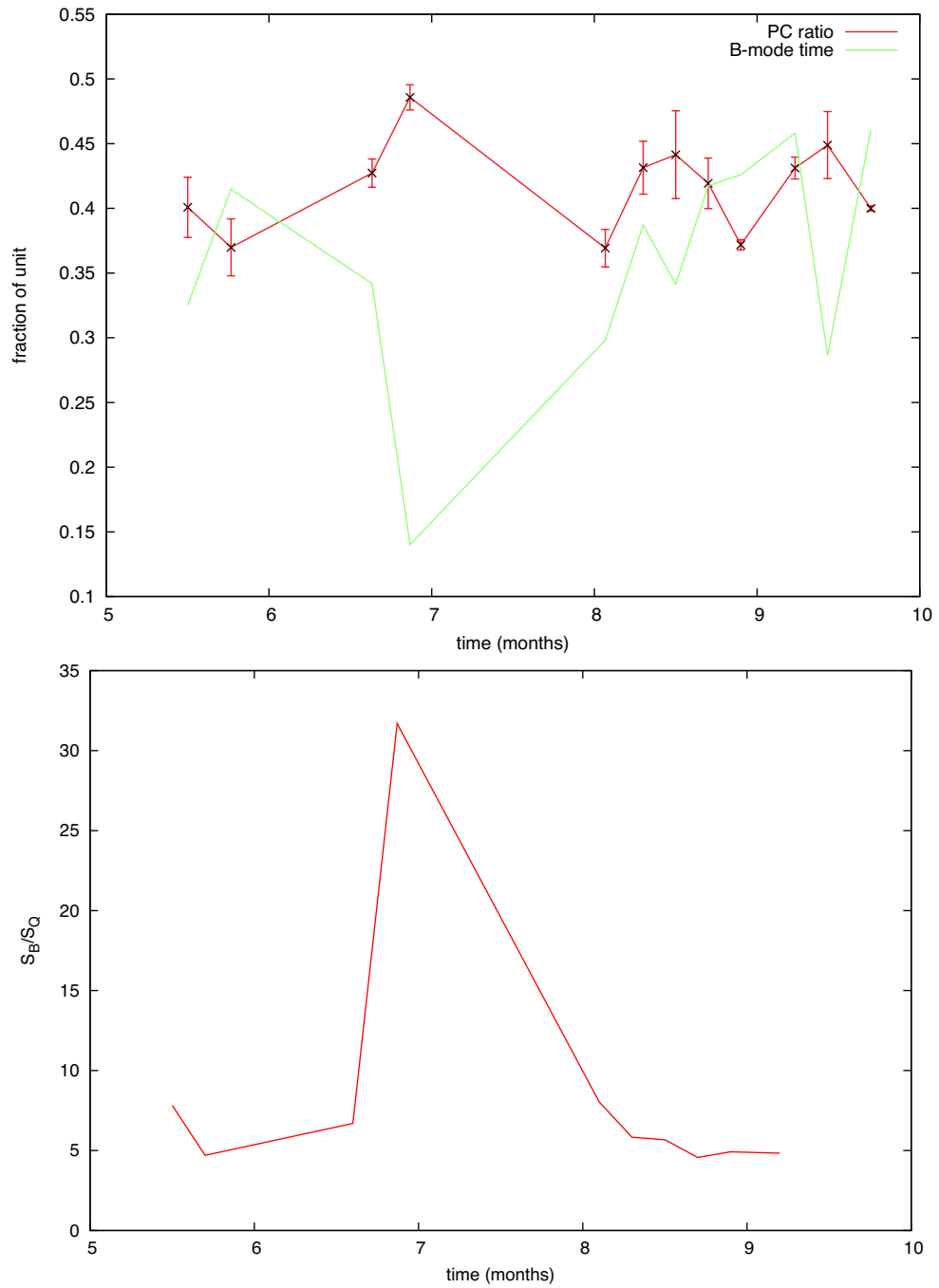


Figure 5.27: (*Top*) the measured A_{PC-B} and the fraction of B-mode time from our twelve observations. (*Bottom*) the flux density ratio between the modes (S_B/S_Q) measured from the same dataset.

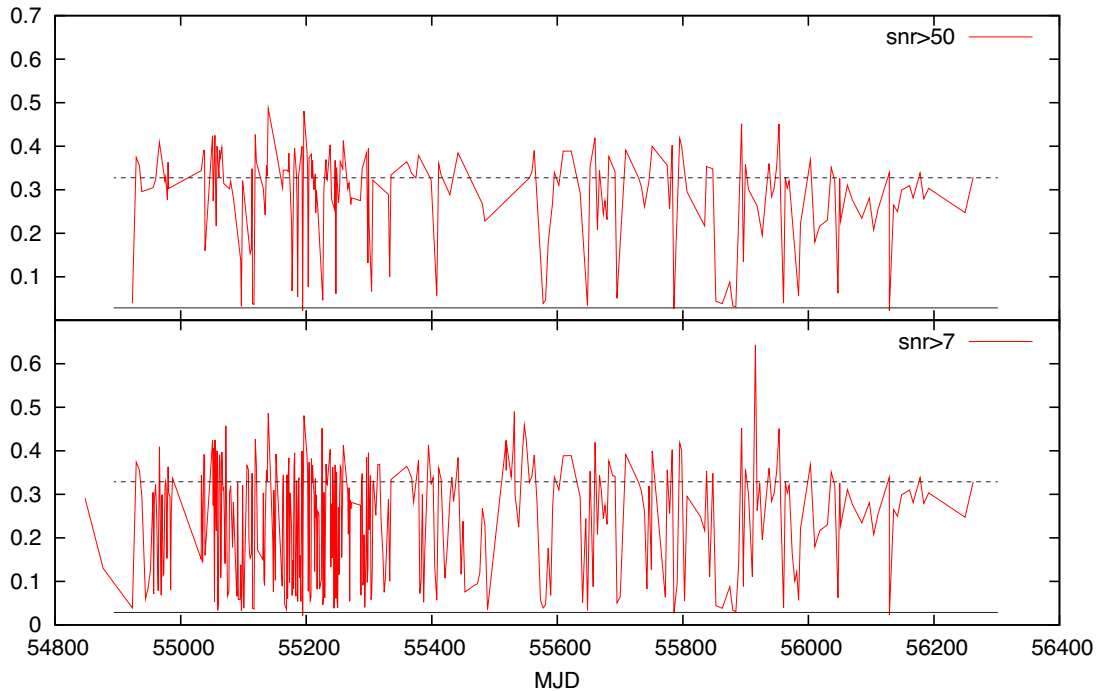


Figure 5.28: Plots of A_{PC} of DFB observations since November 2008, where the *top* panel are observations with $S/N > 50$ and the *bottom* panel are observations with $S/N > 7$.

To investigate the variation further, the ratio A_{PC} of almost 400 non-polarisation-calibrated DFB observations since November 2008 is measured and shown in Fig. 5.28, where the *dashed* and *solid* lines indicate the average ratios of the B- and Q-mode PC from Tab. 5.1, respectively. The observing time was set to 6 minutes, before being increased to 10 minutes in 2012 ($MJD = 55933$), and has been changed to 40 minutes since May 15 ($MJD = 56062$). It appears that the value of A_{PC} can be as high as ~ 0.4 and, as can be expected, is almost never lower than the average minimum Q-mode PC (A_{PC-Q}).

This leads us to the next question of how the distribution of the modal activity should be according to our model. Histograms of A_{PC} from Fig. 5.28 are shown in Fig. 5.29. The distributions appear to be bimodal with the main peak is ~ 3.2 and the second peak near ~ 0.05 . The discrepancy between the high and low S/N which is most apparent around $A_{PC} \sim 0.1$ suggests that low S/N observations are related to the case where the ratio is small, i.e. when the pulsar is in the Q mode. Attempting to reproduce the histogram, we derive simple Monte-Carlo simulations in three scenarios.

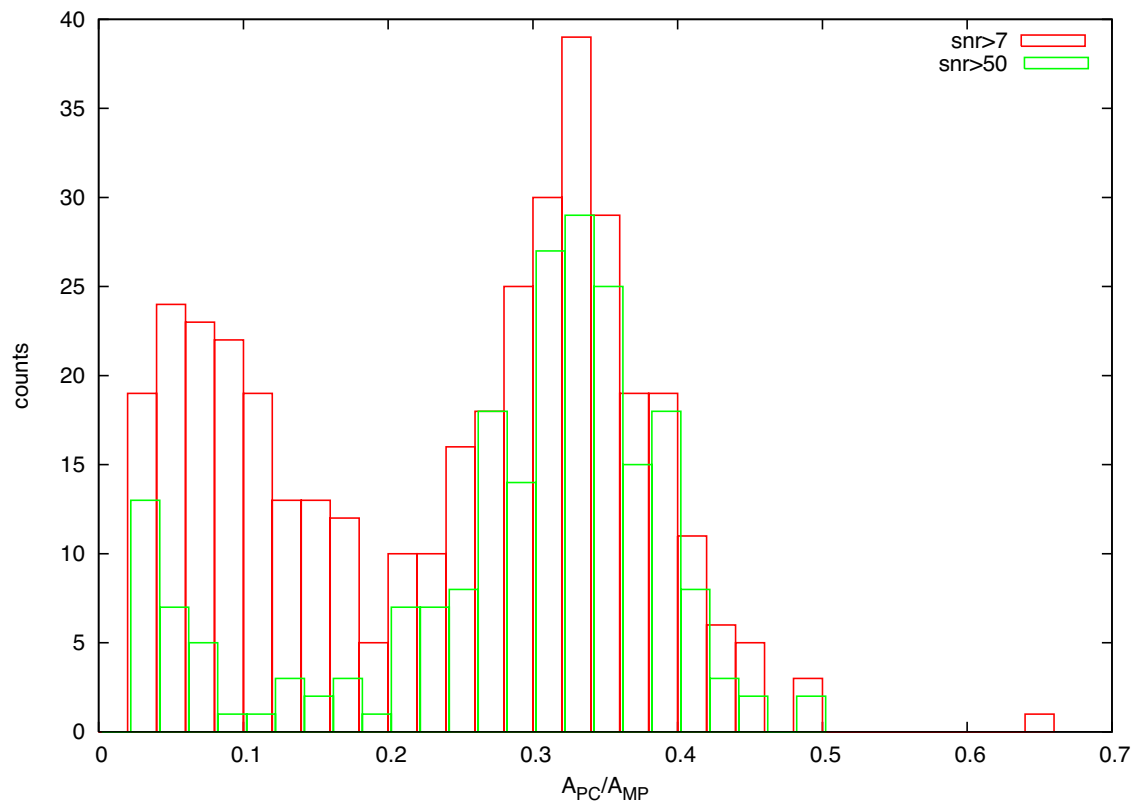


Figure 5.29: Histograms of A_{PC} of DFB observations since November 2008, where the *red* and *green* colour indicate observations with $S/N > 7$ and > 50 , respectively.

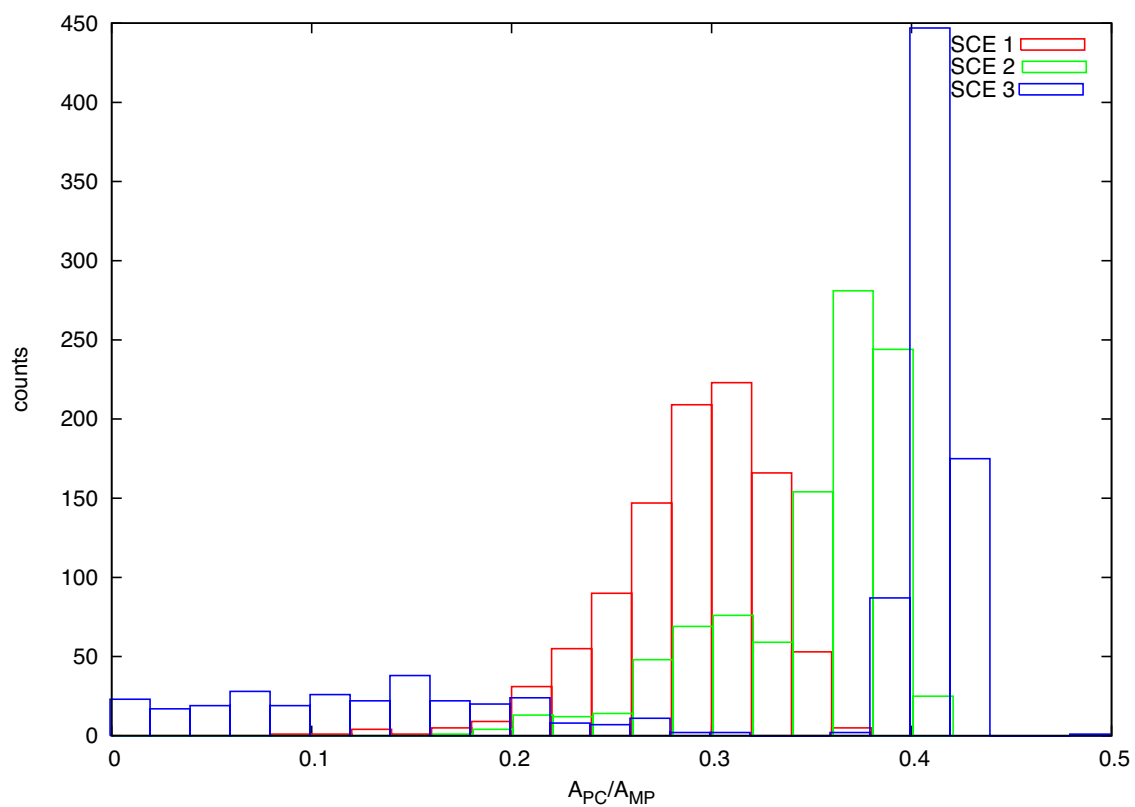


Figure 5.30: Histograms of three models to reproduce the histograms in Fig. 5.29. See text for detail of each model.

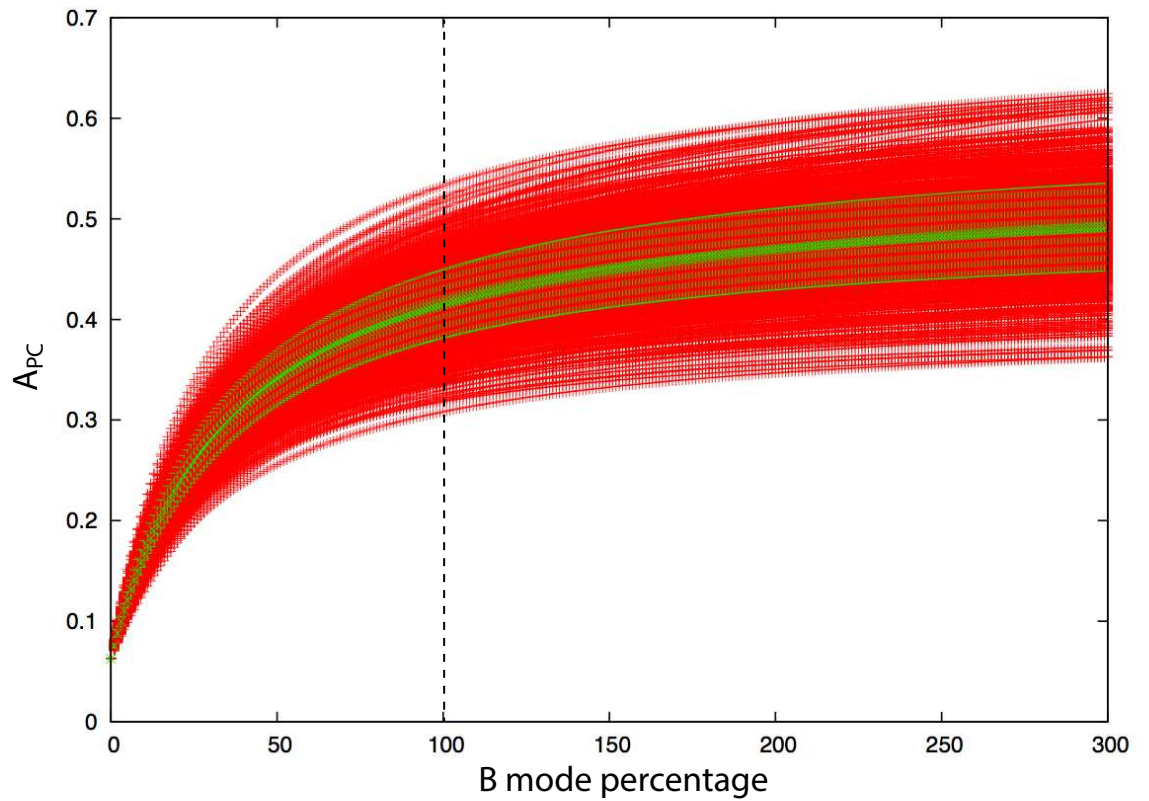


Figure 5.31: 1000 Monte-Carlo runs are done on Eq. 5.3 with statistics measured from twelve 40-min datasets. The *red* points indicate all the solutions, and the *green* points and the errorbars represent the mean and rms derived from the corresponding solutions. B-mode occurrence percentages larger than 100% are not possible.

In the first scenario, The relative amplitude ratio of the B- and Q-mode templates (A_{PC-B} and A_{PC-Q}), measured from Tab. 5.1, are held constant and the fraction of B-mode time is normally distributed around 0.35 (Tab. 5.4) with the standard deviation, σ_{T_B} , of 0.1. The resulting A_{PC} distribution (*red*, Fig. 5.30) appears to be centred around 0.3, which is understood as a combination between A_{PC-B} and A_{PC-Q} . Because varying T_B and σ_{T_B} seems only to shift and flatten the distribution, a second peak is therefore unlikely to originate from this scenario.

To imitate a second peak, we model the pulsar to switch between two fractions of time the pulsar spend in the B mode (T_{B1} and T_{B2}). In this simulation we allow the pulsar to have an equal chance to switch between the T_{B1} and T_{B2} states. In this simulation, we set $T_{B1} = 0.35$ and $T_{B2} = 0.65$, so the B mode can be either dominant mode or the rarer mode. These switches can indeed be presumed to be as a connection to the change in $\dot{\nu}$. For the second case, the histogram (*green*) shows a strong peak at 0.37, followed by a second peak at 0.3, which however does not resemble the observation. The bimodal distribution is caused by the long-term switch between T_{B1} and T_{B2} which have equal chance and hence an equal area underneath the broader leading and narrower trailing part. However, the second peak at 0.3 is too high to account for the peak in our observation at 0.05. This can be understood as due to the fact that T_{B1} and T_{B2} are too still high so that A_{PC} can never be below 0.2.

Thirdly, we demonstrate that the second peak can be brought down from 0.2 to be as low as zero (*blue*) by reducing T_{B1} to 0.05 and increasing T_{B2} to 0.95. So the chances to find the B mode is either extremely large or small. Again there is an equal probability for T_{B1} and T_{B2} . The *blue* distribution shows an even higher main-peak ratio (~ 0.41), while the second component becomes much broader and lower. This is due to the fact that any observation could have its A_{PC} to be either very strong, or very weak. However, this solution still does not resemble the observation well, in terms of the width and location of the components. Also the fact that this case requires T_{B1} to be as low as 0.05 does not seem to be realistic, when comparing to our measurements of T_{B1} in Tab. 5.4. In addition, because σ_{T_B} is normally large, having the value of T_{B1} close to zero will cause a part of the second distribution to be ≤ 0.2 , which is indeed also inconsistent with the observation in Fig. 5.28.

Consequently, we are left with one possibility to be considered which is that

the A_{PC-B} (and A_{PC-Q}) need to be adjusted, i.e. being not constant. This conclusion is also supported by the measurements from our dataset, showing that the A_{PC} of the B-mode template is indeed varying by $\sim 10\%$ within the timescale of five months. We are now led to another question that if the PC ratio is randomly changing, how would it affect Eq. 5.2, which now includes the Q mode's PC as,

$$A_{PC} = \frac{aT_B + bT_Q}{cT_B + dT_Q}, \quad (5.3)$$

where a and c are the peak flux of the PC and the MP components in B mode, and similarly for b and d in the Q mode. According to Tab. 5.1, $a, b, c,$ and d are 1.35, 0.055, 4.09, and 1.68. Errorbars on these values were determined by the standard deviation of the measured values from the twelve observations that are plotted in Fig. 5.26. A Monte-Carlo simulation of 1000 runs was carried out to obtain a distribution of A_{PC} , which is shown in Fig. 5.31 (*red*). For each value of the B mode percentage, a mean and standard deviation are calculated and plotted as the *green* point and its errorbar. This simulation demonstrates that Eq. 5.3 can accurately be used to determine the fraction of time the pulsar spend in the B mode from A_{PC} of an average profile at low value of T_B , before the errorbar becomes too large at $A_{PC} = 0.3$, corresponding to $35\% \pm 15\%$ of the B-mode time. This plot also shows that a single value of T_B will only result in a single-component histogram (Fig. 5.30).

In this subsection, we have demonstrated that the modal statistics are not only stochastic on shorter timescales, but are also changing over the course of five months (which is possibly the same change indentified by Lyne et al. (2010) to be correlated with the change in the spin-down), and furthermore the assumption that the A_{PC-B} is constant is not sufficient to reproduce the observed A_{PC} distribution over the length of four years of the DFB dataset.

To be able to understand the shorter timescale of B- and Q-switches and the longer switches between the different occurrence behaviour of this pulsar, it is inevitable to study the mode-separate, individual observations to at least be able to conclusively determine and measure the change in A_{PC} of the B-mode template, which will lead to a more accurate interpretation of the work of Lyne et. al. (2010).

5.4 Discussions

5.4.1 Pulse Profiles

We have compared the MP’s sub-components (LD, MD and TR) between the B and Q modes and found that their flux distribution is different between the modes (Fig. 5.20) and also at different frequencies (the 325-1532 MHz profile reversal).

The mode-separated profiles in the recent work of LMR12 are clearly inconsistent with their earlier observations (BMR10), shown in Fig. 5.32. The Q mode’s fraction of total time is approximately a factor of three longer, similar in our case, it is still rather strange that the pulse shape in no way resembles the double type. This strongly indicates that, at least at 325 MHz, the MP’s shape is not reliable for identifying the modes. Nevertheless, comparing to higher frequency, the templates seem to remain consistent, i.e. MD-TR type, between FWM81, GJK+94, and our dataset.

PSR B0943+10 is another mode-switching pulsar with a PC (Fig. 5.33) and mode-preferable subpulse modulation. Comparisons of the moding properties between PSRs B1822–09 and PSR B0943+10 are summarised in Tab. 5.5. Despite having similar features as PSRs B1822–09, PSR B0943+10 has a PC when it is in the Q mode and in turn its B mode is detected to have sub-pulse modulation. This pulsar has recently been detected with X-ray pulsations, exclusively in the Q mode, which will be discussed in related to the shift in the PPAs in the next chapter. Another supporting evidence from this pulsar to the indication that the MP’s shape is unreliable for identifying the modes is that at 327 MHz the MP of the B mode appears to be inconsistent between two epochs, MJD 52709 (Fig. 5.34) and MJD 53492-54632 (Fig. 5.33), and instead the MJD-52709 profile seems to rather resemble the Q mode. The PPAs of this pulsar are also interesting as can be seen from the obvious shift between the modes, which will be later discussed in this section.

This is indeed vital information for understanding at what level the magnetosphere is affected by the process of mode-switching, that despite the flux behaviour—the MP’s shape— which is shown to be loosely related to the mode-switching, the rest of the modal properties remain related to their associated modes, e.g. the subpulse, the PPAs (however, subtle change is identified, Fig. 5.9 and 5.10), and the PC-IP anti-occurrences.

Considering another mode-switching pulsar, PSR B0826-34, a rather similar

Table 5.5: Comparisons of modal properties of PSRs B1822–09 and B0943+10.

	B1822–09		B0943+10	
	bright	quiet	bright	quiet
sub-pulse modulation	-	$\sim 43P_1$	$\sim 37P_1$	-
MP-PC separation	-15°	-	-	-50°
L	higher	lower	$\sim 40\%$	$\leq 10\%$
Δ PPA	$\sim 0^\circ$		$\sim 30^\circ$	
X-ray detection	upper-limit		non-thermal	brighter non-thermal
X-ray pulsation	-		-	pulsation

situation was found, i.e. the weak-mode profile at 1374 MHz seems to resemble the strong-mode profile at 408 MHz (Esamdin et al. 2005, their figure 1 and 2). In the strong mode, both the inner and outer emission cones are active at 1374 MHz, while at 408 MHz only the outer part remains, which happens to resemble the ‘weak’ mode at 1374 MHz. It seems as if the two states of the pulsar have different efficiencies in radio-emission generation (i.e. spectral index) between the inner and outer cone, so that in the strong mode at 1374 MHz the inner cone is mostly strong with a considerable amount of the outer cone, while at 408 MHz only the outer emission is active. On the other hand, in the weak mode at 1374 MHz the inner cone is rather inactive, while the outer cone becomes the dominant component, relatively. As summarised in Tab. 5.6, this ‘opposite’ spectral

Table 5.6: A table summarizing the MP’s sub-components brightness at two frequencies. The number 0, 1 and 0.5 for PSR B1822–09 crudely represent the relative component’s height of the LD-MD-TR.

	PSR B1822–09		PSR B0826-34			
	1532 MHz	325 MHz	1374 MHz		408 MHz	
	LD-MD-TR	LD-MD-TR	inner	outer	inner	outer
B	0-1-0.5	1-0-1	strong	fair	-	strong
Q	1-0-1	0-1-0.5	-	strong	n/a	n/a

behaviour is identical to what we found for PSR B1822–09, that the strong mode in one frequency is like the weak mode at the other frequency. However, PSR B0826-34’s weak mode at 408 MHz was not yet identified to resemble the 1374 MHz’s strong mode.

If they are in fact the same phenomenon, we therefore infer a similar picture for PSR B1822–09. The MD component is a different emission component, possibly the ‘core’ or a tight inner cone, than the LD and the TRs—two TRs from TR_B

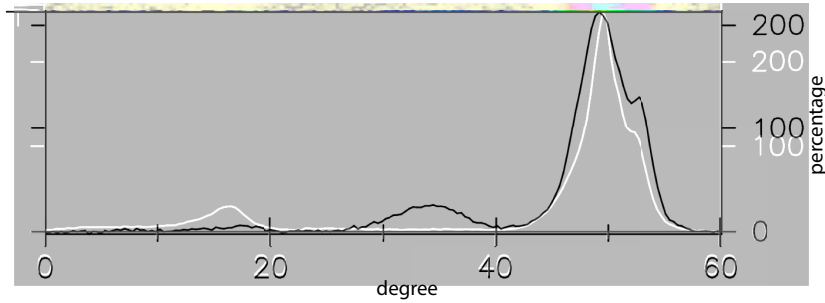


Figure 5.32: Adaptation and overlay from LMR12, the mode separated profiles at 325 MHz from the 8-hour-long observation.

and TR_Q — i.e. outer cone. And the profile reversal is of a similar reason, that the two inner and outer components have different, or rather opposite, efficiency in producing radio emission in each mode at the two frequencies.

In contrast to the variation of the modal profiles at low frequency in Fig. 5.32 and 5.34, described above, the modal profiles of PSR B1822–09 at higher frequency appear to be well-consistent to previous publications, which spans over thirty years. This suggests that the modal templates are more stable at higher frequency.

As shown in Fig. 5.12, we have found that component 1 in the PPA swing has shifted from being exactly 90° separated to component 2 at 325 MHz, gradually moving downwards at 600 MHz, and finally becoming only $\sim 20^\circ$ apart at 1532 MHz, while however at 2650 (FWM81) the separation seems to be closer to 90° again. We suspect that this might be related to propagation effects.

According to the prediction in Beskin & Philippov (2012) that the X-mode wave is identified if the sign of V is similar to the sign of the PPA swing’s slope, and opposite for the O-mode, component 1 and component 2 are then predicted to be of the O- and X-mode waves, respectively, from the appearance of the templates at both 325 and 1532 MHz, consistently (Fig. 5.7 and 5.10). On the suggested prediction that component 1 is of the O-mode wave, we propose that the shift of component 1 is due to the fact that the O-mode wave is refractive. This means that the ‘apparent’ O-mode emission point, which is identical to the non-refracted trajectory of the X-mode emission, is higher than the ‘true’ emission altitude⁹. As concluded in Chapter 3, the propagation effects on the PPA depend

⁹See BP12’s Appendix A, where they use the concept of imaginary source to calculate the trajectory of the O mode.

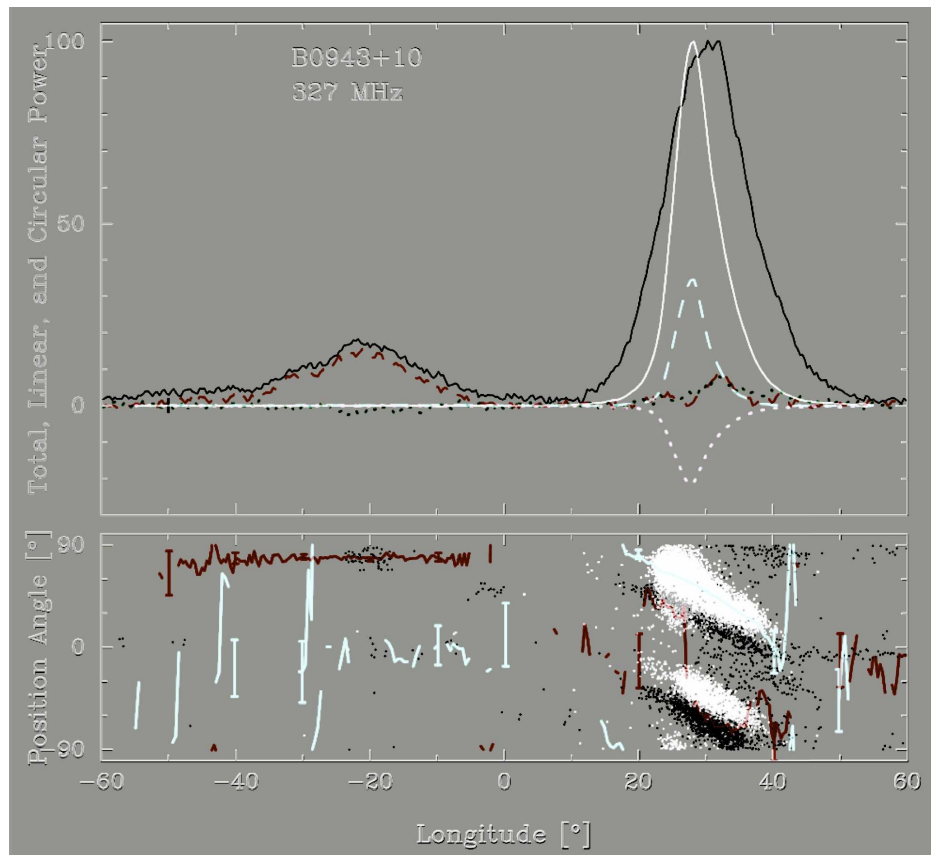


Figure 5.33: Adapted from BMR10’s figure 5, this overlay diagram demonstrates differences in the modal profiles. The pulse intensity I , L and V of the Q mode are denoted with the *black*, *dashed-red* and *dotted-green* lines, where those of the B mode the lines are *white* (top panel). In the *bottom* panel, the *red* line and *black* dots correspond to the average and individual PPAs of the Q mode, and *white* for the B mode.

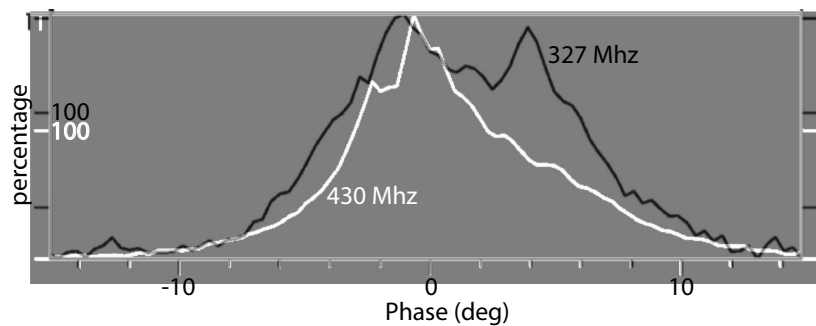


Figure 5.34: The templates of the PSR B0943+10’s B mode at 327 MHz for MJD 52709 (*black*), and 430 MHz for MJD 48914 (*white*).

on the distance between r_A ¹⁰ and r_{PLR} in Eq. 3.2 and Eq. 3.4, which are similarly dependent on $f^{-2/3}$. The difference in the distance at both frequencies is expected to be

$$\frac{(r_{PLR} - r_A)_{325}}{(r_{PLR} - r_A)_{1532}} \propto \left(\frac{1532}{325}\right)^{2/3} \sim 2.8. \quad (5.4)$$

The above calculation indicates that the O-mode wave at 325 MHz propagates through a longer path in the plasma-dominated zone than at 1532 MHz, and therefore is expected to be more affected by the plasma. This is in fact opposite to what is observed, where the effect is more strong at 1532 MHz. Nevertheless, BP12 certainly show that it is possible to obtain non-90° OPM jumps from their simulated mixed-mode profiles. Because our analysis in Chapter 3 only considers the X-mode wave, we are unable to make quantitative conclusions at this point and require further study of how characteristics of the OPM jumps are related to plasma and geometrical parameters.

Assuming a general situation where the point of steepest gradient is expected to be lagging the intensity profile due to the effects of aberration, the observed trend of PSR B1822–09’s PPAs (Fig. 5.9) is believed to be the leading half of the characteristic RVM swing. After removing the two $\sim 20^\circ$ jumps, the PPAs may express a conventional RVM trend, starting from a far leading wing (component 1 of the PPA swing), rising in approach to the magnetic axis after component 2, connecting to component 3. However, this scenario has two flaws: 1) the fact that component 3 of both modes is rather too flat to incorporate the swing; 2) according to BMR10’s 325 profiles (Fig 5.10), components 2 and 3 of the B mode appear to be separated with an OPM jump, as opposed to being rather continuous at 1532 MHz. Unfortunately, due to the lack of signal, we are unable to investigate this jump in single-pulse statistics.

Nevertheless, whatever mechanisms are behind the non-90° jumps, the fact that the Q-mode components 1 and 3 are slightly below and above the B mode’s, respectively, suggests a possibility that the Q-mode’s PPA swing is steeper than the B mode’s swing. Consequently, in terms of the propagation effects (Chapter 3), it appears that a steeper PPA swing indicates a larger number density (λ) and a lower Lorentz factor (γ), while keeping the rest of the parameters fixed (Beskin & Philippov (2012)’s table 3¹¹). This is plausible given the implication in Lyne et al. (2010) that the pulsar has a higher $\dot{\nu}$ when A_{PC} is low, supposedly

¹⁰As it is for the O mode, r_{em} is replaced with r_A .

¹¹However, importantly note that this table is for the single X-mode simulation.

related to the Q mode, which according to Kramer et al. (2006) implies a larger surface charge density, which however is not exactly equivalent to the particle number density (λ).

While there is a very subtle difference in the PPAs of PSR B1822–09, there is a $\sim 30^\circ$ shift in the PPAs between both modes of PSR B0943+10 (Fig. 5.33), which is expected to have a small value of α , given that its W is very wide relative to its $\rho(P)$. Because of a clear difference in the α of PSRs B1822–09 and B0943+10, we are led to investigate further in the next chapter.

To summarise the different aspects of the mode-switching phenomena, the characteristics of flux density are distinct from those of other modal properties such as sub-pulse modulation and the PC, as suggested from the following findings. Firstly, the mode which has the PC (which is the opposite mode which has the sub-pulse modulation) is reversed between PSRs B1822–09 and B0943+10 (Tab. 5.5). Secondly, the pulse profiles of the modes between two epochs are inconsistent, in such a way that a profile of one mode in one epoch resembles the profile of the other mode in the other epoch, while the other modal properties remain with the same modes. This long-term instability is observed for PSRs B1822–09 and B0943+10 in Fig. 5.32 and Fig. 5.34. And thirdly, the frequency reversal of the modal profiles of PSRs B1822–09 and B0826–34 at ~ 300 and ~ 1500 MHz indicates that the relationship between flux density and the mode-switching is frequency-dependent. Nevertheless, it is interesting for future studies to consider that the complicated characteristics of the flux density in the mode-switching are a combination of effects from various mechanisms, such as the radio emission process, the scattering model (Section 5.1.1), and cyclotron absorption (Chapter 3).

Most importantly, these pulsars are mode-switching pulsars after all which means any measurements, at least for the pulse profile, at any frequency can still be subject to change. In the next chapter we study the supposed connection of PSR B1822–09 to other mode-switching and nulling pulsars.

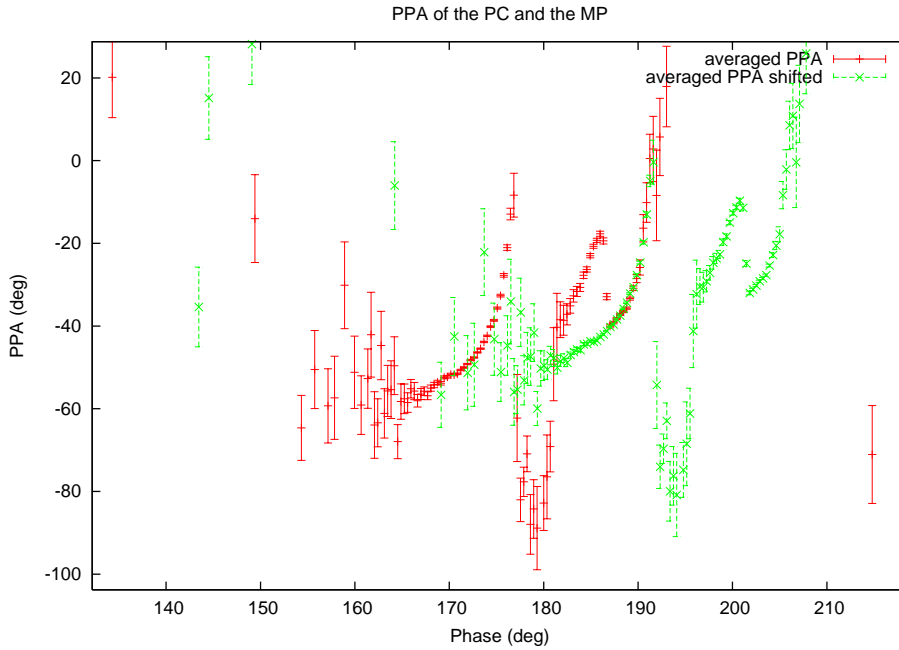


Figure 5.35: To demonstrate that the PC’s PPA (*red*) resembles the swing of the trailing component’s PPA (*green*). The PC’s PPA is shifted by phase+1° and PPA+8°.

5.4.2 Petrova’s Model: the PC-IP dilemma

In terms of polarisation, the most obvious characteristic consistent with Petrova’s model (Section 5.1.1) is the extremely high L of the PC which demonstrates the single-mode of propagation of the outgoing wave in the longitudinal scattering scenarios (also see Fig. 5.24). Because the scattering process is a particle-to-particle reaction, this model also seems to fit rather well to the short-burst or ‘rain-like’ emission of the PC pulses.

Due to the aberration effects, the separation of the PC and the MP, which is $\sim 16^\circ$, suggests an r_s of ~ 20000 km (Petrova 2008b), or around half of r_{LC} . This is large compared to r_{em} of typical pulsars believed to be $\leq 0.1r_{LC}$. However, the rather nice RVM-like swing of the PC’s PPAs (Fig. 5.7) does not cope well with the concept of the aberration shift (Chapter 1, which assumes $r_{em} \ll R_{LC}$) because, due to the delay in the PPA with respect to the intensity profile, the leading part of the PPA swing is expected to be observed.

However, it could be a different situation for the scattering altitude, r_s , which is large comparable to the R_{LC} and may require different interpretation. Nevertheless, assuming that the PC’s PPAs are indeed the from the same foot print of

the field lines as the MP, we show that the swing in the PC's PPAs with a shift of $+15^\circ$ and $+8^\circ$ to the phase and PPA value, respectively, appears to be identical to component 2, as shown in Fig. 5.35. If the PPAs of the PC and component 2 are indeed of the same field lines, the shifted version of PPAs in Fig. 5.35 is fitted with the RVM method, in which the best-fit solutions are shown in Fig. 5.36. The fact that the best-fit α indicates an orthogonal rotator strongly shall support the above interpretation.

In contrast, the fact that it is found to be almost exactly 180° away from the MP makes PSR B1822–09's IP hard to fit into this scattering scenario, considering the extra time the emission takes to travel across the magnetosphere (Petrova 2008a). However, we note that the IP's L is unusually low, which might be what is predicted in the transverse scattering where both of the propagation modes are viable, hence the dilution in L .

Because ω_G does not depend strongly on observing frequency, the MP's separation from the PC and IP components and their pulse widths are therefore not expected to evolve with frequency. This is certainly confirmed for the PC, but not the width of the IP (GJK+94). In terms of the spectrum as discussed by Petrova (2008a), the outgoing wave in the longitudinal modes is predicted to be at a higher frequency than the incoming wave. This then supports GJK+94's finding of the flat spectrum of the PC component, as the energy from low frequency, in which pulsars are inherently brighter, is transported to higher frequency by this mechanism. For the IP, in contrast, the transverse scattering transports the energy from higher frequencies, in which pulsars are inherently weak, to lower frequencies. The spectrum of the IP therefore appears to be steeper than that of the MP (GJK+94's figure 11 and 13). Petrova (2008a) also points out that the state with a large multiplicity (λ) corresponds to the transverse scattering regime, and the opposite for the longitudinal scattering. This would indeed imply that there is more plasma in the Q mode of PSR B1822–09, and less in the B mode, which could be related to the negative number of the flux density calculated from what is inferred from the model for intermittent pulsars (see next chapter).

Although Petrova's model seem to explain the characteristics of the PC and the mode switching well, the IP of PSR B1822–09 which is exactly 180° -separated from the MP and correlating with MP, cannot be obtained from the model as the emission from the backwards scattering should take considerably additional time to travel across the magnetosphere and therefore is not expected to retain its 180°

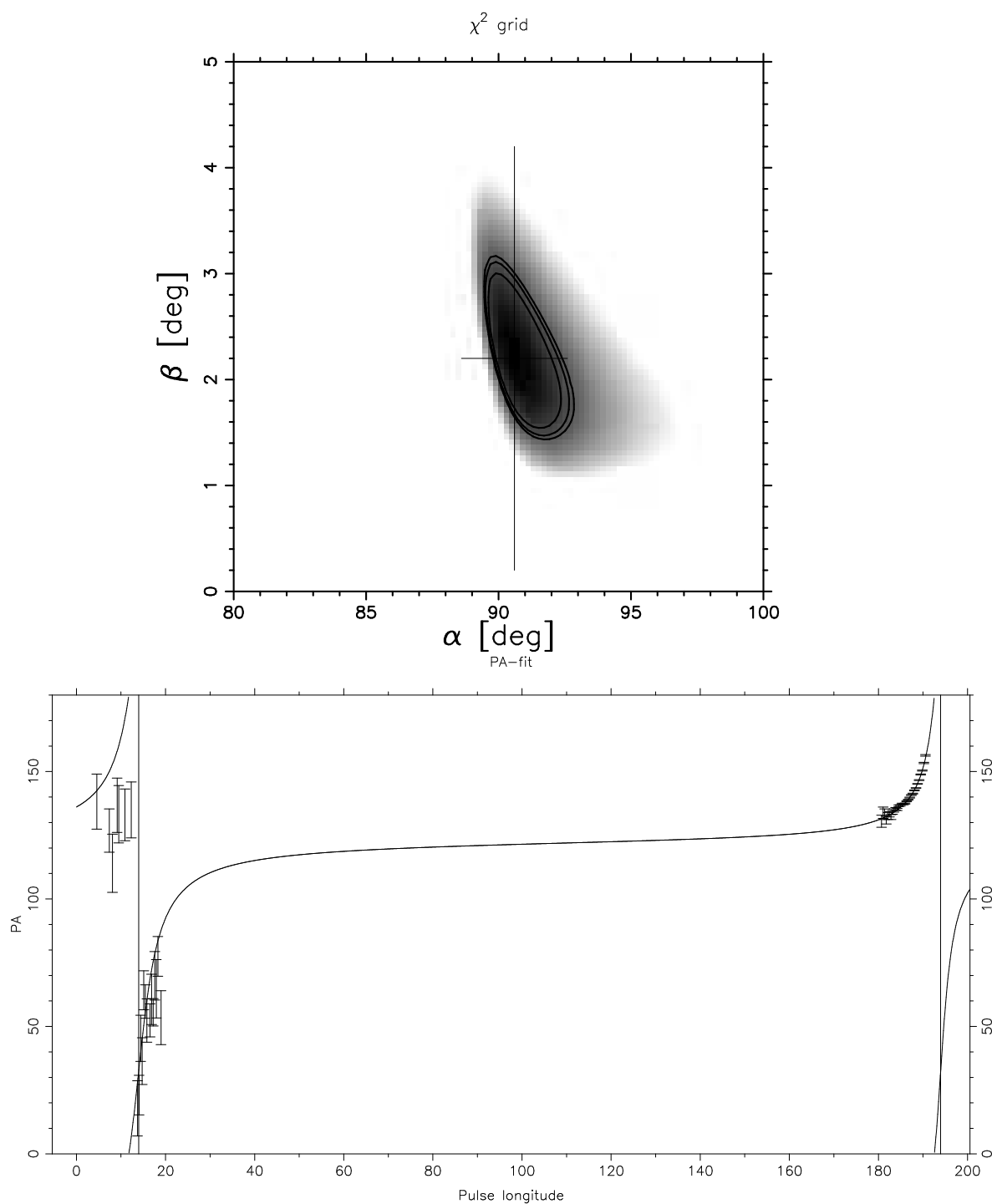


Figure 5.36: (*Top*) The best-fit χ^2 solutions from the RVM method with the best fit at $\alpha, \beta = 91^\circ, 2.2^\circ$ and $\chi^2_{\text{reduced}} = 4.2$. The three contours correspond to 1σ , 2σ , and 3σ levels. (*Bottom*) The best-fit RVM swing plotted with the input PPAs.

separation. Nevertheless, if the scattering process is indeed related to the PC and IP, and hence related to the mode-switching phenomena, it would be interesting to investigate further to understand which parameter(s) play a dominant role in deciding between the two types of scattering, which will therefore lead to a better clue of mechanisms behind the mode-switching.

Chapter 6

From Pulse Radiation to Pulsar Kinetics

In this chapter, we explore the context of intermittent pulsars PSRs B1931+24, J1841+0500 and J1832+0029, for which it is understood that the correlation between the quasi-periodically active emission and the change in spin frequency $\dot{\nu}$ is caused by a changing magnetospheric current (Kramer et al. 2006; Camilo et al. 2012; Lorimer et al. 2012). In the open-field lines region, the charge particles responsible for the radio emission stream along the field lines and escape the magnetosphere as a pulsar wind. This wind causes a magnetic-braking torque, which affects the loss rate of pulsar’s rotational energy, i.e. the spin-frequency derivative ($\dot{\nu}$).

In the work of Lyne et al. (2010), PSR B1822–09 was shown to have a similar $\dot{\nu}$ -switching behaviour. We explore the possibility of explaining this pulsar and the other profile-switching pulsars in Lyne et al. (2010) with the same model for intermittent pulsars. In addition, with the currently known sample of intermittent pulsars, we independently derive the inclination angle (α) of those pulsars, using the beam model in Section 1.1, to compare with those predicted by the magnetosphere model of Li et al. (2012b).

6.1 B1931+24: The One Where It All Began

With a rich amount of timing data available from the Lovell Telescope, Kramer et al. (2006) (hereafter KLO06) found that PSR B1931+21 appears to be quasi-periodically active (known as ‘intermittency’) in which it is in the ‘ON’ mode for ~ 5 days and

then becomes undetectable during the ‘OFF’ mode for ~ 30 days. By inspecting the ‘timing noise’ of the pulsar closely, they discovered that it is actually caused by the fact that this pulsar spins down faster when it is in the ON state. Having derived two separate $\dot{\nu}$ values for the ON and OFF states ($\dot{\nu}_{\text{ON}}$ and $\dot{\nu}_{\text{OFF}}$), they are able to achieve a timing model which fits the observations with good precision. They interpreted the correlation between the intermittency and the switching $\dot{\nu}$ as a change in the loss rate of the pulsar’s kinetic energy depending on whether or not there is a current of charged particles created. With this hypothesis, they show that the resulting charge density ($\bar{\rho}$) appears to be very close to the canonical Goldreich-Julian density ($\bar{\rho}_{\text{GJ}}$)¹. This can be understood by considering the loss rate of the pulsar’s rotational energy in each state,

$$\dot{E}_{\text{ON}}^{\text{total}} = \dot{E}_{\text{ON}}^{\text{w}} + \dot{E}_{\text{ON}}^{\text{others}}, \quad (6.1)$$

$$\dot{E}_{\text{OFF}}^{\text{total}} = \dot{E}_{\text{OFF}}^{\text{w}} + \dot{E}_{\text{OFF}}^{\text{others}}, \quad (6.2)$$

where \dot{E}^{others} represents the contribution to \dot{E} due to other mechanisms, such as the magnetic dipole radiation or high-energy radiation, and $\dot{E}_{\text{ON}}^{\text{total}} = 4\pi^2 I \nu \dot{\nu}_{\text{ON}}$ and $\dot{E}_{\text{OFF}}^{\text{total}} = 4\pi^2 I \nu \dot{\nu}_{\text{OFF}}$. The energy loss rate due to magnetic-braking torque (T) from the current flow, i.e. the pulsar wind \dot{E}^{w} , is approximated to be

$$\dot{E}^{\text{w}} = 2\pi T \nu; \quad T \sim \frac{2}{3c} I_{\text{pc}} B_0 R_{\text{pc}}^2, \quad (6.3)$$

where B_0 is the surface magnetic field strength and $I_{\text{pc}} \sim \pi R_{\text{pc}}^2 \bar{\rho} c$ is the electric current flow on the surface, crossing the polar cap of a radius of R_{pc} (Harding et al. 1999, hereafter HCK99).

A one-hour-long Arecibo observation was conducted to confirm that the radio emission from the pulsar completely ceased during the OFF state, as there is always a possibility that the emission is instead very weak (Lyne 2012), as for example is observed for PSR B0826–34 (Section 5.4.1). The absence of radio emission likely implies that $\dot{E}_{\text{OFF}}^{\text{w}}$ is very small compared to $\dot{E}_{\text{ON}}^{\text{w}}$. Assuming that $\dot{E}_{\text{ON}}^{\text{others}} \approx \dot{E}_{\text{OFF}}^{\text{others}}$, Eqs. 6.1 and 6.2 can be written as

$$\dot{E}_{\text{ON}}^{\text{w}} = \dot{E}_{\text{ON}}^{\text{total}} - \dot{E}_{\text{OFF}}^{\text{total}}. \quad (6.4)$$

¹Note that $\bar{\rho}$ is used to indicate a charge density to avoid confusion with the beam opening angle (ρ).

Substituting \dot{E}^{total} (Eq. 6.3) and \dot{E}^{w} (Eq. 6.3) in Eq. 6.4, the charge current density is a function of $\Delta\dot{\nu} = -|\dot{\nu}_{ON} - \dot{\nu}_{OFF}|$ as

$$\bar{\rho} = \frac{3I_{\text{pc}}\Delta\dot{\nu}}{R_{\text{pc}}^4 B_0} = 102 \text{ esu/cm}^3, \quad (6.5)$$

where $B_0 = 3.2 \times 10^{19} \sqrt{-\dot{\nu}_{\text{OFF}}/\nu^3}$ G and the polar cap radius $R_{\text{pc}} = \sqrt{2\pi R^3 \nu/c}$ km, assuming a canonical neutron star radius of 10 km and a moment of inertia of $I = 10^{45}$ g cm². This current density, calculated for PSR B1931+21, is remarkably close to its Goldreich-Julian density, $\bar{\rho}_{\text{GJ}} = B_0 \nu/c = 99 \text{ esu/cm}^3$, which is the required charged density to sustain the induced electric field (\bar{E}_{induced}).

KLO06 therefore showed that the current density of the pulsar wind is sufficient to account for the pulsar's slow-down mechanism. Although these observations indicates that the $\dot{\nu}$ changes are related to intermittency, there is no suggestion of the underlying mechanism for the $\dot{\nu}$ change.

6.2 A Magnetospheric Model

Li et al. (2012a) have proposed a magnetospheric model to demonstrate and predict how the change in $\dot{\nu}$ is dependent on α , by comparing the two states of the magnetosphere (ON=plasma-rich, OFF=vacuum). The underlying mechanism can be explained as follows. To avoid a discontinuity of the induced electric fields near the light cylinder, it is required that there is an electric current, returning from the light cylinder back to the polar cap to complete the ‘circuit’ (Contopoulos et al. 1999’s figure 3). It is understood that this current is responsible for the magnetic-braking torque in Eq. 6.3. Because the structure of the induced electric fields depends on α , $\dot{\nu}_{\text{ON}}/\dot{\nu}_{\text{OFF}}$ is therefore dependent on α .

Recently another two pulsars, PSRs J1832+0029 (Kramer 2008; Lyne 2009; Lorimer et al. 2012, hereafter LLM12) and J1841+0500 (Camilo et al. 2012, hereafter CRC12) were reported to be active intermittently. With more observational results now available, Li et al. (2012b) (hereafter LST12) have updated their model (Li et al. 2012a) by allowing plasma to be trapped in the closed-field-line region, while the open-field-line zone is vacuum-like, during the OFF state. The model now can account for the published values of $\dot{\nu}_{\text{ON}}$ and $\dot{\nu}_{\text{OFF}}$. The solution obtained by LST12 are shown in Fig. 6.1. Absent from the plot, the uncertainty level is described to increase from $\sim 10\%$ at $\alpha = 90^\circ$ to $\sim 30\%$ when $\alpha = 30^\circ$.

Table 6.1: The measured and calculated parameters from a KLO06’s type of calculation (*top* half) and LST12’s model (*bottom* half). The symbol † indicates that numbers quoted from LLM12.

PSR	B1822-09	B1931+24	J1841+0500	J1832+0029
P (s)	0.769	0.814	0.913	0.534
τ (Myr)	0.23	1.6	0.4	1.6
$\dot{\nu}_{\text{ON}} - \dot{\nu}_{\text{OFF}} \times 10^{-15}$ (Hz/s)	-2.9	16.3	N.A.	5.55
$\bar{\rho}$ (esu/cm ³)	-14.6 ²	100	400 [†]	62
$\bar{\rho}_{\text{GJ}}$ (esu/cm ³)	260	99	130 [†]	44
$\dot{\nu}_{\text{ON}}/\dot{\nu}_{\text{OFF}}$	1.03	1.51	2.65	1.77
α_{LST12} (°)	90 ³	65	35	55
$W_{5\%}^{300\text{MHz}}$ (°)	16	20	31	25
ρ [5.5 ↔ 7.5] (°)	6.3 ↔ 8.6	6.1 ↔ 8.3	5.8 ↔ 7.9	7.5 ↔ 10.3
$\alpha_{\rho-P}$ [5.5 ↔ 7.5] (°)	52 ↔ 90	38 ↔ 56	22 ↔ 30	37 ↔ 55
α (°)	~ 90	-	-	-
Reference	Ch.5	KLO06	CRC12	LLM12

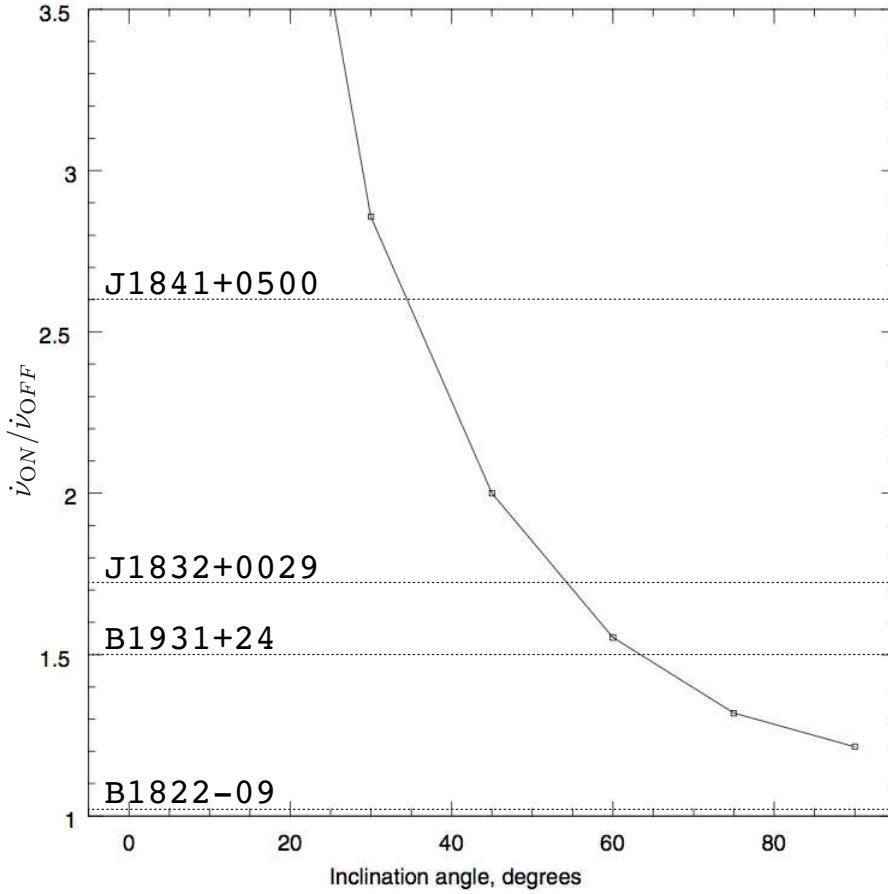


Figure 6.1: The relationship between $\dot{\nu}_{ON}/\dot{\nu}_{OFF}$ and α as predicted by LST12. The four horizontal lines indicates the measured values of PSRs B1822-09, B1931+21, J1841+0500 and J1832+0029.

Following similar calculations by KLO06, the inferred $\bar{\rho}$ and $\bar{\rho}_{GJ}$ of PSRs J1841+0500 and J1832+0029 are summarised in Tab. 6.1.

From the work in Chapter 1 and 2, we estimate the inclination angle ($\alpha_{\rho-P}$), independently, to compare with LST12's values (α_{LST12}) (Fig. 6.1). Because the pulsars in this sample have large periods, they have small values of $\rho \propto P^{-1/2}$, and hence have small values of β . This means we can apply Eq. 1.21, as

$$\frac{W_{5\%}^{300\text{MHz}}}{2} \approx \frac{\rho}{\sin \alpha_{\rho-P}}, \quad (6.6)$$

where $\rho = k \cdot P^{-1/2}$ and $W_{5\%}^{300\text{MHz}}$ is the pulse width, at 5% of peak intensity at

300 MHz, estimated⁴ from the references in the table, except for PSRs B1931+24 and J1832+0029, for which the values are measured from Fig. 6.2 and Fig. 6.3, respectively. Lower and upper limits of ρ are calculated using $k = 5.5^\circ$ and 7.5° to indicate a level of uncertainty.

It is not surprising for PSR B1822–09’s spin-down ratio to be much small (1.03) than LST12’s prediction, given that the mode-switching phenomenon is believed to be a mild (or partial) supply disruption of the charged particles, rather than a complete disappearance of the current.

The calculated $\alpha_{\rho-P}$ for PSRs B1931+24, J1841+0500 and J1832+0029 appear to be slightly smaller than the values predicted by LST12. However, taking into account the uncertainty in LST12’s model, we conclude that both α ’s are consistent, within the uncertainty.

In Fig. 6.2, a polarisation profile of PSR B1931+24 observed with the Arecibo telescope at 430 MHz is shown. The flip of V strongly suggests that the profile’s peak corresponds to the magnetic axis, and hence indicates that a part of the trailing side is missing. With a rather wide profile and a high degree of linear polarisation, the intrinsic PPAs are unfortunately too narrow to be constraining and is more over heavily distorted. This is demonstrated by the three RVM swings in the *bottom* panel, which are for $\alpha = 90^\circ, 75^\circ$ and 60° . Similarly for PSR J1841+0500, the α measured from the PPA swings is unreliable because of two complicated OPM jumps and the apparent high level of distortion (CRC12).

⁴And interpolated if they are at different frequency.

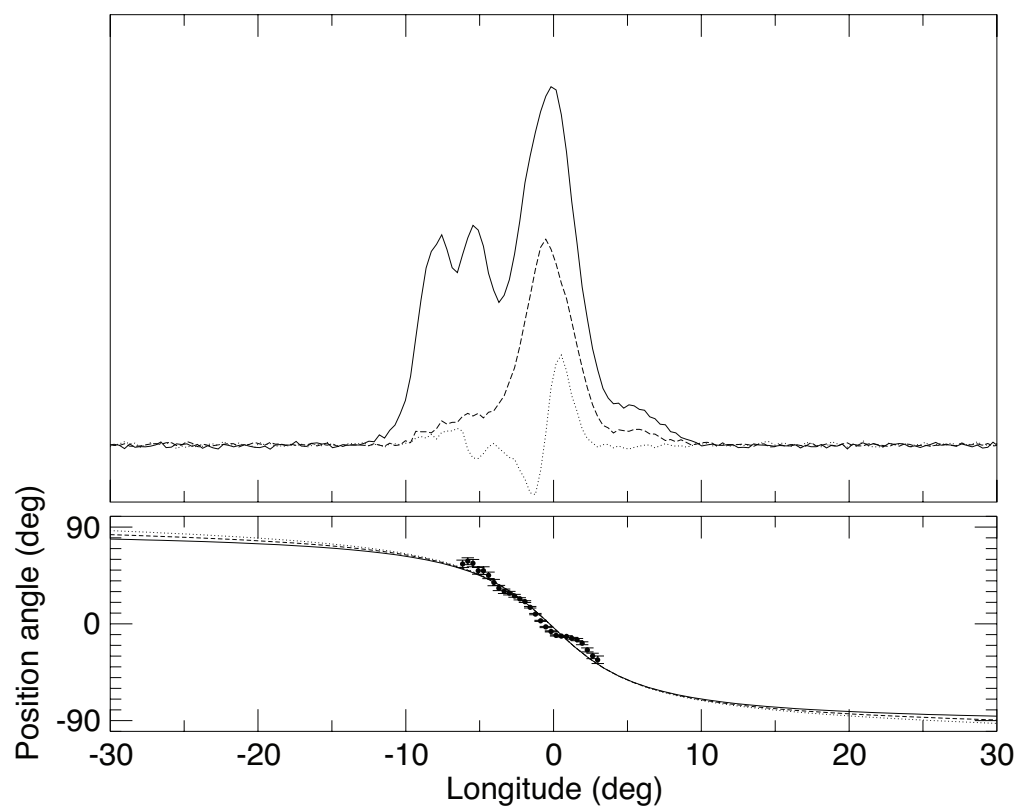


Figure 6.2: A polarisation profile of PSR B1931+24 observed with the Princeton Mk-IV system using the Arecibo 300-m telescope at 430 MHz, where the *dash* and *dotted* lines are the linear and circular polarisation, respectively (*top* panel). Three PPA swings modelled with $\alpha = 90^\circ, 75^\circ$ and 60° are plotted the PPA curve (*bottom* panel). (Lorimer, D.R., Stairs, I.H., Kramer, M. *private communication*)

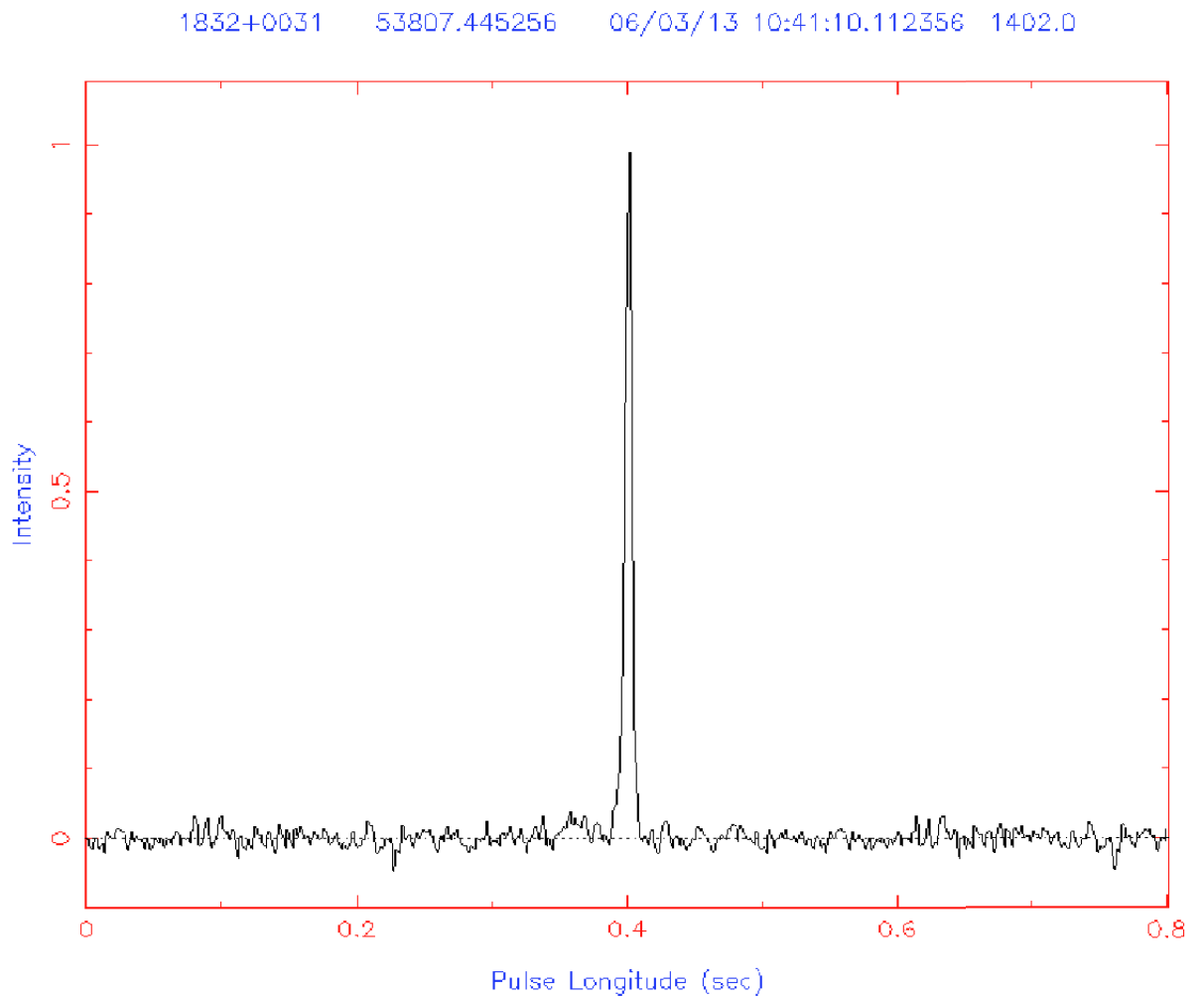


Figure 6.3: An average pulse profile of PSR J1832+0029, at 1.4 GHz, produced from a total observing time of 85 hours by the Lovell Telescope (Jordan, C. *private communication*).

6.3 From Intermittency to Profile-switching

In this section we apply the concepts of LST12’s model, which explains intermittent pulsars and profile-switching pulsars, on the assumption that the two phenomena are caused by similar mechanisms, but different in magnitudes.

6.3.1 Charged Current and Flux Density

PSR B1822–09 has been demonstrated to have pulse profile changes resulting in variations in $\dot{\nu}$ (Lyne et al. 2010). In the previous chapter we have demonstrated that the precursor (PC)/main-pulse (MP) peak ratio of the average profiles is not an accurate indicator for the time the pulsar spends in the B mode, which may explain why the correlation between the peak ratio and $\Delta\dot{\nu}$ is not perfect, except the two very large changes (Fig. 5.25). In this section we assume that the change in $\dot{\nu}$ of PSR B1822–09 is caused, similar as for the intermittent pulsars, by a change in the charge current flow in the polar cap region, which consequently is also responsible for the switches in the fraction of the modal time (see scenarios 2 and 3 of the MC simulations in Section 5.3.3). Therefore, we employ a modified form of Eq. 6.4, as

$$\dot{E}_Q - \dot{E}_B = \dot{E}_Q^w - \dot{E}_B^w. \quad (6.7)$$

The fact that the pulsar spins down faster when it is in the Q mode, $\dot{E}_Q(\dot{\nu} = -88.9 \times 10^{-15} \text{ Hz/s}) \geq \dot{E}_B(\dot{\nu} = -86 \times 10^{-15} \text{ Hz/s})$, indicates that $\dot{E}_Q^w \geq \dot{E}_B^w$, which results in a negative $\bar{\rho}$ if we assume that the radio flux density (S) is proportional to $\bar{\rho}$. This is, however, not surprising given that, in the previous chapter, the pulse intensity of this pulsar was concluded to be very loosely related to the mode-switching phenomenon, as opposed to other modal properties (see Section 5.4.1).

In addition, there appears to be a similar anti-correlation, indicated for PSR B0943+10, where the pulsar’s Q mode is suggested to have a stronger current flow because X-ray pulsations are exclusively detected in this mode (Section 5.4.2). And, Karastergiou et al. (2011) have shown that PSR J0738–4042 expresses a similar anti-correlation when a leading component becomes brighter, incorporating the decrease in $\dot{\nu}$, which is also similar to the PSR J1602–5100 (van Leeuwen 2012⁵). However, the fact that these two pulsars are observed to switch only

⁵http://www.astro.uni-bonn.de/NS2012-2/Brook_0738-4042.pdf

once, as opposed to pulsars in LHK+10, suggests that this phenomena have a very long timescale, possibly because the change on the beam takes place very locally on the pulsar beam.

It is understood that the radio luminosity may depend on various factors, such as, the number of accelerated particles, how efficient the production of coherent emission is, and the effect of cyclotron absorption, which give rises to both a correlating and an anti-correlating relationship between S and $\bar{\rho}$, including the dependency on the viewing angle (the LOS) as parts of the beam may have different properties. We therefore explore further to the question of whether there is a relationship between S and $\bar{\rho}$. The combined study of intermittent pulsars and moding pulsars may indeed offer a chance to answer this question.

We have estimated the difference in S of the pulsars listed in Lyne et al. (2010) and Lyne (2012), in which the statistics are summarised in Tab. 6.2. Note that only pulsars with significant change in S are included. It now appears that there are equal numbers of correlation and anti-correlation cases. As will be explained below, this can be interpreted as an effect of the LOS being different for different pulsars. As Lyne et al. (2010) suggested that there is an indication that the core region seems to be stronger in the high $\dot{\nu}$ state, i.e. correlating, we extend this picture to also include the observed anti-correlation.

We propose here that the core region of the pulsar beam indeed has a correlating S - $\bar{\rho}$ relationship, while the conal region has an anti-correlation. This picture is therefore able to explain the pulsars with symmetric profiles, i.e. with known component-types, as depicted in Fig. 6.3.1. For LOS (*b*), which might be applicable to PSRs B1828–11 and B2035+36, those for which we can identify the core and cone, the high $\dot{\nu}$ state the profiles' core components are stronger than the conal part. Also for PSR J0738–4042, where the sub-component in the leading part of the profile becomes brighter relative to the other components, this picture might be valid.

As in Chapter 5, Backus et al. (2010) have shown that for PSR B1822–09 the IP has a weak leading part of the profile, which results in a total MP-IP separation of 180° . This suggests that the IP is the trailing cone. The fact that the IP is observed during the Q-mode, which is more dominant in the high $\dot{\nu}$ state, therefore results in an anti-correlation between S and $\bar{\rho}$. In our picture this is explained with LOS (*a*). Also, note that if the LOS would be such that its IP was the only component to be observed, PSR B1822–09 would have appeared to

be an intermittent pulsar with $\dot{\nu}_{\text{ON}}(=\dot{\nu}_{\text{Q}}) > \dot{\nu}_{\text{OFF}}(=\dot{\nu}_{\text{B}})$.

Furthermore, we recall the profile-shape reversal phenomenon between two frequencies of PSRs B1822–09, B0826–34 and B0943+10 (Section 5.4), in which we found that the pulse shapes, i.e. relative intensity between individual components, of the bright and weak modes can be opposite (Tab. 5.6) or vary differently at different epochs (Fig. 5.32 and 5.34). This indicates that the relationship between S and $\bar{\rho}$ can also be frequency- and time-dependent. For example, at 1532 MHz, the MP of PSR B1822–09 in the B mode (low $\dot{\nu}$ state) is core-dominated, while in the Q mode (high $\dot{\nu}$ state) it is cone-dominated (Tab. 5.6). Although the correlation at 1532 MHz is indeed opposite to what is expected from our proposed model. At 325 MHz the MP of the B and Q modes are reversed, making the $S - \bar{\rho}$ correlation consistent with our picture at this frequency.

At this stage, we can only conclude that S may depend on $\bar{\rho}$ differently, depending on the location of the emission source in the magnetosphere—both in terms of distance from the magnetic axis, i.e. core versus conal components, and on the observing frequency, i.e. altitude. Consequently, this indicates that S is not a good indicator for $\bar{\rho}$, which can be calculated from $\dot{\nu}$. Further simultaneous multi-frequency analysis on these mode-switching pulsars shall provide more information on how the dependency of S on $\bar{\rho}$ develops with observing frequency. Nevertheless, as discussed in Section 5.4.2, Petrova (2008a) suggests that because large multiplicity (λ) value corresponds to the transverse scattering of the Q mode, and the opposite for the B mode. Petrova’s model seems to be able to explain the opposite correlation between S and $\bar{\rho}$, at least for the moding pulsars which have PCs, PSRs B1822–09 and B0943+10.

Lyne (2012) also presents a new orthogonal profile- $\dot{\nu}$ -switching pulsar, PSR J2047+5029 (Janssen et al. 2009, Janssen et al., in prep.), where the MP in the normal mode, which has a larger $\dot{\nu}$, is stronger than the MP in the abnormal mode by a factor of ten. However, what is interesting is that despite the change in the MP’s intensity together with the change in the spin-down, the IP retains its shape and intensity. This is indeed another indication that the change in the plasma flow of profile-changing pulsars can take place locally, and, consequently, it should be also interesting to investigate whether intermittent pulsars can have a single-pole shutdown of the plasma flow.

According to Eq. 6.5, with $R_{\text{PC}} = 1.7 \times 10^4$ cm and $B_0 = 6 \times 10^{12}$ G, the expected difference in $\bar{\rho}$ between the two modes is ~ 17 esu/cm³, which is a

Table 6.2: The (anti)correlation between S and $\bar{\rho}$, and the $\dot{\nu}$ ratio of the $\dot{\nu}$ -profile-switching pulsars. †: Switch once. ‡: correlated mode-switching X-ray and radio pulsations. *: http://www.astro.uni-bonn.de/NS2012-2/Brook_0738-4042.pdf.

PSR	correlation	$\dot{\nu}_1/\dot{\nu}_2$	Reference
J0738–4042	-†	-	Karastergiou et al.*
B0943+10	-‡	-	Hermesen et al. (2013)
J1602–5100	-†	-	Karastergiou et al.*
B1822–09	-	1.033	Lyne (2012)
B1828–11	+	1.007	Lyne (2012)
B2035+36	+	1.13	Lyne (2012)
J2043+2740	+	1.06	Lyne (2012)
J2047+5029	+	1.030	Janssen et al. in prep.

factor of six smaller than that of PSR B1931+24. In fact, *all* profile-switching pulsars presented in Lyne (2012) have values of $\dot{\nu}$ ratio well below the LST12’s line of intermittent pulsars in Fig. 6.1, especially for the measurements from the two orthogonal pulsars, PSRs B1822–09 and J2047+5029, which is where the prediction is most likely to be violated.

This is consistent with the statement that the variation for mode-switching pulsars is smaller because it is due to a *partial* disruption of the charged particle supply, as opposed to a total shut-off in the intermittent pulsars. And, consequently, the separation between the measured values and the upper limit from the model reflects how close the profile-switching pulsars are in becoming intermittent pulsars. Note that if α is known, then the observed ratio of $\dot{\nu}$ should be below the curve in Fig. 6.1. Nevertheless, starting from intermittent pulsars which are relatively well understood, we can use the mode-switching pulsars to study local effects, i.e. the geometry, in the pulsar beam and magnetosphere, which cannot be done with the intermittent pulsars because there is no emission at all in the OFF state.

6.3.2 Impact On Polarisation Properties

If the charged current density ($\bar{\rho}$) in mode-switching pulsars is changing between modes, it may as well have an impact on the polarisation properties of these modes differently. Indeed, in the paper by Hibschan & Arons (2001) it was suggested that the current flow is affecting the measured the absolute PPAs (slightly distorts

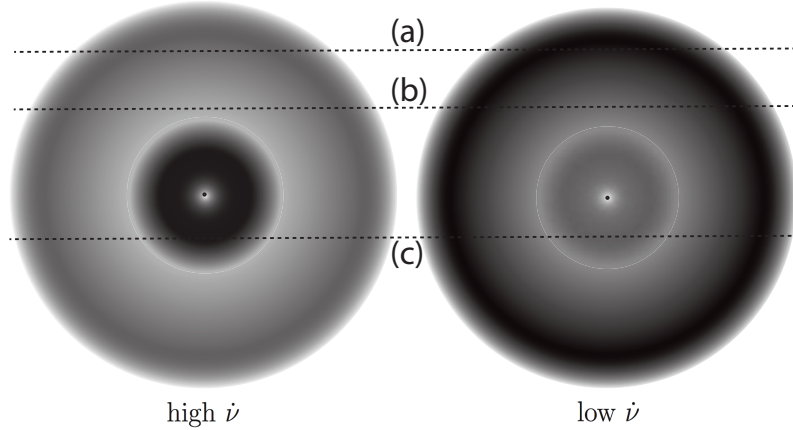


Figure 6.4: The proposed model to explain the observed relationship between the flux density and the charged current density. In this figure a *darker* colour indicates brighter flux. The correlation is opposite for the core- and conal-type components such that the core is relatively bright in the high $\dot{\nu}$ state and the opposite for the cone component. The three *dotted* lines represent the LOS's path for: (a) the anti-correlation which is seen for a pulsar of which only the cone is observed, such as the IPs of PSRs B1822–09; (b) both the correlation and the anti-correlation are observed in mixed-type profiles, for PSRs J0738–4042, B1828–11 and B2035+36.

its shape). As we will explain later, the amount of the shift in the PPAs is depending on the inclination angle (α), such that we expect no shift for orthogonal rotators and a larger shift for aligned rotators. Certainly, this effect is implicitly assumed also in the plasma propagation effects discussed in Chapter 3, although, it was not implemented in the used simulation codes. Fortunately, we are now at the position to use the moding pulsars, PSRs B1822–09 and B0943+10, that we discussed in Chapter 5, to test this model and hence make a connection to discussions previously described in this chapter.

We found that, in terms of plasma perturbations affecting the polarisation, the results from the polarisation analysis of PSRs B1822–09 and B0943+10 in Chapter 5 are consistent with the results from LST12's model (Fig. 6.1). For PSR B1822–09, which is an orthogonal rotator, there is no distinct variation between the PPAs of the modes, while there appears to be a 30° offset in the PPA values for PSR B0943+10, which is believed to be a nearly-aligned rotator, as will be shown below. As a direct consequence of LST12's model, in which the difference in $\bar{\rho}$ of the two modes is inversely proportional to α , pulsars with small α are then expected to have a larger difference in the plasma charge density and hence

a larger offset between the perturbation on the PPAs of both modes. This is indeed consistent for both $\alpha \sim 0^\circ$ and 90° in the calculation by Hibschan & Arons (2001) (Eq. 6.8 below). Unfortunately, despite having a small α , the spin-down switching of PSR B0943+10 remains unmeasurable. This might be because a fundamental limitation arising from switches which are too fast for $\dot{\nu}$'s measurements to be made.

Because our analysis on the effects of wave propagation in chapter 3, using Beskin & Philippov (2012)'s model, does not include the contribution of the charged-particle current, i.e the wind, in the magnetic field term, we are unable to estimate the perturbation on PPAs using the code in Chapter 3. However, the just-described shift in the PPAs offers a new and unexpected way to determine the change in $\bar{\rho}$, after all. We recall the calculation made by Hibschan & Arons (2001), in which they derive the perturbation on the PPAs due to the charged current as

$$\Delta\Psi_{HA01} = \frac{10}{3} \frac{r_{em}}{R_{LC}} \frac{I}{I_{GJ}} \cos\alpha \cdot \left(1 - \frac{7}{40} \sin^2\theta_\beta\right) \text{ rad}, \quad (6.8)$$

where I_{GJ} is the current correspond to $\bar{\rho}$, and θ_β is the colatitude of the magnetic field in polar co-ordinates (r, θ, ϕ) .

Assuming that the PPA offset of PSR B0943+10 ($\sim 30^\circ$) (Fig. 5.33) is due to the difference between $\Delta\Psi_{HA01}^{B-mode}$ and $\Delta\Psi_{HA01}^{Q-mode}$, caused by the fact that the currents in both modes are different, we calculate $\Delta I = |I_B(\bar{\rho}_B) - I_Q(\bar{\rho}_Q)|$ as follows. Using Eq. 6.6 with $k_{cone} \sim 6^\circ$ and the fact that this pulsar has a very wide profile ($W \sim 43^\circ$) and a long period ($P \sim 1.1$ s) results in a very small α ($\sim 15^\circ$). Approximating $\sin^2\theta_\beta \sim 0$, and with a typical emission height of pulsars $r/R_{LC} = 0.1$, we obtain $\Delta I/I_{GJ}$ to be ~ 1.5 . And because $I \propto \bar{\rho}$ and with $\bar{\rho}_{GJ} \sim 60$ esu/cm³, the difference in $\bar{\rho}$ between the B and Q modes ($\Delta\bar{\rho}$) is therefore ~ 90 esu/cm³.

Taking this further by reversing KLO06's calculation in Section 6.1, we estimate the expected $\Delta\dot{\nu}$ as

$$\Delta\dot{\nu} = \frac{\Delta\bar{\rho} R_{pc}^4 B_0}{3I} \sim 2 \times 10^{-15} \text{ Hz/s}, \quad (6.9)$$

which is smaller than the measured $\Delta\dot{\nu}$ of the three intermittent pulsars (Tab. 6.1). This is what we expect given that PSR B0943+10 is a mode-switching pulsar, and therefore should have relative small changes in the current, hence its smaller $\dot{\nu}$. In comparison to PSR B1822-09, the ratio between the calculated $\Delta\dot{\nu}$ and

$\bar{\rho}_{GJ}$ in Tab. 6.1, which is ~ 17 , and incorporated with the fact that its α is close to $\sim 90^\circ$, Eq. 6.8 indicates a minimal change in $\Delta\Psi_{HA01}$ between the modes of PSR B1822–09, which is indeed consistent with the observation.

Nevertheless, among other estimated variables, using r_{em} derived from Eq. 1.24, the resulting r_{em}/R_{LC} (~ 0.01) indicates the value of $\Delta\dot{\nu}$ to be $\sim 20 \times 10^{-15}$ Hz/s, which is larger than the value when $r_{em}/R_{LC} = 0.1$ (and the $\dot{\nu}$ itself) by an order of magnitude. If this is to be the case, the fact that the $\Delta\dot{\nu}$ of PSR B0943+10 cannot yet be determined may post a question of the validity of Eq. 1.24.

6.4 Conclusions

Pioneered by KLO06, a direct connection between the pulsar's spin stability and the pulsar radio emission has been established, with two other cases by CRC12 and LLM12. After demonstrating that the timing noise in PSR B1931+24 is essentially caused by switches between $\dot{\nu}_{\text{ON}}$ and $\dot{\nu}_{\text{OFF}}$, KLO06 provide an explanation that the change in $\dot{\nu}$ and the intermittency are related via the same phenomena, i.e. the escaping charged particles in the open-field-lines zone.

The magnetospheric model of LST12 predicts a relation between the $\dot{\nu}_{\text{ON}}/\dot{\nu}_{\text{OFF}}$ ratio and the inclination angle (α) as due to the fact that the amplitude of the return current depends strongly on α . In order to test LST12's results, we derive $\alpha_{\rho-P}$ using the $\bar{\rho}-P$ relationship defined in Chapter 1. Within the errorbars, the estimated $\alpha_{\rho-P}$ are consistent with LST12's prediction for the three intermittent pulsar and PSR B1822-09.

Implications of LST12's model for the mode-switching pulsars are made in terms of studying the flux density (S) and the perturbation on the PPAs. At the current stage, we are able to identify an equal number of pulsars with a correlation and an anti-correlation between S and $\Delta\bar{\rho}$, derived from $\Delta\dot{\nu}$. For some cases, there appears to be a pattern where the core component tends to have a correlation, with an anti-correlation for the cone component. However, there is also an indication that this is frequency-dependent. We suggest that the complicated relation between S and $\bar{\rho}$ is a result of combinations of both correlative (e.g. the number of accelerating particles or the process of coherent emission) and anti-correlative (e.g. plasma frequency and cyclotron absorption) individual mechanisms, which vary at different frequencies. (Simultaneous) multi-frequency observations are vital for further studies of this relationship.

We are able to confirm that the perturbations on the PPAs of PSRs B1822-09 and B0943+10, due to the difference in the current flow, are consistent with LST12's model. For PSR B0943+10, a difference in the charged current density can be associated with the vertical offset between the PPAs in both modes. This appears to provide a reasonable $\Delta\dot{\nu}$, which is smaller than those of the intermittent pulsars, as is expected, and is remarkably close the pulsar's $\dot{\nu}$.

Chapter 7

Summary

We have studied pulsar polarisation aspects in order to obtain the geometry of pulsar beams and the effects of propagation in the magnetosphere in Chapters 2 and 3. The methods of polarisation calibration were explored and tested on datasets obtained with the Lovell Telescope in Chapter 4. In Chapter 5, a detailed analysis of the moding pulsar PSR B1822–09 was made using high-quality datasets observed with the Lovell Telescope, calibrated using the best method tested in Chapter 4. In the last chapter we applied the magnetospheric model used for explaining intermittent pulsars to profile-switching (or ‘moding’) pulsars, in which we found supporting evidence that the correlation between the change in the spin-down ($\dot{\nu}$) and pulse profile shapes of these two types of pulsars are due to similar mechanisms.

The conclusions are:

- The geometry measured using the Rotating Vector Model (RVM) is not usually well constrained because: 1) information from the polarisation position angle (PPA) is limited, i.e. the typical pulse width of pulsars is only a fraction of the full rotational phase; 2) above the height at which the emission originates, the PPAs can still be affected by other mechanisms, i.e. aberration and propagation effects. In order to reduce the impact of the first effect, improvements can be made by adding the additional constraint of the geometrical relationship between the beam width and the pulse width.
- The propagation effects can noticeably alter RVM-originated PPA swings. However, relative to their canonical values, the combination of plasma and

geometry parameters for which the RVM swing is minimally perturbed is: 1) large Lorentz factor; 2) small particle number density; 3) high plasma frequency; 4) low emission altitude; 5) when the inclination angle between the rotational and the magnetic axes (α) is close to $\sim 90^\circ$. This combination of the plasma parameters can be summarised into minimising the distance between the emission height, which is the point where the PPA is defined according to the RVM, and the polarisation-limiting radius, which is a radius at which the PPAs are no longer affected by the plasma effects. The dependency on α of the effects, which becomes stronger when $\alpha \rightarrow 0^\circ$, appears to be consistent to results of the plasma-related models by Li et al. (2012b) and Hibschan & Arons (2001), in conclusions below.

- The prediction of the propagation model by Beskin & Philippov (2012), that the pulse component is dominated by X-mode waves if the signs of the steepest gradient of the PPA swing and a Stokes V are the same, and opposite for the O-mode, is supported by statistics measured from pulse profiles published in Weltevredre & Johnston (2008a). However, the prediction seems to work only for profiles with a simple shape and sometimes the identification changes because the sign of V is opposite at different frequencies. It is therefore suggested that this model needs to be updated to explain more complicated profiles and the frequency dependency.
- Polarisation calibration for the Lovell Telescope data is still a work in progress. Nevertheless, we have shown that, depending on the availability of CAL observations, the *pac* method can be used. CAL observations are recordings of a pure linearly polarised signal injected directly into the feed. The *pac* software makes use of the known properties of this signal in order to derive parameters describing properties of the signal chain, which can be used to calibrate data recorded using the same observational set-up. We also found that the leakage terms, although with large scatter, are $\leq 20^\circ$ and centered around zero of the signal chain, on average.
- By comparing the moding pulsar PSRs B1822–09 and B0943+10, we found that the mode-switching phenomena appear to involve processes in the magnetosphere at all altitudes. Above the neutron star surface, the sub-pulse modulation, which is believed to be related to the transverse electric drift force in the polar gap region, appears to be mode-preferable for both pulsars.

The fact that the pulse shapes of both the Burst and Quiescence modes for the pulsars are stable (with respect to their switching timescales) indicates that the radio emission zone is correlating with the moding phenomena. Lastly, higher up in the magnetosphere, the fact that the PPA swings are also different in both modes suggests that the state of the plasma in the propagating zone is also switching depending on the modes. Note that one may also expect that the differences in the profiles and PPAs between the modes can also be related to aberration effects, that at different plasma states the emission height can be shifted, and hence the magnitude of aberration effects are different. However, this will result in an offset or in a different pulse width in the pulse profiles.

- Despite the above conclusion that the moding phenomena affect all of the magnetospheric levels, there is evidence that different component types, i.e. the core or cone, may respond to the switching differently, depending on observing frequency.
- The scattering model by Petrova (Petrova 2008a; Petrova 2008b; Petrova 2009) can explain the properties of the precursor (PC) of PSR B1822–09 in *most* aspects, except that it predicts the PC’s PPAs to be flat due to aberration effects. It can also explain the charge current density of moding pulsars PSRs B1822–09 and B0943+10, that the Quiescence mode (which is the weak mode) is predicted to have *more* charge density, according to the magnetospheric model for intermittent pulsars.
- The inclination angles (α) of intermittent pulsars PSRs B1931+24, J1841+0500 and J1832+0029 predicted from the magnetospheric model by Li et al. (2012b)—which explains that different states of the magnetosphere, i.e. switching pulse profiles, are related to the change in $\dot{\nu}$, depending on α of the pulsar—are consistent with those estimated from the geometrical relationship between the beam width and the pulse width, studied in Chapter 2, within their errorbars.
- The ratio between the $\dot{\nu}$ values of each state of the moding pulsars, measured by Lyne (2012), appears to be consistent with the results of the model by Li et al. (2012b), which is derived for intermittent pulsars, based on the assumption that the intermittent and moding pulsars are both governed

by similar mechanisms, i.e. the total (intermittent) or partial (moding) disruption of charged particle supply to the magnetosphere. This means that the $\dot{\nu}$ ratio of moding pulsars is expected to be smaller than that of intermittent pulsars, which is consistent with the data; particularly, for the $\dot{\nu}$ ratios of PSRs B1822–09 and J2047+5029 that their α values are close to 90° , which is the α value corresponding to the minimum $\dot{\nu}$ ratio and hence being most likely to be violated.

- By applying the calculation for the charge current density ($\bar{\rho}$) of intermittent pulsars derived by Kramer et al. (2006) to the moding pulsars in our sample, there appear to be equal numbers of cases with a correlation and an anti-correlation between the change in the pulse profile’s flux density and the change in $\bar{\rho}$. There are cases where the profile shape of modes reverses between frequencies. However, due to the fact that there is a limited number in our sample, we are unable to identify any pattern of how the flux density is related to the $\bar{\rho}$ at different frequencies and different parts of the pulsar beam.
- By applying the updated RVM equation by Hibsichman & Arons (2001), which includes the effect on the PPA due to the current of escaping charged particles, to the shift in the PPA values between the modes of PSR B0943+10, we found that the resulting $\bar{\rho}$ is consistent with the same order of the values of intermittent pulsars, which are calculated from the method in Kramer et al. (2006). The difference in the $\dot{\nu}$ of this pulsar can also be predicted. In addition, the fact that the offset in the PPAs is larger for PSR B0943+10, which is shown to be a nearly-aligned rotator, and that the offset is very small for PSR B1822–09, which is an orthogonal orthogonal rotator, is consistent with the results of the magnetospheric model by Li et al. (2012b), which predicts that the $\dot{\nu}$ ratio is at a minimum at $\alpha = 90^\circ$ and maximum at $\alpha \sim 0^\circ$. The result from this calculation can indeed be seen as evidence showing that the change in the PPAs of moding pulsars is due to the change in the states of the pulsar’s magnetosphere, similar to, although not as extreme as, the intermittent pulsars.
- Despite being able to understand that there is a connection between the pulsar’s rotational energy and the radio emission, we are yet to explore these questions, such as what are the reasons behind these switching states

of pulsar and why are there only two states?

Knowing the geometry of the pulsar beam is shown to be useful for understanding the phenomena taking place at different locations in the pulsar's magnetosphere, especially when incorporated with other independent constraints from measurements of the pulsar's spin-down rate. Further studies on combining additional constraints from different sources, e.g. γ -ray models, providing a more accurate geometry, will provide even further implications to constrain theoretical pulsar models. Analysis of the polarisation properties of other moding pulsars, as done with PSRs B1822-09 and B0943+10, will provide more information about how the flux density is related to $\bar{\rho}$, which will eventually lead to implications on pulsar radiation theory in general. Nevertheless, one of the limitations is often the number of measurements; a wide-field multi-beam radio telescope, e.g. LOFAR or the SKA, will certainly be necessary for monitoring and increasing the number of the known intermittent and mode-switching pulsars in the future.

Appendix A

Plots of $\text{RVM}_{\rho-W}$ Fits

This appendix contains the fitting resulting of the $\text{RVM}_{\rho-W}$ method in Chapter 2. The χ^2 diagrams are shown with the 1σ , 2σ and 3σ contours (*solid*) and the ρ contour (*dotted*). For the profile plots, the *top* panel shows the pulse intensity (*solid*), linear (*dashed*) and circular (*dotted*) profiles, while the *bottom* panel shows the polarisation position angle (PPA) overlaid with the best-fit RVM curve.

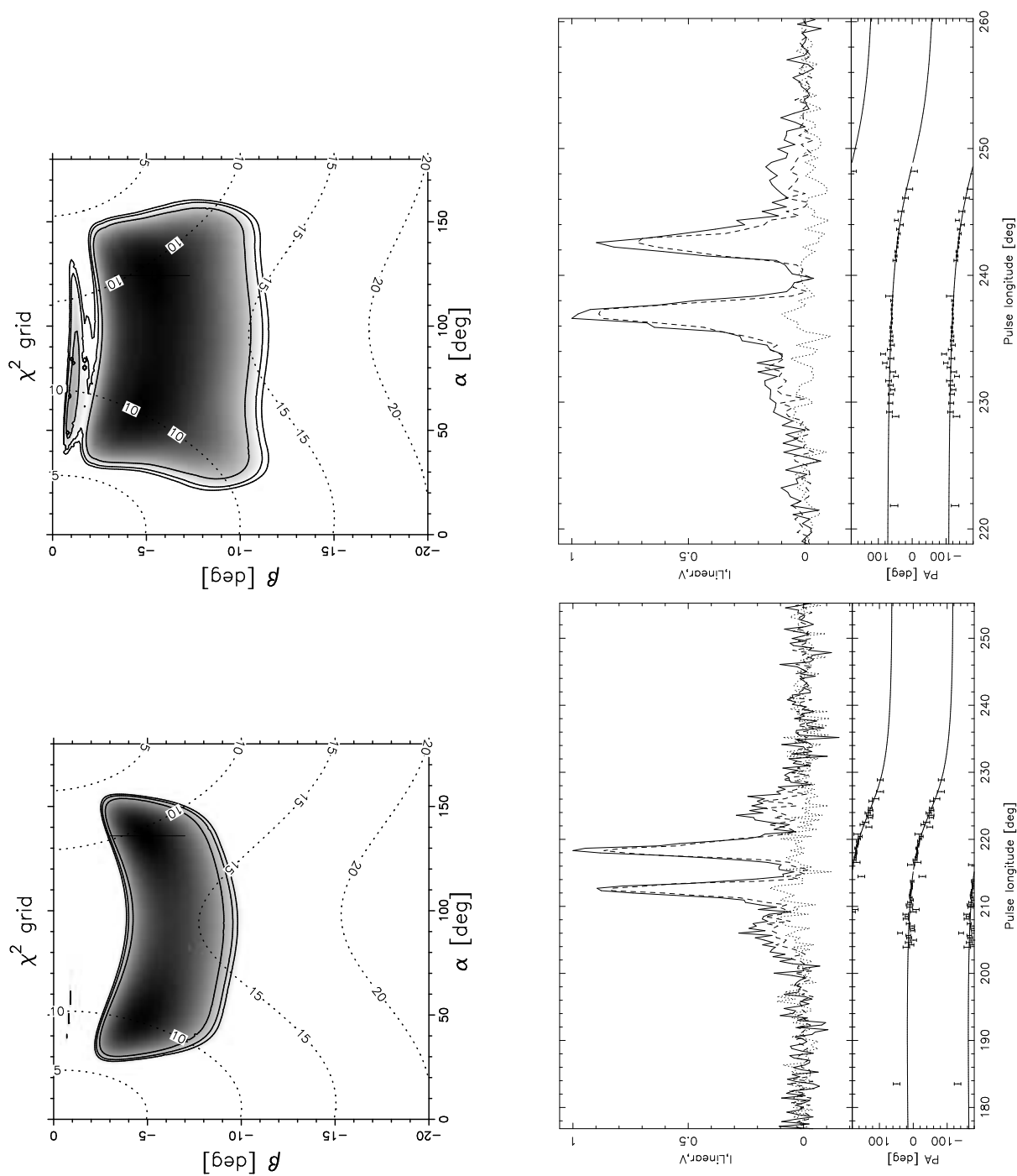


Figure A.1: PSR J0631+1036: (*top to bottom*) the plots are at 10 and 20 cm.

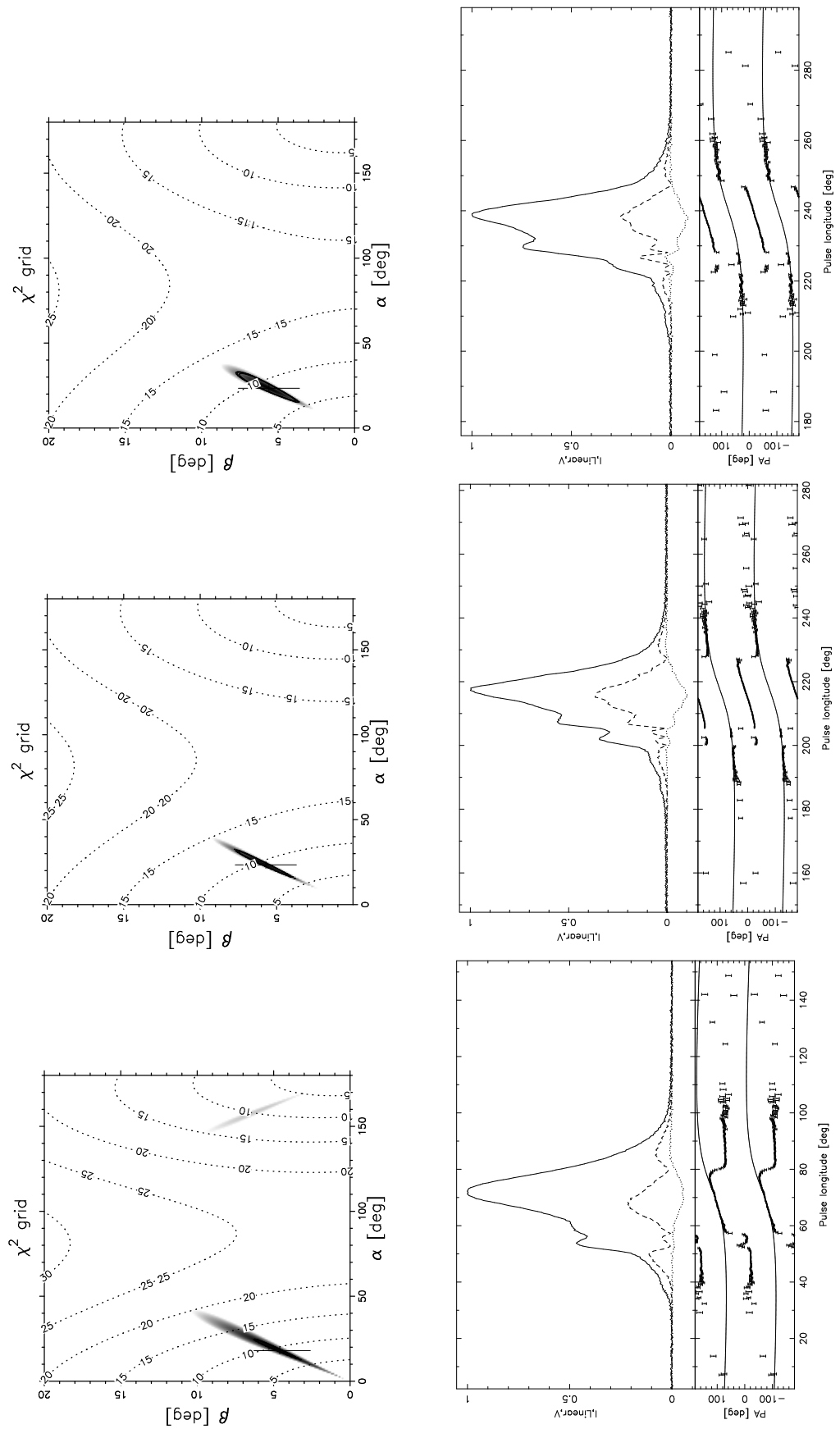


Figure A.2: PSR J0738-4042: (top to bottom) the plots are at 10, 20 and 50 cm.

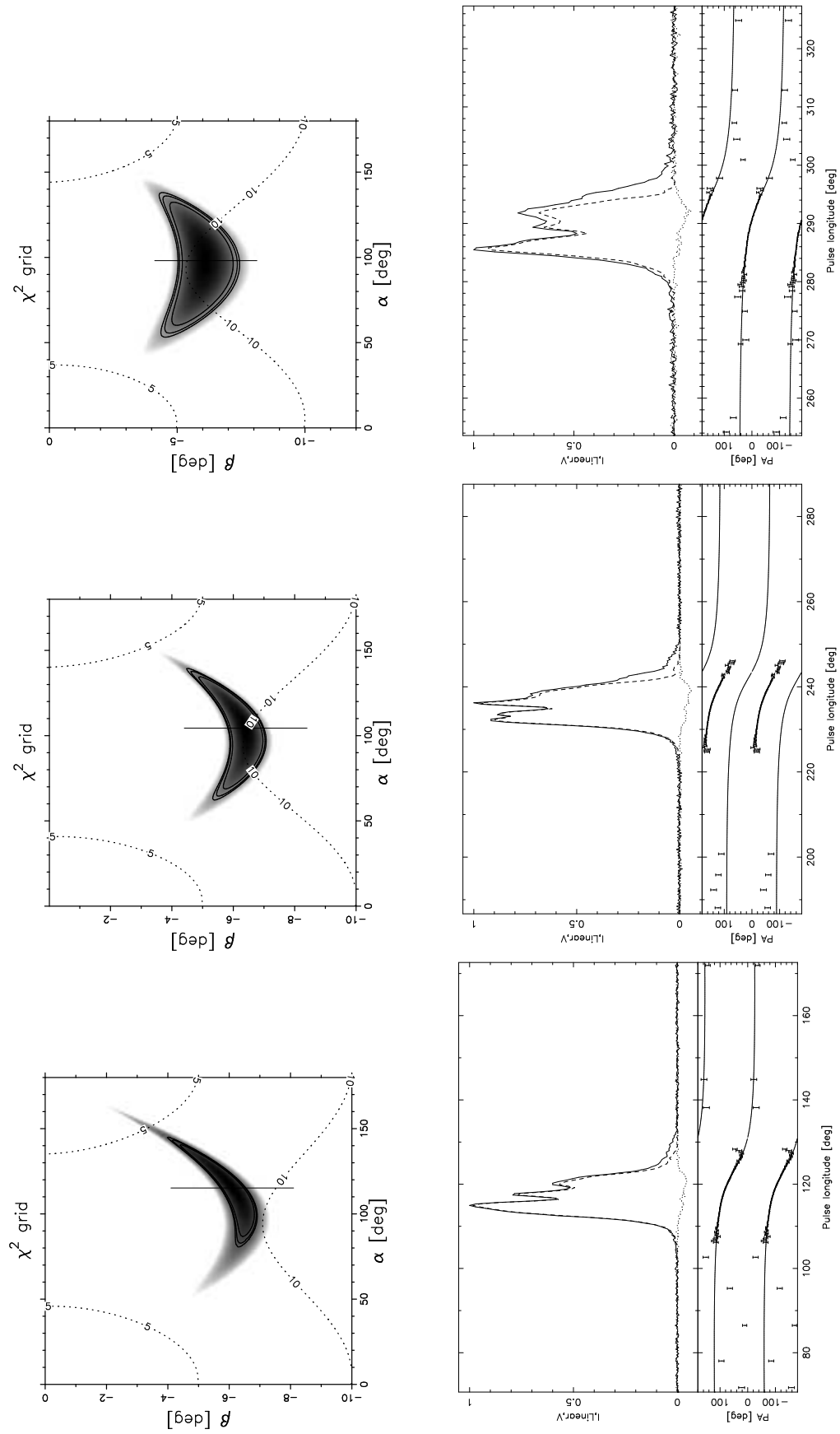


Figure A.3: PSR J0742-2822: (top to bottom) the plots are at 10, 20 and 50 cm.

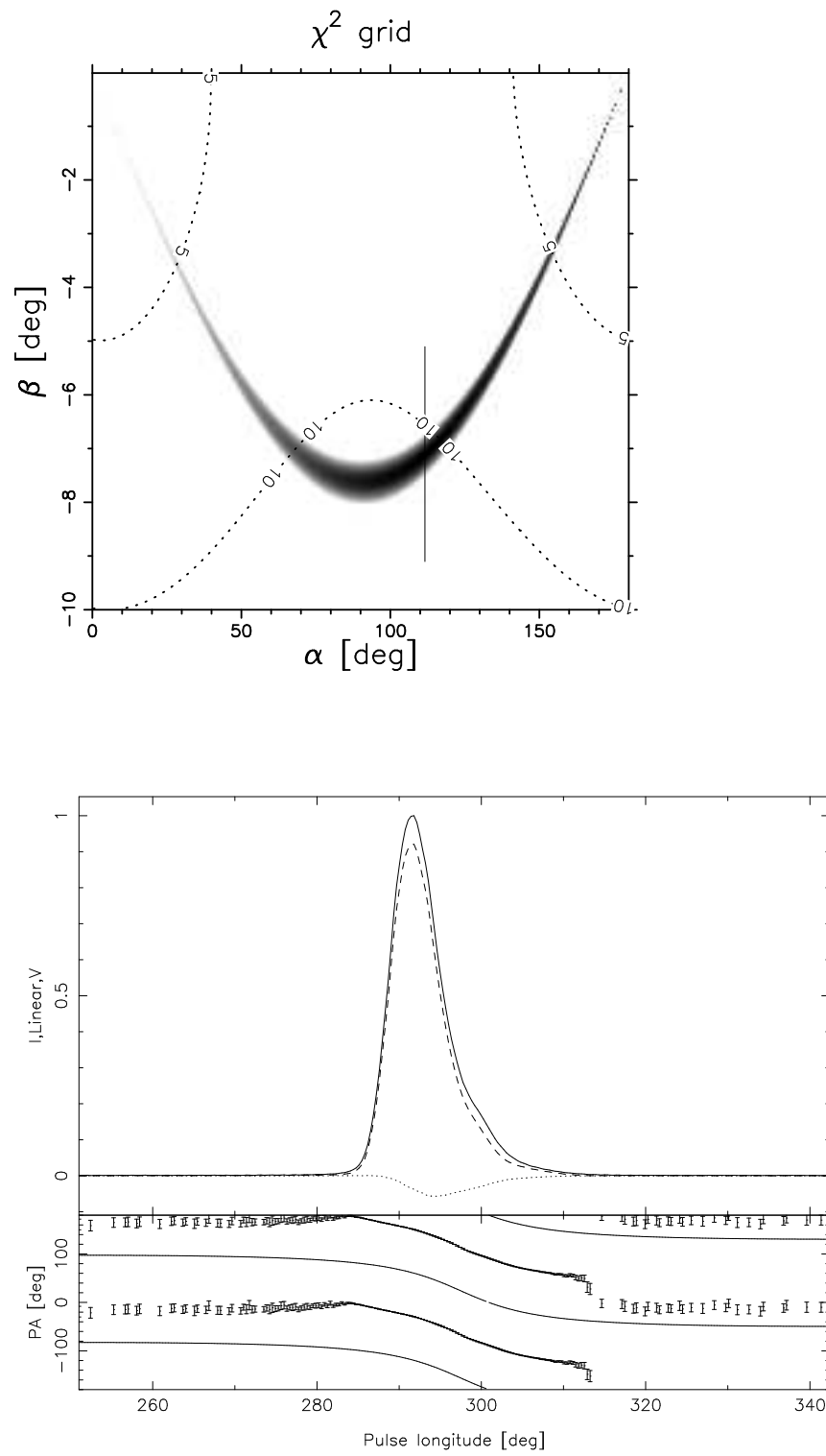


Figure A.4: PSR J0835-4510: at 20 cm.

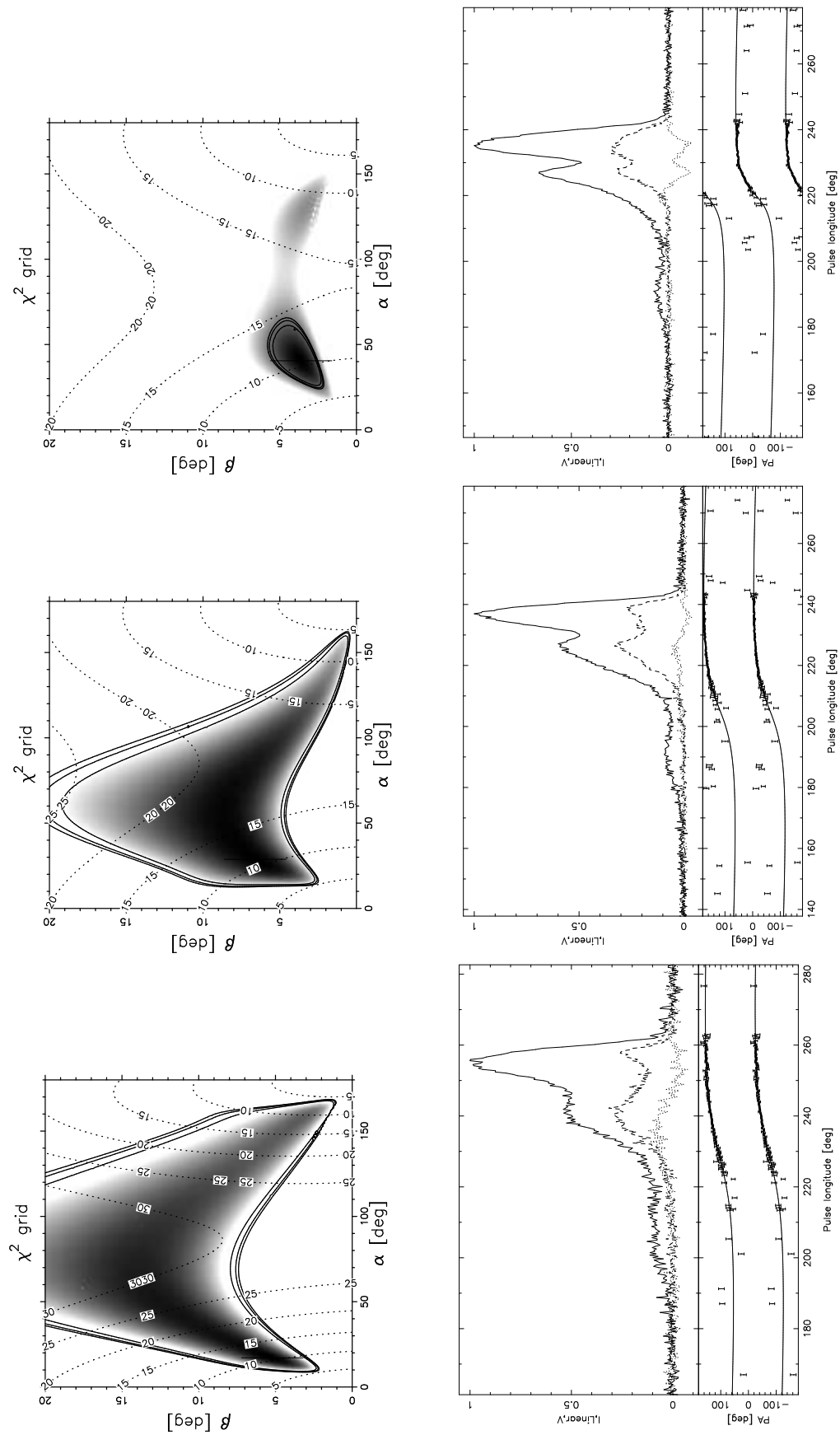


Figure A.5: PSR J0907-5157: (top to bottom) the plots are at 10, 20 and 50 cm.

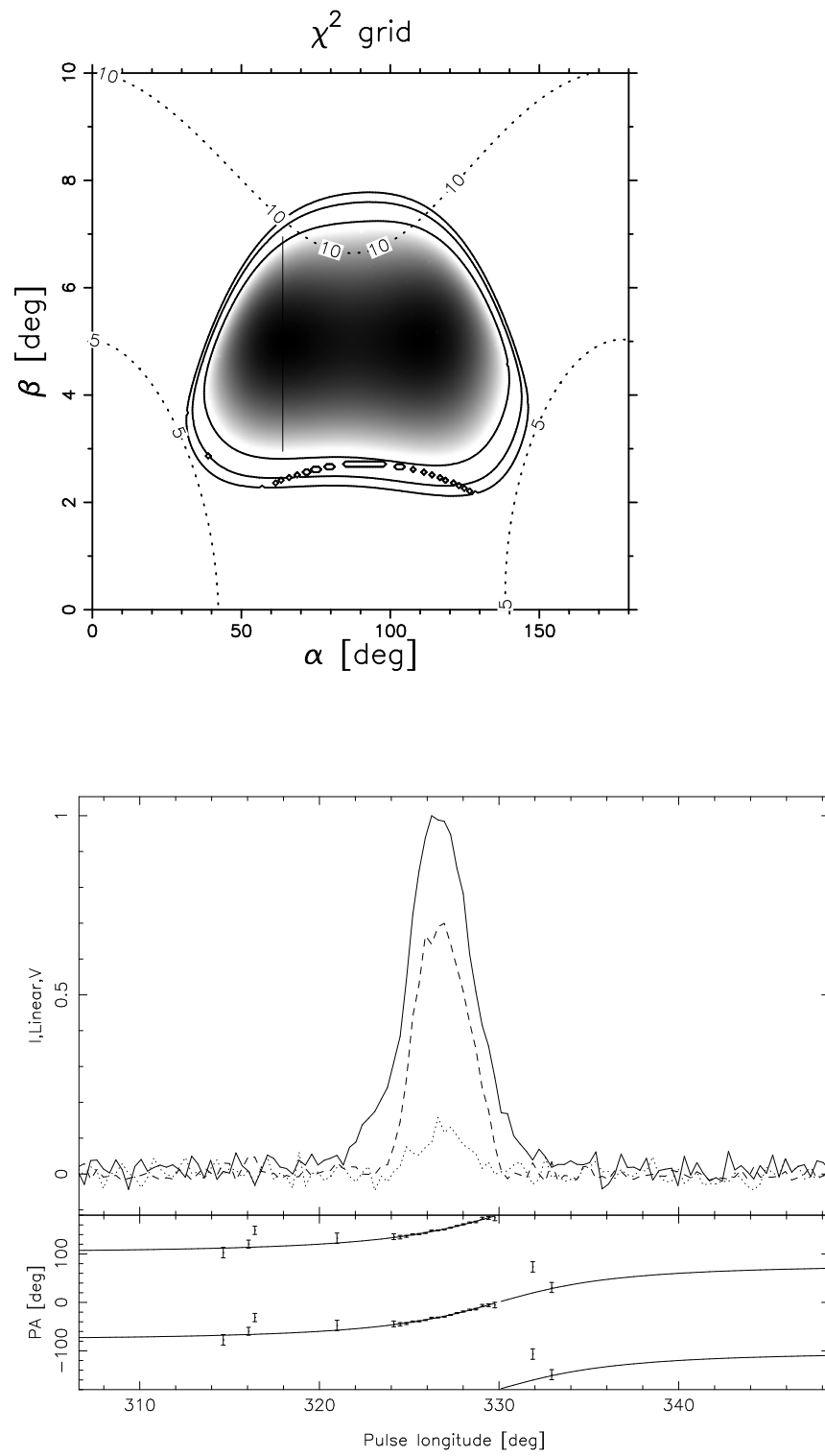


Figure A.6: PSR J0922+0638: at 10 cm.

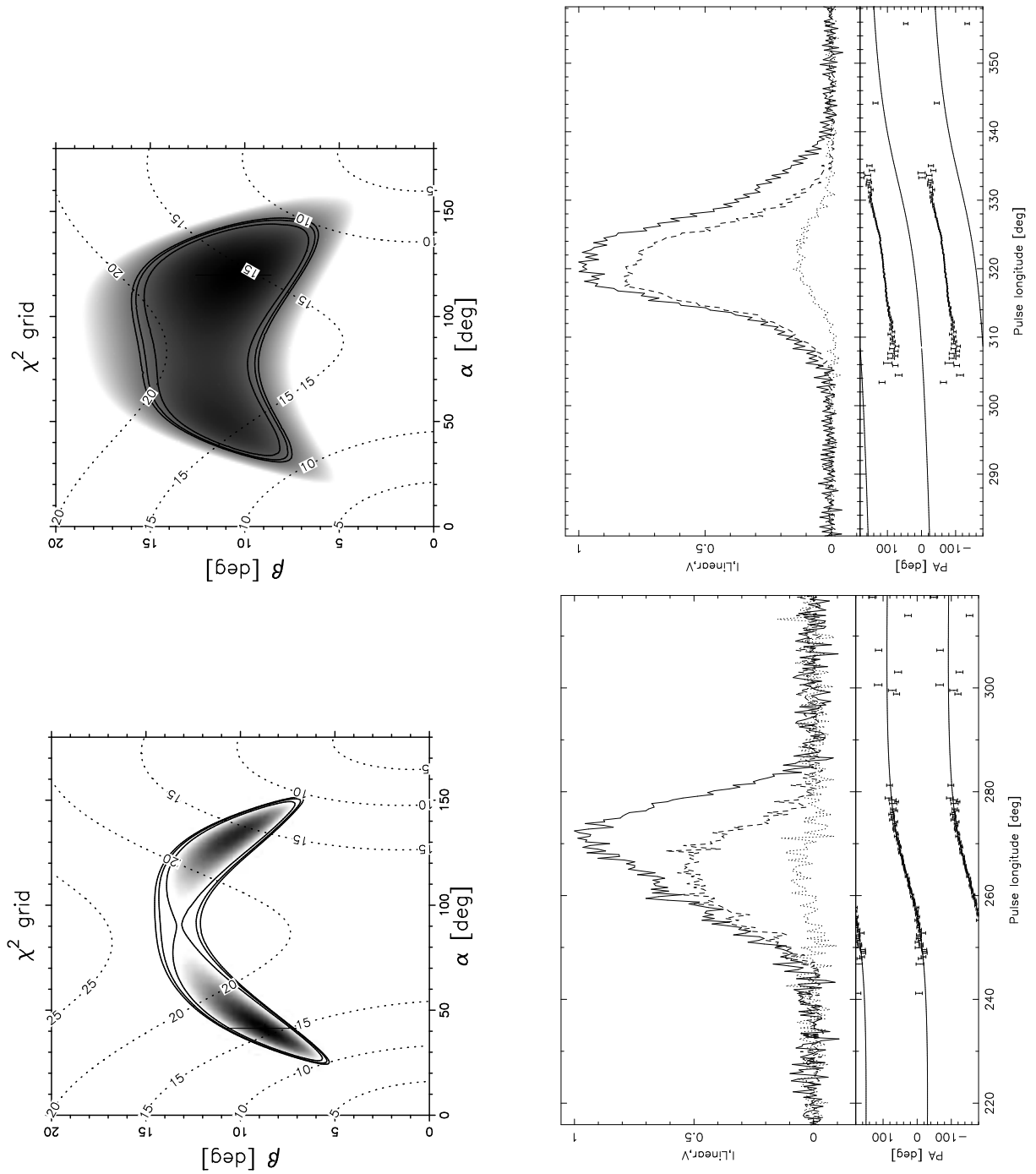


Figure A.7: PSR J1048-5832: (top to bottom) the plots are at 10 and 50 cm.

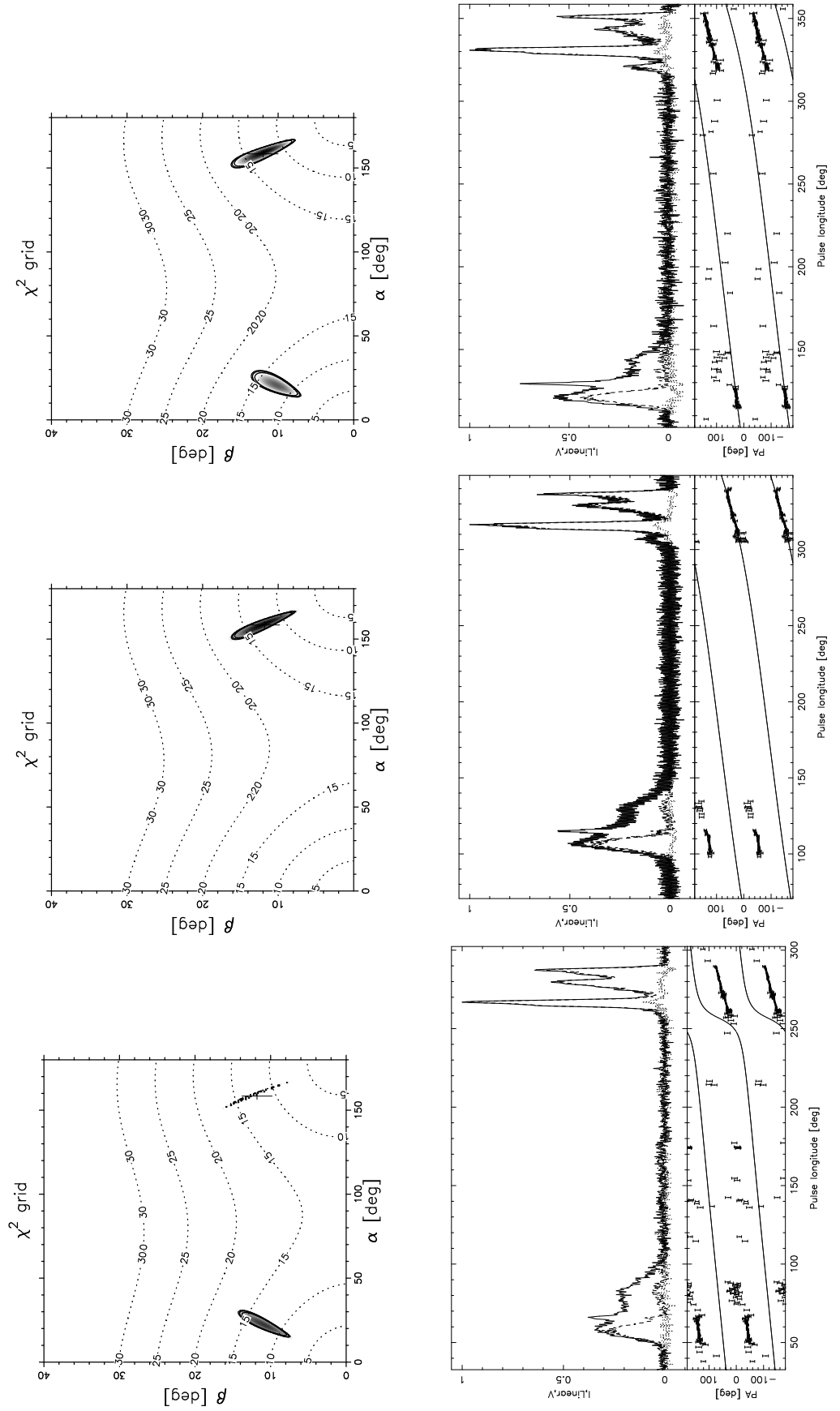


Figure A.8: PSR J1057-5226: (top to bottom) the plots are at 10, 20 and 50 cm.

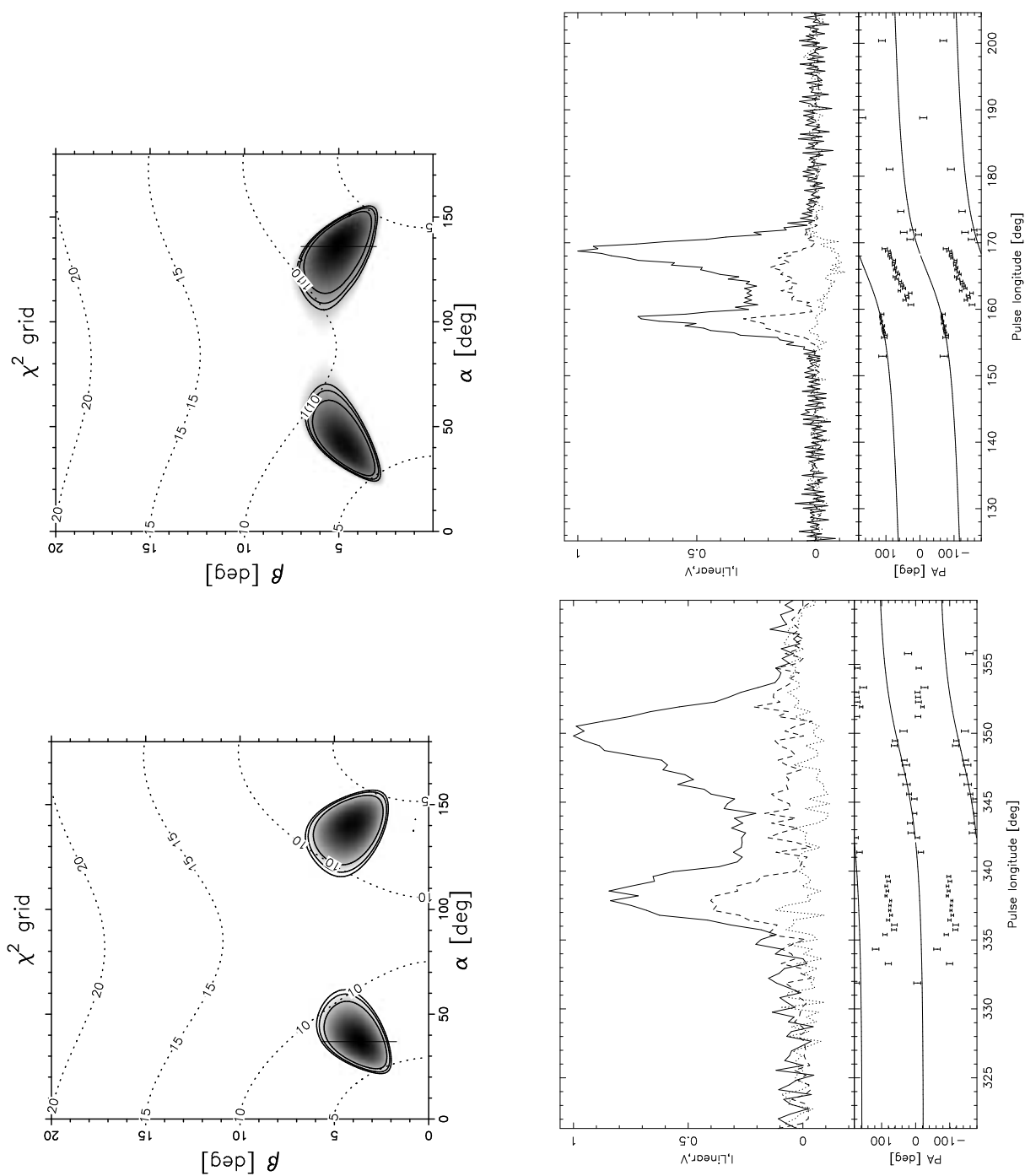


Figure A.9: PSR J1110-5637: (top to bottom) the plots are at 20 and 50 cm.

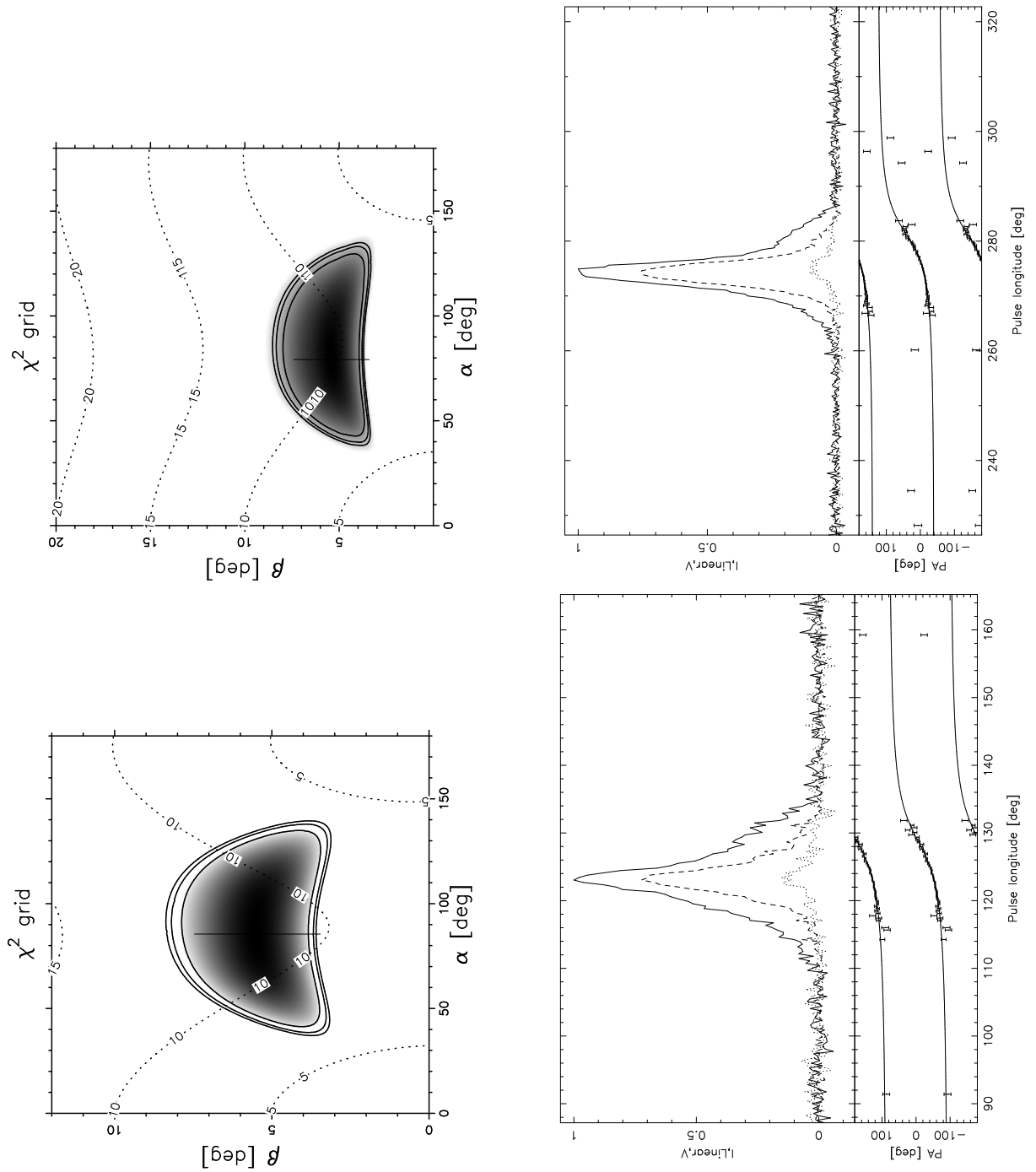


Figure A.10: PSR J1253-5820: (top to bottom) the plots are at 20 and 50 cm.

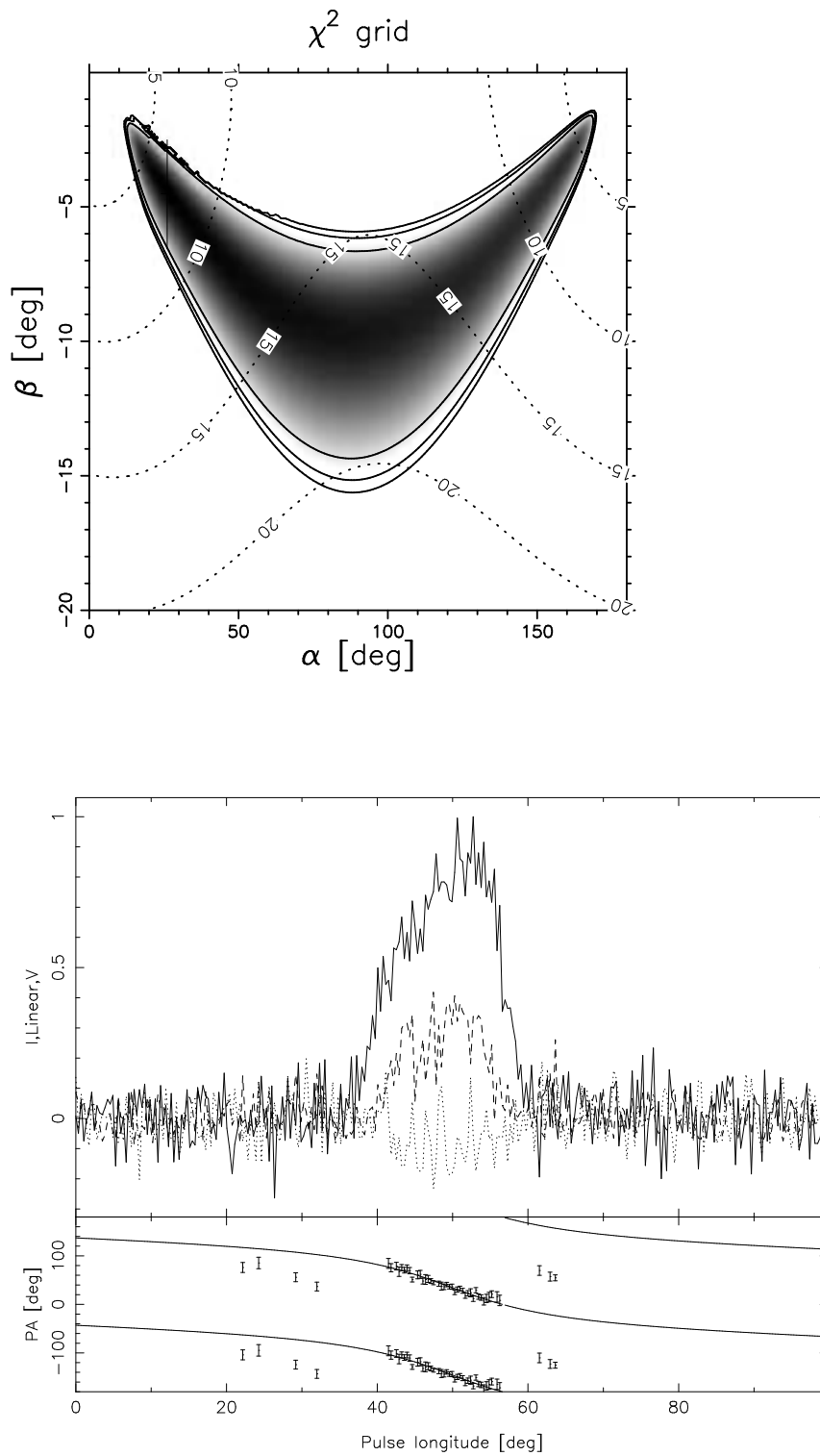


Figure A.11: PSR J1352-6803: (*top to bottom*) the plots are at 20 and 50 cm.

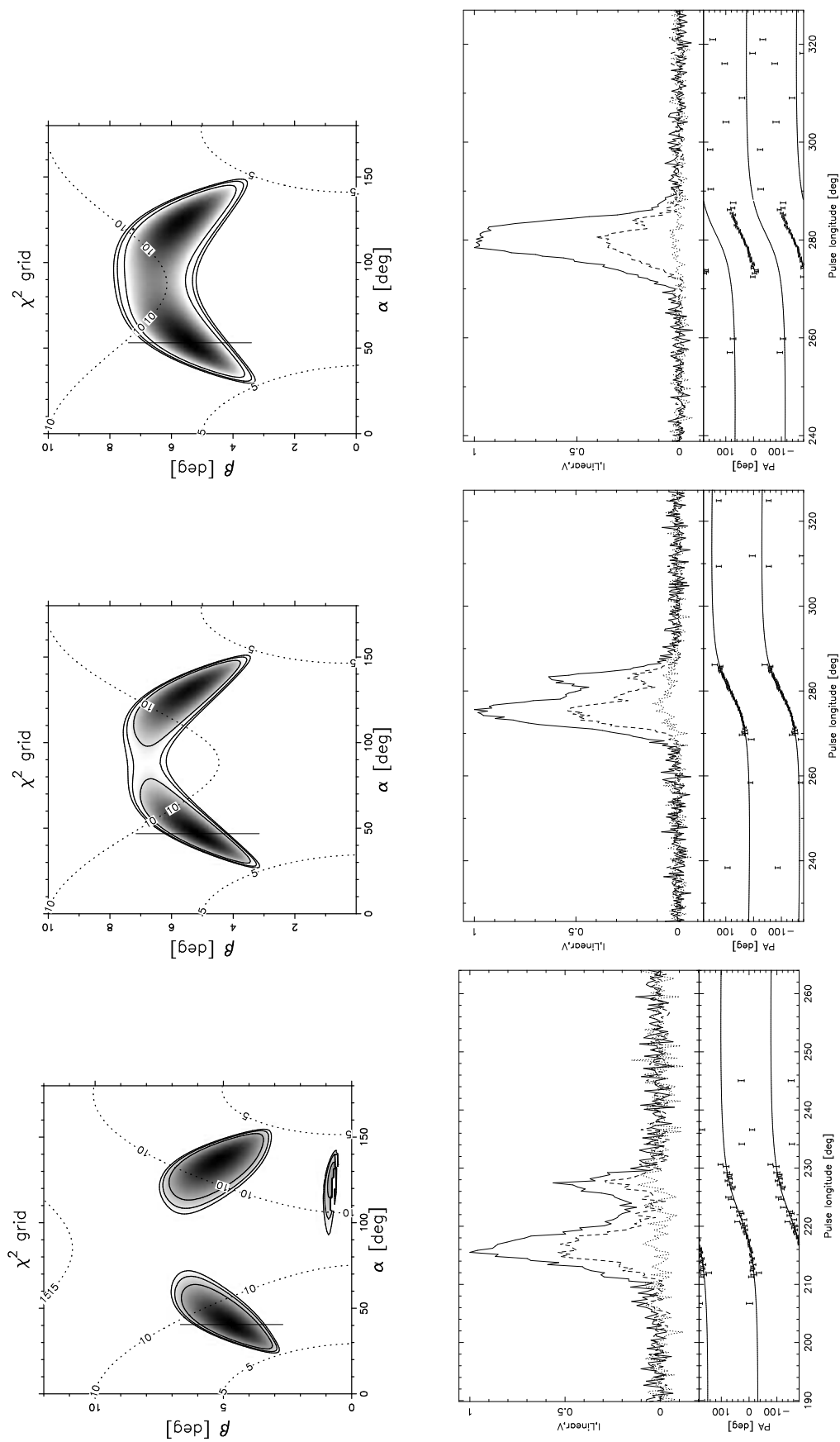


Figure A.12: PSR J1535-4114: (top to bottom) the plots are at 10, 20 and 50 cm.

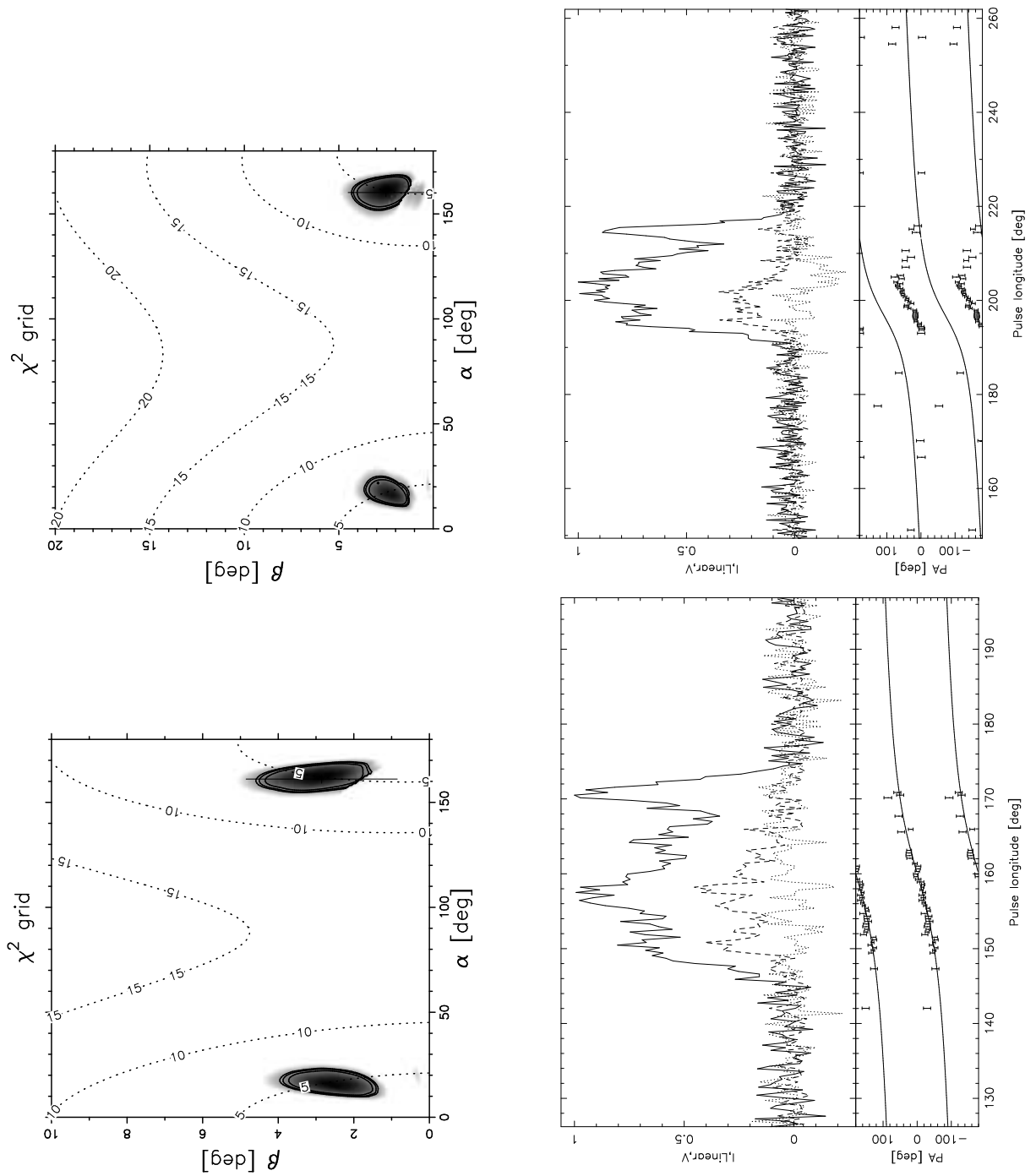


Figure A.13: PSR J1536-3602: (*top to bottom*) the plots are at 20 and 50 cm.

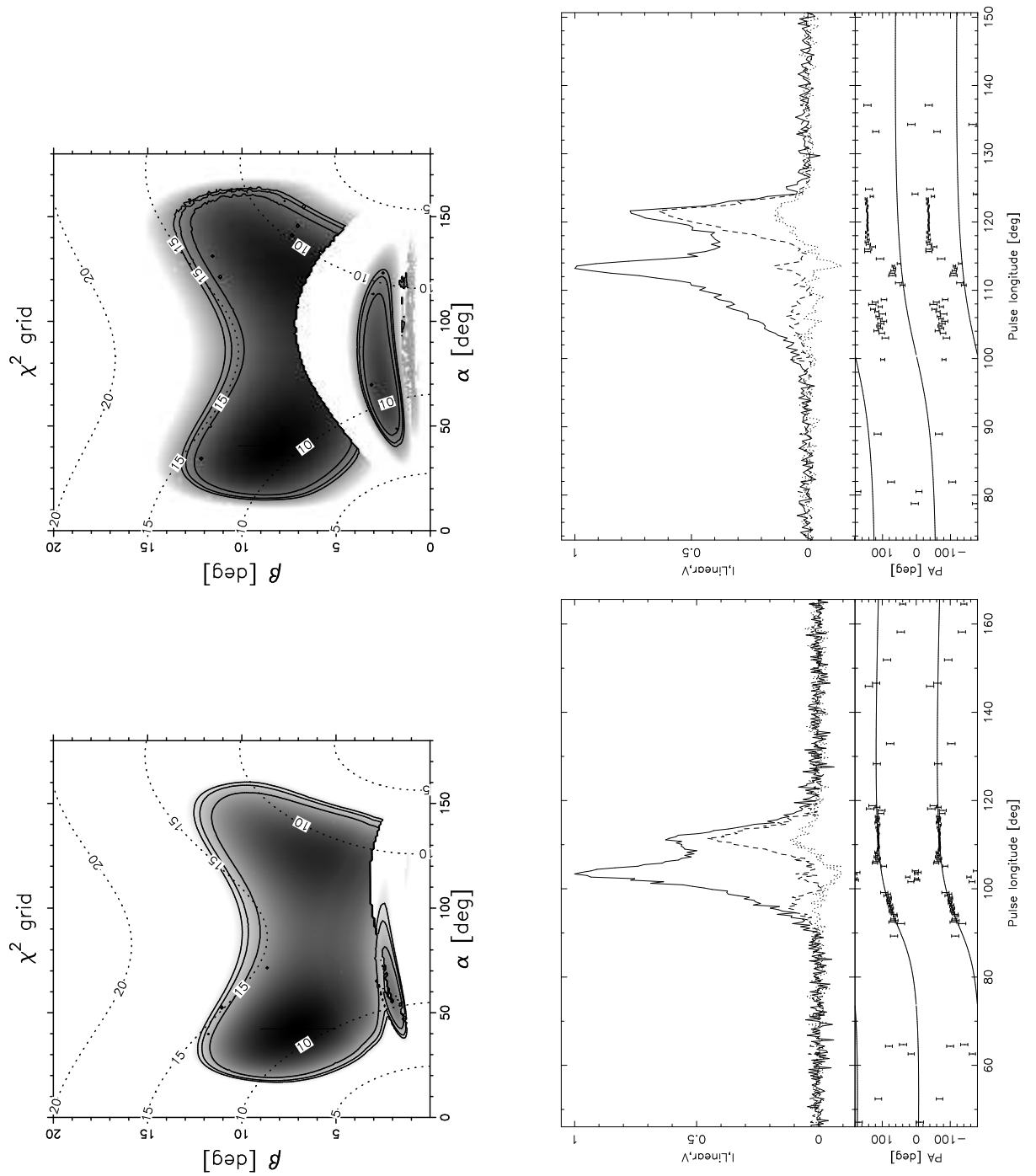


Figure A.14: PSR J1539-5626: (*top to bottom*) the plots are at 10 and 20 cm.

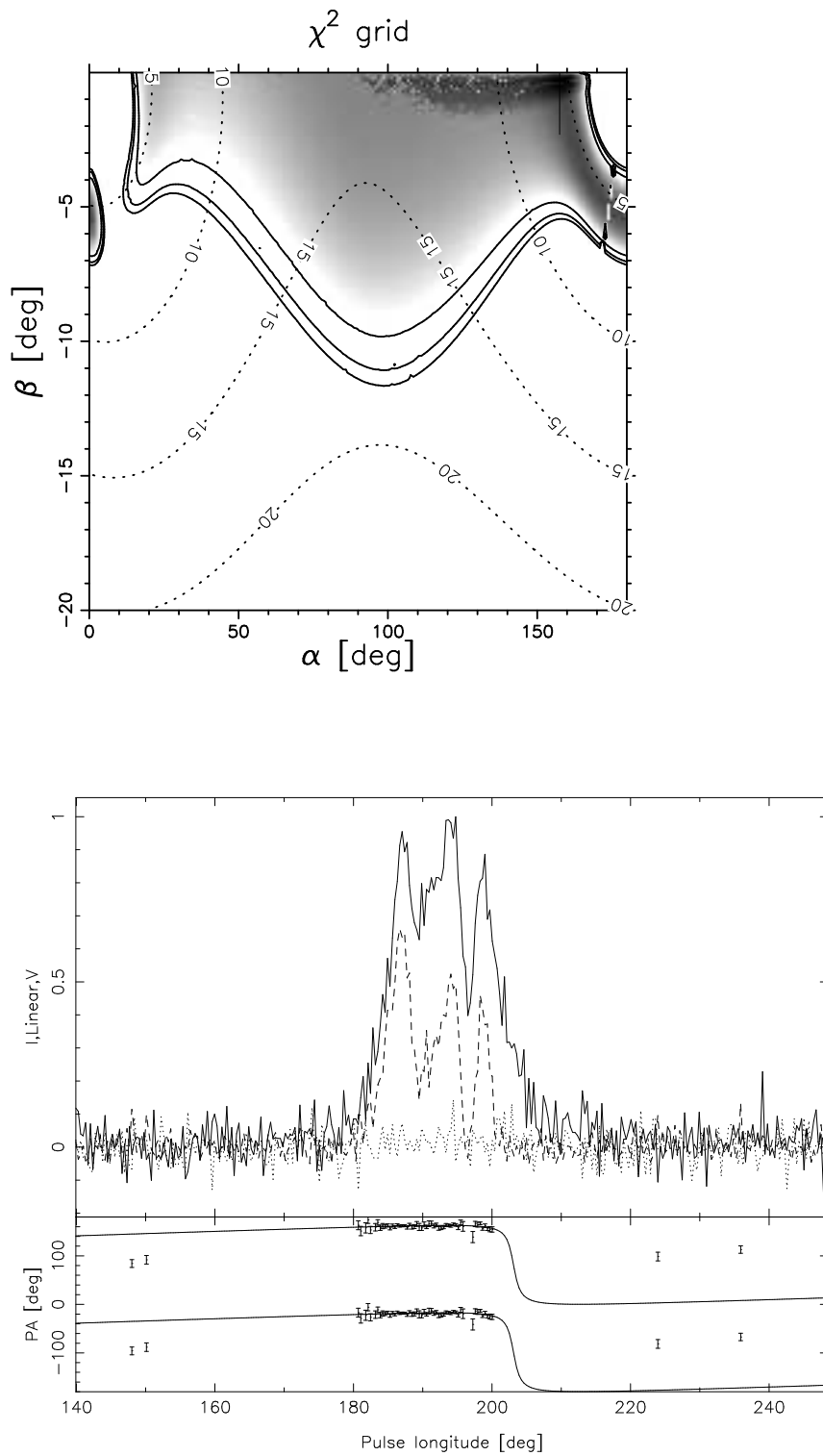


Figure A.15: PSR J1641-2347: (*top to bottom*) the plots are at 20 cm.

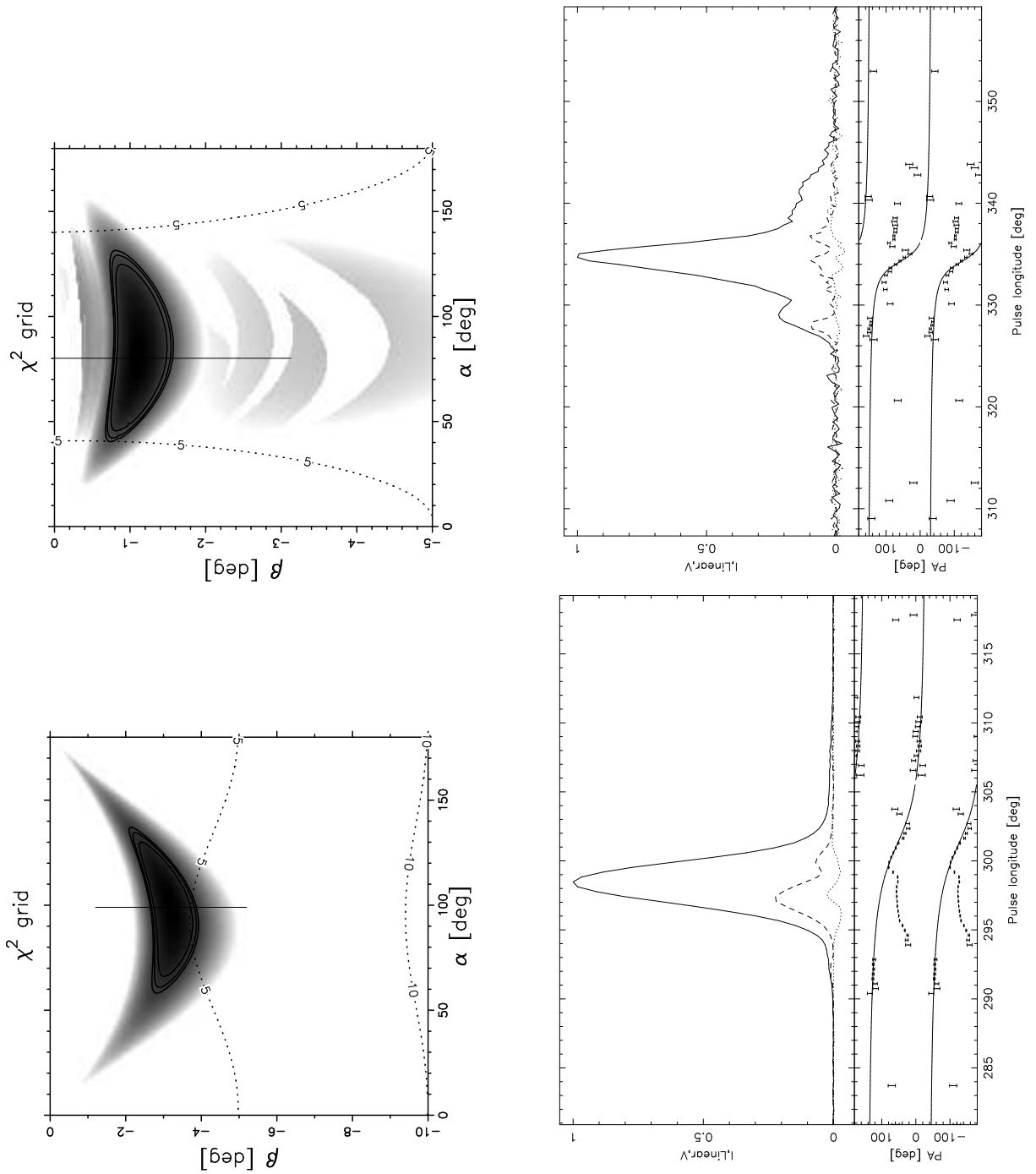


Figure A.16: PSR J1645-0317: (*top to bottom*) the plots are at 10 and 50 cm.

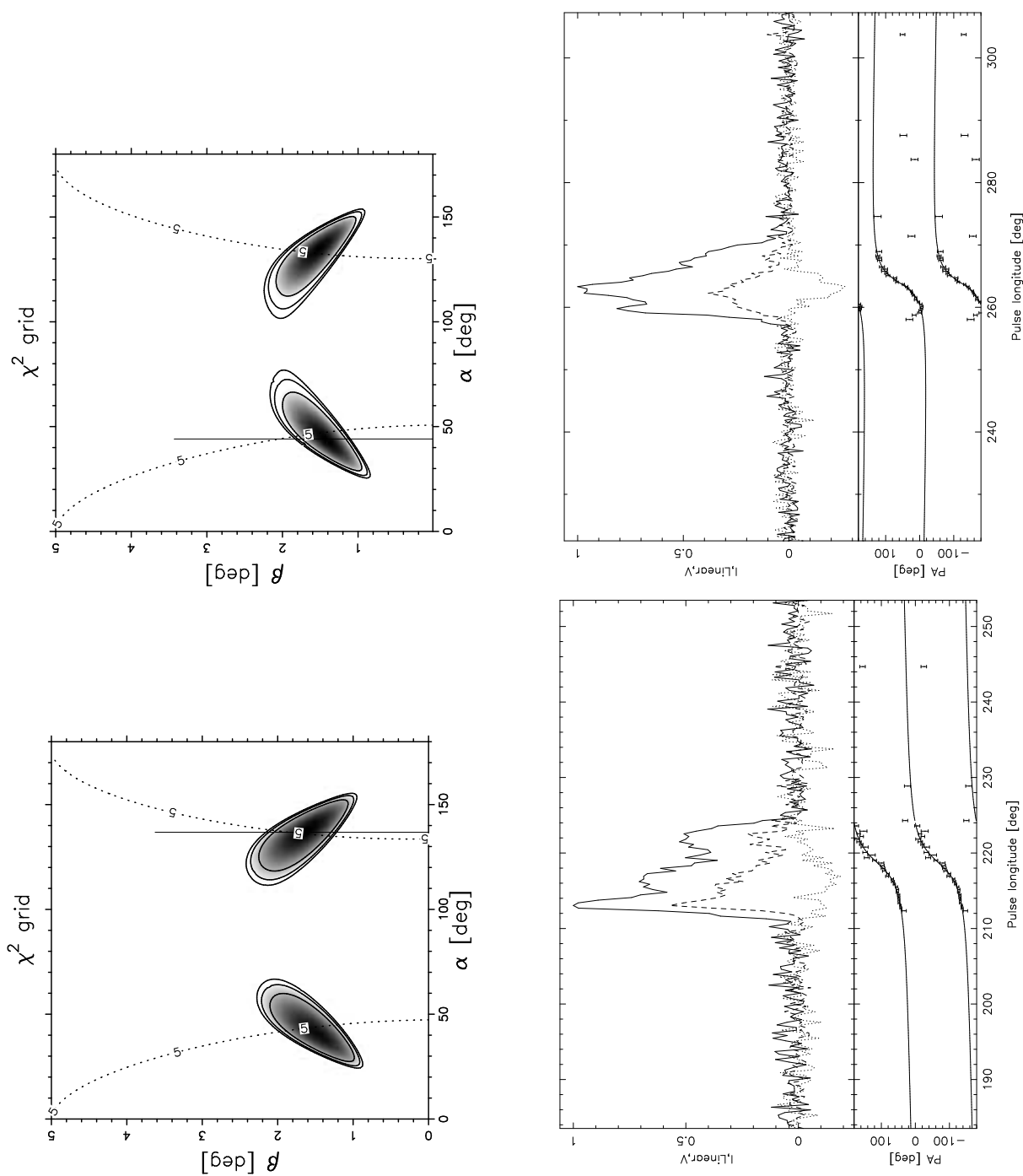


Figure A.17: PSR J1700-3312: (*top to bottom*) the plots are at 20 and 50 cm.

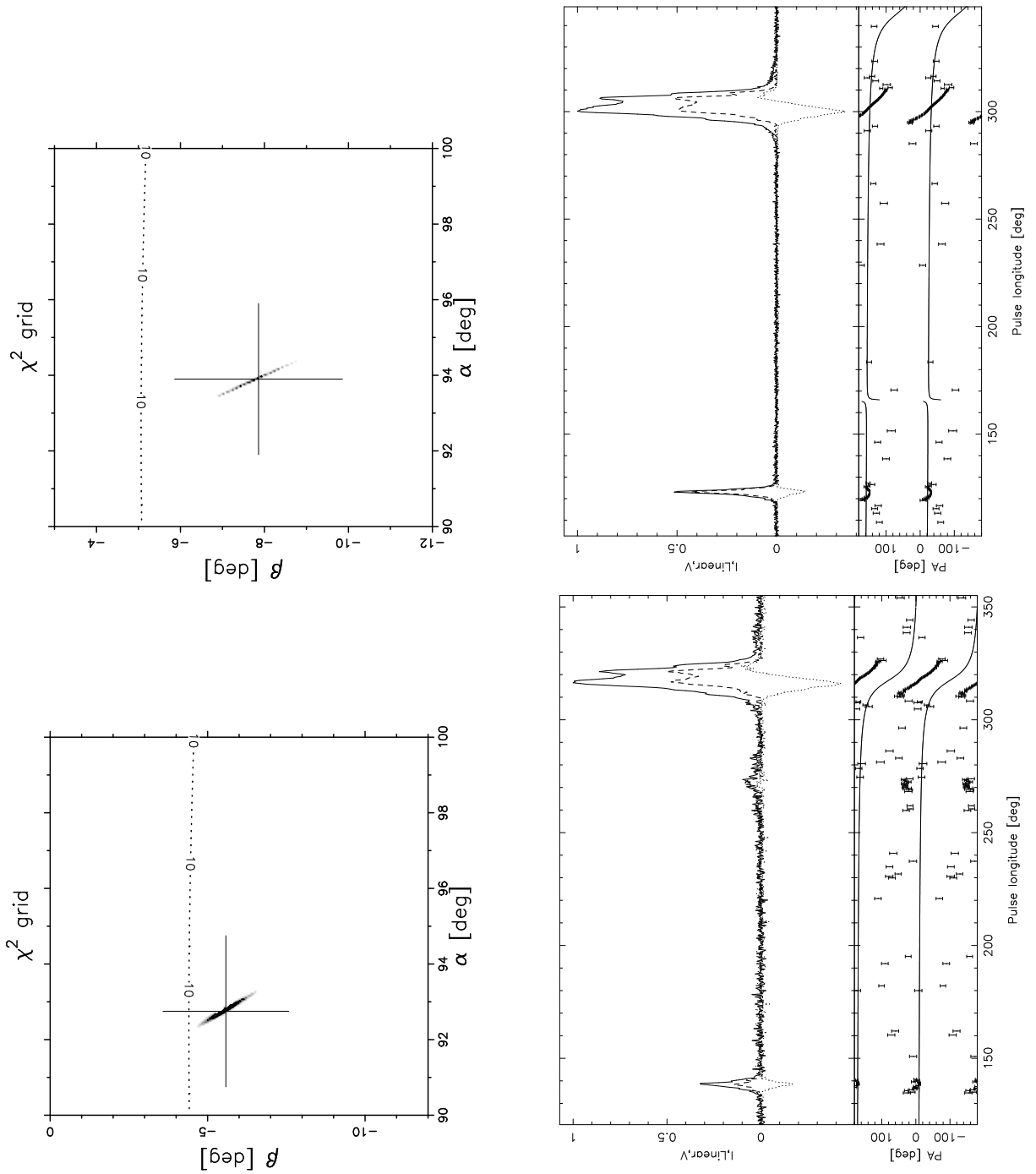


Figure A.18: PSR J1705-1906: (top to bottom) the plots are at 10, 20 and 50 cm.

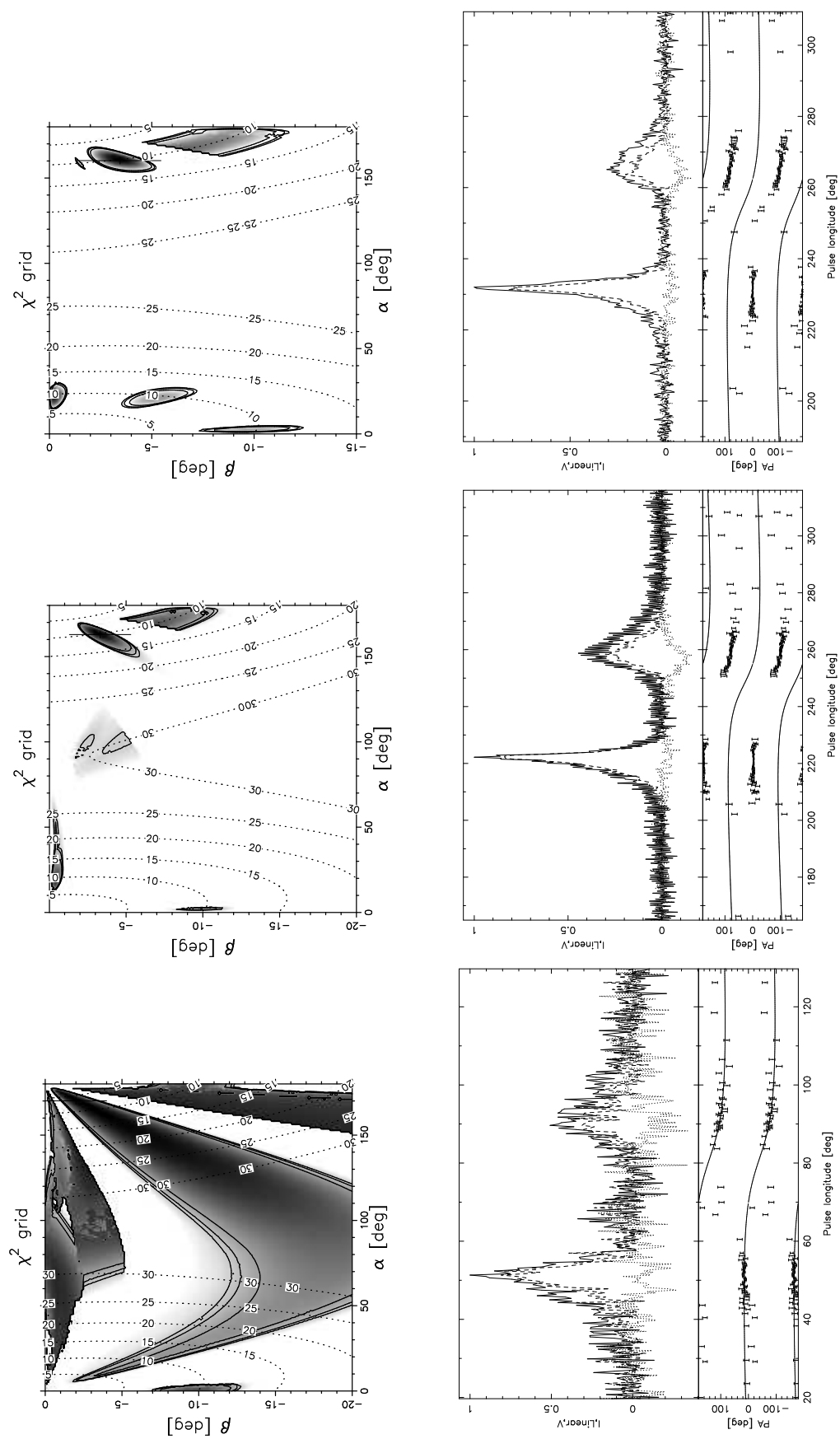


Figure A.19: PSR J1733-3716: (top to bottom) the plots are at 10, 20 and 50 cm.

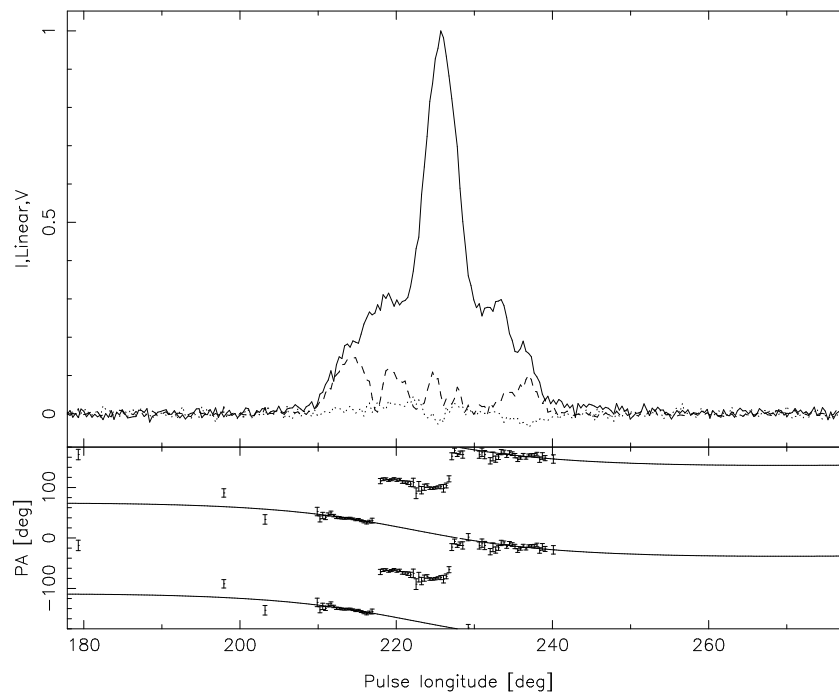
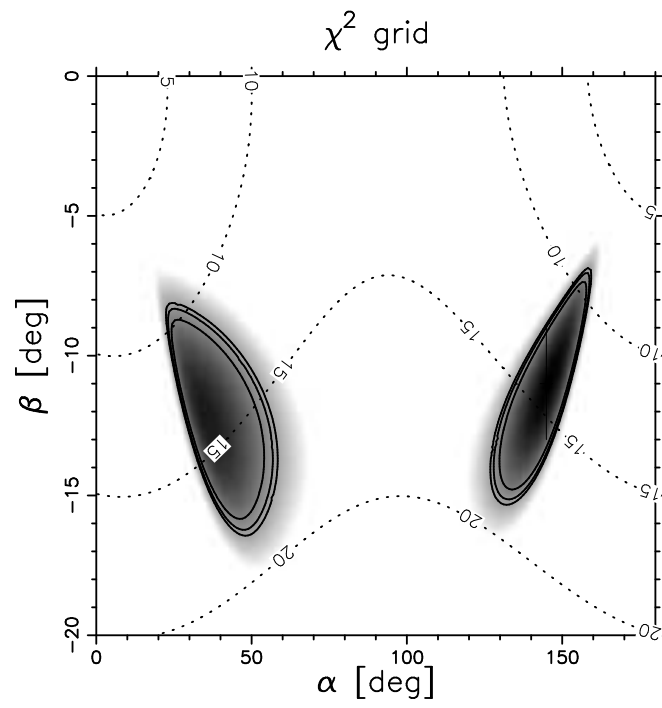


Figure A.20: PSR J1807-0847: at 50 cm.

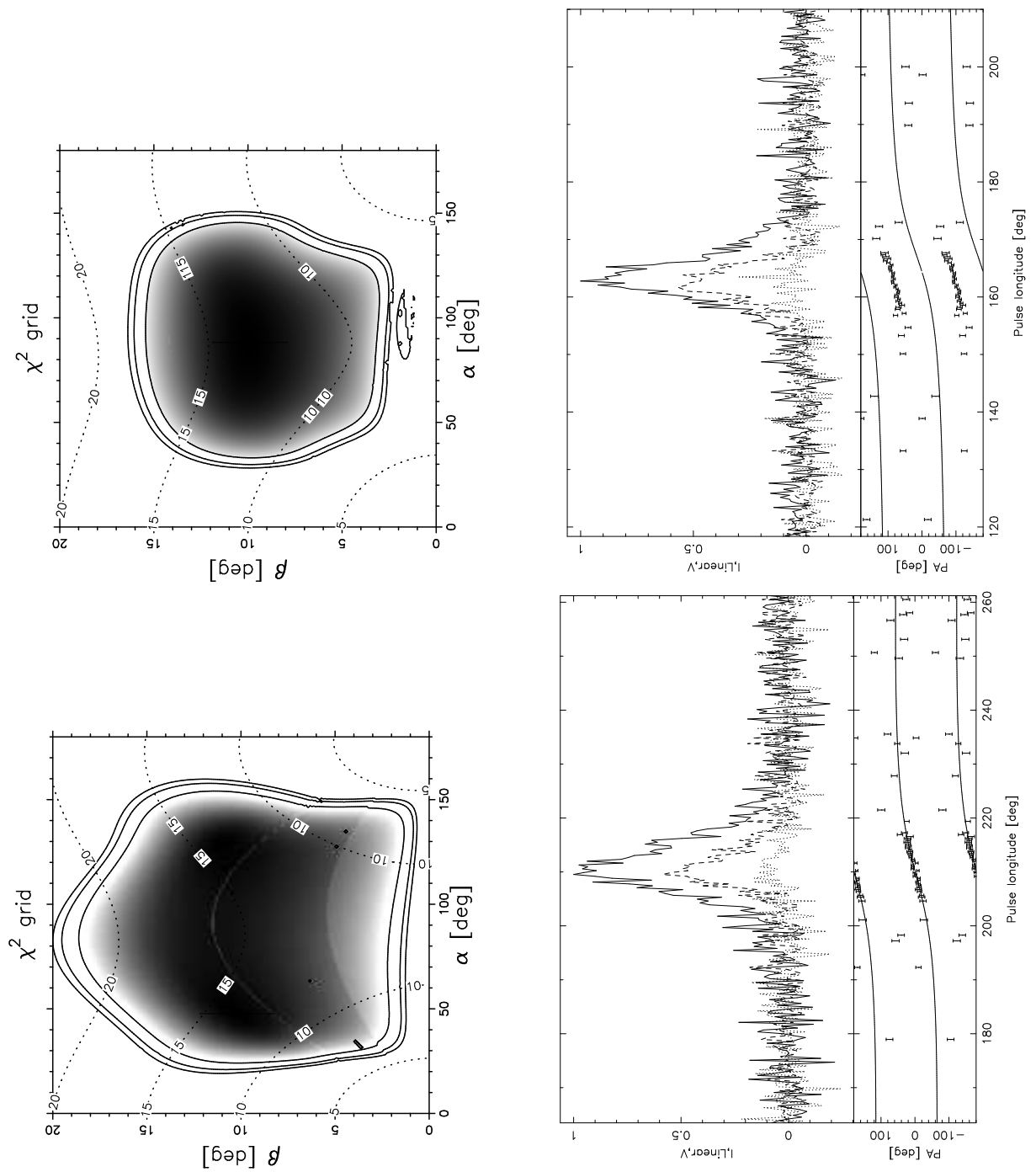


Figure A.21: PSR J1835-1106: (*top to bottom*) the plots are at 10 and 50 cm.

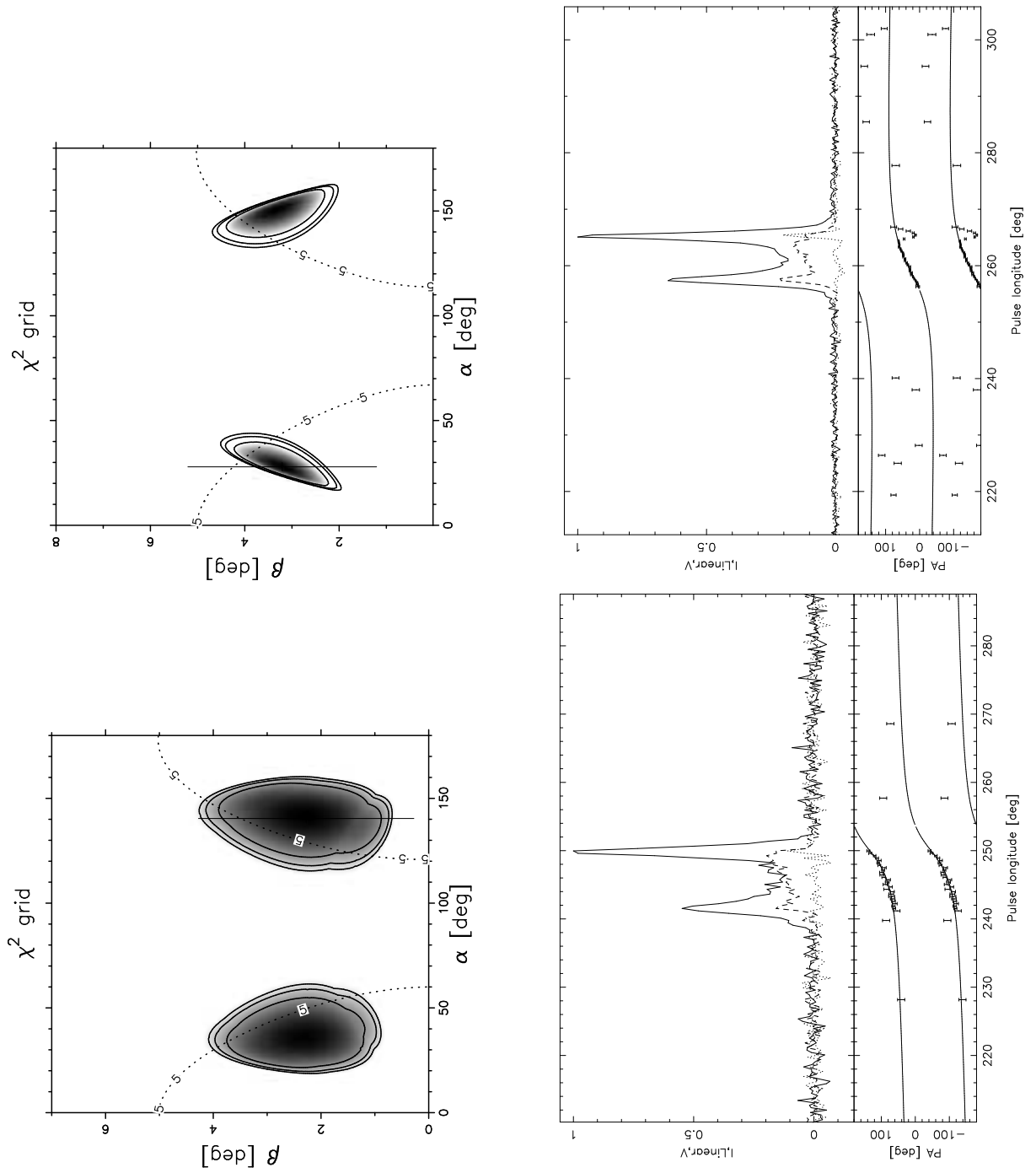


Figure A.22: PSR J1901-0906: (*top to bottom*) the plots are at 20 and 50 cm.

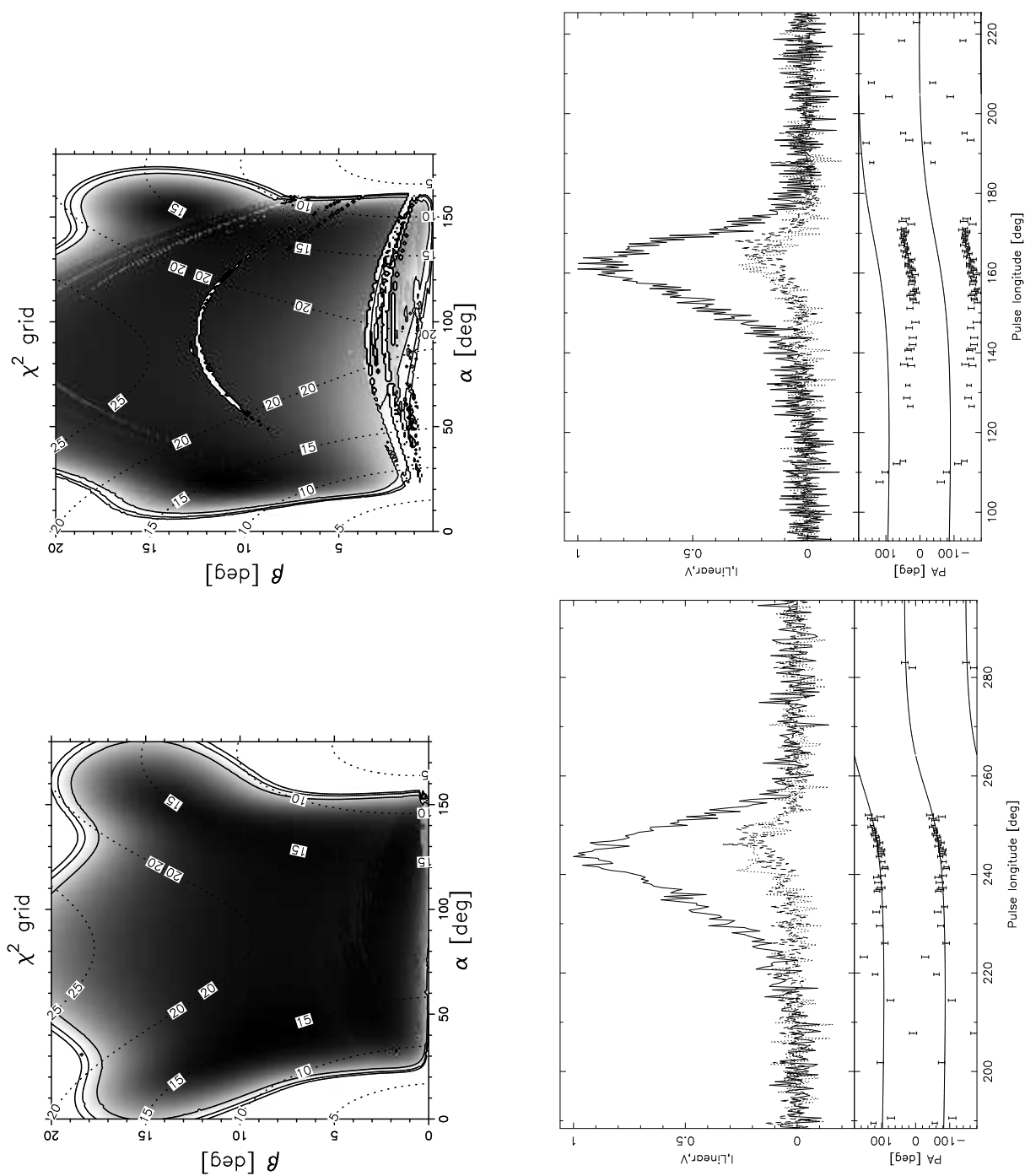


Figure A.23: PSR J1904+0004: (top to bottom) the plots are at 20 and 50 cm.

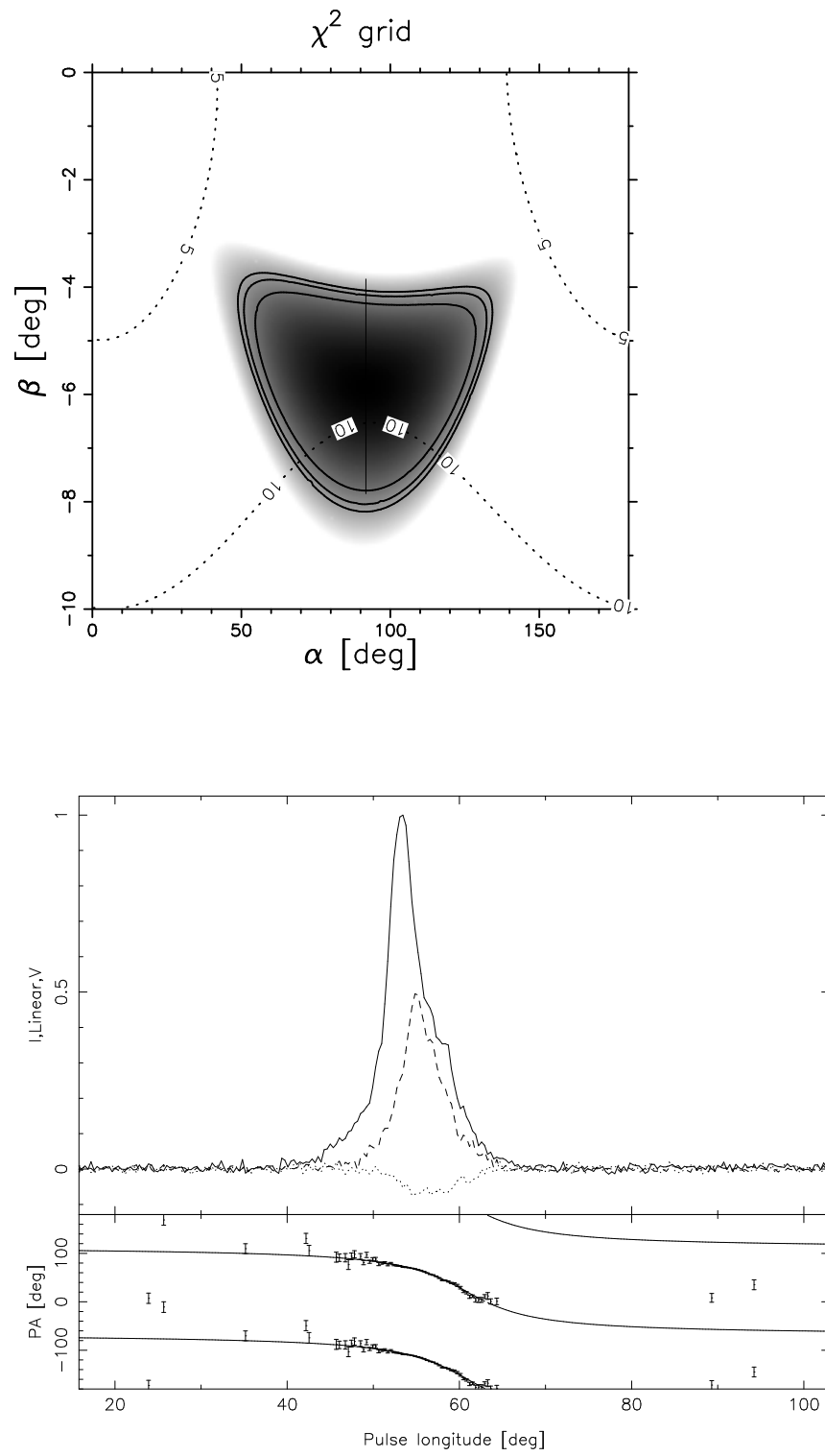


Figure A.24: PSR J1917+1353: (top to bottom) the plots are at 50 cm.

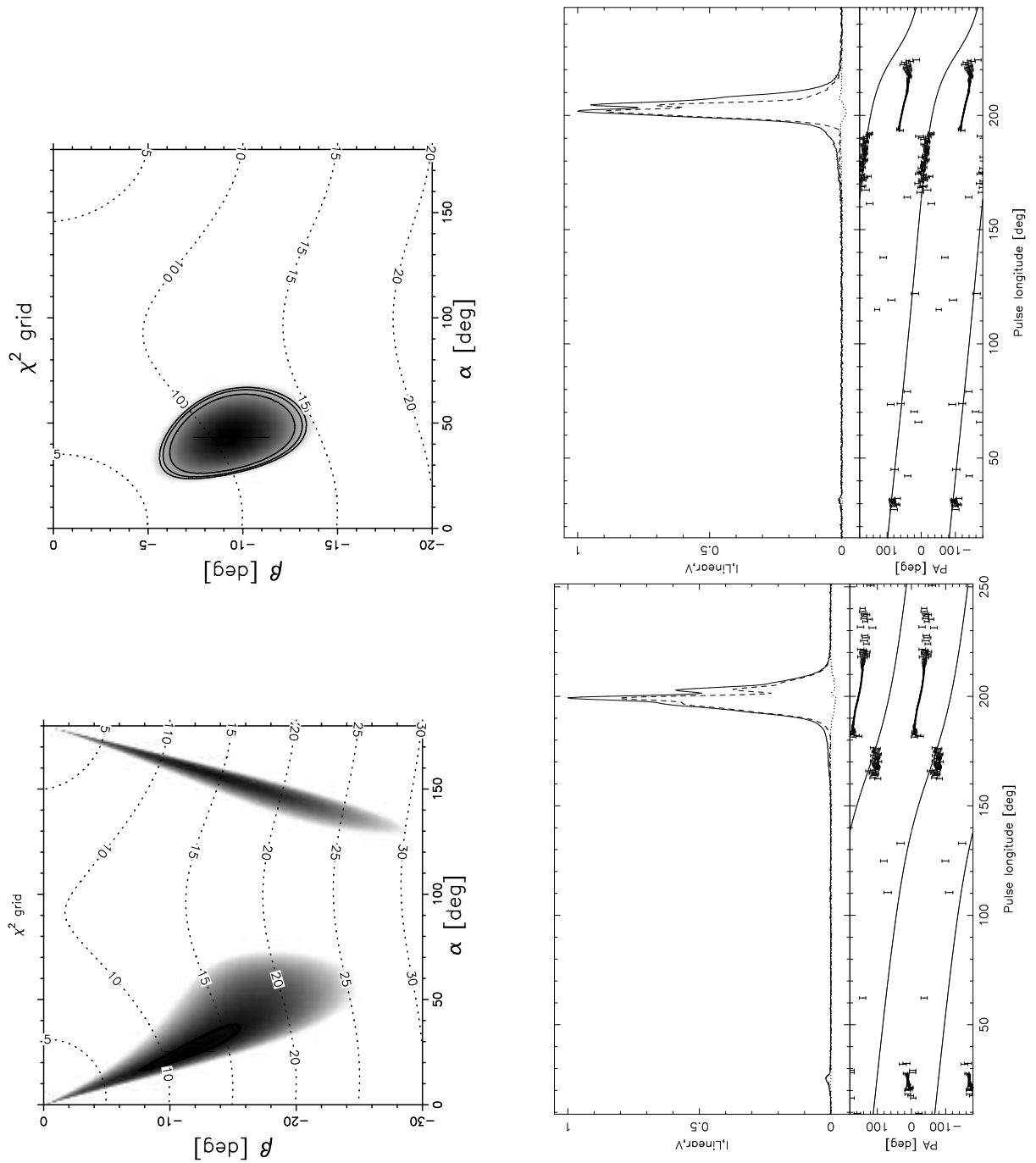


Figure A.25: PSR J1932+1059: (*top to bottom*) the plots are at 10 and 50 cm.

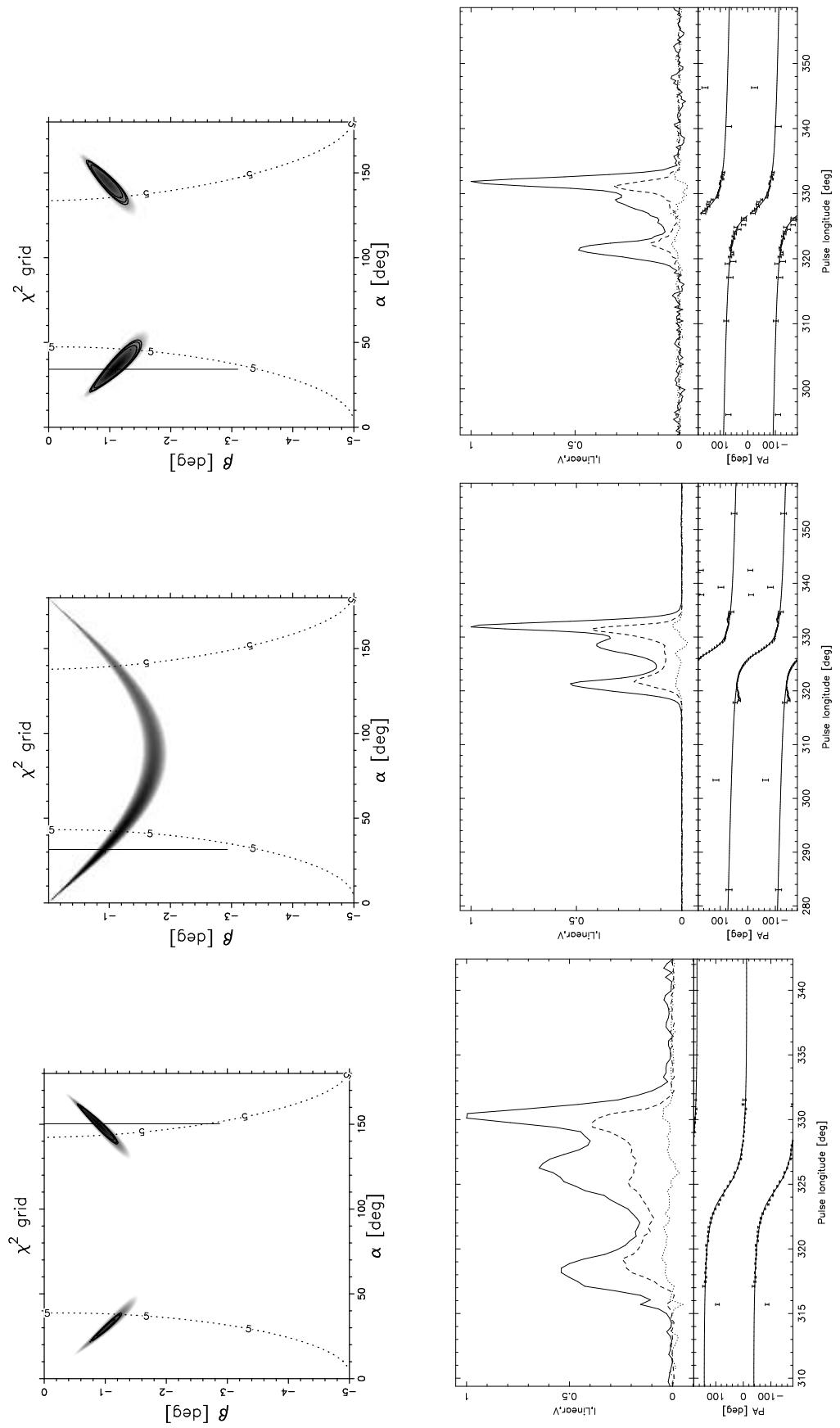


Figure A.26: PSR J2048-1616: (top to bottom) the plots are at 10, 20 and 50 cm.

Appendix B

Simulations of the Propagation Model

Using the propagation model by Beskin & Philippov (2012), described in Chapter 3, we present the simulated pulse profiles and PPAs from combinations of parameters, which are the plasma frequency (f), the Lorentz factor (γ), the multiplicity of particle number (λ) and emission altitude (r_{em}).

Individual pages are combinations of r_{em} and λ , while each page contains all the combinations of γ (from *top* to *bottom* row) and f (from *left* to *right* column). For each set of solutions, the *top* panel displays the profile of I (*solid-blue*) and V (*solid-magenta*), and the *dotted-blue* line represents the profile before taking the cyclotron absorption into account. The intensity unit is in percentage. The *bottom* panel shows the simulated PPA swing (*solid*) and the original-RVM PPA swing (*dotted*).

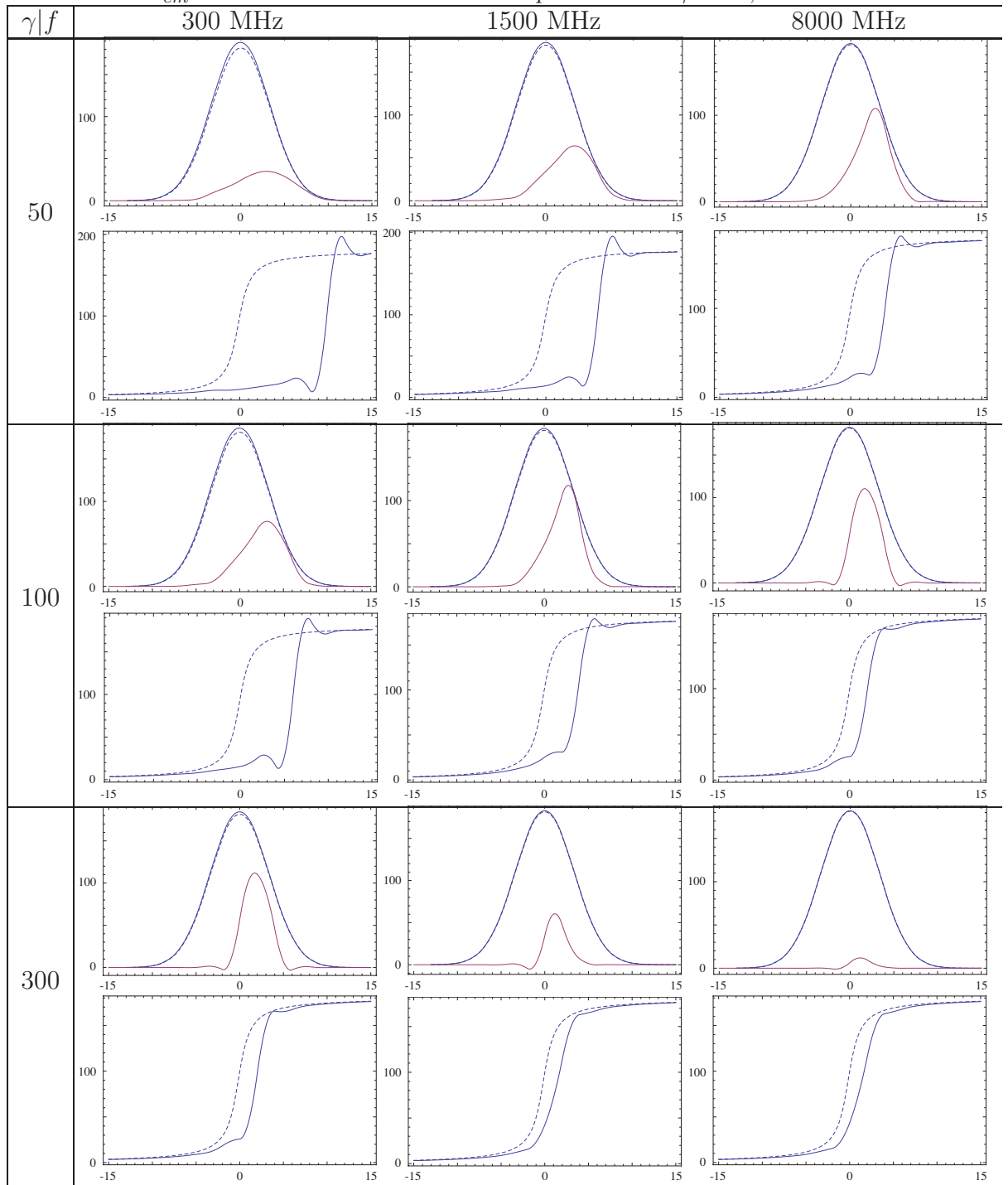
Table B.1: $r_{em} = 100$ km and $\lambda = 100$. From *top* to *bottom*: $\gamma = 50, 100$ and 300 .

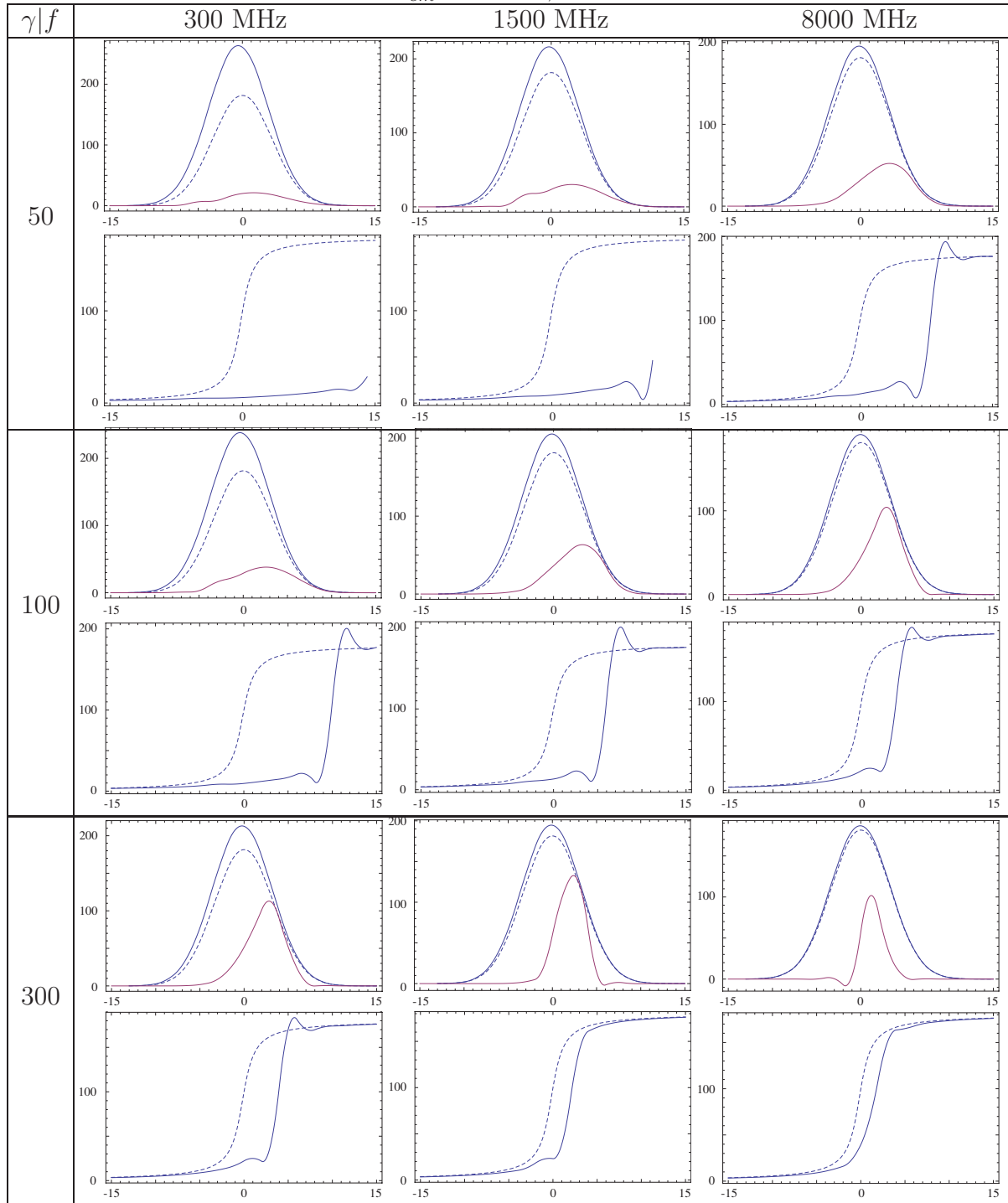
Table B.2: $r_{em} = 100$ km, $\lambda = 1000$.

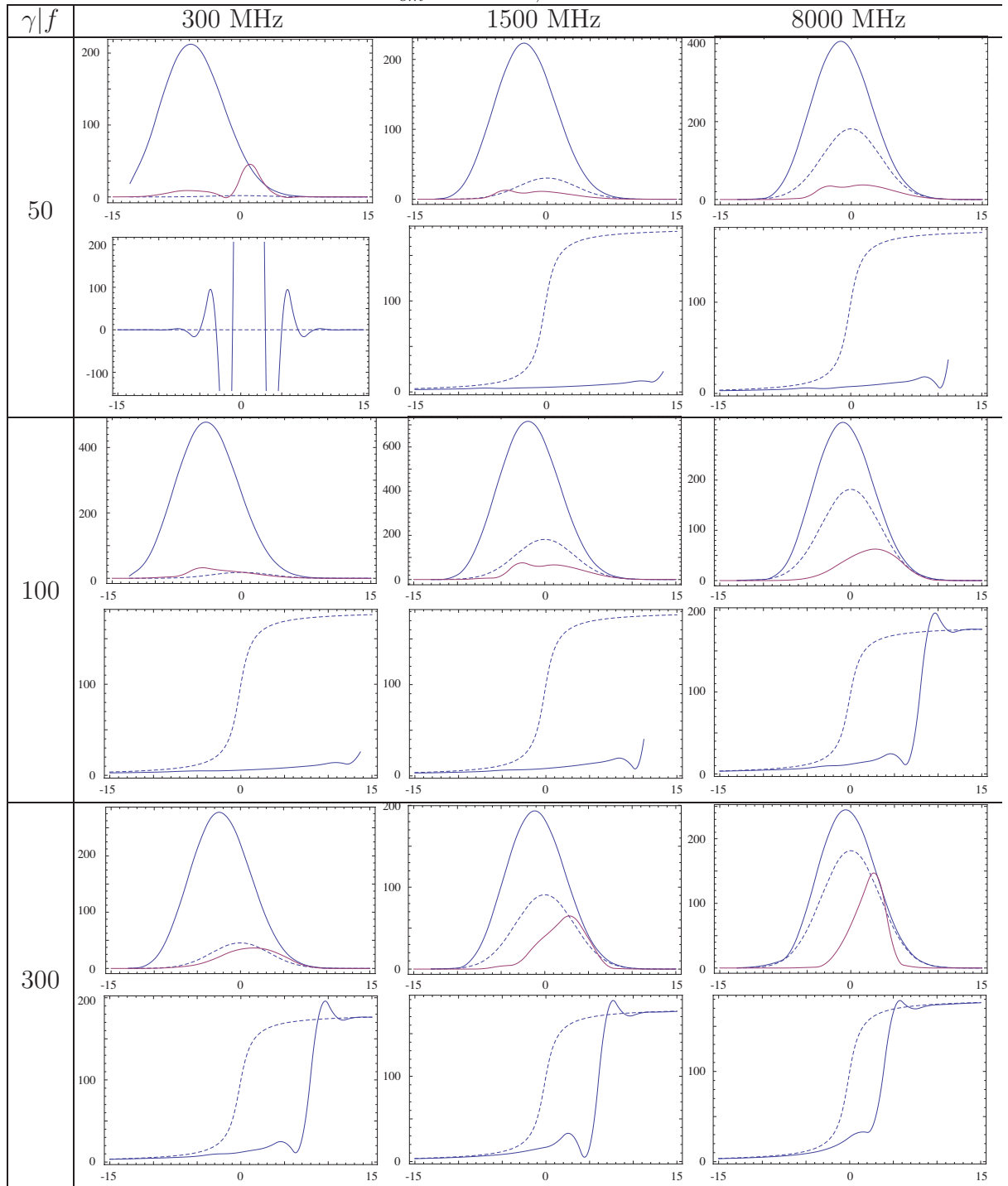
Table B.3: $r_{em} = 100$ km, $\lambda = 10000$.

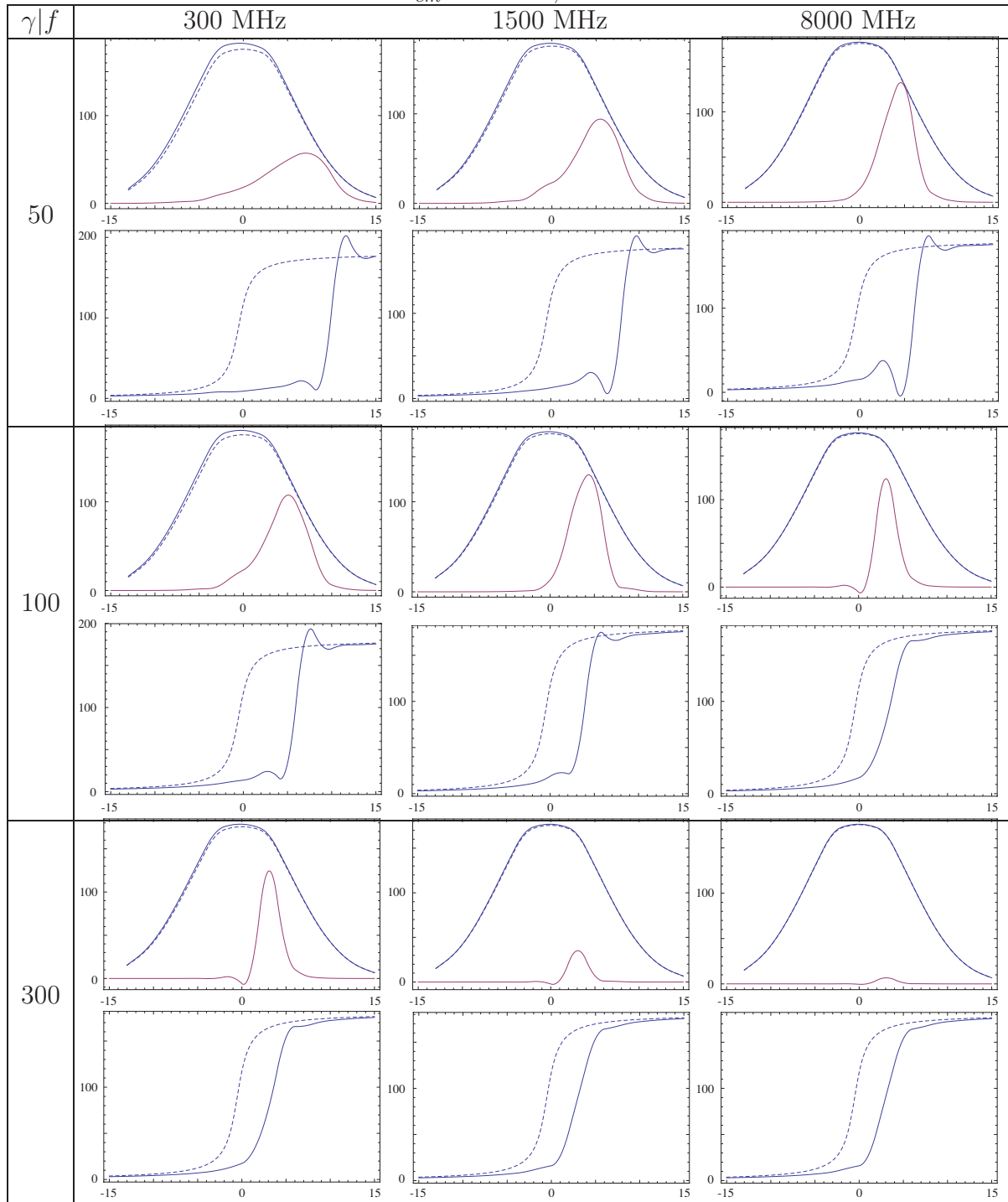
Table B.4: $r_{em} = 300$ km, $\lambda = 100$.

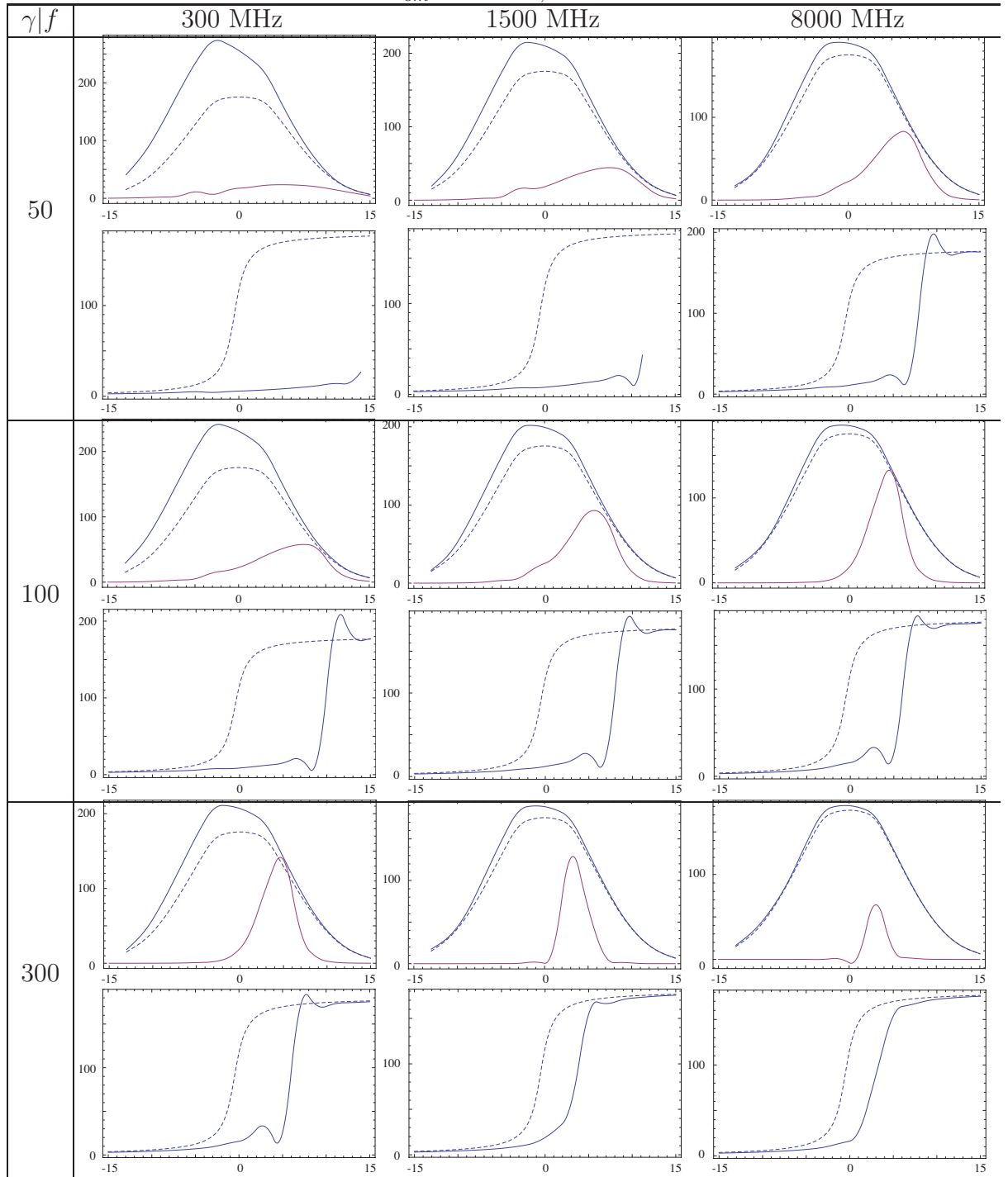
Table B.5: $r_{em} = 300$ km, $\lambda = 1000$.

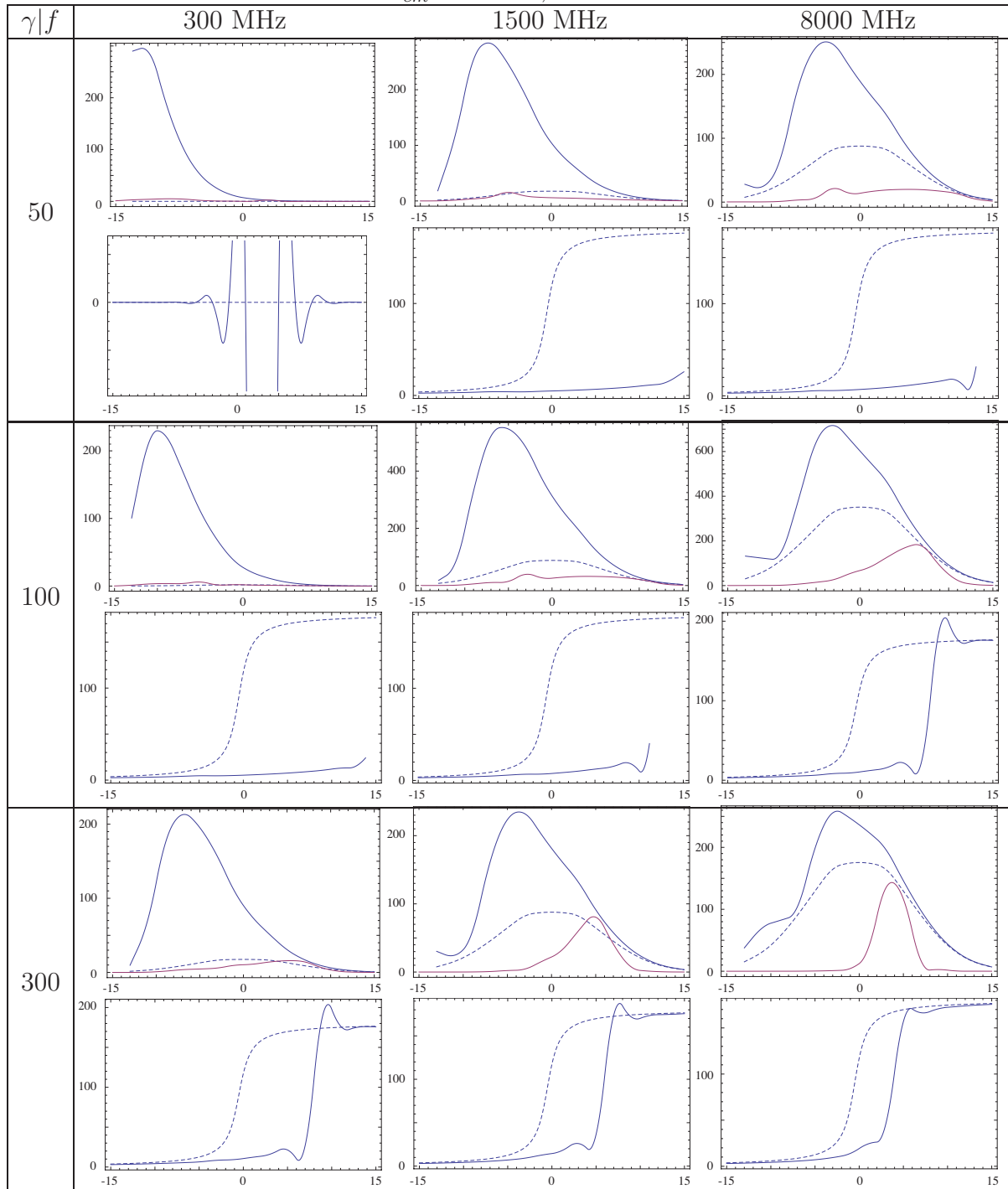
Table B.6: $r_{em} = 300$ km, $\lambda = 10000$.

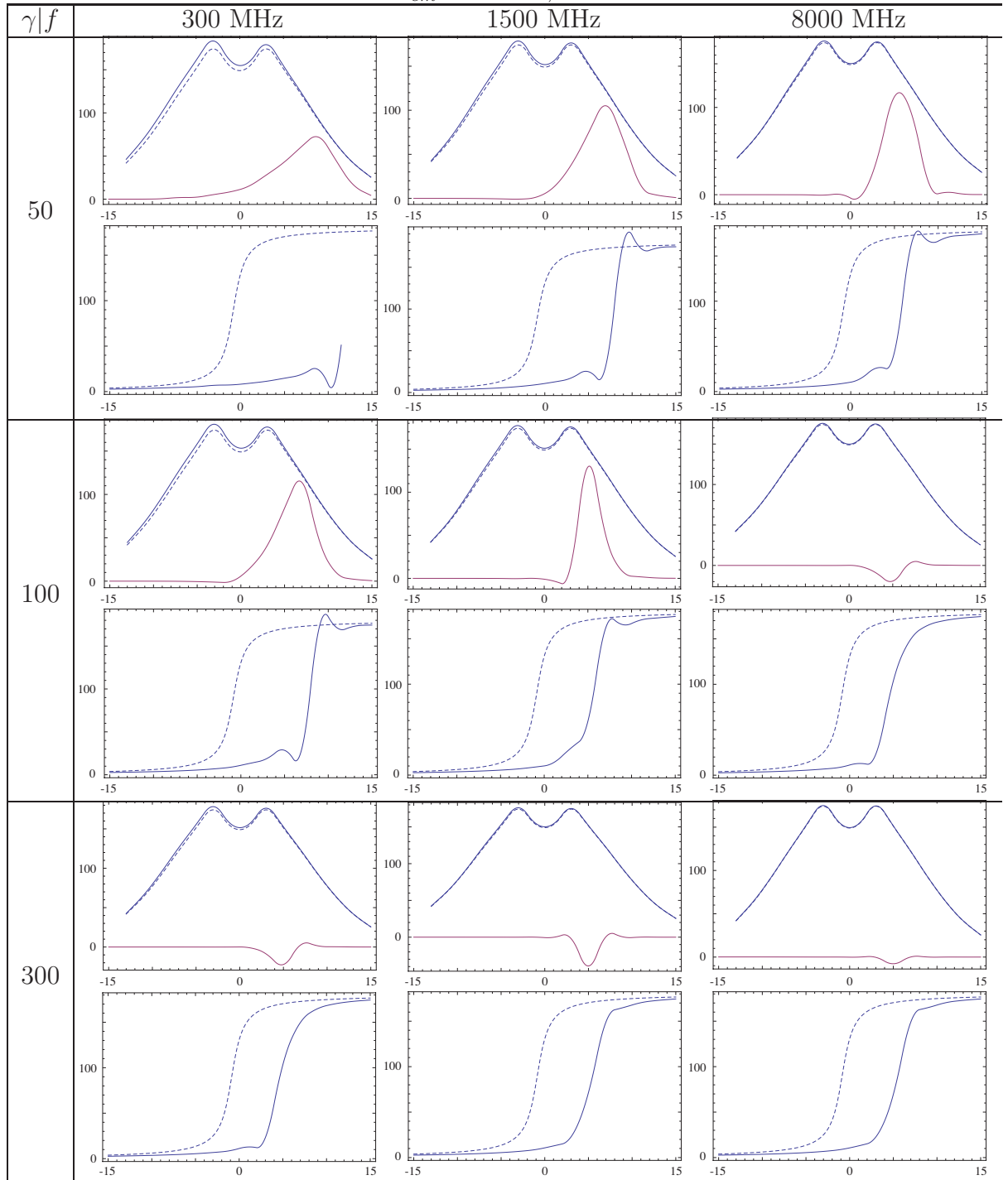
Table B.7: $r_{em} = 500$ km, $\lambda = 100$.

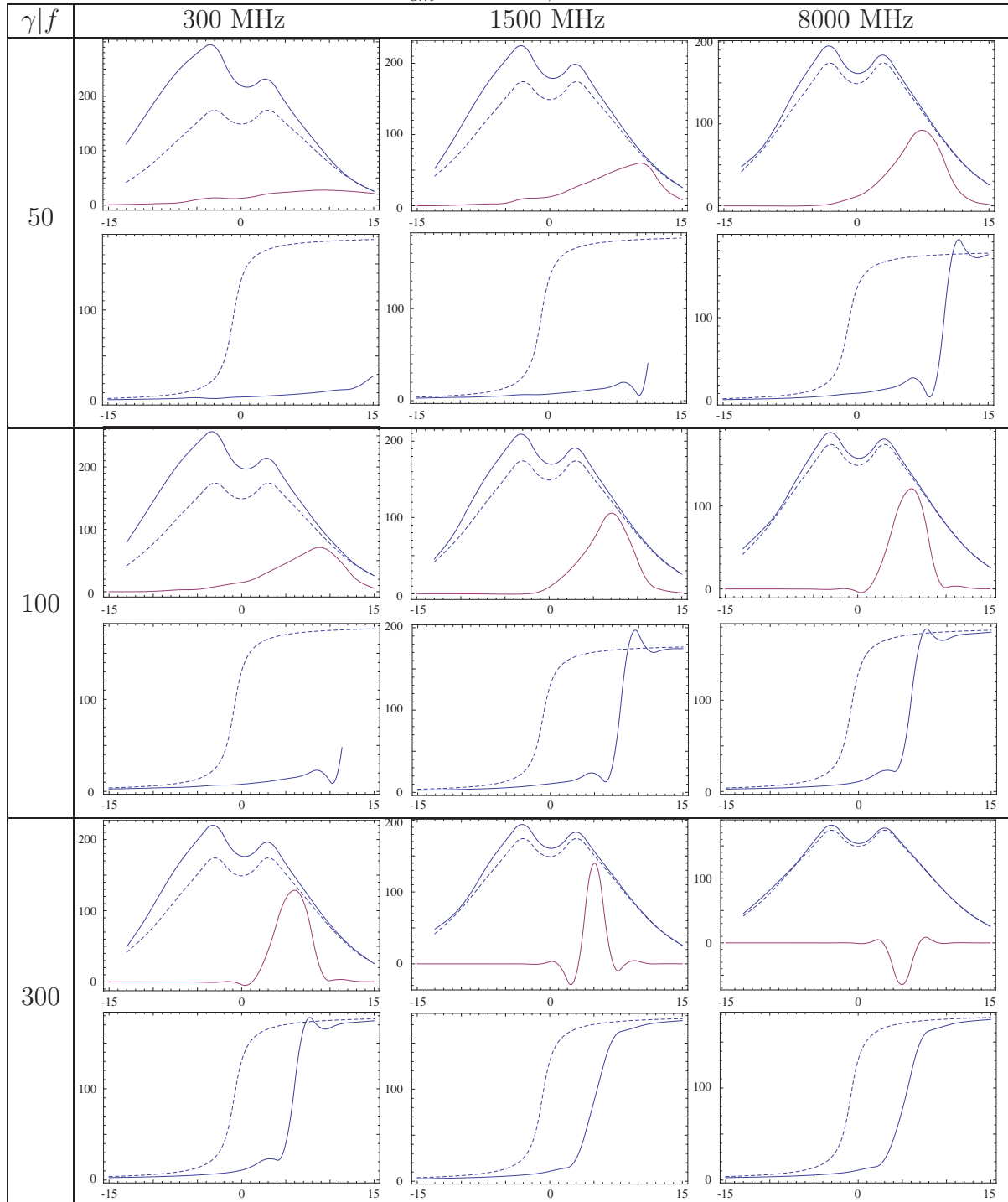
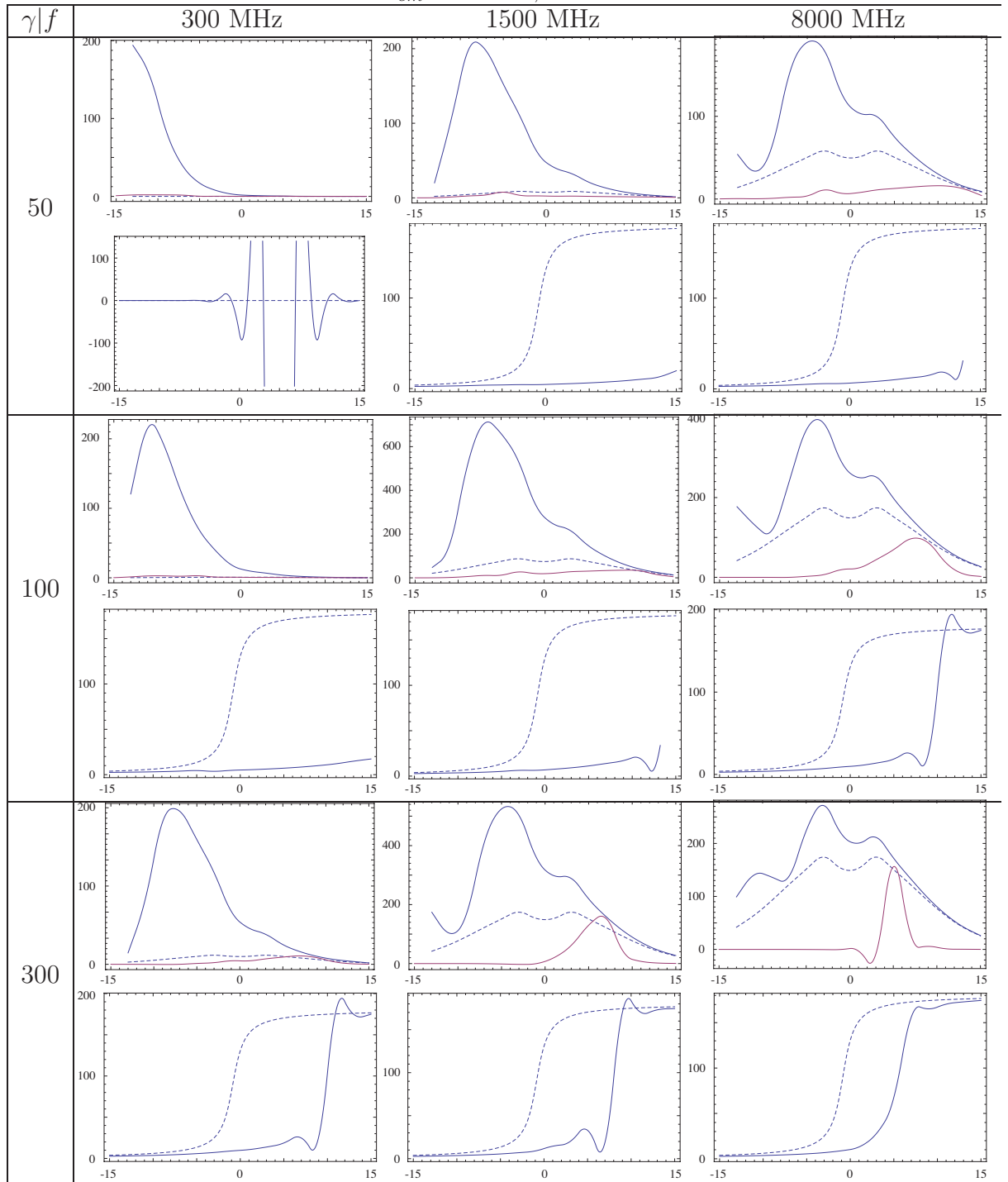
Table B.8: $r_{em} = 500$ km, $\lambda = 1000$.

Table B.9: $r_{em} = 500$ km, $\lambda = 10000$.

Bibliography

- Alpar M.A., Guseinov O.H., Kiziloglu U., Oegelman H., 1995, *A&A*, 297, 470
- Arons J., 1983, *ApJ*, 266, 215
- Arons J., Barnard J.J., 1986, *ApJ*, 302, 120
- Backer D.C., Rankin J.M., Campbell D.B., 1976, *Nature*, 263, 202
- Backus I., Mitra D., Rankin J.M., 2010, *MNRAS*, 404, 30
- Barnard J.J., 1986, *ApJ*, 303, 280
- Barnard J.J., Arons J., 1986, *ApJ*, 302, 138
- Beskin V.S., Philippov A.A., 2012, *MNRAS*, 425, 814
- Beskin V.S., Gurevich A.V., Istomin Y.N., 1988, *Ap&SS*, 146, 205
- Beskin V.S., Gurevich A.V., Istomin Y.N., 1993, *Physics of the Pulsar Magnetosphere*. Cambridge University Press
- Blaskiewicz M., Cordes J.M., Wasserman I., 1991, *ApJ*, 370, 643
- Born M., Wolf E., 1999, *Principles of Optics*. Cambridge University Press
- Britton M.C., 2000, *ApJ*, 532, 1240
- Brown L.E., Hartmann D.H., 1993, *Astrophys. Space Sci.*, 209, 285
- Burke B.F., Smith F.G., 2002, *An introduction to Radio Astronomy*. Cambridge University Press, Cambridge
- Cady E.B., Ritchings R.T., 1977, *Nature*, 269, 126

- Camilo F., Ransom S.M., Chatterjee S., Johnston S., Demorest P., 2012, *ApJ*, 746, 63
- Candy B.N., Blair D.G., 1983, *MNRAS*, 205, 281
- Contopoulos I., Kazanas D., Fendt C., 1999, *ApJ*, 511, 351
- Dyks J., 2008, *MNRAS*, 391, 859
- Dyks J., Zhang B., Gil J., 2005, *ApJ*, 626, L45
- Edwards R.T., Stappers B.W., 2004, *A&A*, 421, 681
- Esamdin A., Lyne A.G., Graham-Smith F., Kramer M., Manchester R.N., Wu X., 2005, *MNRAS*, 356, 59
- Everett J.E., Weisberg J.M., 2001, *ApJ*, 553, 341
- Fowler L.A., Wright G.A.E., Morris D., 1981, *A&A*, 93, 54
- Freire P.C.C., Ransom S.M., Bégin S., Stairs I.H., Hessels J.W.T., Frey L.H., Camilo F., 2008, *ApJ*, 675, 670
- Gangadhara R.T., Gupta Y., 2001, *ApJ*, 555, 31
- Gil J., Kijak K., 1993, *A&A*, 273, 563
- Gil J.A., Han J.L., 1996, *ApJ*, 458, 265
- Gil J.A., Gronkowski P., Rudnicki W., 1984, *A&A*, 132, 312
- Gil J.A., et al., 1994, *A&A*, 282, 45
- Goldreich P., Julian W.H., 1969, *ApJ*, 157, 869
- Gould D.M., 1994, Structure and polarisation of pulsar radio emission beams. Ph.D. thesis, The University of Manchester
- Gould D.M., Lyne A.G., 1998, *MNRAS*, 301, 235
- Hamaker J.P., Bregman J.D., Sault R.J., 1996, *A&AS*, 117, 137
- Harding A.K., Contopoulos I., Kazanas D., 1999, *ApJ*, 525, L125
- Hermsen W., et al., 2013, *Science*, 339, 436

- Hibschman J.A., Arons J., 2001, *ApJ*, 546, 382
- von Hoensbroech A., Xilouris K.M., 1997a, *A&AS*, 126, 121
- von Hoensbroech A., Xilouris K.M., 1997b, *A&A*, 324, 981
- Huguenin G.R., Manchester R.N., Taylor J.H., 1971, *ApJ*, 169, 97
- Jackson J.D., 1962, *Classical Electrodynamics*. Wiley
- Janssen G.H., Stappers B.W., Braun R., van Straten W., Edwards R.T., Rubio-Herrera E., van Leeuwen J., Weltevrede P., 2009, *A&A*, 498, 223
- Jaroenjittichai P., 2009, *The Rotating Vector Model and Applications*. MSc thesis, The University of Manchester
- Johnston S., 2002, *Pub. of the ASA*, 19, 277
- Johnston S., van Straten W., Kramer M., Bailes M., 2001, *ApJ*, 549, L101
- Johnston S., Hobbs G., Vigeland S., Kramer M., Weisberg J.M., Lyne A.G., 2005, *MNRAS*, 364, 1397
- Johnston S., Karastergiou A., Willett K., 2006, *MNRAS*, 369, 1916
- Johnston S., Karastergiou A., Mitra D., Gupta Y., 2008, *MNRAS*, 388, 261
- Jones R.C., 1941, *J. Opt. Soc. Am.*, 31, 488
- Kapoor R.C., Shukre C.S., 1998, *ApJ*, 501, 228
- Karastergiou A., 2009, *MNRAS*, 392, L60
- Karastergiou A., Johnston S., 2006, *MNRAS*, 365, 353
- Karastergiou A., Roberts S.J., Johnston S., Lee H., Weltevrede P., Kramer M., 2011, *MNRAS*, 415, 251
- Keith M.J., Johnston S., Weltevrede P., Kramer M., 2010, *MNRAS*, 402, 745
- Kijak J., 2001, *MNRAS*, 323, 537
- Kijak J., Gil J., 1997, *MNRAS*, 288, 631
- Kijak J., Gil J., 2003, *ApJ*, 397, 969

- Kijal J., Gil J., 1998, *MNRAS*, 299, 855
- Kolonko M., Gil J., Maciesiak K., 2004, *A&A*, 428, 943
- Komesaroff M.M., Morris D., Cooke D.J., 1970, *Astrophys. Lett.*, 5, 37
- Kramer M., 1994, *A&AS*, 107, 527
- Kramer M., 2008, In Bassa C., Wang Z., Cumming A., Kaspi V.M., eds., *40 Years of Pulsars: Millisecond Pulsars, Magnetars and More*, vol. 983 of American Institute of Physics Conference Series, pp. 11–19
- Kramer M., Johnston S., 2008, *MNRAS*, 390, 87
- Kramer M., Wielebinski R., Jessner A., Gil J.A., Seiradakis J.H., 1994, *A&AS*, 107, 515
- Kramer M., Lyne A.G., O'Brien J.T., Jordan C.A., Lorimer D.R., 2006, *Science*, 312, 549
- Latham C., Mitra D., Rankin J., 2012, *ArXiv*
- Lattimer J.M., Prakash M., 2001, *ApJ*, 550, 426
- Li J., Spitkovsky A., Tchekhovskoy A., 2012a, *ApJ*, 746, 60
- Li J., Spitkovsky A., Tchekhovskoy A., 2012b, *ApJ*, 746, L24
- Li X.H., Han J.L., 2003, *A&A*, 410, 253
- Lorimer D.R., Kramer M., 2005, *Handbook of Pulsar Astronomy*. Cambridge University Press
- Lorimer D.R., Lyne A.G., McLaughlin M.A., Kramer M., Pavlov G.G., Chang C., 2012, *ApJ*, 758, 141
- Lyne A., 2012, *ArXiv*
- Lyne A., Hobbs G., Kramer M., Stairs I., Stappers B., 2010, *Science*, 329, 408
- Lyne A.G., 2009, In Becker W., ed., *Astrophysics and Space Science Library*, vol. 357 of *Astrophysics and Space Science Library*, p. 67
- Lyne A.G., Manchester R.N., 1988, *MNRAS*, 234, 477

- Lyne A.G., Smith F.G., 2004, *Pulsar Astronomy*, 3rd ed. Cambridge University Press, Cambridge
- McKinnon M.M., 1993, *ApJ*, 413, 317
- Melrose D., Stoneham R., 1977, *Proc. Astr. Soc. Aust.*, 3, 120
- Mitra D., Rankin J.M., 2011, *ApJ*, 727, 92
- Naghizadeh-Khouei J., Clarke D., 1993, *A&A*, 274, 968
- Narayan R., Vivekanand M., 1982, *A&A*, 113, L3
- Noutsos A., Johnston S., Kramer M., Karastergiou A., 2008, *MNRAS*, 386, 1881
- Petrova S.A., 2008a, *ApJ*, 673, 400
- Petrova S.A., 2008b, *MNRAS*, 384, L1
- Petrova S.A., 2009, In Saikia D.J., Green D.A., Gupta Y., Venturi T., eds., *The Low-Frequency Radio Universe*, vol. 407 of *Astronomical Society of the Pacific Conference Series*, p. 333
- Press W.H., Flannery B.P., Teukolsky S.A., Vetterling W.T., 1986, *Numerical Recipes: The Art of Scientific Computing*. Cambridge University Press, Cambridge
- Radhakrishnan V., Cooke D.J., 1969, *Astrophys. Lett.*, 3, 225
- Rankin J.M., 1983, *ApJ*, 274, 333
- Rankin J.M., 1990, *ApJ*, 352, 247
- Rankin J.M., 1993, *ApJ*, 405, 285
- Rice J.A., 1995, *Mathematical Statistics and Data Analysis*, 2nd ed. Duxbury Press, Kentucky
- Ruderman M.A., Sutherland P.G., 1975, *ApJ*, 196, 51
- Stairs I.H., 2004, *Science*, 304, 547
- Stinebring D.R., Cordes J.M., Rankin J.M., Weisberg J.M., Boriakoff V., 1984, *ApJS*, 55, 247

- Sturrock P.A., 1971, *ApJ*, 164, 529
- Tauris T.M., Manchester R.N., 1998, *MNRAS*, 298, 625
- van Leeuwen J., 2012, *ArXiv*
- van Straten W., 2004, *ApJS*, 152, 129, preprint, astro-ph/0401536
- van Straten W., 2006, *ApJ*, 642, 1004
- van Straten W., Demorest P., Osłowski S., 2012, *ArXiv*
- Wang H.G., Qiao G.J., Xu R.X., Liu Y., 2006, *MNRAS*, 366, 945
- Wardle J., Kronberg P., 1974, *ApJ*, 194, 249
- Weltevrede P., Johnston S., 2008a, *MNRAS*, 391, 1210
- Weltevrede P., Johnston S., 2008b, *MNRAS*, 387, 1755
- Weltevrede P., Wright G., 2009, *MNRAS*, 395, 2117
- Weltevrede P., Wright G., Johnston S., 2012, *MNRAS*, 424, 843
- Weltevrede P., et al., 2010, *ApJ*, 708, 1426
- Wu X., Manchester R.N., Lyne A.G., Qiao G., 1993, *MNRAS*, 261, 630
- Xilouris K.M., 1991, *A&A*, 248, 323
- Young M.D.T., Chan L.S., Burman R.R., Blair D.G., 2010, *MNRAS*, 402, 1317